ACS APPLIED MATERIALS & INTERFACES

www.acsami.org

Research Article

Long-Lived Interlayer Excitons in WS_2/Ruddlesden–Popper Perovskite van der Waals Heterostructures

Ashish Soni, Supriya Ghosal, Milon Kundar, Swapan K. Pati, and Suman Kalyan Pal*

Cite This: *ACS Appl. Mater. Interfaces* 2024, 16, 35841–35851

Read Online

ACCESS | Metrics & More | Article Recommendations | Supporting Information

ABSTRACT: Two-dimensional (2D) transition metal dichalcogenides (TMDs) and perovskites hold substantial promise for various optoelectronic applications such as light emission, photodetection, and energy harvesting. However, each of these materials possesses certain limitations that can be overcome by synergistically combining them to form heterostructures, thereby unveiling intriguing optical properties. In this study, we present an uncomplicated technique for crafting a van der Waals (vdW) heterojunction comprising monolayer WS_2 and a Ruddlesden–Popper (RP) perovskite, namely $(TEA)_2PbI_4$. By utilizing ultrafast transient absorption (TA) spectroscopy, we explored the charge carrier dynamics within the $WS_2/(TEA)_2PbI_4$ heterostructure. Our findings uncover a type-II band alignment in the heterostructure, facilitating rapid (within 260 fs) hole transfer from WS_2 to the perovskite and leading to the formation of interlayer excitons (IXs) with a much longer lifetime (728 ps). This strategic approach has the potential to contribute to the development of hybrid systems aimed at achieving high-performance optoelectronic devices.

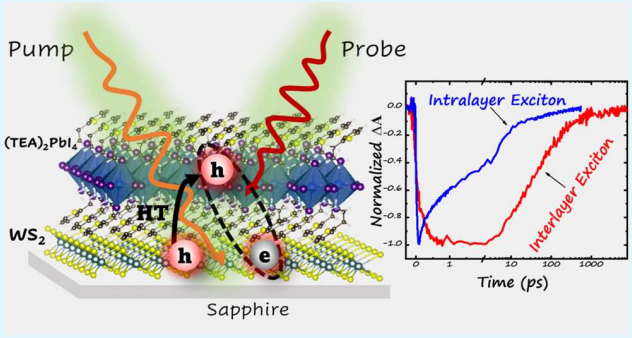

KEYWORDS: *ultrafast optics, transition metal dichalcogenides (TMDs), 2D materials, type-II heterostructure, 2D Ruddlesden–Popper perovskite, interlayer excitons*

Downloaded via EMORY UNIV on December 9, 2024 at 00:00:05 (UTC).
See https://pubs.acs.org/sharingguidelines for options on how to legitimately share published articles.

INTRODUCTION

Atomically thin two-dimensional (2D) transition metal dichalcogenides such as MoS_2, WS_2, WSe_2, etc., are recognized as a captivating class of materials with remarkable potential for low energy consumption and ultrathin optoelectronic applications.[1−3] The development of various growth techniques for the precise synthesis of 2D materials has paved the way for the emergence of vdW heterostructure-based high-performance optoelectronic devices.[4,5] Recently, another family of 2D materials, known as 2D Ruddlesden–Popper (RP) perovskites, has garnered significant attention due to their intriguing properties, including remarkable absorption coefficient, high photoluminescence quantum yield, high carrier mobility, and several other advantages that surpass those of their 3D counterparts.[6−8] Historically, RP phases are named after S. N. Ruddlesden and P. Popper, who first synthesized and described this unique structure in 1957.[9] These phases are a type of layered structure composed of alternating perovskite-type and rocksalt-type structures but do not contain any organic spacer cations. However, a 2D-RP perovskite typically exhibits a layered structure in which inorganic perovskite layers are separated by a layer of an organic spacer cation. The general formula for 2D-RP perovskite is $L_2A_{n-1}M_nX_{3n+1}$, wherein L represents the spacer cation, A denotes a monovalent cation, M stands for a divalent metal cation, X represents a halide ion, and n indicates the number of inorganic octahedral layers separated by the spacer.[10] The incorporation of an organic spacer enhances the reliability of 2D-RP perovskites in terms of humidity stability,[11] structural integrity,[12,13] and thermal resilience.[14,15] These inherent attributes establish 2D-RP perovskites as viable candidates for efficient, sustainable, and high-performance optoelectronic devices. In contrast to TMDs, perovskites have demonstrated the ability to retain unique properties not only in monolayers but also in microscopic thin-film devices such as solar cells[16] or light-emitting diodes (LEDs).[17,18]

TMDs exhibit fascinating properties such as an exceptionally large binding energy,[19,20] spin or valley degree of freedom,[21,22] and exciton hall effects.[23] Several 2D TMD heterojunctions have been documented to host long-lived IXs, where electrons and holes occupy distinct layers due to charge transfer.[24−28] The integration of TMDs and 2D perovskites within vdW heterostructures holds the potential to enhance the efficiency

Received: May 5, 2024
Revised: June 13, 2024
Accepted: June 14, 2024
Published: June 27, 2024

ACS Publications

© 2024 American Chemical Society

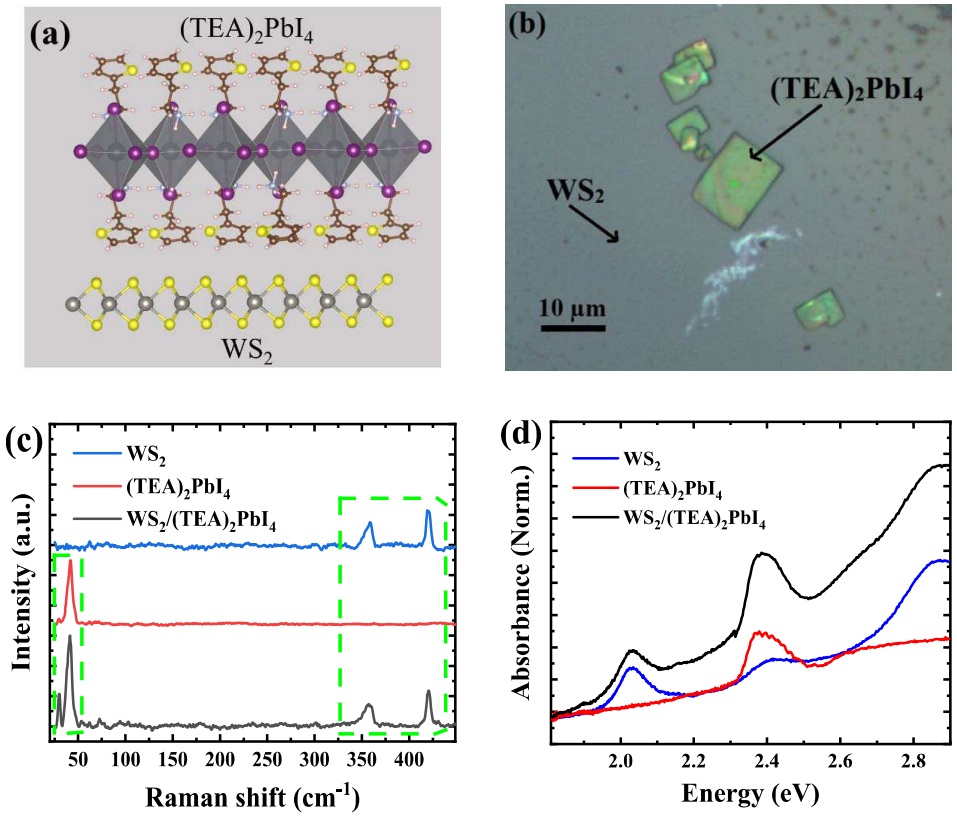

Figure 1. (a) Schematic illustration of the heterostructure of the $(TEA)_2PbI_4$ perovskite and monolayer WS_2. (b) Optical microscope image of the heterojunction formed by stacking $(TEA)_2PbI_4$ on the WS_2 monolayer. (c) Raman spectra of pristine WS_2 (blue), pristine $(TEA)_2PbI_4$ (red), and $WS_2/(TEA)_2PbI_4$ heterostructure (black). (d) Absorption spectra (normalized at ~1.75 eV) of pristine WS_2 (blue), pristine $(TEA)_2PbI_4$ perovskite (red), and $WS_2/(TEA)_2PbI_4$ heterostructure (black).

of heterojunction optoelectronic devices by leveraging the properties of the constituent materials. Thus, the concept of amalgamating TMDs and 2D perovskites serves not only to expand the library of novel heterostructures but also to unlock numerous avenues for exploring the diverse optoelectronic characteristics of these hybrid structures. Additionally, 2D heterostructures boast well-defined interfaces devoid of surface dangling bonds, resulting in reduced interface trap density and improved performance of functional devices.[29,30] The stacking, utilizing a bond-free approach, of RP perovskites with 2D TMDs is a straightforward strategy for creating a class of heterostructures that could lead to novel, synergistic, electronic, and optoelectronic phenomena.[31−34]

In recent years, there has been a proliferation of publications focusing on photodetection utilizing heterojunctions based on 2D perovskites and TMDs.[35−37] The amalgamation of perovskite and monolayer TMDs has been shown to significantly enhance the efficiency of carrier generation, thereby rendering the heterojunctions valuable for applications in photodetection and light harvesting.[36,38] For instance, Wang et al.[38] have demonstrated that 2D perovskites serve as excellent light-absorbing components, thereby augmenting the overall performance of photodetectors based on 2D TMDs. However, investigations into the fundamental processes occurring at the interface of 2D perovskites and TMD materials remain notably scarce. Noteworthy contributions include the observation of a large enhancement of photoluminescence (PL) in heterostructures of WS_2 and quasi-2D-RP perovskites.[39] This enhancement was attributed to an indirect-to-direct transition in the electronic structure of bilayer WS_2 due to charge transfer across the interface, as inferred from first-principles calculations. Additionally, Chen et al. reported the emission of IXs in 2D perovskites/WSe_2 heterostructures and speculated, based on band alignment, that such excitons are formed due to photoinduced hole transfer from WSe_2 to 2D perovskites.[40] More recently, Karpińska et al. demonstrated hole and energy transfer in WS_2/2D perovskite heterostructures.[41] They supported their theoretical predictions with steady-state reflectivity and photoluminescence studies. However, despite these advancements, the dynamics of interfacial charge transfer processes and IXs remain largely unexplored.

Here, we delve into the realm of ultrafast exciton dynamics within the vdW heterojunction involving monolayer WS_2 and a 2D-RP perovskite, employing transient absorption spectroscopy. Our findings illuminate the rapid charge transfer phenomena across the junction and the consequent emergence of IXs. Notably, these IXs display longer lifetimes compared to the intralayer excitons found in the individual constituent layers. This investigation establishes a robust avenue for achieving efficient charge transfer and cultivating long-lasting IXs through the strategic arrangement of monolayer WS_2 and 2D perovskite.

RESULTS AND DISCUSSION

$WS_2/(TEA)_2PbI_4$ Heterostructure. Figure 1a illustrates the schematic diagram of the fabricated WS_2/2D-RP perovskite heterostructure, consisting of a $(TEA)_2PbI_4$ perovskite layer on

https://doi.org/10.1021/acsami.4c07346
ACS Appl. Mater. Interfaces 2024, 16, 35841−35851

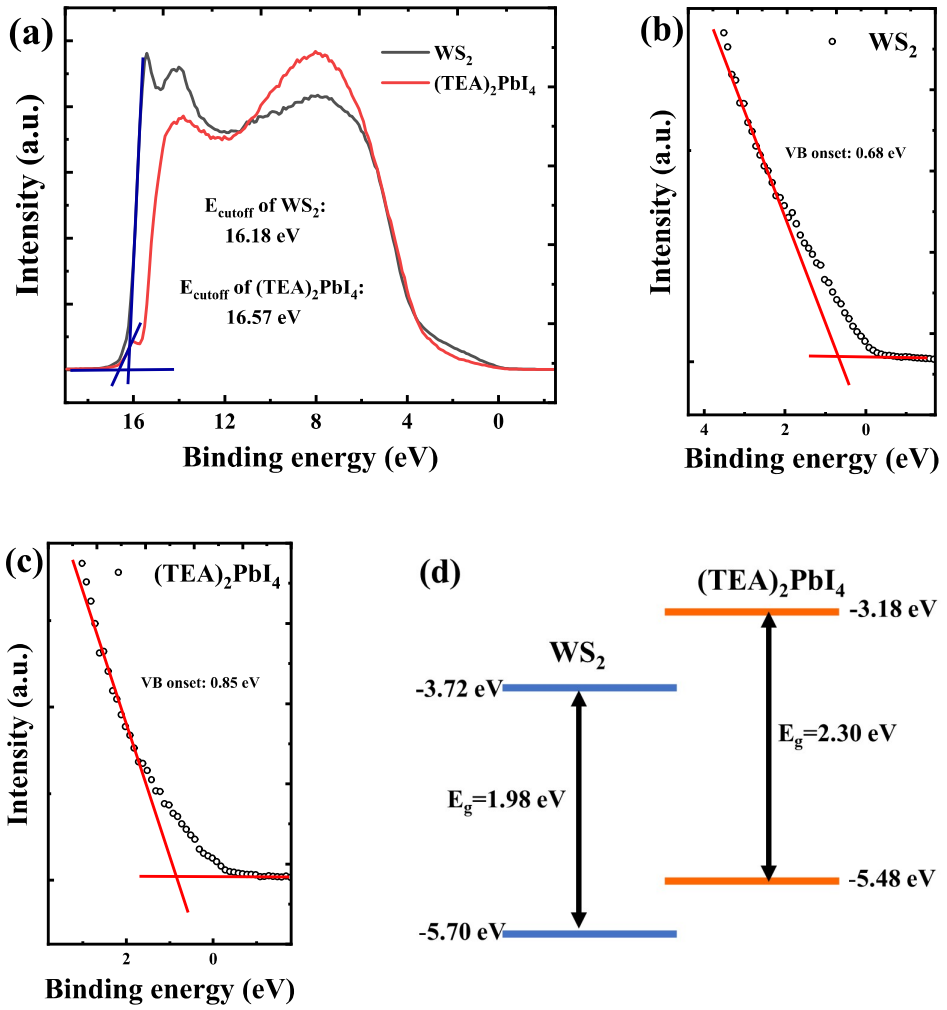

Figure 2. (a) Ultraviolet photoelectron spectroscopy (UPS) spectra of monolayer WS_2 (black) and 2D $(TEA)_2PbI_4$ perovskite (red). Enlarged view of the valence band onset of (b) WS_2 and (c) 2D $(TEA)_2PbI_4$, respectively. (d) Schematic representation of the band alignment of the WS_2/$(TEA)_2PbI_4$ heterojunction.

top of a WS_2 monolayer. The heterostructure was created by dry transfer of a perovskite layer onto a WS_2 monolayer grown via large-area chemical vapor deposition (CVD). A comprehensive account of the transfer process and heterostructure fabrication can be found in the experimental section. Optical imaging and Raman spectroscopy were used to verify the successful transfer of the perovskite onto the WS_2. Figure 1b depicts the optical microscope image of the WS_2/$(TEA)_2PbI_4$ heterostructure film, showing $(TEA)_2PbI_4$ flecks on the WS_2 film. The thickness of the $(TEA)_2PbI_4$ layer in the heterostructure was measured by using atomic force microscopy (AFM) and found to be 48.5 nm (Figure S1). The Raman peaks of bare WS_2, attributed to the E_{2g}^1 (in-plane vibration) and A_g^1 (out-of-plane vibration) modes, appear at 354 and 416 cm^{-1}, respectively (Figure 1c, black curve). These values align closely with prior research,[42] substantiating the monolayer character of WS_2. Raman mapping was conducted to confirm the thickness homogeneity of monolayer WS_2 across a sizable substrate area (Figure S2). The intensities of both the E_{2g}^1 and A_g^1 Raman modes display a consistent distribution (within experimental error) across the entire sample, suggesting a uniform thickness growth of WS_2 over a large area. On the other hand, $(TEA)_2PbI_2$ exhibits a Raman signature at 41.3 cm^{-1} (Figure 1c, red curve). The XRD patterns of $(TEA)_2PbI_4$ (Figure S3) reveal a small angle diffraction peak around 5.8°, corroborating the 2D nature of the perovskite.[10,43] The optical absorption spectra of WS_2, $(TEA)_2PbI_4$, and their heterostructure were measured at room temperature and are presented in Figure 1d. The absorption spectrum of WS_2 contains peaks at 2.03, 2.41, and 2.8 eV, corresponding to the A, B, and C excitonic transitions, respectively (Figure 1d, blue curve).[44] In contrast, the perovskite shows a single sharp absorption peak, attributed to its excitonic transition (Figure 1d, red curve).[10] Evidently, the absorption spectrum of the heterostructure encompasses the excitonic characteristics of both WS_2 and $(TEA)_2PbI_4$ (Figure 1d, red curve).

Band Alignment. We determined the band-edge energy for WS_2 and $(TEA)_2PbI_4$ by using ultraviolet photoelectron spectroscopy (UPS). The UPS spectra were recorded using a monochromatic He−I source with a radiation energy $E_{He(I)}$ = 21.2 eV, as presented in Figure 2. The work functions ($E_{He(I)} - E_{cutoff}$) of WS_2 and 2D $(TEA)_2PbI_4$ (calculated by estimating cutoff energy, E_{cutoff} from Figure 2a) are 5.02 and 4.63 eV, respectively. The valence band (VB) onset energies (E_{onset}) were evaluated by extrapolating the linear fit of the leading

https://doi.org/10.1021/acsami.4c07346
ACS Appl. Mater. Interfaces 2024, 16, 35841−35851

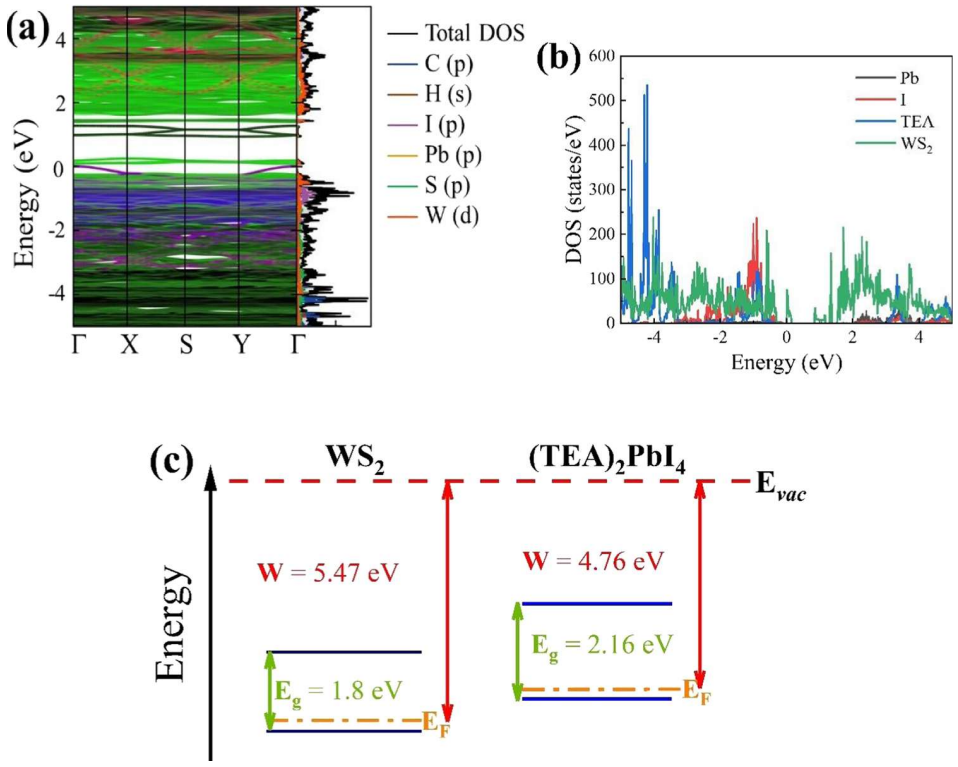

Figure 3. (a) Combined electronic band structure and density of states of the $WS_2/(TEA)_2PbI_4$ heterostructure with a focus on the significant atomic contributions. The corresponding color codes are indicated in the inset of the figure. (b) Density of states of the $WS_2/(TEA)_2PbI_4$ heterostructure highlighting the contributions of PbI_4, TEA, and WS_2 layers. (c) Band alignment of $(TEA)_2PbI_4$ and monolayer WS_2 in the heterostructure. Vacuum energy levels and Fermi levels are represented by red and orange dashed lines.

edges of VB spectra (Figure 2b,c). The values of E_{onset} for $(TEA)_2PbI_4$ and WS_2 are found to be at 0.85 and 0.68 eV, respectively. The VBM energy (E_{VBM}) and conduction band minimum (CBM) energy (E_{CBM}) were determined from the following equations,

$$E_{VBM} = -(E_{He(I)} - E_{cutoff} + E_{onset}) \quad (1)$$

$$E_{CBM} = E_{VBM} + E_{bandgap} \quad (2)$$

We used the reported values of band gap energy ($E_{bandgap}$) to compute the values of E_{CBM}. The $E_{bandgap}$ values for WS_2 and $(TEA)_2PbI_4$ are 1.98 and 2.30 eV, respectively.[10,45] A diagram illustrating the band positions of WS_2 and $(TEA)_2PbI_4$, drawn by using calculated values of E_{VBM} and E_{CBM}, is presented in Figure 2d. Notably, from the absorption spectrum of the heterostructure (Figure 1d), it is evident that the low-energy edges of the excitonic peaks of WS_2 and $(TEA)_2PbI_4$ do not appreciably change in the heterostructure. This indicates that the band gap of the individual materials does not undergo significant alteration upon forming the heterostructure, and Figure 2d effectively represents the band alignment of the heterostructure. Clearly, our van der Waals heterostructure possesses a type-II band alignment. The energy difference between VBMs (CBMs) of WS_2 and $(TEA)_2PbI_4$ is 0.22 eV (0.54 eV), a factor that could favor charge transfer across the interface.

DFT Calculations. To verify experimental findings, we also conducted theoretical studies on the $WS_2/(TEA)_2PbI_4$ heterostructure using density functional theory (see Theoretical analysis section of Supporting Information). Before the heterostructure was formed, both the perovskite and WS_2 monolayers were optimized separately. The energetic stability of the $WS_2/(TEA)_2PbI_4$ heterostructure was confirmed by analyzing the binding energy (E_b) according to the following relation[46]

$$E_b = E_{WS_2/(TEA)_2PbI_4} - E_{(TEA)_2PbI_4} - E_{WS_2} \quad (3)$$

where $E_{WS_2/(TEA)_2PbI_4}$, $E_{(TEA)_2PbI_4}$, and E_{WS_2} are the total energies for $WS_2/(TEA)_2PbI_4$ heterostructure, $(TEA)_2PbI_4$, and WS_2 monolayer, respectively. The binding energy per unit area of the $WS_2/(TEA)_2PbI_4$ heterostructure is found to be −0.0639 eV/Å^2 from eq 3. The optimized geometry has further been utilized for analyzing electronic structure, charge density profile, and band alignment (Figure 3). The analysis of the electronic band structure reveals that the 2D perovskite system $(TEA)_2PbI_4$ and monolayer WS_2 both exhibit a semiconducting nature, with direct band gaps of 2.16 and 1.80 eV, respectively. These DFT calculated band positions of WS_2 and $(TEA)_2PbI_4$ agree well with the band alignment from experimental measurement as well as with the previous report.[47] In the heterostructure, the projected band structure analysis indicates that the top of the valence band is predominantly formed by contributions from the PbI_4 layer, while the minimum of the conduction band is largely contributed by the WS_2 monolayer (Figure S4(d)).

The importance of band alignment in explaining the charge transfer in layered heterostructure has been highlighted in the previous literature.[48,49] By considering the vacuum level as a reference energy position, we conducted an analysis of the band alignment of the $WS_2/(TEA)_2PbI_4$ heterostructure. Utilizing vacuum energy levels, work functions, and VBM and CBM energy values, we accurately determined the band

https://doi.org/10.1021/acsami.4c07346
ACS Appl. Mater. Interfaces 2024, 16, 35841−35851

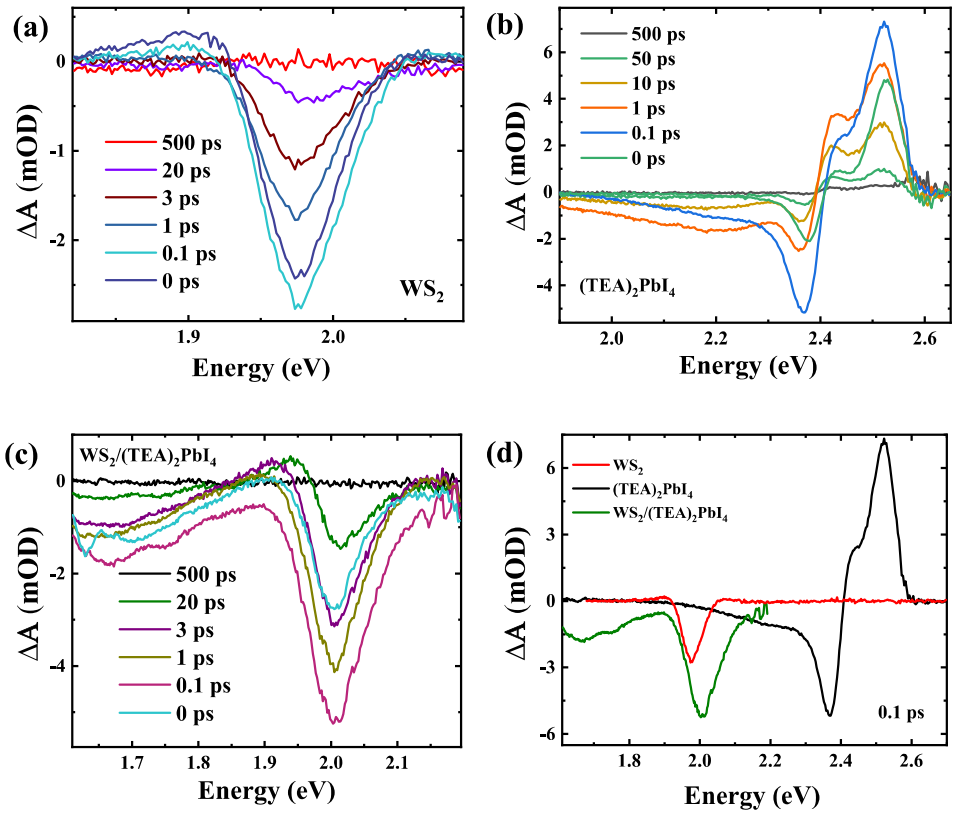

Figure 4. Plots of the transient absorption spectra of (a) WS_2 (excitation energy 2.21 eV and fluence 4.8×10^{13} cm^{-2}), (b) $TEA)_2PbI_4$ (excitation energy 2.58 eV and fluence 4.8×10^{13} cm^{-2}), and (c) $WS_2/(TEA)_2PbI_4$ (excitation energy 2.21 eV and fluence 5.7×10^{13} cm^{-2}), respectively. (d) Comparison of TA spectra at 0.1 ps for different samples.

alignment of the heterostructure (Figure 3c). Our analysis reveals a type-II band alignment, where the CBM of WS_2 falls within the forbidden region of the $(TEA)_2PbI_4$ perovskite system, while the VBM of WS_2 is lower in energy compared to the VBM of $(TEA)_2PbI_4$, resulting in a staggered configuration. The band analysis suggests a hole transfer from the VBM of WS_2 to the VBM of $(TEA)_2PbI_4$ and electron transfer in the opposite direction. Nonetheless, the charge density analysis of the $WS_2/(TEA)_2PbI_4$ reveals similar charge transfer pathways in the heterostructure (refer to the Theoretical analysis section of Supporting Information for further details). Moreover, we estimated the exciton binding energy (E_{ex}) in the individual materials and their heterostructure using a hydrogen atom-like model of exciton (see Theoretical analysis section of Supporting Information). The obtained values of E_{ex} are 0.715 eV for WS_2, 0.381 eV for $(TEA)_2PbI_4$, and 0.407 eV for their heterostructure. The much higher value of the exciton binding energy in the heterostructure compared to the room temperature thermal energy suggests the possibility of IXs formation in the $WS_2/(TEA)_2PbI_4$ heterostructure.

Photoinduced Absorption. Transient absorption (TA) spectroscopy has emerged as a valuable tool for investigating dynamic processes. Hence, we employed TA spectroscopy to monitor the behavior of photoexcited charge carriers in WS_2, $(TEA)_2PbI_4$, and their heterostructure. In TA measurements, a pump pulse stimulates the movement of electrons from the VB to the conduction band (CB). Subsequently, a broad-spectrum pulse is utilized to analyze the photoinduced alterations in the sample by monitoring changes in absorbance (ΔA) across both energy and time dimensions. Initially, we recorded the TA spectra of WS_2 and $(TEA)_2PbI_4$ over a wide spectral range (1.6−2.8 eV). At an excitation photon energy of 2.21 eV, the TA spectra of WS_2 exhibited a photobleaching (PB) band at 1.98 eV and a photoinduced absorption (PIA) peak at 1.89 eV (Figure 4a). The steady-state absorption corresponding to the A-excitonic transition of WS_2 is observed around 1.98 eV, thereby attributing the PB feature to the A-exciton. The origin of PIA in the TA spectra of WS_2 has been extensively discussed in our prior work on monolayer WS_2.[50] In that work, we established that the PIA band primarily arises from the absorption of the probe light by charge carriers trapped by defects.

In Figure 4b, TA spectra of $(TEA)_2PbI_4$ are depicted, obtained by using an excitation photon energy of 2.58 eV. The spectra exhibit both a negative and a positive band at energies of 2.36 and 2.5 eV, respectively. Notably, the distinct negative TA band emerges at an energy corresponding to the ground state absorption band of the perovskite due to excitons (Figure 1d). Consequently, the negative TA band at 2.36 eV in $(TEA)_2PbI_4$ can be attributed to excitons formed by the state filling of the electrons and holes. To comprehend the appearance of the PIA band in the TA spectra of the perovskite, we conducted a comparison of TA kinetics measured at 2.36 and 2.5 eV (Figure S5). The nearly identical nature of TA kinetics at these two energies suggests that the positive feature around 2.5 eV in the TA spectra likely originates from the absorption of the probe light by carriers situated at the band edge.

Next, TA spectra of the $WS_2/(TEA)_2PbI_4$ heterostructure were acquired using an excitation photon energy of 2.21 eV

https://doi.org/10.1021/acsami.4c07346
ACS Appl. Mater. Interfaces 2024, 16, 35841−35851

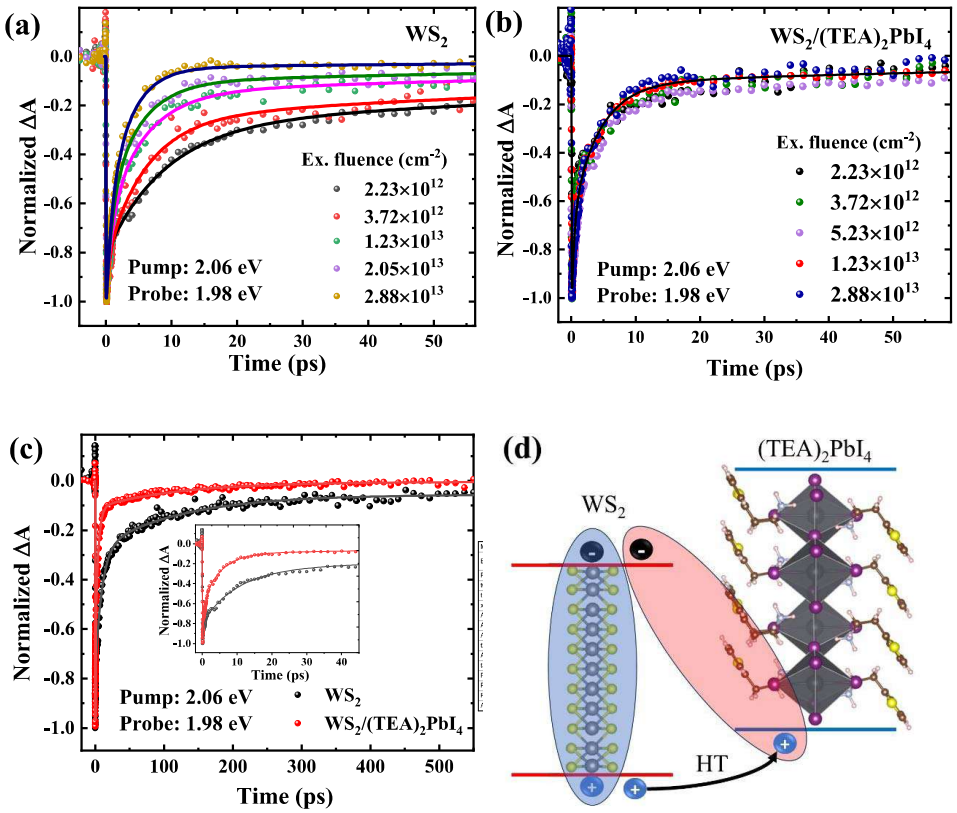

Figure 5. (a) Normalized excitation fluence-dependent kinetics of monolayer WS_2 measured with 2.06 eV excitation and 1.98 eV probe pulses. (b) Pump fluence-dependent decay kinetics of the $WS_2/(TEA)_2PbI_4$ heterostructure. (c) Comparison between the decay kinetics of the bleach signal for WS_2 and the $WS_2/(TEA)_2PbI_4$ heterostructure at 2.06 eV excitation and 2.23×10^{12} cm^{-2} fluence. (d) Schematic of the hole transfer process in the $WS_2/(TEA)_2PbI_4$ heterostructure.

and a pump fluence of 5.7×10^{13} cm^{-2} (Figure 4c). We proceeded to compare the TA spectra (at 0.1 ps) of WS_2, $(TEA)_2PbI_4$, and their heterostructure (Figure 4d) to discern the distinctions among the photoinduced processes occurring in these three systems. The PB band observed around 2 eV in the heterostructure can be attributed to the intralayer A-exciton in WS_2, as it closely aligns with the PB peak of the A-excitonic transition in pristine WS_2. Notably, the TA spectra of the heterostructure do not reveal the characteristic signature of the pristine perovskite, owing to the excitation energy being lower than the perovskite's band gap. However, a new negative band emerges in the TA spectra of the heterostructure centered at around 1.7 eV (Figure 4c,d). This low-energy bleach band in the TA spectra is likely the result of the formation of an IX within the $WS_2/(TEA)_2PbI_4$ heterostructure.

Charge Transfer in Heterostructure. Furthermore, we measured the decay kinetics of WS_2 and the $WS_2/(TEA)_2PbI_4$ heterostructure, using an excitation energy of 2.06 eV. This specific energy excites only the A-exciton of WS_2. To probe the bleach signal of the A-exciton of WS_2 in both samples, a laser pulse with a photon energy of 1.98 eV was employed. The decay kinetic measurements were carried out within the linear range of pump fluence (Figure S6). The time evolution of the PB signal of WS_2 at varying pump fluences of up to 50 ps is depicted in Figure 5a and Figure S7(a). The pump fluence-dependent TA kinetics indicate that the dynamics of carriers in WS_2 are influenced by the concentration of photocarriers. The PB kinetics were fitted with a multiexponential function described by

$$\Delta A = A_1 \exp\left(-\frac{t}{T_1}\right) + A_2 \exp\left(-\frac{t}{T_2}\right) + A_3 \exp\left(-\frac{t}{T_3}\right) \quad (4)$$

where, T_i (i = 1, 2, 3) is the time constant and A_i represents fractional contribution of the i^{th} decay component. The fitting outcomes (Table S3) reveal the presence of three decay components: a rapid one ($T_1 \sim 0.34-1.1$ ps), an intermediate one ($T_2 \sim 3.5-9$ ps), and a slower one ($T_3 \sim 120$ ps). The rapid initial decay could arise from two possible mechanisms: the formation of excitons from free charge carriers[51] or the trapping of band-edge charge carriers by defect states.[50,52] Given that our excitation was in close proximity to the band edge, the likelihood of direct exciton formation is quite high, implying that excitons predominantly contribute to the maximum bleach signal. Conversely, the lifetime (T_1) of the swift decay component increases as the pump fluence rises (Table S3). This phenomenon could be attributed to the trapping of bound charge carriers (excitons) within the system,[53−55] thus leading to the initial decay. The intermediate decay time (T_2) shortens with the rise in excitation fluence, suggesting that this decay stems from carrier-density-dependent Auger processes.[50,56,57] The third long decay component (with decay constant T_3) can be attributed to exciton recombination, aligning with findings in previous literature.[50,58]

Figure 5b shows normalized bleach kinetics of the $WS_2/(TEA)_2PbI_4$ heterostructure up to 50 ps under different

https://doi.org/10.1021/acsami.4c07346
ACS Appl. Mater. Interfaces 2024, 16, 35841−35851

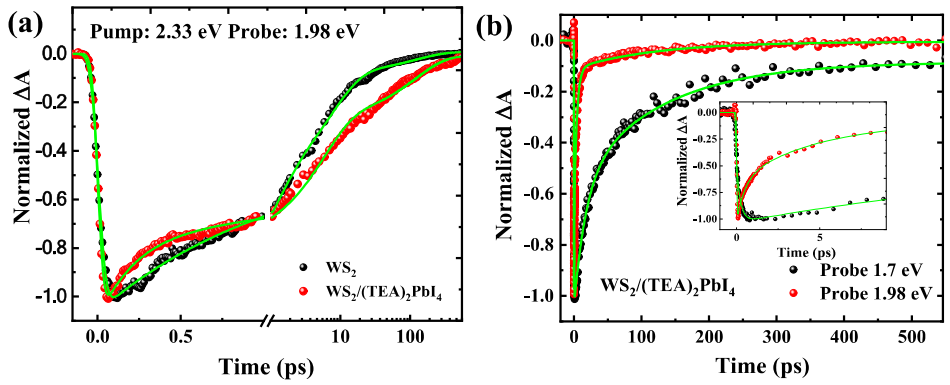

Figure 6. (a) Comparison of decay kinetics for WS_2 vs $WS_2/(TEA)_2PbI_4$ heterostructure at 1.98 eV, pumped at 2.33 eV. (b) Comparison between the two different bleach signals at 1.7 and 1.98 eV in the $WS_2/(TEA)_2PbI_4$ heterostructure sample.

Table 1. IXs in 2D TMD-Based Heterostructures[a]

heterostructure	formation mechanism	lifetime of IX (ns)	measurement technique	temperature	reference
$WS_2/(TEA)_2PbI_4$	HT	0.728	TA kinetics	RT	this work
graphene/MoS_2	ET	0.018	TA kinetics	RT	59
MoS_2/WS_2	HT	0.648	TA kinetics	RT	60
3 L $MoSe_2$/3L WS_2	ET	0.030−0.045	TA kinetics	RT	61
2 L WSe_2/PbI_4	HT	0.4−1.6	PL kinetics	78 K	62
1 L WSe_2/PbI_4	HT	3−9	PL kinetics	78 K	62
WS_2/PbI_4	ET	4.22	PL kinetics	3 K	63
2D-RP/WSe_2	HT	22	valley-polarized PL kinetics	80 K	28

[a]HT-hole transfer, ET-electron transfer, RT-room temperature.

excitation fluences (TA kinetics up to 550 ps are presented in Figure S7(b)). The likelihood of Auger recombination in the heterostructure is minimal, as evidenced by the nearly constant TA kinetics, irrespective of the excitation fluence. Subsequently, we conducted a comparison of the decay kinetics of the PB signal corresponding to the A- excitonic transition in both WS_2 and the $WS_2/(TEA)_2PbI_4$ heterostructure (measured at an excitation fluence of 2.23×10^{12} cm^{-2}). The findings indicated that the decay kinetics in the heterostructure are comparatively faster than those in WS_2 (Figure 5c). Multiexponential fitting of these TA kinetics was performed to derive the time constants of the associated decay components (Table S4). Evidently, from the fitting outcomes, it is discernible that the shortest time component as well as the average decay lifetime is reduced in the heterostructure. As observed from the band alignment of the heterostructure (obtained from both experiment and theory), there is a possibility of hole transfer from WS_2 to $(TEA)_2PbI_4$ due to the VBM of the former lying below that of the perovskite. Thus, the faster decay dynamics in the heterostructure could be attributed to the transfer of photoexcited charge carriers from the VB of WS_2 to that of $(TEA)_2PbI_4$. The charge transfer process is schematically depicted in Figure 5d.

Next, we used a pump-photon energy of 2.33 eV, which is sufficient to excite both WS_2 and $(TEA)_2PbI_4$ in the heterostructure. The decay kinetics of the PB signal at 1.98 eV, corresponding to the A-exciton of WS_2, were measured and compared (Figure 6a). It is evident that bleach recovery in WS_2 occurs more rapidly than that in $WS_2/(TEA)_2PbI_4$. Exponential functions were applied to fit both kinetics, and the fitted parameters are detailed in Table S5. The fitting results indicate that the initial decay of the A-excitonic bleach in the $WS_2/(TEA)_2PbI_4$ heterostructure (~0.22 ± 0.01 ps) is significantly faster compared to that of WS_2 (~0.93 ± 0.04 ps). These observations further support the idea that interlayer charge transfer is occurring within the heterostructure.

Interlayer Exciton. The emergence of a new bleach band around 1.7 eV in the TA spectra of the $WS_2/(TEA)_2PbI_4$ heterostructure was previously noted (Figure 4c). To ascertain the origin of this low-energy band, TA kinetics measurements were conducted at 1.7 eV, utilizing an excitation photon energy of 2.06 eV. This choice of pump energy was made intentionally to selectively excite WS_2 while avoiding excitation of $(TEA)_2PbI_4$. The resulting TA kinetics at 1.7 eV exhibits significant differences compared to those at 1.98 eV (Figure 6b). Notably, the bleach recovery at 1.7 eV is significantly slower compared to that at 1.98 eV. Nevertheless, the TA signal at 1.7 eV displays a prolonged rise (inset of Figure 6b). Through fitting the kinetics at 1.7 eV, we identified one rise component (T_1(rise) ~ 0.26 ± 0.01 ps) and two decay components (T_2 = 24.44 ± 1.04 ps and T_3 > 513 ps). The rise time of the TA signal at 1.7 eV is comparable to the fast decay of the bleach signal at 1.98 eV (corresponding to the A-exciton of WS_2) within the heterostructure. This observation suggests the formation of a new species through the dissociation of excitons in WS_2 due to hole transfer (within 260 fs) to the perovskite. In $(TEA)_2PbI_4$, the transferred hole can combine with an electron in WS_2 to give rise to IXs, leading to the appearance of the bleach band in the TA spectra. It is important to note that the TA signal of the heterostructure at 1.7 eV does not fully decay within 550 ps, indicating a slower recombination (longer lifetime) of IXs. To estimate the lifetime of these IXs, we extended our measurements of TA kinetics at 1.7 eV up to an 8 ns pump−probe delay (Figure S8). The TA kinetics at 1.7 eV is effectively fitted with a multiexponential function, indicating that IXs can undergo

https://doi.org/10.1021/acsami.4c07346
ACS Appl. Mater. Interfaces 2024, 16, 35841−35851

decay through various pathways (Figure S8). Notably, the largest time constant obtained is 728.23 ± 0.22 ps (Table S6), markedly exceeding the lifetimes of intralayer excitons in WS_2 (~120 ps, Table S3) and $(TEA)_2PbI_4$ (~20 ps, Figure S5). These findings provide strong evidence in support of our assertion regarding the presence of long-lived IXs within the $WS_2/(TEA)_2PbI_4$ heterostructure.

To further confirm the presence of IXs in the $WS_2/(TEA)_2PbI_4$ heterostructure, we conducted photoluminescence (PL) measurements using a confocal microscope. The PL images of the heterostructure are provided in Figure S9. Under excitation with a 488 nm laser, we observed red emissions in the range 575−625 nm, corresponding to the emission of WS_2, along with green emissions (500−550 nm) from $(TEA)_2PbI_4$. Interestingly, excitation with a 560 nm laser, which selectively excites WS_2, resulted in a weak red emission (662 and 738 nm) from the heterostructure. The energy difference between the CB of WS_2 and the VB of $(TEA)_2PbI_4$ is ~1.7 eV (Figure 2d). The radiative recombination of the IX formed by combining a hole in the VB of the perovskite and an electron in the CB of WS_2 is expected to emit a photon of energy 1.7 eV. Therefore, the observed PL in the energy range 1.68−1.87 eV could be attributed to the IXs formed via hole transfer from WS_2 to $(TEA)_2PbI_4$ (Figure 5d).

In Table 1, a summary of findings from previous studies on IXs observed in TMD-based heterostructures, including TMD/TMD and TMD/perovskite configurations, is presented to compare the lifetimes of IXs formed in these systems. It is apparent from the table that the lifetime of IXs was determined not only at different temperatures but also using various techniques. Remarkably, the IX lifetime in $WS_2/(TEA)_2PbI_4$ exceeds that of the TMD/TMD and graphene/TMD heterostructures investigated at room temperature using TA spectroscopy. However, the observed lifetime is shorter than those measured at low temperatures, which is reasonable considering that thermally activated recombination routes are not as prevalent at lower temperatures. These observations suggest that IXs in type-II heterostructures composed of 2D TMDs and perovskites can lead to longer carrier lifetimes and enhanced long-range charge transport. Consequently, the performance of TMD-based optoelectronic devices, typically constrained by short excitonic lifetimes, may be enhanced due to the formation of IXs in 2D TMD/perovskite heterostructures.

CONCLUSIONS

To summarize, our study delves into the intricate mechanisms governing charge transfer at the $WS_2/(TEA)_2PbI_4$ heterostructure interface, employing the precision of femtosecond pump−probe techniques. Through our XPS and theoretical investigations, we have revealed a distinct type-II band alignment within the heterostructure, setting the stage for charge transfer from WS_2 to $(TEA)_2PbI_4$. The appearance of a new bleach band in the TA spectra of the heterostructure strongly suggests the formation of IXs. Our TA kinetics measurements in the heterostructure, focusing on the A-exciton bleach band of WS_2, have shown a reduction in exciton lifetime attributed to hole transfer at the interface. Notably, the kinetics measurements reveal the rapid formation of these IXs within a remarkably brief duration of 260 fs. Furthermore, these IXs exhibit an impressive extended lifetime, surpassing 700 ps. The outcomes of this study are poised to propel significant advancements in optoelectronic devices centered around van der Waals heterostructures.

METHODS

Sample Preparation. *$(TEA)_2PbI_4$.* 2D perovskite $(TEA)_2PbI_4$ was prepared by dissolving 0.2 mmol of 2-thiopheneethylamine iodide (TEAI) salt and 0.1 mmol of lead iodide (PbI_2) powder with a stoichiometric ratio in 100 μL of dimethylformamide (DMF) to obtain a precursor solution. Fifty microliters of the perovskite precursor solution was then quickly added to 10 mL of toluene and stirred until completely dissolved. After centrifugation at 5000 rpm for 30 s, 2D perovskite $(TEA)_2PbI_4$ was obtained.

$WS_2/(TEA)_2PbI_4$ Heterostructure. WS_2 monolayer film grown on a sapphire substrate was purchased from Ossila Pvt. Ltd. $(TEA)_2PbI_4$ perovskite prepared by chemical synthesis method (as discussed previously) was drop casted on a silicon substrate and kept under an IR lamp to dry it properly. Then the sample was kept in vacuum for 1 h to remove the residual toluene solvent. 2D $(TEA)_2PbI_4$ perovskite crystals then exfoliated from the drop casted film using a Poly(dimethylsiloxane) (PDMS) stamp and transferred on the WS_2 film by dry transfer technique. Thus, the prepared $WS_2/(TEA)_2PbI_4$ heterostructure was kept in the desiccator before and after a measurement to avoid any contamination and oxidation.

UV−Vis Absorption and Raman Measurements. A Shimadzu UV-2450 spectrometer (Agilent Technologies) was used to measure the absorption spectra of WS_2, $(TEA)_2PbI_4$, and their heterostructure within an energy range of 1.7−3 eV. Moreover, a Horiba Jobin-Yvon (Lab-RAM HR evolution) Raman spectrometer was used for recording Raman spectra in the backscattering configuration under an optical microscope at room temperature. The sample was excited by a laser of wavelength 633 nm through a 100× objective lens. A monochromator analyzed the signals using a grating with 1800 line/mm. A Peltier-cooled charge-coupled device detector in a backscattering configuration was used to detect the signals. All of the measurements were performed on the sapphire substrate at room temperature.

Computational Methods. Theoretical calculations were carried out in the framework of density functional theory as implemented in the Vienna *Ab initio* Simulation Package (VASP).[64] The projector augmented wave (PAW) method was employed to describe the ion-electron interaction.[65] The generalized gradient approximation (GGA) in the form of a Perdew−Burke−Ernzerhof (PBE) was selected to approximate the exchange and correlation effects. Prior to further calculations, 2D hybrid perovskite $(TEA)_2PbI_4$, monolayer WS_2, and the combined heterostructure $WS_2/(TEA)_2PbI_4$ were geometrically optimized until the unbalanced force components converge below a threshold value of 0.03 eV/Å. Self-consistent electronic loop convergence was achieved using a plane-wave cutoff energy of 550 eV in accordance with a total energy convergence tolerance around 5×10^{-5} eV. Brillouin zone (BZ) integrations were performed using a $9 \times 9 \times 1$ Monkhorst Pack (MP) k-grid sampling. A vacuum space of 30 Å was included in the perpendicular direction to prevent interactions between periodic images. To accurately model this heterostructure, van der Waals (vdW) corrections were incorporated at the many-body dispersion energy levels using the zero damping DFT-D3 method developed by Grimme.[66] Work functions (W) of the monolayers and heterostructure were calculated by using the following relation.

$$W = E_C - E_F \tag{5}$$

Here E_C and E_F represent the vacuum energy level and Fermi level of the system, respectively.

Transient Absorption Spectroscopy. A Ti:sapphire laser amplifier (Spitfire Ace, Spectra Physics) was employed for ultrafast transient absorption (TA) measurements. The pump and probe pulses were obtained from the amplifier by splitting the output beam (pulse width <35 fs and wavelength ~800 nm) into two components. The pump and probe pulses of different energies (used in single kinetics measurements) were obtained from the automated optical

https://doi.org/10.1021/acsami.4c07346
ACS Appl. Mater. Interfaces 2024, 16, 35841−35851

parametric amplifier (TOPAS Prime from Spectra Physics). In broadband TA measurement, the probe beam was a white-light continuum (WLC) generated by focusing a small fraction of 800 nm light on a CaF_2 (calcium fluoride) crystal. A delay stage was used in the probe path to control the time delay between the probe and pump beams. The absorbance of the probe beam was detected under the conditions with and without pump with the help of a mechanical chopper. TA spectra were recorded by dispersing the beam with a grating spectrograph (Acton Spectra Pro SP 2358) followed by a CCD array. Two photodiodes having variable gain were used to record TA kinetics.[50]

Confocal Microscopy. A Nikon Eclipse Ti inverted microscope was used for the confocal microscopy, and images were acquired using Nikon Nis-Element software. Diode lasers of wavelengths of 488 and 560 nm were used for sample excitation. The PL images were captured by choosing proper dichroic-filter sets.

■ ASSOCIATED CONTENT

Supporting Information

The Supporting Information is available free of charge at https://pubs.acs.org/doi/10.1021/acsami.4c07346.

Thickness measurement of the 2D $(TEA)_2PbI_4$ perovskite film using AFM; Raman mapping of monolayer WS_2; XRD pattern of 2D perovskite; theoretical analysis; comparison of TA kinetics measured at positive (PIA) and negative (PIB) bands of the TA spectra of $(TEA)_2PbI_4$; fluence-dependent decay kinetics of monolayer WS_2 and heterostructure probed at 1.98 eV; long decay kinetics (up to 8 ns) of the IXs; confocal PL imaging and results of multiexponential fitting of various TA kinetics in tabular form (PDF)

■ AUTHOR INFORMATION

Corresponding Author

Suman Kalyan Pal − *School of Physical Sciences, Indian Institute of Technology Mandi, Mandi 175005 Himachal Pradesh, India; Advanced Materials Research Centre, Indian Institute of Technology Mandi, Mandi 175005 Himachal Pradesh, India;* orcid.org/0000-0003-2498-6217; Email: suman@iitmandi.ac.in

Authors

Ashish Soni − *School of Physical Sciences, Indian Institute of Technology Mandi, Mandi 175005 Himachal Pradesh, India; Advanced Materials Research Centre, Indian Institute of Technology Mandi, Mandi 175005 Himachal Pradesh, India;* orcid.org/0000-0001-7429-576X

Supriya Ghosal − *Theoretical Sciences Unit, School of Advanced Materials (SAMat), Jawaharlal Nehru Centre for Advanced Scientific Research (JNCASR), Bangalore 560064, India;* orcid.org/0000-0003-0423-0914

Milon Kundar − *School of Physical Sciences, Indian Institute of Technology Mandi, Mandi 175005 Himachal Pradesh, India; Advanced Materials Research Centre, Indian Institute of Technology Mandi, Mandi 175005 Himachal Pradesh, India*

Swapan K. Pati − *Theoretical Sciences Unit, School of Advanced Materials (SAMat), Jawaharlal Nehru Centre for Advanced Scientific Research (JNCASR), Bangalore 560064, India;* orcid.org/0000-0002-5124-7455

Complete contact information is available at: https://pubs.acs.org/10.1021/acsami.4c07346

Notes

The authors declare no competing financial interest.

■ ACKNOWLEDGMENTS

Funding from the Science and Engineering Research Board (SERB), Government of India (Grant No. CRG/2018/003045) is gratefully acknowledged. A.S., M.K., and S.K.P. acknowledge the Advanced Materials Research Center (AMRC) of IIT Mandi for providing experimental facilities. S.K.Pati acknowledges SERB J C Bose National Fellowship and DST, Govt. of India for financial support. S.G. and S.K.Pati sincerely acknowledge NSM PARAMYUKTI for the computational facilities.

■ REFERENCES

(1) Li, F.; Xu, B.; Yang, W.; Qi, Z.; Ma, C.; Wang, Y.; Zhang, X.; Luo, Z.; Liang, D.; et al. High-Performance Optoelectronic Devices Based on van der Waals Vertical $MoS_2/MoSe_2$ Heterostructures. *Nano Res.* **2020**, *13*, 1053−1059.

(2) Sharma, A.; Mahlouji, R.; Wu, L.; Verheijen, M. A.; Vandalon, V.; Balasubramanyam, S.; Hofmann, J. P.; Kessels, W. M. M.; Bol, A. A. Large Area, Patterned Growth of 2D MoS_2 and Lateral MoS_2−WS_2 Heterostructures for Nano- and Opto-Electronic Applications. *Nanotechnology* **2020**, *31*, No. 255603, DOI: 10.1088/1361-6528/ab7593.

(3) Yan, B.; Ning, B.; Zhang, G.; Zhou, D.; Shi, X.; Wang, C.; Zhao, H. Ultra-Thin GeSe/WS_2 Vertical Heterojunction with Excellent Optoelectronic Performances. *Adv. Opt. Mater.* **2022**, *10*, No. 2102413, DOI: 10.1002/adom.202102413.

(4) Shim, J.; Kang, D.-H.; Kim, Y.; Kum, H.; Kong, W.; Bae, S.-H.; Almansouri, I.; Lee, K.; Park, J.-H.; et al. Recent Progress in van der Waals (vdW) Heterojunction-Based Electronic and Optoelectronic Devices. *Carbon* **2018**, *133*, 78−89.

(5) Massicotte, M.; Schmidt, P.; Vialla, F.; Schädler, K. G.; Reserbat-Plantey, A.; Watanabe, K.; Taniguchi, T.; Tielrooij, K. J.; Koppens, F. H. L. Picosecond Photoresponse in van der Waals Heterostructures. *Nat. Nanotechnol.* **2016**, *11*, 42−46.

(6) Xie, H.; Hao, S.; Bao, J.; Slade, T. J.; Snyder, G. J.; Wolverton, C.; Kanatzidis, M. G. All-Inorganic Halide Perovskites as Potential Thermoelectric Materials: Dynamic Cation Off-Centering Induces Ultralow Thermal Conductivity. *J. Am. Chem. Soc.* **2020**, *142*, 9553−9563.

(7) Zheng, Y.; Niu, T.; Ran, X.; Qiu, J.; Li, B.; Xia, Y.; Chen, Y.; Huang, W. Unique Characteristics of 2D Ruddlesden−Popper (2DRP) Perovskite for Future Photovoltaic Application. *J. Mater. Chem. A* **2019**, *7*, 13860−13872.

(8) Tian, X.; Zhang, Y.; Zheng, R.; Wei, D.; Liu, J. Two-Dimensional Organic−Inorganic Hybrid Ruddlesden−Popper Perovskite Materials: Preparation, Enhanced Stability, and Applications in Photodetection. *Sustain. Energy Fuels* **2020**, *4*, 2087−2113.

(9) Ruddlesden, S. N.; Popper, P. New Compounds of the K_2NiF_4 Type. *Acta Crystallogr.* **1957**, *10*, 538−539.

(10) Kundar, M.; Bhandari, S.; Chung, S.; Cho, K.; Sharma, S. K.; Singh, R.; Pal, S. K. Surface Passivation by Sulfur-Based 2D $(TEA)_2PbI_4$ for Stable and Efficient Perovskite Solar Cells. *ACS Omega* **2023**, *8*, 12842−12852.

(11) Smith, I. C.; Hoke, E. T.; Solis-Ibarra, D.; McGehee, M. D.; Karunadasa, H. I. A Layered Hybrid Perovskite Solar-Cell Absorber with Enhanced Moisture Stability. *Angew. Chem., Int. Ed.* **2014**, *53*, 11232−11235.

(12) Mitzi, D. B. Templating and Structural Engineering in Organic−Inorganic Perovskites. *J. Chem. Soc., Dalton Trans.* **2001**, 1−12.

(13) Quan, L. N.; Yuan, M.; Comin, R.; Voznyy, O.; Beauregard, E. M.; Hoogland, S.; Buin, A.; Kirmani, A. R.; Zhao, K.; et al. Ligand-Stabilized Reduced-Dimensionality Perovskites. *J. Am. Chem. Soc.* **2016**, *138*, 2649−2655.

(14) Protesescu, L.; Yakunin, S.; Bodnarchuk, M. I.; Krieg, F.; Caputo, R.; Hendon, C. H.; Yang, R. X.; Walsh, A.; Kovalenko, M. V. Nanocrystals of Cesium Lead Halide Perovskites ($CsPbX_3$, X = Cl, Br, and I): Novel Optoelectronic Materials Showing Bright Emission with Wide Color Gamut. *Nano Lett.* **2015**, *15*, 3692−3696.
(15) Zhang, T.; Dar, M. I.; Li, G.; Xu, F.; Guo, N.; Grätzel, M.; Zhao, Y. Bication Lead Iodide 2D Perovskite Component to Stabilize Inorganic A-$CsPbI_3$ Perovskite Phase for High-Efficiency Solar Cells. *Sci. Adv.* **2017**, *3*, No. e1700841, DOI: 10.1126/sciadv.1700841.
(16) Tsai, H.; Nie, W.; Blancon, J.-C.; Stoumpos, C. C.; Asadpour, R.; Harutyunyan, B.; Neukirch, A. J.; Verduzco, R.; Crochet, J. J.; et al. High-Efficiency Two-Dimensional Ruddlesden−Popper Perovskite Solar Cells. *Nature* **2016**, *536*, 312−316.
(17) Lin, K.; Xing, J.; Quan, L. N.; de Arquer, F. P. G.; Gong, X.; Lu, J.; Xie, L.; Zhao, W.; Zhang, D.; et al. Perovskite Light-Emitting Diodes with External Quantum Efficiency Exceeding 20 Per Cent. *Nature* **2018**, *562*, 245−248.
(18) Tsai, H.; Nie, W.; Blancon, J.-C.; Stoumpos, C. C.; Soe, C. M. M.; Yoo, J.; Crochet, J.; Tretiak, S.; Even, J.; et al. Stable Light-Emitting Diodes Using Phase-Pure Ruddlesden−Popper Layered Perovskites. *Adv. Mater.* **2018**, *30*, No. 1704217, DOI: 10.1002/adma.201704217.
(19) Hanbicki, A. T.; Currie, M.; Kioseoglou, G.; Friedman, A. L.; Jonker, B. T. Measurement of High Exciton Binding Energy in the Monolayer Transition-Metal Dichalcogenides WS_2 and WSe_2. *Solid State Commun.* **2015**, *203*, 16−20.
(20) Soni, A.; Kushavah, D.; Lu, L.-S.; Chang, W.-H.; Pal, S. K. Efficient Multiple Exciton Generation in Monolayer MoS_2. *J. Phys. Chem. Lett.* **2023**, *00306*, 2965−2972, DOI: 10.1021/acs.jpclett.3c00306.
(21) Soni, A.; Pal, S. K. Valley Degree of Freedom in Two-Dimensional van der Waals Materials. *J. Phys. D: Appl. Phys.* **2022**, *55*, No. 303003.
(22) Koperski, M.; Molas, M. R.; Arora, A.; Nogajewski, K.; Bartos, M.; Wyzula, J.; Vaclavkova, D.; Kossacki, P.; Potemski, M. Orbital, Spin and Valley Contributions to Zeeman Splitting of Excitonic Resonances in $MoSe_2$, WSe_2 and WS_2 Monolayers. *2D Mater.* **2019**, *6*, No. 015001.
(23) Kormányos, A.; Zólyomi, V.; Fal'ko, V. I.; Burkard, G. Tunable Berry Curvature and Valley and Spin Hall Effect in Bilayer MoS_2. *Phys. Rev. B* **2018**, *98*, No. 035408.
(24) Liu, Y.; Elbanna, A.; Gao, W.; Pan, J.; Shen, Z.; Teng, J. Interlayer Excitons in Transition Metal Dichalcogenide Semiconductors for 2D Optoelectronics. *Adv. Mater.* **2022**, *34*, No. 2107138, DOI: 10.1002/adma.202107138.
(25) Arora, A.; Drüppel, M.; Schmidt, R.; Deilmann, T.; Schneider, R.; Molas, M. R.; Marauhn, P.; de Vasconcellos, S. M.; Potemski, M.; et al. Interlayer Excitons in a Bulk van der Waals Semiconductor. *Nat. Commun.* **2017**, *8*, No. 639, DOI: 10.1038/s41467-017-00691-5.
(26) Miao, S.; Wang, T.; Huang, X.; Chen, D.; Lian, Z.; Wang, C.; Blei, M.; Taniguchi, T.; Watanabe, K.; et al. Strong Interaction between Interlayer Excitons and Correlated Electrons in WSe_2/WS_2 Moiré Superlattice. *Nat. Commun.* **2021**, *12*, No. 3608, DOI: 10.1038/s41467-021-23732-6.
(27) Yu, J.; Kuang, X.; Zhong, J.; Cao, L.; Zeng, C.; Ding, J.; Cong, C.; Wang, S.; Dai, P.; et al. Observation of Double Indirect Interlayer Exciton in WSe_2/WS_2 Heterostructure. *Opt. Express* **2020**, *28*, 13260−13268.
(28) Singh, S.; Gong, W.; Stevens, C. E.; Hou, J.; Singh, A.; Zhang, H.; Anantharaman, S. B.; Mohite, A. D.; Hendrickson, J. R.; et al. Valley-Polarized Interlayer Excitons in 2D Chalcogenide−Halide Perovskite−van der Waals Heterostructures. *ACS Nano* **2023**, *17*, 7487−7497.
(29) Liu, Y.; Weiss, N. O.; Duan, X.; Cheng, H.-C.; Huang, Y.; Duan, X. van der Waals Heterostructures and Devices. *Nat. Rev. Mater.* **2016**, *1*, No. 16042, DOI: 10.1038/natrevmats.2016.42.
(30) Leng, K.; Wang, L.; Shao, Y.; Abdelwahab, I.; Grinblat, G.; Verzhbitskiy, I.; Li, R.; Cai, Y.; Chi, X.; et al. Electron Tunneling at the Molecularly Thin 2D Perovskite and Graphene van der Waals Interface. *Nat. Commun.* **2020**, *11*, No. 5483, DOI: 10.1038/s41467-020-19331-6.
(31) Liu, Y.; Huang, Y.; Duan, X. van der Waals Integration before and Beyond Two-Dimensional Materials. *Nature* **2019**, *567*, 323−333.
(32) Geim, A. K.; Grigorieva, I. V. van der Waals Heterostructures. *Nature* **2013**, *499*, 419−425, DOI: 10.1038/nature12385.
(33) Novoselov, K. S.; Mishchenko, A.; Carvalho, A.; Castro Neto, A. H. 2D Materials and van der Waals Heterostructures. *Science* **2016**, *353*, No. aac9439, DOI: 10.1126/science.aac9439.
(34) Jariwala, D.; Marks, T. J.; Hersam, M. C. Mixed-Dimensional van der Waals Heterostructures. *Nat. Mater.* **2017**, *16*, 170−181.
(35) Erkılıç, U.; Solís-Fernández, P.; Ji, H. G.; Shinokita, K.; Lin, Y.-C.; Maruyama, M.; Suenaga, K.; Okada, S.; Matsuda, K.; et al. Vapor Phase Selective Growth of Two-Dimensional Perovskite/WS_2 Heterostructures for Optoelectronic Applications. *ACS Appl. Mater. Interfaces* **2019**, *11*, 40503−40511.
(36) Fu, Q.; Wang, X.; Liu, F.; Dong, Y.; Liu, Z.; Zheng, S.; Chaturvedi, A.; Zhou, J.; Hu, P.; et al. Ultrathin Ruddlesden−Popper Perovskite Heterojunction for Sensitive Photodetection. *Small* **2019**, *15*, No. 1902890, DOI: 10.1002/smll.201902890.
(37) Xie, C.; Liu, C.-K.; Loi, H.-L.; Yan, F. Perovskite-Based Phototransistors and Hybrid Photodetectors. *Adv. Funct. Mater.* **2020**, *30*, No. 1903907, DOI: 10.1002/adfm.201903907.
(38) Wang, Q.; Zhang, Q.; Luo, X.; Wang, J.; Zhu, R.; Liang, Q.; Zhang, L.; Yong, J. Z.; Yu Wong, C. P.; et al. Optoelectronic Properties of a van der Waals WS_2 Monolayer/2D Perovskite Vertical Heterostructure. *ACS Appl. Mater. Interfaces* **2020**, *12*, 45235−45242.
(39) Yang, A.; Blancon, J.-C.; Jiang, W.; Zhang, H.; Wong, J.; Yan, E.; Lin, Y.-R.; Crochet, J.; Kanatzidis, M. G.; et al. Giant Enhancement of Photoluminescence Emission in WS_2-Two-Dimensional Perovskite Heterostructures. *Nano Lett.* **2019**, *19*, 4852−4860.
(40) Chen, Y.; Liu, Z.; Li, J.; Cheng, X.; Ma, J.; Wang, H.; Li, D. Robust Interlayer Coupling in Two-Dimensional Perovskite/Monolayer Transition Metal Dichalcogenide Heterostructures. *ACS Nano* **2020**, *14*, 10258−10264.
(41) Karpińska, M.; Liang, M.; Kempt, R.; Finzel, K.; Kamminga, M.; Dyksik, M.; Zhang, N.; Knodlseder, C.; Maude, D. K.; et al. Nonradiative Energy Transfer and Selective Charge Transfer in a $WS_2/(PEA)_2PbI_4$ Heterostructure. *ACS Appl. Mater. Interfaces* **2021**, *13*, 33677−33684.
(42) Barbosa, A. N.; Figueroa, N. S.; Giarola, M.; Mariotto, G.; Freire, F. L. Straightforward Identification of Monolayer WS_2 Structures by Raman Spectroscopy. *Mater. Chem. Phys.* **2020**, *243*, No. 122599.
(43) Lanzetta, L.; Marin-Beloqui, J. M.; Sanchez-Molina, I.; Ding, D.; Haque, S. A. Two-Dimensional Organic Tin Halide Perovskites with Tunable Visible Emission and Their Use in Light-Emitting Devices. *ACS Energy Lett.* **2017**, *2*, 1662−1668.
(44) Zhu, B.; Chen, X.; Cui, X. Exciton Binding Energy of Monolayer WS_2. *Sci. Rep.* **2015**, *5*, No. 9218, DOI: 10.1038/srep09218.
(45) Terrones, H.; López-Urías, F.; Terrones, M. Novel Hetero-Layered Materials with Tunable Direct Band Gaps by Sandwiching Different Metal Disulfides and Diselenides. *Sci. Rep.* **2013**, *3*, No. 1549, DOI: 10.1038/srep01549.
(46) Fang, Q.; Li, M.; Zhao, X.; Yuan, L.; Wang, B.; Xia, C.; Ma, F. van der Waals Graphene/MoS_2 Heterostructures: Tuning the Electronic Properties and Schottky Barrier by Applying a Biaxial Strain. *Mater. Adv.* **2022**, *3*, 624−631.
(47) Muoi, D.; Hieu, N. N.; Phung, H. T. T.; Phuc, H. V.; Amin, B.; Hoi, B. D.; Hieu, N. V.; Nhan, L. C.; Nguyen, C. V.; et al. Electronic Properties of WS_2 and WSe_2 Monolayers with Biaxial Strain: A First-Principles Study. *Chem. Phys.* **2019**, *519*, 69−73.
(48) Mandal, S. K.; Ghosal, S.; Karmakar, D.; Jana, D. Ru-Doped ZnS as an Enhanced Visible Light-Driven Photocatalyst. In *Advances in Catalysts Research.*; Springer Nature Switzerland: Cham, 2024; pp 131−169.

(49) Limas, N. G.; Manz, T. A. Introducing DDEC6 Atomic Population Analysis: Part 4. Efficient Parallel Computation of Net Atomic Charges, Atomic Spin Moments, Bond Orders, and More. *RSC Adv.* **2018**, *8*, 2678−2707.
(50) Soni, A.; Kushavah, D.; Lu, L.-S.; Chang, W.-H.; Pal, S. K. Ultrafast Exciton Trapping and Exciton−Exciton Annihilation in Large-Area CVD-Grown Monolayer WS_2. *J. Phys. Chem. C* **2021**, *125*, 23880−23888.
(51) Ceballos, F.; Cui, Q.; Bellus, M. Z.; Zhao, H. Exciton Formation in Monolayer Transition Metal Dichalcogenides. *Nanoscale* **2016**, *8*, 11681−−11688.
(52) Liu, H.; Wang, C.; Zuo, Z.; Liu, D.; Luo, J. Direct Visualization of Exciton Transport in Defective Few-Layer WS_2 by Ultrafast Microscopy. *Adv. Mater.* **2020**, *32*, No. 1906540, DOI: 10.1002/adma.201906540.
(53) Xu, S.; Yang, J.; Jiang, H.; Su, F.; Zeng, Z. Transient Photoconductivity and Free Carrier Dynamics in a Monolayer WS_2 Probed by Time Resolved Terahertz Spectroscopy. *Nanotechnology* **2019**, *30*, No. 265706.
(54) Cunningham, P. D.; McCreary, K. M.; Hanbicki, A. T.; Currie, M.; Jonker, B. T.; Hayden, L. M. Charge Trapping and Exciton Dynamics in Large-Area CVD Grown MoS_2. *J. Phys. Chem. C* **2016**, *120*, 5819−5826.
(55) Wang, T.; Hopper, T. R.; Mondal, N.; Liu, S.; Yao, C.; Zheng, X.; Torrisi, F.; Bakulin, A. A. Hot Carrier Cooling and Trapping in Atomically Thin WS_2 Probed by Three-Pulse Femtosecond Spectroscopy. *ACS Nano* **2023**, *17*, 6330−6340.
(56) Cunningham, P. D.; McCreary, K. M.; Jonker, B. T. Auger Recombination in Chemical Vapor Deposition-Grown Monolayer WS_2. *J. Phys. Chem. Lett.* **2016**, *7*, 5242−5246.
(57) Lee, Y.; Ghimire, G.; Roy, S.; Kim, Y.; Seo, C.; Sood, A. K.; Jang, J. I.; Kim, J. Impeding Exciton−Exciton Annihilation in Monolayer WS_2 by Laser Irradiation. *ACS Photonics* **2018**, *5*, 2904−2911.
(58) Tsai, H.-S.; Huang, Y.-H.; Tsai, P.-C.; Chen, Y.-J.; Ahn, H.; Lin, S.-Y.; Lu, Y.-J. Ultrafast Exciton Dynamics in Scalable Monolayer MoS_2 Synthesized by Metal Sulfurization. *ACS Omega* **2020**, *5*, 10725−10730.
(59) Zou, Y.; Ma, Q.-S.; Zhang, Z.; Pu, R.; Zhang, W.; Suo, P.; Sun, K.; Chen, J.; Li, D.; et al. Observation of Ultrafast Interfacial Exciton Formation and Relaxation in Graphene/MoS_2 Heterostructure. *J. Phys. Chem. Lett.* **2022**, *13*, 5123−5130.
(60) Zhu, L.; Song, Z.; Li, R.; Zhu, H. Hot Carrier Dynamics in MoS_2/WS_2 Heterostructure. *Nanotechnology* **2022**, *33*, No. 195701.
(61) Bian, A.; Fu, S.; Wang, P.; Zhao, K.; He, J.; Zhang, X.; He, D.; Wang, Y.; Zhao, H. Ultrafast Charge Transfer and Carrier Dynamics in a WS_2/$MoSe_2$ Few-Layer van der Waals Heterostructure. *J. Mater. Chem. C* **2022**, *10*, 5328−5335.
(62) Yao, W.; Yang, D.; Chen, Y.; Hu, J.; Li, J.; Li, D. Layer-Number Engineered Momentum-Indirect Interlayer Excitons with Large Spectral Tunability. *Nano Lett.* **2022**, *22*, 7230−7237.
(63) Kim, J. Y.; Kim, T. J.; Lee, S.-h.; Lee, E.; Kim, J.; Joo, J. Temperature- and Power-Dependent Characteristics of Heterointerlayer Excitons Emitting in the Visible Region of a WS_2/PbI_2 Nanostructure: Implications in Excitonic Devices. *ACS Appl. Nano Mater.* **2022**, *5*, 11167−11175.
(64) Kresse, G.; Furthmüller, J. Efficiency of ab-Initio Total Energy Calculations for Metals and Semiconductors Using a Plane-Wave Basis Set. *Comput. Mater. Sci.* **1996**, *6*, 15−50.
(65) Kresse, G.; Joubert, D. From Ultrasoft Pseudopotentials to the Projector Augmented-Wave Method. *Phys. Rev. B* **1999**, *59*, 1758−1775.
(66) Tkatchenko, A.; DiStasio, R. A.; Car, R.; Scheffler, M. Accurate and Efficient Method for Many-Body van der Waals Interactions. *Phys. Rev. Lett.* **2012**, *108*, No. 236402.

https://doi.org/10.1021/acsami.4c07346
ACS Appl. Mater. Interfaces 2024, 16, 35841−35851

THE JOURNAL OF PHYSICAL CHEMISTRY LETTERS
A JOURNAL OF THE AMERICAN CHEMICAL SOCIETY

pubs.acs.org/JPCL Letter

Efficient Multiple Exciton Generation in Monolayer MoS_2

Ashish Soni, Dushyant Kushavah, Li-Syuan Lu, Wen-Hao Chang, and Suman Kalyan Pal*

Cite This: J. Phys. Chem. Lett. 2023, 14, 2965−2972 Read Online

ACCESS | Metrics & More | Article Recommendations | Supporting Information

ABSTRACT: Utilization of the excess energy of photoexcitation that is otherwise lost as thermal effects can improve the efficiency of next-generation light-harvesting devices. Multiple exciton generation (MEG) in semiconducting materials yields two or more excitons by absorbing a single high-energy photon, which can break the Shockley−Queisser limit for the conversion efficiency of photovoltaic devices. Recently, monolayer transition metal dichalcogenides (TMDs) have emerged as promising light-harvesting materials because of their high absorption coefficient. Here, we report efficient MEGs with low threshold energy and high (86%) efficiency in a van der Waals (vdW) layered material, MoS_2. Through different experimental approaches, we demonstrate the signature of exciton multiplication and discuss the possible origin of decisive MEG in monolayer MoS_2. Our results reveal that vdW-layered materials could be a potential candidate for developing mechanically flexible and highly efficient next-generation solar cells and photodetectors.

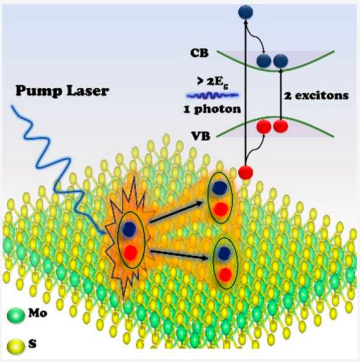

Downloaded via INDIAN INST OF TECH MANDI on March 20, 2023 at 15:31:20 (UTC).
See https://pubs.acs.org/sharingguidelines for options on how to legitimately share published articles.

Transition metal dichalcogenides (TMDs) possess a layered structure with weak interlayer interactions and hence can be thinned downed to one atomic layer. The atomically thin TMDs exhibit many fascinating properties, including a wide range of optical bandgaps, mechanical flexibility, high absorption coefficient (1 order of magnitude higher than conventional semiconductors), near-ideal optical bandgap for solar energy harvesting, and self-passivated surface.[1−6] These intriguing optoelectronic properties of two-dimensional (2D) TMDs make them promising candidates for flexible photodetectors and photovoltaics[7] where light converts into electron−hole (e−h) pairs. A detailed balance calculation predicted that the power conversion efficiency (PCE) of single-junction solar cells of 2D TMD can reach up to 27%.[8] But, the PCE achieved to date in thin-film single-junction TMD solar cells is relatively low (∼5−6%).[9,10]

MEG is a process where additional electron−hole pairs (excitons) are generated from a high-energy absorbed photon. A photon of energy ($h\nu$) higher than the optical bandgap (E_g) can excite the ground state population to a higher energy band and create hot electron−hole pairs in a semiconducting material. Usually, these high-energy electron−hole pairs cool down to the band edge by losing their excess energy ($h\nu - E_g$) in the form of heat. However, in the process of MEG, a high-energy charge carrier (electron in the conduction band or hole in the valence band) relaxes to the band edge by lifting an electron from the valence band to the conduction band, thus producing a new exciton. Therefore, the efficiency of the conversion of light into charge pairs can be greatly enhanced when multiple excitons are produced by hot carriers without losing their excess energy as heat. The MEG process can be characterized by the quantum yield (QY) (number of excitons generated per absorbed photon) and the threshold photon energy, i.e., the energy at which MEG starts. If there are $2(n)$ excitons generated from a single absorbed photon, then QY is said to be $2(n)$. In the ideal case, QY reaches the value $2(n)$ at a photon energy twice (n times) the optical bandgap energy. In bulk semiconductors, carrier multiplication is known as impact ionization (II), whereas it is called MEG in quantum-confined structures. The efficiency of MEG is very low in the bulk semiconductors because of the strong electron−phonon scattering and high screening of Coulombic interactions.[11,12] The MEG threshold in bulk materials is almost four times the optical bandgap energy.[13] On the contrary, MEG has been seen to be improved in the low-dimensional material as the carrier relaxation rate through electron−phonon interactions can be reduced because of the discrete energy of the charge carriers due to strong confinement in the reduced dimension.[14,15]

In 2002, Nozik proposed that MEG is more efficient in nanomaterials than their bulk counterpart.[16] Later, MEG has been demonstrated in many colloidal quantum dots, nanorods, carbon nanotubes, and graphene.[17,18] Because of the strong quantum confinement arising from their reduced dimensionality, 2D materials could be an interesting platform to study MEG. Indeed, Zhou et al.[19] investigated MEG in few-layer black phosphorus (BP). Though MEG parameters are very promising, BP has high chemical reactivity, which leads to

Received: February 1, 2023
Accepted: March 15, 2023

ACS Publications © XXXX American Chemical Society

https://doi.org/10.1021/acs.jpclett.3c00306
J. Phys. Chem. Lett. 2023, 14, 2965−2972

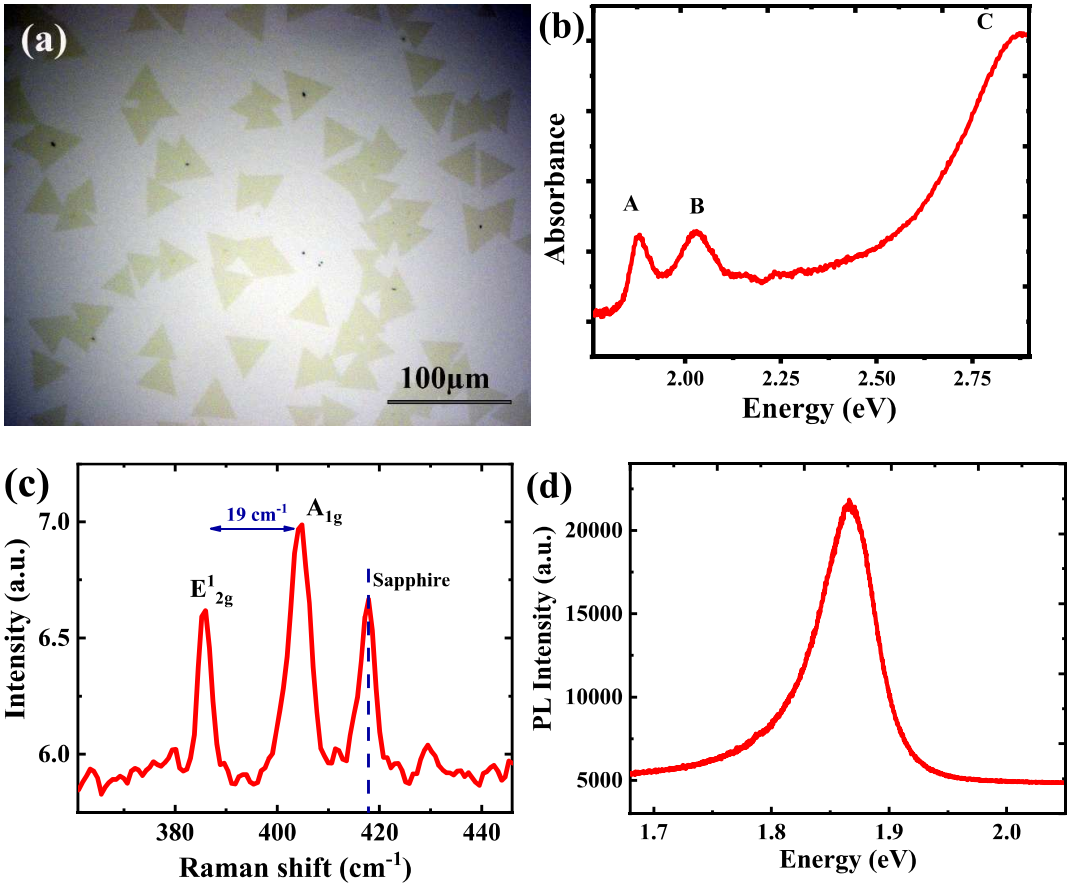

Figure 1. (a) Optical image of CVD grown monolayer MoS_2 on the sapphire substrate. (b) Absorption spectrum of CVD grown MoS_2 sample. (c) Raman spectrum of monolayer MoS_2 obtained with 532 nm laser light. (d) Photoluminescence spectrum of MoS_2 monolayer (excitation photon energy, 2.33 eV).

quick degradation of BP in ambient conditions.[20,21] Kim and colleagues recently observed efficient MEG in TMD ($MoTe_2$ and WSe_2) films.[22] The monolayer TMDs would be beneficial for realizing more compact and flexible optoelectronic devices for the future. Therefore, it is important to investigate MEG in monolayer TMDs. Among the family of layered TMDs, MoS_2 is one of the most investigated materials. It has been proven to be a promising material for low-cost, scalable, and novel optoelectronic devices.[23−25] Moreover, monolayer MoS_2 and BP can form a p−n heterojunction of type II, which could generate free carriers via exciton dissociation and hence could be useful for efficient extraction of multiple carriers either from multiple excitons formed in BP or MoS_2. However, possibility of photoinduced carrier multiplication in mono- or multilayer MoS_2 remains unexplored.

Herein, we demonstrate MEG in atomically thin MoS_2 using ultrafast transient absorption spectroscopy. The monolayer sample was excited with photons of energies higher than the optical bandgap energy (i.e., $E_{ex} > E_g$). The photoinduced bleach (PIB) signal measured at excitation energy greater than $2E_g$ was found to be much stronger than that of the signal for band-edge excitation, suggesting MEG in the MoS_2 sample. The delayed rise of a PIB signal for excitation energy greater than $2E_g$ further supports carrier multiplication, which occurs via an inverse Auger process within 160 fs. We report enhanced MEG with a threshold down to $2.1E_g$ and slope efficiency up to 86% in monolayer MoS_2.

Monolayer MoS_2. Atomically thin MoS_2 flakes were prepared on a double-polished optically transparent sapphire substrate via chemical vapor deposition (CVD). Optical microscopy image in Figure 1a confirms formation of triangular flakes of MoS_2 which spread over the whole substrate. The linear absorption spectrum of the sample measured at room temperature is presented in Figure 1b, which depicts three distinct peaks centered at 1.88 eV (660 nm), 2.03 eV (610 nm), and 2.88 eV (430 nm).[26−28] The first two peaks labeled by A and B correspond to excitonic transition at the K/K' point of the Brillouin zone. These two peaks arise as a result of the transitions between split valence and conduction bands due to spin−orbit coupling in MoS_2.[29−31] The high-energy peak, i.e., C with strong absorption, is associated with the transitions involving the bands between the Γ and K points of the Brillouin zone[32,33] and has been ascribed to the van Hove singularities in the density of state (DOS).[34] It is worth noting that the absorption spectrum of our prepared sample resembles the spectrum of monolayer MoS_2.[31] To confirm the sample quality and estimate the layer number present in the sample, Raman spectroscopy was employed. Similar to the previously reported Raman spectrum,[35] our sample exhibits two characteristic peaks corresponding to E^1_{2g} (in-plane vibration) and A_{1g} (out-of-plane vibration) at 385 and 404 cm^{-1}, respectively. The peak shift difference between the two Raman peaks is 19 cm^{-1} and $E^1_{2g}/A_{1g} = 1.04 \approx 1$, which are suggesting the monolayer nature of our MoS_2 flakes.[35,36] It should be noted that the third peak (~419 cm^{-1}) in the

https://doi.org/10.1021/acs.jpclett.3c00306
J. Phys. Chem. Lett. 2023, 14, 2965−2972

Raman spectrum is due to the sapphire substrate.[37,38] For completeness, the photoluminescence (PL) spectrum of our sample was measured following excitation by a 2.33 eV laser light. The PL spectrum has a peak at 1.86 eV, and it is matching well with the previously reported PL spectrum of monolayer MoS_2.[39−41]

Photoinduced Transient Absorption Study. Femtosecond pump−probe technique was employed to monitor the ultrafast dynamics of the optically generated charge carrier in monolayer MoS_2. The dependence of the transient absorption (TA) of monolayer MoS_2 on the probe photon energy at different time delays (between pump and probe beams) is presented in Figure 2. This spectral measurement was carried

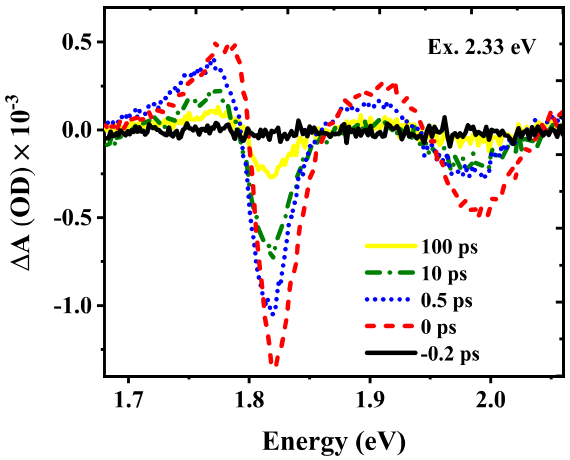

Figure 2. Transient absorption spectra for monolayer MoS_2 measured at a pump photon energy of 2.33 eV and pump fluence of 3.7×10^{13} cm^{-2}.

out at an excitation energy of 2.33 eV (532 nm) and fluence 3.7×10^{13} cm^{-2} at room temperature. It can be seen that the TA spectra are featured with two negative (at 1.82 and 2.0 eV) and two positive bands (~1.76 and 1.91 eV). The reason for the positive band in the TA spectra is an increase of photoinduced absorption, whereas the negative band arises due to a decrease of photoinduced absorption of the probe.[42,43] After excitation, the photogenerated charge carriers undergo thermalization followed by phase space filling, resulting in a decrease of absorption of the time-delayed probe as

$$\Delta A = A_{\text{pump on}} - A_{\text{pump off}} \quad (1)$$

where A is the absorbance. The absorption peaks at 1.88 and 2.03 eV in the steady state absorption spectrum of monolayer MoS_2 (Figure 1b) corresponds to A- and B-excitons, respectively. Therefore, the negative features at 1.82 and 2.0 eV could be ascribed to photoinduced bleach (PIB) due to A- and B-excitonic transitions, respectively.[44] The positive peaks around 1.76 and 1.91 eV could arise due to a number of processes, viz., the broadening of the main bleach feature, bandgap renormalization, or photoinduced absorption (PIA) of excited carriers. However, these features could also be due to biexciton formation, as reported by previous literature.[44−47]

Decay Kinetics of Photoexcited Carriers. Transient absorption (TA) spectroscopy has been proven to be a very successful technique to study the MEG in quantum-confined semiconductor nanostructures.[48−50] Previous studies on MEG in quantum dots reported an abrupt change in the decay kinetics of the PIB signal in changing the excitation energy from below to above the threshold energy of MEG.[13,14,51,52] The change in PIB kinetics was attributed to the Auger recombination of the generated multiple excitons within the same quantum dot. Therefore, it is crucial to investigate the carrier dynamics to check the possibility of MEG in a material. First, we recorded the PIB signal at 1.86 eV for different pump fluence in monolayer MoS_2 at an excitation photon energy of 2.33 eV ($1.20E_g$), where MEG is not possible (Figure 3a). The variation of maximum absorption of the PIB signal (ΔA_{max}) with absorbed photon fluence (see the Supporting Information for determination of absorbed photon fluence from incident fluence) was plotted (inset of Figure 3a) and obtained a straight line up to an absorbed photon fluence of 1.0×10^{14} cm^{-2}.

Furthermore, the decay kinetics of the PIB signal can be fitted globally with a multiexponential model given as follows:

$$\Delta A = A_1 \exp(-t/T_1) + A_2 \exp(-t/T_2) + \ldots \quad (2)$$

where T_i (i = 1, 2, 3, ...) is the decay time and A_i (i = 1, 2, 3, ...) represents the amplitude of the ith decay component. We fitted PIB kinetics using eq 2, and fitting results are presented in Supporting Information Table S1. The decay kinetics at lower

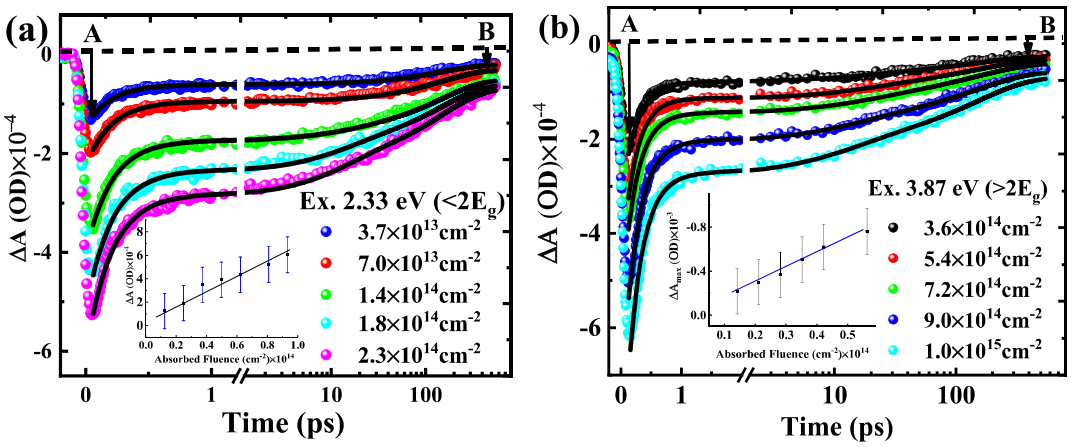

Figure 3. PIB kinetics probed at direct A-exciton (1.86 eV) transition using pump photon energies of (a) 2.33 eV and (b) 3.87 eV (at different pump fluences). Solid lines are the results of global fitting. Inset: Variation of maximum PIB signal with absorbed photon fluence.

https://doi.org/10.1021/acs.jpclett.3c00306
J. Phys. Chem. Lett. 2023, 14, 2965−2972

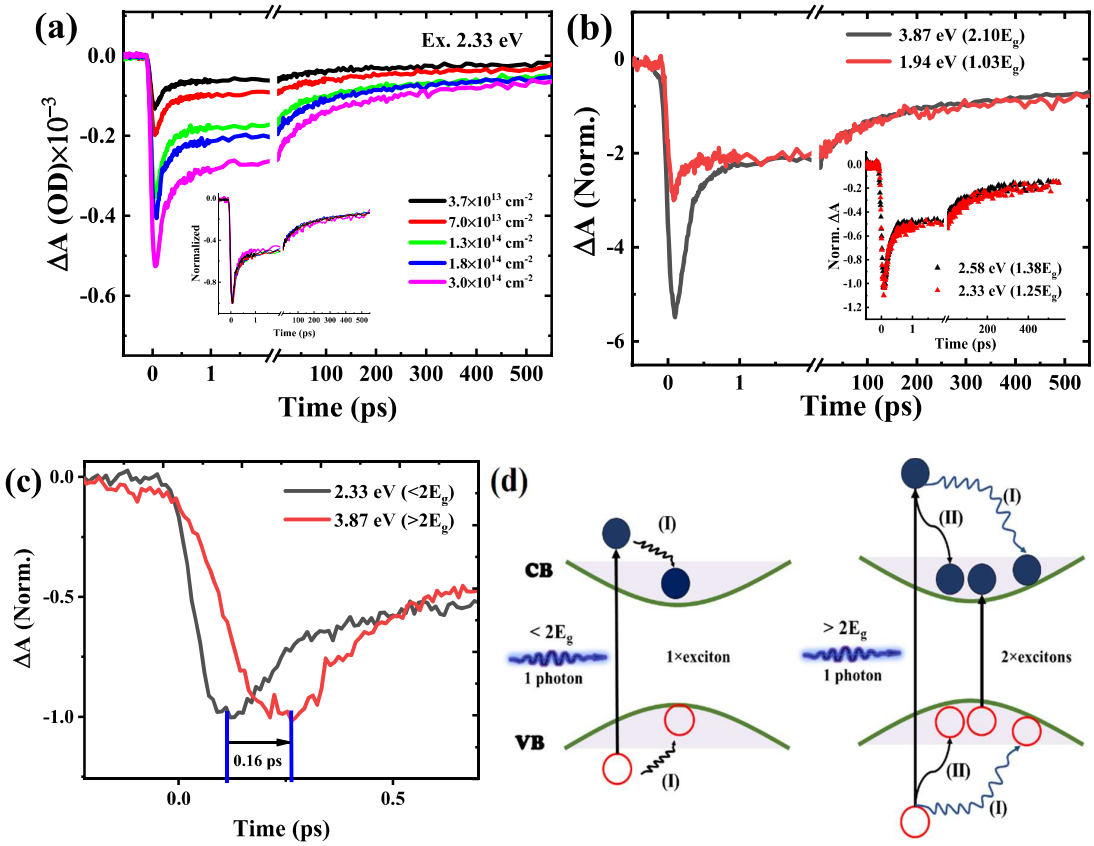

Figure 4. (a) Kinetics of PIB at different pump fluences measured with photon energy of 2.33 eV (inset: PIB kinetics after normalization). (b) Bleach kinetics at different pump energies (1.94 and 3.87 eV) normalized at a long delay time (inset: PIB kinetics at two energies ($<2E_g$) after normalization). (c) Build-up dynamics of PIB signal for below and above threshold excitations. (d) Schematic representation of possible relaxation pathways in the cases of below and above threshold excitations.

fluences can be fitted with a biexponential function (a fast sub-picosecond and a slow decay component with time constants ~0.2 ps and ~150 ps, respectively), but one extra time component (~13 ps) is required to properly fit the data at high pump fluences. The rapid rise of the bleach signal is due to the phase space filling of charge carriers near the conduction band. Considering a report on large-area monolayer MoS_2 by Cunningham et al.,[53] we attribute the fast component of the decay to carrier capture by either trap or mid-gap defect states. The slowest decay of the PIB signal could be ascribed to the radiative recombination of excitons.[53,54] The intermediate time component observed at pump fluences above 7.0×10^{13} cm^{-2} possibly arises due to the Auger recombination of excitons as it matches well with the reported time constant for the Auger recombination in MoS_2.[55]

Next, we measured the fluence-dependent PIB kinetics for 3.87 eV ($2.1E_g$) excitation photon energies, which can be seen in Figure 3b. The maximum PIB signal varies linearly with absorbed photon fluence until an absorbed photon fluence of 0.4×10^{14} cm^{-2} (inset of Figure 3b). Interestingly, the PIB kinetics at this pump energy ($>2E_g$) fitted well globally with three time components: ~0.23, 14, and ~150 ps (fitting results are presented in Supporting Information Table S2). The origin of the decay components could be the same as that mentioned before for pump photon energy of 2.33 eV.

Observation of MEG. We measured PIB kinetics for excitation photon energies 1.94, 2.6, 2.88, and 4.4 eV in addition to 2.33 and 3.87 eV. To determine the linear regime of the pump fluence, we plotted ΔA_{max} with the pump photon fluence (Supporting Information Figure S2).[14,22,56] The decay kinetics measured at excitation energy 2.33 eV and at different pump fluences are shown in Figure 4a. All of the PIB kinetics measured at an excitation energy of 2.33 eV almost collapse on the same curve after normalization (inset of Figure 4a). A similar trend has been observed for other excitation photon energies (see Supporting Information Figure S3). These observations infer a very similar nature of decay dynamics at all measured fluences, and the maximum PIB signal is proportional to the number of generated excitons. Hence, we have compared the density of generated excitons by comparing TA kinetics at different photon energies after normalizing at 200 ps (where the signal is due to a long-lived single exciton) to detect the MEG,[14,57,58] and shown in Figure 4b. It is clear from Figure 4b that the maximum PIB signal becomes double as the excitation energy (E_{ex}) is increased to more than $2E_g$; i.e., $2E_g < E_{ex} < 3E_g$. However, the inset of Figure 4b (normalized TA kinetics) indicates that decays follow precisely the same dynamics for all of the excitation energies less than $2E_g$. These observations suggest that the number of excitons generated per absorbed photon is more for excitation photon energies $> 2E_g$ than that for excitation energies less than $2E_g$.

Next, we have compared the build-up dynamics of the PIB signals probed at A-excitonic transition for 2.33 eV ($1.2E_g$) and 3.87 eV ($2.1E_g$) pump energies (Figure 4c). A quick rise for pump energy $< 2E_g$ has been found, which can be attributed to the hot carrier relaxation process via phonon emission (I),

https://doi.org/10.1021/acs.jpclett.3c00306
J. Phys. Chem. Lett. 2023, 14, 2965−2972

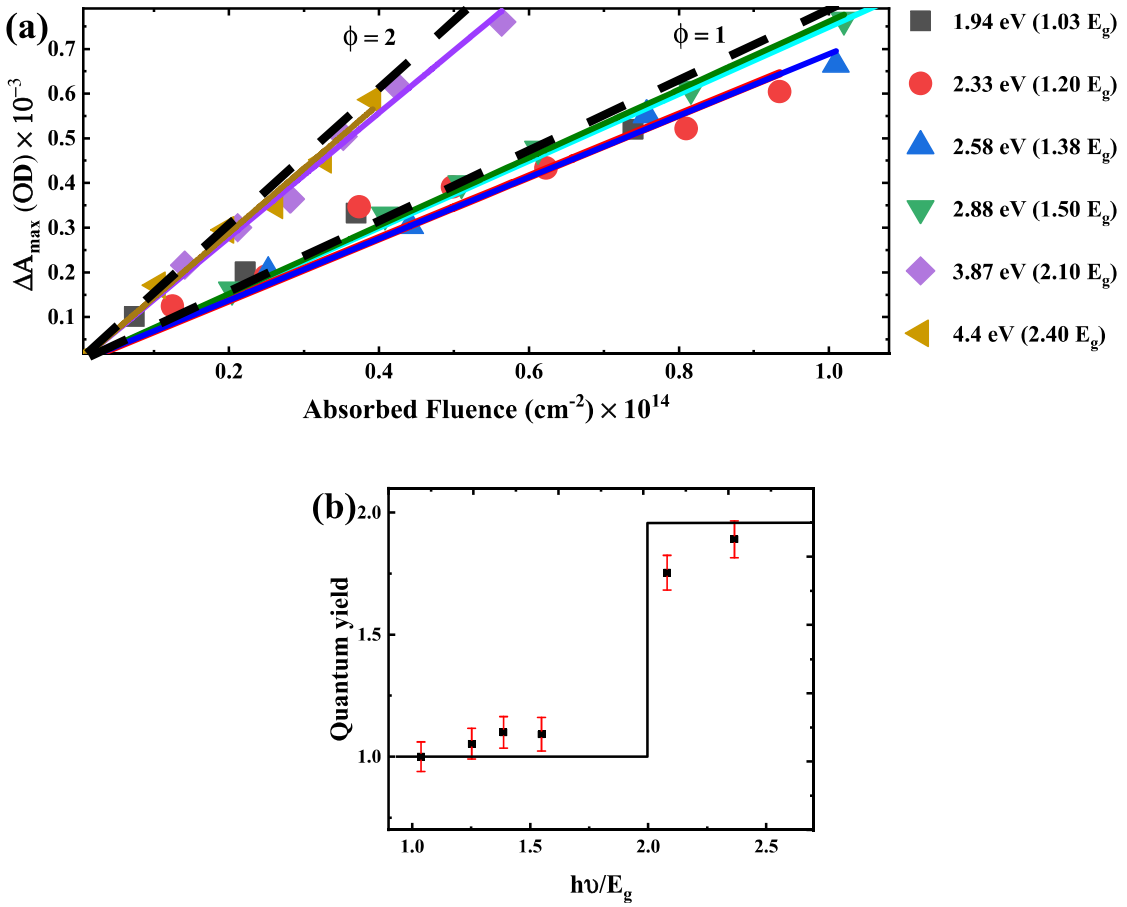

Figure 5. (a) Variation of maximum PIB signal as a function of absorbed photon fluence at different pump energies. The solid lines represent the linear fits to experimental data points. MEG quantum yields 1 and 2 are indicated by the dashed lines for reference. (b) Plot of MEG efficiency as a function of excitation energy normalized to the optical bandgap energy of the monolayer MoS_2. The data points correspond to the yield calculated from the A/B ratio (A and B are indicated in Figure 3).

whereas a relatively slow rise is observed in the case of pump energy > $2E_g$. The slower rise time of the PIB signal for high-energy excitation had previously been reported as a possible fingerprint of MEG by Kim et al.[22] Therefore, the slower rise time of the PIB signal for excitation photon energy above $2E_g$ provides further evidence of MEG (II) in monolayer MoS_2. The processes responsible for the relaxation of hot carriers for excitation photon energy < $2E_g$ and > $2E_g$ are schematically presented in Figure 4d.

Furthermore, we globally fitted bleach signals measured at pump energies of 2.33 eV ($1.2E_g$), 3.87 eV ($2.1E_g$), and 4.4 eV ($2.4E_g$) with an absorbed photon fluence of 2.8×10^{13} cm^{-2} using eq 2 (Supporting Information Figure S4). It is evident from the fitting results (Supporting Information Table S3) that an additional decay component (time constant ~ 17 ps) is present for pump energies > $2E_g$, which corresponds to the Auger recombination of excitons (as mentioned before). The presence of the additional decay channel provides further evidence for the generation of multiple excitons which decay via Auger processes with faster rate as compared to single-exciton decay.

The maximum intensity (ΔA_{max}) of the PIB signal can be considered as a measure of exciton density if it increases linearly with the absorbed photon fluence. Therefore, to compare the number of excitons generated at different excitation energies, we plotted ΔA_{max} of the PIB signal at different excitation energies as a function of the absorbed photon fluence (Figure 5a). It is apparent from Figure 5a that the maximum PIB intensity increases linearly with the absorbed pump fluence for all pump energies. The maximum PIB signal (ΔA_{max}) depends on the quantum yield (ϕ) of exciton generation and the absorbed pump fluence (F_{abs}) as

$$\Delta A_{max} = \phi \sigma F_{abs} \quad (3)$$

where F_{abs} = fraction of absobed photon × pump fluence and σ is the transient bleach cross-section for the probe.[14] It follows from eq 3 that the slope of a fitted line in Figure 5a represents the exciton generation yield. Without multiple carrier generation, the slope should remain constant for all of the excitation energies less than $2E_g$ (i.e., 2.33, 2.58, and 2.88 eV), which is indeed the case; i.e., the slope of ΔA_{max} vs absorbed fluence is almost the same (Figure 5a). For excitation energies greater than $2E_g$, the slope of the straight lines is similar for all excitation energies (E_{ex}). But, the slope of ΔA_{max} vs F_{abs} lines for $E_{ex} > 2E_g$ is about twice that of $E_{ex} < 2E_g$ lines (Figure 5a). Such abrupt and sudden increase in the slopes of ΔA_{max} vs F_{abs} lines at excitation energies above $2E_g$ could be associated with multiple exciton generation in monolayer MoS_2.

Quantification of MEG Quantum Yield. To determine the values of QY of MEG, we followed the procedure proposed by de Weerd et al.[48] The maximum value of ΔA has been taken as a measure of the number of generated excitons (indicated by A

https://doi.org/10.1021/acs.jpclett.3c00306
J. Phys. Chem. Lett. 2023, 14, 2965−2972

in Figure 3). As the excitons did not decay to zero within the measured time, we normalized the multiplicity of excitons to the B (PIB signal at the tail, Figure 3) value. The experimental MEG QY at an energy greater than MEG threshold can be determined from the following relation:

$$\phi(E_{at}) = \frac{A(E_{at})/B(E_{at})}{A(E_{bt})/B(E_{bt})} \quad (4)$$

where E_{at} and E_{bt} represent excitation energies above and below the MEG threshold, respectively. The MEG QYs obtained from eq 4 are plotted as a function of pump photon energy normalized with the optical bandgap energy of MoS_2 in Figure 5b. A step-like increase in MEG QY after threshold energy (i.e., above $2E_g$) can be clearly seen. To estimate the MEG efficiency, we used the following model:[12]

$$\phi = \eta_{cm}\left(\frac{h\nu}{E_g} - 1\right) \quad (5)$$

where $h\nu$ is the excitation energy and η_{cm} is the efficiency of MEG. We fitted the QYs obtained from eq 4 with the above-mentioned model (Supporting Information Figure S5), which yields an MEG efficiency of 86%. The observed large value of high MEG efficiency infers that a major portion of excess photon energy is converted in e−h pair via MEG. Recently Liu et al.[59] theoretically investigated MEG in several monolayer TMDs. They predicted that the threshold energy for MEG in monolayer TMDs can be as low as $1.75E_g$ and MEG is most efficient in MoS_2 among all TMDs. Our results are in line with the previous theoretical prediction and suggest that the multiple exciton generation in monolayer MoS_2 is sufficient to highlight its potential in solar energy conversion and light-harvesting applications.

In summary, by probing the carrier dynamics at various pump energies, we have demonstrated efficient MEG in monolayer MoS_2. An additional component in the decay dynamics of photogenerated carriers has been observed due to Auger recombination of multiple excitons which are formed at excitation energies higher than twice the optical bandgap energy. The longer build-up time of the PIB signal corresponding to the above MEG-threshold excitation suggests that the MEG process is not instantaneous. The generation of additional excitons is delayed because they are formed via relaxation of the photogenerated hot excitons. The threshold energy for the MEG is found to be as low as double the optical bandgap energy, and MEG efficiency can go up to ∼86%. Our results provide global insight into the MEG process in monolayer MoS_2 and carrier multiplication in 2D MoS_2, making it a promising material for highly efficient harvesting of light energy into electricity, enabling development of 2D TMD based high-efficiency optoelectronic devices.

EXPERIMENTAL METHODS

Sample Preparation. Monolayer MoS_2 flakes were synthesized on a sapphire substrate by chemical vapor deposition (CVD) technique in a 1 in. horizontal hot tube furnace. Molybdenum trioxide powder (MoO_3) and sulfur powder were used as the growth reactant. The transition metal source and sapphire substrate were placed at the central high-temperature heating zone, while the sulfur powder was placed upstream and heated using a heating belt. The monolayer MoS_2 was grown at 850 °C in the center of the heating zone, and the sulfur temperature was kept at 135 °C. A mixed gas of H_2/Ar with flow rate of 8 sccm/80 sccm was used as the carrier gas under a base pressure of 80 Torr during the growth process.

Absorption Spectroscopy. A Shimadzu UV-2450 spectrometer (Agilent Technologies, USA) was used to measure the extinction spectrum within an excitation range of 1.7 to 4.96 eV. The measurement was performed on the sapphire substrate at room temperature.

Raman and PL Spectroscopy. A Horiba Jobin-Yvon LabRAM HR evolution Raman spectrometer was used for recording Raman and photoluminescence (PL) spectra in the backscattering configuration under an optical microscope at room temperature. The sample was excited by a laser of wavelength 532 nm through a 100× objective lens. A monochromator analyzed the signals using gratings with 600 and 1800 lines/mm for PL and Raman measurements, respectively. A Peltier cooled charge-coupled device detector in the backscattering configuration was used to detect the signal.

Femtosecond Transient Absorption (TA) Spectroscopy. A femtosecond Ti:sapphire amplifier (pulse width < 35 fs and wavelength ∼ 800 nm) was employed in the ultrafast transient absorption (TA) measuring system.[60] The pump and probe pulses were generated from the amplifier (Spitfire Ace, Spectra Physics) by splitting the output into two components. The pump and probe pulses of different energies (used in single kinetics measurements) were obtained from the nonlinear optical parametric amplifier (TOPAS). In broadband TA measurement, the probe beam was a white-light continuum (WLC) generated by focusing a small fraction of 800 nm light (from Spitefire Ace) on a sapphire crystal. The 800 nm beam was adjusted using an iris and neutral density (ND) filter to obtain a stable and continuous white-light probe. A delay stage in the probe path, run by a stepper motor, controls the time delay between probe and pump beams. The probe beam was split into the reference and the sample beams. These two beams were detected separately to eliminate the unsolicited noises. The probe beam was focused by a concave mirror with a hole at the center to allow the overlapping of the pump and probe beams at focus. The absorbance of the probe beam was detected under the conditions with and without pump, with the help of a mechanical chopper of frequency 500 Hz. A Berek compensator was used to control the polarization of the pump beam. The probe beam polarization was set at the "magic angle" with the pump beam. TA spectra were recorded by dispersing the beam with a grating spectrograph (Acton Spectra Pro SP 2358) followed by a CCD array. Two photodiodes having variable gain were used to record TA kinetics. TA decay traces were fitted with multiexponential functions by taking the instrument response function into account.

ASSOCIATED CONTENT

Supporting Information

The Supporting Information is available free of charge at https://pubs.acs.org/doi/10.1021/acs.jpclett.3c00306.

Detailed experimental section; analysis of Rayleigh scattering correction in absorption spectra; determination of absorbed photon density and linear relation between pump fluence and maximum PIB signal at different pump photon energies; details of multi-

https://doi.org/10.1021/acs.jpclett.3c00306
J. Phys. Chem. Lett. 2023, 14, 2965−2972

exponential global fitting parameters of PIB kinetics and quantum yield of MEG at different pump photon energies (PDF)

AUTHOR INFORMATION

Corresponding Author

Suman Kalyan Pal − *School of Physical Sciences and Advanced Materials Research Centre, Indian Institute of Technology Mandi, Mandi 175005 Himachal Pradesh, India;* orcid.org/0000-0003-2498-6217; Email: suman@iitmandi.ac.in

Authors

Ashish Soni − *School of Physical Sciences and Advanced Materials Research Centre, Indian Institute of Technology Mandi, Mandi 175005 Himachal Pradesh, India;* orcid.org/0000-0001-7429-576X

Dushyant Kushavah − *School of Physical Sciences and Advanced Materials Research Centre, Indian Institute of Technology Mandi, Mandi 175005 Himachal Pradesh, India;* orcid.org/0000-0001-5745-9435

Li-Syuan Lu − *Department of Electrophysics, National Yang Ming Chiao Tung University, Hsinchu 30010, Taiwan*

Wen-Hao Chang − *Department of Electrophysics, National Yang Ming Chiao Tung University, Hsinchu 30010, Taiwan; Research Center for Applied Sciences, Academia Sinica, Nankang, Taipei 11529, Taiwan*

Complete contact information is available at: https://pubs.acs.org/10.1021/acs.jpclett.3c00306

Notes

The authors declare no competing financial interest.

ACKNOWLEDGMENTS

A.S., D.K., and S.K.P. are thankful to the Advanced Materials Research Centre (AMRC) of IIT Mandi for providing experimental facilities. S.K.P. acknowledges the financial support from the Science and Engineering Research Board (SERB), Government of India (Grant No. CRG/2018/003045).

REFERENCES

(1) Lembke, D.; Bertolazzi, S.; Kis, A. Single-Layer MoS_2 Electronics. *Acc. Chem. Res.* **2015**, *48*, 100−110.

(2) Kim, S.; Konar, A.; Hwang, W.-S.; Lee, J. H.; Lee, J.; Yang, J.; Jung, C.; Kim, H.; Yoo, J.-B.; Choi, J.-Y.; et al. High-Mobility and Low-Power Thin-Film Transistors Based on Multilayer MoS_2 Crystals. *Nat. Commun.* **2012**, *3*, 1011.

(3) Mak, K. F.; Lee, C.; Hone, J.; Shan, J.; Heinz, T. F. Atomically Thin MoS_2: A New Direct-Gap Semiconductor. *Phys. Rev. Lett.* **2010**, *105*, 136805.

(4) Jariwala, D.; Davoyan, A. R.; Tagliabue, G.; Sherrott, M. C.; Wong, J.; Atwater, H. A. Near-Unity Absorption in van der Waals Semiconductors for Ultrathin Optoelectronics. *Nano Lett.* **2016**, *16*, 5482−5487.

(5) Wang, L.; Huang, L.; Tan, W. C.; Feng, X.; Chen, L.; Huang, X.; Ang, K.-W. 2D Photovoltaic Devices: Progress and Prospects. *Small Methods* **2018**, *2*, 1700294.

(6) Soni, A.; Pal, S. K. Valley Degree of Freedom in Two-Dimensional van der Waals Materials. *J. Phys. D* **2022**, *55*, 303003.

(7) Li, H.-M.; Lee, D.; Qu, D.; Liu, X.; Ryu, J.; Seabaugh, A.; Yoo, W. J. Ultimate Thin Vertical p−n Junction Composed of Two-Dimensional Layered Molybdenum Disulfide. *Nat. Commun.* **2015**, *6*, 6564.

(8) Jariwala, D.; Davoyan, A. R.; Wong, J.; Atwater, H. A. Van der Waals Materials for Atomically-Thin Photovoltaics: Promise and Outlook. *ACS Photonics* **2017**, *4*, 2962−2970.

(9) Memaran, S.; Pradhan, N. R.; Lu, Z.; Rhodes, D.; Ludwig, J.; Zhou, Q.; Ogunsolu, O.; Ajayan, P. M.; Smirnov, D.; Fernández-Domínguez, A. I.; et al. Pronounced Photovoltaic Response from Multilayered Transition-Metal Dichalcogenides PN-Junctions. *Nano Lett.* **2015**, *15*, 7532−7538.

(10) Nassiri Nazif, K.; Daus, A.; Hong, J.; Lee, N.; Vaziri, S.; Kumar, A.; Nitta, F.; Chen, M. E.; Kananian, S.; Islam, R.; et al. High-Specific-Power Flexible Transition Metal Dichalcogenide Solar Cells. *Nat. Commun.* **2021**, *12*, 7034.

(11) Pijpers, J. J. H.; Ulbricht, R.; Tielrooij, K. J.; Osherov, A.; Golan, Y.; Delerue, C.; Allan, G.; Bonn, M. Assessment of Carrier-Multiplication Efficiency in Bulk PbSe and PbS. *Nat. Phys.* **2009**, *5*, 811−814.

(12) Beard, M. C.; Midgett, A. G.; Hanna, M. C.; Luther, J. M.; Hughes, B. K.; Nozik, A. J. Comparing Multiple Exciton Generation in Quantum Dots To Impact Ionization in Bulk Semiconductors: Implications for Enhancement of Solar Energy Conversion. *Nano Lett.* **2010**, *10*, 3019−3027.

(13) Schaller, R. D.; Pietryga, J. M.; Klimov, V. I. Carrier Multiplication in InAs Nanocrystal Quantum Dots with an Onset Defined by the Energy Conservation Limit. *Nano Lett.* **2007**, *7*, 3469−3476.

(14) Aerts, M.; Bielewicz, T.; Klinke, C.; Grozema, F. C.; Houtepen, A. J.; Schins, J. M.; Siebbeles, L. D. A. Highly Efficient Carrier Multiplication in PbS Nanosheets. *Nat. Commun.* **2014**, *5*, 3789.

(15) Beard, M. C. Multiple Exciton Generation in Semiconductor Quantum Dots. *J. Phys. Chem. Lett.* **2011**, *2*, 1282−1288.

(16) Nozik, A. J. Quantum Dot Solar Cells. *Phys. E: Low-Dimens. Syst. Nanostructures* **2002**, *14*, 115−120.

(17) Padilha, L. A.; Stewart, J. T.; Sandberg, R. L.; Bae, W. K.; Koh, W.-K.; Pietryga, J. M.; Klimov, V. I. Aspect Ratio Dependence of Auger Recombination and Carrier Multiplication in PbSe Nanorods. *Nano Lett.* **2013**, *13*, 1092−1099.

(18) Shabaev, A.; Hellberg, C. S.; Efros, A. L. Efficiency of Multiexciton Generation in Colloidal Nanostructures. *Acc. Chem. Res.* **2013**, *46*, 1242−1251.

(19) Zhou, Q.; Zhou, H.; Tao, W.; Zheng, Y.; Chen, Y.; Zhu, H. Highly Efficient Multiple Exciton Generation and Harvesting in Few-Layer Black Phosphorus and Heterostructure. *Nano Lett.* **2020**, *20*, 8212−8219.

(20) Castellanos-Gomez, A.; Vicarelli, L.; Prada, E.; Island, J. O.; Narasimha-Acharya, K. L.; Blanter, S. I.; Groenendijk, D. J.; Buscema, M.; Steele, G. A.; Alvarez, J. V.; et al. Isolation and Characterization of Few-Layer Black Phosphorus. *2d Mater.* **2014**, *1*, No. 025001.

(21) Dai, J.; Zeng, X. C. Structure and Stability of Two Dimensional Phosphorene with = O or = NH Functionalization. *RSC Adv.* **2014**, *4*, 48017−48021.

(22) Kim, J.-H.; Bergren, M. R.; Park, J. C.; Adhikari, S.; Lorke, M.; Frauenheim, T.; Choe, D.-H.; Kim, B.; Choi, H.; Gregorkiewicz, T.; et al. Carrier Multiplication in van der Waals Layered Transition Metal Dichalcogenides. *Nat. Commun.* **2019**, *10*, 5488.

(23) Nardi, M. V.; Timpel, M.; Ligorio, G.; Zorn Morales, N.; Chiappini, A.; Toccoli, T.; Verucchi, R.; Ceccato, R.; Pasquali, L.; List-Kratochvil, E. J. W.; et al. Versatile and Scalable Strategy To Grow Sol−Gel Derived 2H-MoS_2 Thin Films with Superior Electronic Properties: A Memristive Case. *ACS Appl. Mater. Interfaces* **2018**, *10*, 34392−34400.

(24) Li, X.; Zhu, H. Two-Dimensional MoS_2: Properties, Preparation, and Applications. *J. Materiomics* **2015**, *1*, 33−44.

(25) Timpel, M.; Ligorio, G.; Ghiami, A.; Gavioli, L.; Cavaliere, E.; Chiappini, A.; Rossi, F.; Pasquali, L.; Gärisch, F.; List-Kratochvil, E. J. W.; et al. 2D-MoS_2 goes 3D: Transferring Optoelectronic Properties of 2D MoS_2 to a Large-area Thin Film. *NPJ. 2D Mater. Appl.* **2021**, *5*, 64.

(26) Dumcenco, D.; Ovchinnikov, D.; Marinov, K.; Lazić, P.; Gibertini, M.; Marzari, N.; Sanchez, O. L.; Kung, Y.-C.; Krasnozhon,

D.; Chen, M.-W.; et al. Large-Area Epitaxial Monolayer MoS_2. *ACS Nano* **2015**, *9*, 4611−4620.
(27) Ansari, N.; Moradi, M. Optical Absorption in Air/Monolayer MoS_2/S (S = SiO_2 or Si) Trilayer Stacks at Oblique Incidence. *Superlattices Microstruct.* **2017**, *104*, 104−111.
(28) Bernardi, M.; Ataca, C.; Palummo, M.; Grossman, J. C. Optical and Electronic Properties of Two-Dimensional Layered Materials. *Nanophotonics* **2017**, *6*, 479−493.
(29) Fan, X.; Singh, D. J.; Zheng, W. Valence Band Splitting on Multilayer MoS_2: Mixing of Spin−Orbit Coupling and Interlayer Coupling. *J. Phys. Chem. Lett.* **2016**, *7*, 2175−2181.
(30) Zhang, Y.; Li, H.; Wang, H.; Liu, R.; Zhang, S.-L.; Qiu, Z.-J. On Valence-Band Splitting in Layered MoS_2. *ACS Nano* **2015**, *9*, 8514−8519.
(31) Castellanos-Gomez, A.; Quereda, J.; van der Meulen, H. P.; Agraït, N.; Rubio-Bollinger, G. Spatially Resolved Optical Absorption Spectroscopy of Single- and Few-Layer MoS_2 by Hyperspectral Imaging. *Nanotechnology* **2016**, *27*, 115705.
(32) Yue, Y.-Y.; Wang, Z.; Wang, L.; Wang, H.-Y.; Chen, Y.; Wang, D.; Chen, Q.-D.; Gao, B.-R.; Wee, A. T. S.; Qiu, C.-W.; et al. Many-Particle Induced Band Renormalization Processes in Few- and Mono-Layer MoS_2. *Nanotechnology* **2021**, *32*, 135208.
(33) Bieniek, M.; Szulakowska, L.; Hawrylak, P. Band Nesting and Exciton Spectrum in Monolayer MoS_2. *Phys. Rev. B* **2020**, *101*, 125423.
(34) Britnell, L.; Ribeiro, R. M.; Eckmann, A.; Jalil, R.; Belle, B. D.; Mishchenko, A.; Kim, Y. J.; Gorbachev, R. V.; Georgiou, T.; Morozov, S. V.; et al. Strong Light-Matter Interactions in Heterostructures of Atomically Thin Films. *Science* **2013**, *340*, 1311−1314.
(35) Li, H.; Zhang, Q.; Yap, C. C. R.; Tay, B. K.; Edwin, T. H. T.; Olivier, A.; Baillargeat, D. From Bulk to Monolayer MoS_2: Evolution of Raman Scattering. *Adv. Funct. Mater.* **2012**, *22*, 1385−1390.
(36) Lee, C.; Yan, H.; Brus, L. E.; Heinz, T. F.; Hone, J.; Ryu, S. Anomalous Lattice Vibrations of Single- and Few-Layer MoS_2. *ACS Nano* **2010**, *4*, 2695−2700.
(37) Ho, Y.-T.; Ma, C.-H.; Luong, T.-T.; Wei, L.-L.; Yen, T.-C.; Hsu, W.-T.; Chang, W.-H.; Chu, Y.-C.; Tu, Y.-Y.; Pande, K. P.; et al. Layered MoS_2 Grown on C -Sapphire by Pulsed Laser Deposition. *Phys. Status Solidi - Rapid Res. Lett.* **2015**, *9*, 187−191.
(38) Lee, K.; Chen, Y.-H.; Lin, H.-Y.; Cheng, C.-C.; Chen, P.-Y.; Wu, T.-Y.; Shih, M. H.; Wei, K.-H.; Li, L.; Chang, C.-W. Plasmonic Gold Nanorods Coverage Influence on Enhancement of the Photoluminescence of Two-Dimensional MoS_2 Monolayer. *Sci. Rep.* **2015**, *5*, 16374.
(39) Plechinger, G.; Mann, J.; Preciado, E.; Barroso, D.; Nguyen, A.; Eroms, J.; Schüller, C.; Bartels, L.; Korn, T. A direct Comparison of CVD-Grown and Exfoliated MoS_2 using Optical Spectroscopy. *Semicond. Sci. Technol.* **2014**, *29*, No. 064008.
(40) Amani, M.; Burke, R. A.; Ji, X.; Zhao, P.; Lien, D.-H.; Taheri, P.; Ahn, G. H.; Kirya, D.; Ager, J. W.; Yablonovitch, E.; et al. High Luminescence Efficiency in MoS_2 Grown by Chemical Vapor Deposition. *ACS Nano* **2016**, *10*, 6535−6541.
(41) Shree, S.; George, A.; Lehnert, T.; Neumann, C.; Benelajla, M.; Robert, C.; Marie, X.; Watanabe, K.; Taniguchi, T.; Kaiser, U.; et al. High Optical Quality of MoS_2 Monolayers Grown by Chemical Vapor Deposition. *2d Mater.* **2020**, *7*, No. 015011.
(42) Kumar, N.; He, J.; He, D.; Wang, Y.; Zhao, H. Charge Carrier Dynamics in Bulk MoS_2 Crystal Studied by Transient Absorption Microscopy. *J. Appl. Phys.* **2013**, *113*, 133702.
(43) Soni, A.; Kushavah, D.; Lu, L.-S.; Chang, W.-H.; Pal, S. K. Ultrafast Exciton Trapping and Exciton−Exciton Annihilation in Large-Area CVD-Grown Monolayer WS_2. *J. Phys. Chem. C* **2021**, *125*, 23880−23888.
(44) Aleithan, S. H.; Livshits, M. Y.; Khadka, S.; Rack, J. J.; Kordesch, M. E.; Stinaff, E. Broadband Femtosecond Transient Absorption Spectroscopy for a CVD MoS_2 Monolayer. *Phys. Rev. B* **2016**, *94*, No. 035445.
(45) Sim, S.; Park, J.; Song, J.-G.; In, C.; Lee, Y.-S.; Kim, H.; Choi, H. Exciton Dynamics in Atomically Thin MoS_2: Interexcitonic Interaction and Broadening Kinetics. *Phys. Rev. B* **2013**, *88*, No. 075434.
(46) Sie, E. J.; Frenzel, A. J.; Lee, Y.-H.; Kong, J.; Gedik, N. Intervalley Biexcitons and Many-Body Effects in Monolayer MoS_2. *Phys. Rev. B* **2015**, *92*, No. 125417.
(47) Schmidt, R.; Berghäuser, G.; Schneider, R.; Selig, M.; Tonndorf, P.; Malić, E.; Knorr, A.; Michaelis De Vasconcellos, S.; Bratschitsch, R. Ultrafast Coulomb-Induced Intervalley Coupling in Atomically Thin WS_2. *Nano Lett.* **2016**, *16*, 2945−2950.
(48) de Weerd, C.; Gomez, L.; Capretti, A.; Lebrun, D. M.; Matsubara, E.; Lin, J.; Ashida, M.; Spoor, F. C. M.; Siebbeles, L. D. A.; Houtepen, A. J.; et al. Efficient Carrier Multiplication in $CsPbI_3$ Perovskite Nanocrystals. *Nat. Commun.* **2018**, *9*, 4199.
(49) Goodwin, H.; Jellicoe, T. C.; Davis, N. J. L. K.; Böhm, M. L. Multiple Exciton Generation in Quantum Dot-Based Solar Cells. *Nanophotonics* **2018**, *7*, 111−126.
(50) Siemons, N.; Serafini, A. Multiple Exciton Generation in Nanostructures for Advanced Photovoltaic Cells. *J. Nanotechnol.* **2018**, *2018*, 7285483.
(51) Beard, M. C.; Knutsen, K. P.; Yu, P.; Luther, J. M.; Song, Q.; Metzger, W. K.; Ellingson, R. J.; Nozik, A. J. Multiple Exciton Generation in Colloidal Silicon Nanocrystals. *Nano Lett.* **2007**, *7*, 2506−2512.
(52) Binks, D. J. Multiple Exciton Generation in Nanocrystal Quantum Dots − Controversy, Current Status and Future Prospects. *Phys. Chem. Chem. Phys.* **2011**, *13*, 12693−12704.
(53) Cunningham, P. D.; McCreary, K. M.; Hanbicki, A. T.; Currie, M.; Jonker, B. T.; Hayden, L. M. Charge Trapping and Exciton Dynamics in Large-Area CVD Grown MoS_2. *J. Phys. Chem. C* **2016**, *120*, 5819−5826.
(54) Wang, H.; Zhang, C.; Rana, F. Ultrafast Dynamics of Defect-Assisted Electron−Hole Recombination in Monolayer MoS_2. *Nano Lett.* **2015**, *15*, 339−345.
(55) Sun, D.; Rao, Y.; Reider, G. A.; Chen, G.; You, Y.; Brézin, L.; Harutyunyan, A. R.; Heinz, T. F. Observation of Rapid Exciton−Exciton Annihilation in Monolayer Molybdenum Disulfide. *Nano Lett.* **2014**, *14*, 5625−5629.
(56) Tielrooij, K. J.; Song, J. C. W.; Jensen, S. A.; Centeno, A.; Pesquera, A.; Zurutuza Elorza, A.; Bonn, M.; Levitov, L. S.; Koppens, F. H. L. Photoexcitation Cascade and Multiple Hot-Carrier Generation in Graphene. *Nat. Phys.* **2013**, *9*, 248−252.
(57) Schaller, R. D.; Agranovich, V. M.; Klimov, V. I. High-Efficiency Carrier Multiplication Through Direct Photogeneration of Multi-Excitons via Virtual Single-Exciton States. *Nat. Phys.* **2005**, *1*, 189−194.
(58) Trinh, M. T.; Houtepen, A. J.; Schins, J. M.; Hanrath, T.; Piris, J.; Knulst, W.; Goossens, A. P. L. M.; Siebbeles, L. D. A. In Spite of Recent Doubts Carrier Multiplication Does Occur in PbSe Nanocrystals. *Nano Lett.* **2008**, *8*, 1713−1718.
(59) Liu, Y.; Frauenheim, T.; Yam, C. Carrier Multiplication in Transition Metal Dichalcogenides Beyond Threshold Limit. *Adv. Sci.* **2022**, *9*, 2203400.
(60) Sarkar, A. S.; Mushtaq, A.; Kushavah, D.; Pal, S. K. Liquid Exfoliation of Electronic Grade Ultrathin Tin(II) Sulfide (SnS) with Intriguing Optical Response. *NPJ. 2D Mater. Appl.* **2020**, *4*, 1.

https://doi.org/10.1021/acs.jpclett.3c00306
J. Phys. Chem. Lett. 2023, 14, 2965−2972

scientific reports

Check for updates

OPEN

Substrate-induced modulation of transient optical response of large-area monolayer MoS_2

Ashish Soni[1,2], Nagendra S. Kamath[1,2], Yun-Yang Shen[3], Harshita Seksaria[4], Abir De Sarkar[4], Wen-Hao Chang[3,5] & Suman Kalyan Pal[1,2]✉

The intrinsic properties of two-dimensional (2D) transition-metal dichalcogenides (TMDs) are profoundly influenced by their interface conditions. Engineering the TMD/substrate interface is crucial for harnessing the unique optoelectronic properties of 2D TMDs in device applications. This study delves into how the transient optical properties of monolayer (ML) MoS_2 are affected by the substrate and film preparation processes, specifically focusing on the generation and recombination pathways of photoexcited carriers. Our experimental and theoretical analyses reveal that induced strain and defects during transfer process play pivotal roles in shaping these optical properties. Through femtosecond transient absorption measurements, we uncover the impact of substrate alterations on the carrier trapping process in ML MoS_2. Moreover, we investigate exciton-exciton annihilation (EEA), demonstrating that the EEA rate varies with different substrates and significantly decreases at low temperatures (77 K). This research paves the way for customizing the optoelectronic properties of TMDs through strategic interface engineering, potentially leading to the creation of highly efficient electronic devices such as optoelectronic memory, light-emitting diodes, and photodetectors.

Keywords TMDs, Ultrafast transient absorption spectroscopy, Exciton-exciton annihilation, Carrier trapping, Substrate effect, Density functional theory

Two-dimensional (2D) semiconductors have garnered significant interest in the scientific community due to their unique electronic, optical, and physical properties. Among them, 2D TMDs are particularly promising candidates. They possess a direct bandgap in their MLs and exhibit strong light-matter interactions due to quantum confinement effects, resulting in high absorption and unusual spin-orbit coupling effects[1,2]. The binding energy of excitons in ML TMDs is considerably higher due to increased Coulomb interactions[3,4] and reduced dielectric screening[5]. Consequently, quasi-particles such as excitons[3,6], trion[7,8], and biexcitons[9] can exist in ML TMDs even at room temperature.

The high binding energy and enhanced stability of excitons make 2D TMDs excellent materials for lighting applications[10–12]. Additionally, TMDs are suitable for other atomically thin optoelectronic devices, including transistors[13], phototransistors[14], energy conversion[15,16], and storage devices[17]. Large-area ML TMDs are indispensable for realizing ultralight optoelectronic devices for practical and industrial applications[18–20]. However, the growth of large-area ML TMDs by chemical vapor deposition (CVD) requires high growth temperatures, suitable substrates, and precursors, which limits their potential applications[21,22]. To overcome these limitations, a viable method for device fabrication involving TMDs is the transfer of as-grown samples onto desired substrates. This layer transfer is also crucial for removing growth precursors to avoid unwanted doping[23], and fabrication of flexible[24] and heterostructure devices[25,26]. In principle, the scattering by impurities and defects at the TMD/substrate interface can affect carrier mobility, thereby altering the performance of TMD-based optoelectronic devices[27,28]. Previous reports suggest that transfer process can induce strain and charge doping, ultimately impacting the carrier mobility and electronic band structure of 2D TMDs[29,30]. The electronic structure of 2D TMDs changes due to induced strain during transfer process[31]. The bandgap of layered TMDs is reported to be reduced under non-uniform strain[32,33].

Understanding the dynamics of charge carriers in layered TMDs is fundamental for the realization of TMD-based electronic and optoelectronic devices. For light-emitting devices, non-radiative carrier recombination

[1]School of Physical Sciences, Indian Institute of Technology Mandi, Kamand, Mandi, Himachal Pradesh 175005, India. [2]Advanced Materials Research Centre, Indian Institute of Technology Mandi, Kamand, Mandi, Himachal Pradesh 175005, India. [3]Department of Electrophysics, National Yang Ming Chiao Tung University, Hsinchu 30010, Taiwan. [4]Institute of Nano Science and Technology, Knowledge City, Sector 81, Mohali 140306, India. [5]Research Center for Applied Sciences, Academia Sinica, Nankang, Taipei 11529, Taiwan. ✉email: suman@iitmandi.ac.in

channels, such as defect capturing and Auger recombination, are critical factors that diminish charge carrier lifetime and limit the emission quantum yield or brightness of optoelectronic devices[34–36]. In recent years, researchers have sought to increase the emission quantum yield of 2D TMDs using various electronic and chemical approaches[31,37,38]. These efforts have enhanced emission efficiency at lower excitation densities, but at higher densities, exciton-exciton annihilation (EEA) limits the emission yield. In this context, the effect of substrates on exciton dynamics in TMDs remains largely unexplored. Understanding how substrates influence EEA and subsequently impact excitonic lifetime is imperative for advancing high-performance optoelectronic devices based on 2D TMDs.

In this work, we employed femtosecond transient absorption (TA) spectroscopy to probe the substrate-induced effects on the dynamical behavior of excitons in ML MoS_2 supported on sapphire, quartz, and Si/SiO_2. Steady-state spectroscopic measurements reveal that the optical properties of as-grown MoS_2 are markedly different from transferred samples due to the creation of new defects during the transfer process. Density functional theory (DFT) was used to unveil the effect of induced strain on the optical properties of MoS_2. Our TA studies demonstrate that exciton dynamics in 2D MoS_2 depend not only on the substrate but also on the sample preparation process (as-grown or transferred). The EEA rate decreases significantly when MoS_2 grown on sapphire is transferred to a Si/SiO_2 substrate. Moreover, the EEA rate is temperature-dependent and reduces at low temperatures. We discuss plausible explanations for the variation of EEA rate with substrate and temperature, emphasizing the role of defect capturing and thermally assisted exciton-exciton interaction. This detailed study illuminates the complex interplay between substrate-induced defects and strain on exciton dynamics in 2D TMDs during transfer processes, offering critical insights for the advancement of optoelectronic devices.

Results and discussion

Optical and structural characterization

Large-area ML MoS_2 was grown on double-side polished (DSP) sapphire and subsequently transferred onto various substrates, including DSP quartz, DSP sapphire, and Si/SiO_2. Continuous ML MoS_2 films on these substrates are evident from the optical images depicted in Figure S1(a-d). The absorption (red curve) and photoluminescence (PL) (blue curve) spectra for all MoS_2 samples were measured at room temperature, as shown in Fig. 1a–d. Figure 1a indicates that the as-grown MoS_2 exhibits two distinct absorption peaks at 1.91 eV and 2.04 eV, corresponding to the A and B excitons, which arise from the optical transitions between the spin-split valence band (VB) and the conduction band (CB)[1,39,40]. The band nesting effect in ML MoS_2 leads to a C-exciton transition (according to Wilson and Yoffe's nomenclature), which becomes prominent at higher energies, around 2.87 eV[6,41].

The absorption spectra of the transferred samples are presented in Fig. 1b–d. In these samples, the A-exciton peak is observed to shift towards lower energy, with the shift following the order: DSP quartz (1.90 eV) to DSP sapphire (1.89 eV) to Si/SiO_2 (1.89 eV). The PL spectrum of as-grown ML MoS_2 shows emission peaks corresponding to the A (~ 1.86 eV) and B (~ 1.97 eV) excitons, as depicted in Fig. 1a. A broadening of the emission spectra (recorded under identical excitation energy) and the emergence of a shoulder peak (~ 1.75 eV) are observed in the transferred MoS_2 on sapphire and quartz substrates (Fig. 1b,c). This additional shoulder peak in the PL spectra of transferred MoS_2 could be attributed to either emission from defect states or trion emission, which will be discussed further. In contrast, the PL spectrum (recorded under identical excitation energy) of MoS_2 transferred onto Si/SiO_2 is similar to that of the as-grown sample.

The ML nature of our samples was confirmed using Raman spectroscopy and verified for homogeneity by optical microscopy (Figure S1). Thickness measurements, performed using atomic force microscopy (AFM), indicated that the thicknesses of the transferred samples are slightly greater than those of the as-grown MoS_2 (Figure S2). This increase in thickness is likely due to the formation of air bubbles between the layer and the substrate during the transfer process. The Raman spectrum of as-grown MoS_2 exhibits peaks at approximately 385.6 cm^{-1} and 405 cm^{-1}, corresponding to the in-plane (E^1_{2g}) and out-of-plane (A_{1g}) vibrations, respectively (Fig. 2a). The separation between these two peaks is about 19.4 cm^{-1}, confirming the monolayer nature of the MoS_2 film[42–45]. A small Raman peak observed at 419 cm^{-1} in both the as-grown and transferred samples on sapphire (Fig. 2a) is attributed to the Raman signature of the sapphire substrate[46,47]. In the transferred MoS_2 samples, the Raman peak corresponding to the E^1_{2g} mode shows a slight blueshift compared to the as-grown sample. This shift is attributed to strain release or defects in the transferred samples. The strain release in ML MoS_2 likely arises from variations in the thermal expansion coefficient during the transfer process[48–50]. It has been reported that strain primarily affects the in-plane vibration (E^1_{2g}) of MoS_2, while the out-of-plane vibration (A_{1g}) remains unaffected[51,52], which is consistent with our observations.

To investigate the impact of the change of substrate on PL properties of ML MoS_2, the emission spectra (recorded at room temperature under identical excitation energy) were fitted using a combination of Gaussian and Lorentzian (Voigt) functions. Theoretically, the linewidth broadening of excitonic PL in ML TMDs follows a Lorentzian shape. However, inhomogeneities introduced by ripples or bubbles require the inclusion of a Gaussian component to accurately model the spectra[53]. We found that a minimum of four components was necessary to adequately fit the PL spectra for all samples (Fig. 2b). The PL spectrum of as-grown MoS_2 displays distinct A and B-exciton peaks centered around ~ 1.86 eV and ~ 1.97 eV, respectively[1]. An additional peak at 1.81 eV is attributed to charged exciton or trion emission, as reported in previous studies[8,54]. Figure 2b shows that both A-exciton and trion emission peaks are red-shifted in the transferred MoS_2 samples. These red-shifts cannot be attributed to the release of strain when the MoS_2 layer was transferred to different substrates, as strain release typically results in a blue-shift in PL spectrum[55]. Instead, the observed red-shifts suggest the introduction of a different type of strain. While strain release generally causes a blue-shift in the PL spectrum, the prominent red-shift observed here indicates that other factors are at play. AFM mapping of the transferred samples (Figure

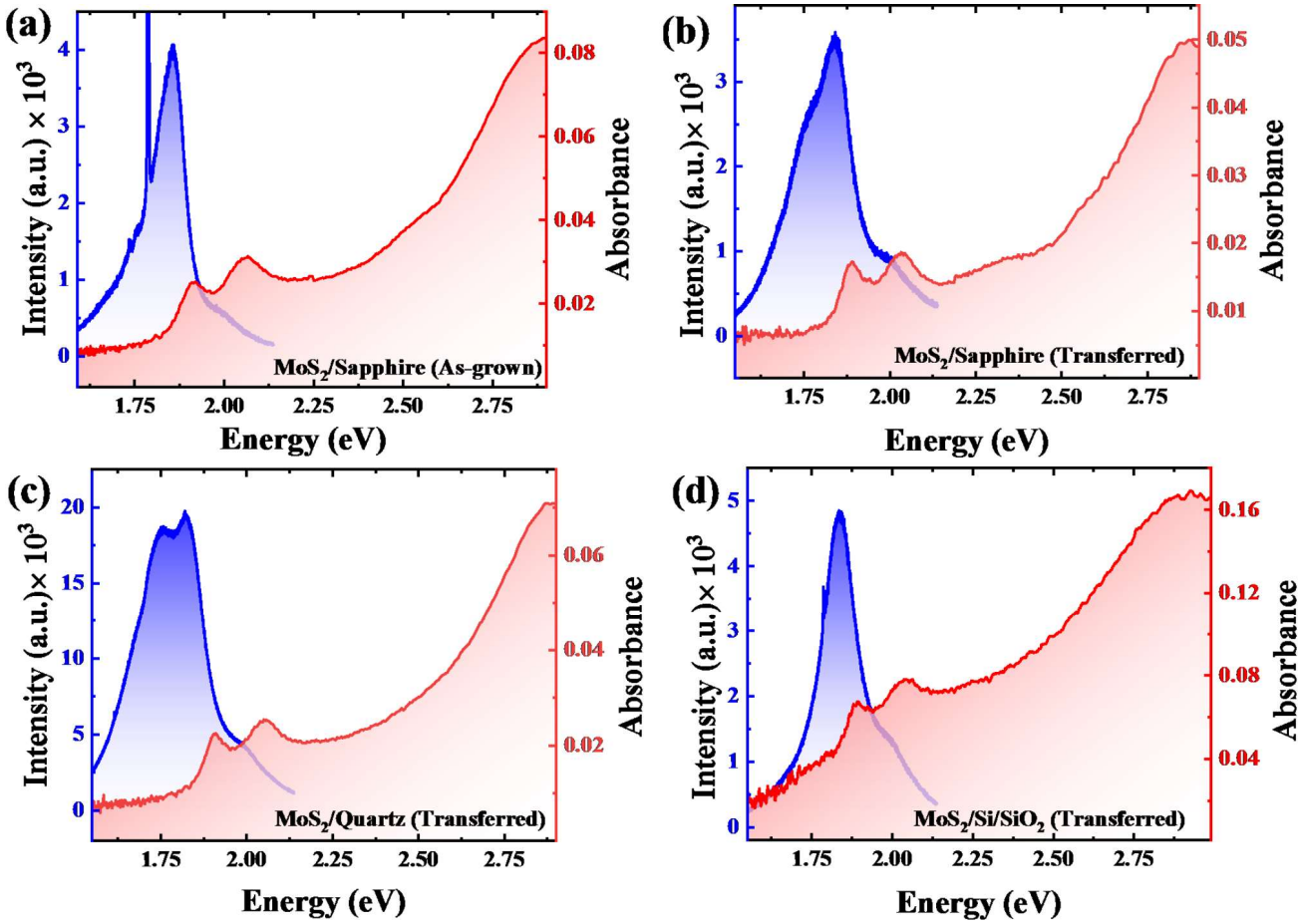

Fig. 1. Absorption (the red solid lines) and PL (the blue solid lines) spectra of CVD-grown large area ML MoS_2 (**a**) grown on sapphire and transferred on (**b**) sapphire, (**c**) quartz and (**d**) Si/SiO_2 substrates.

S3) reveals the presence of bubbles or ripples, which are likely responsible for the non-uniform strain. Therefore, the observed red-shift in the PL spectra is attributed to the non-uniform strain induced by these bubbles or ripples formed during the transfer process. Harats et al. reported a similar red-shift in the PL spectrum and trion formation due to non-uniform strain in WS_2, as predicted by the drift-diffusion model[56]. Various studies have investigated the impact of strain on the PL properties of ML MoS_2, indicating that the optical bandgap is modified by strain[33,57,58]. Additionally, the lowest energy peak in the PL spectra (labelled as "D") is attributed to emission from defect-bound excitons[59,60]. The relative contributions of A-exciton, B-exciton, trion, and defect emissions were determined from the fitting of PL spectra (Table S1). We found that the percentage of defect emission is higher in samples transferred onto sapphire (18%) and quartz (33%) substrates compared to Si/SiO_2 (13%) and the as-grown MoS_2 (12%). These results indicate a significant increase in defect states in MoS_2 transferred to sapphire and quartz substrates, in contrast to the sample transferred onto Si/SiO_2.

Theoretical modelling of strain induced by transfer processes

As previously discussed, the A-exciton absorption peak of ML MoS_2 shifts with transfer of the substrate. This shift is attributed to strain induced by the formation of ripples or bubbles and lattice parameters mismatch between the ML and the substrate[61,62]. To elucidate the effect of strain on the optical properties of MoS_2, we calculated the band structure of ML MoS_2 using density functional theory (DFT) under various tensile strains. Our calculations show that the bandgap of pristine MoS_2 decreases with increasing tensile strain (Figure S4), aligning with prior theoretical reports[45,63–65]. Additionally, to investigate the effects of specific substrates, we modelled MoS_2 placed on quartz and sapphire substrates (Fig. 3a,b). The lattice mismatches and associated strains are relatively small (1.2% for MoS_2/quartz and 3.5% for MoS_2/sapphire) while maintaining a hexagonal unit cell. The calculated bandgaps for MoS_2 on quartz and sapphire are 2.02 eV and 1.10 eV, respectively (Fig. 3c,d). The change in the calculated bandgap is significantly larger than the experimentally observed value. Several factors could contribute to this discrepancy. First, the experiments were conducted at room temperature (300 K), whereas the calculations were performed at 0 K. Second, only strain due to lattice mismatch was considered in the calculations, while other factors, such as ripples or bubbles present in actual samples, were not accounted for. However, DFT calculations exhibit the same trend of decreasing bandgap from quartz to sapphire as observed in the experiment (Fig. 1b,c), suggesting that strain can alter the bandgap of ML MoS_2.

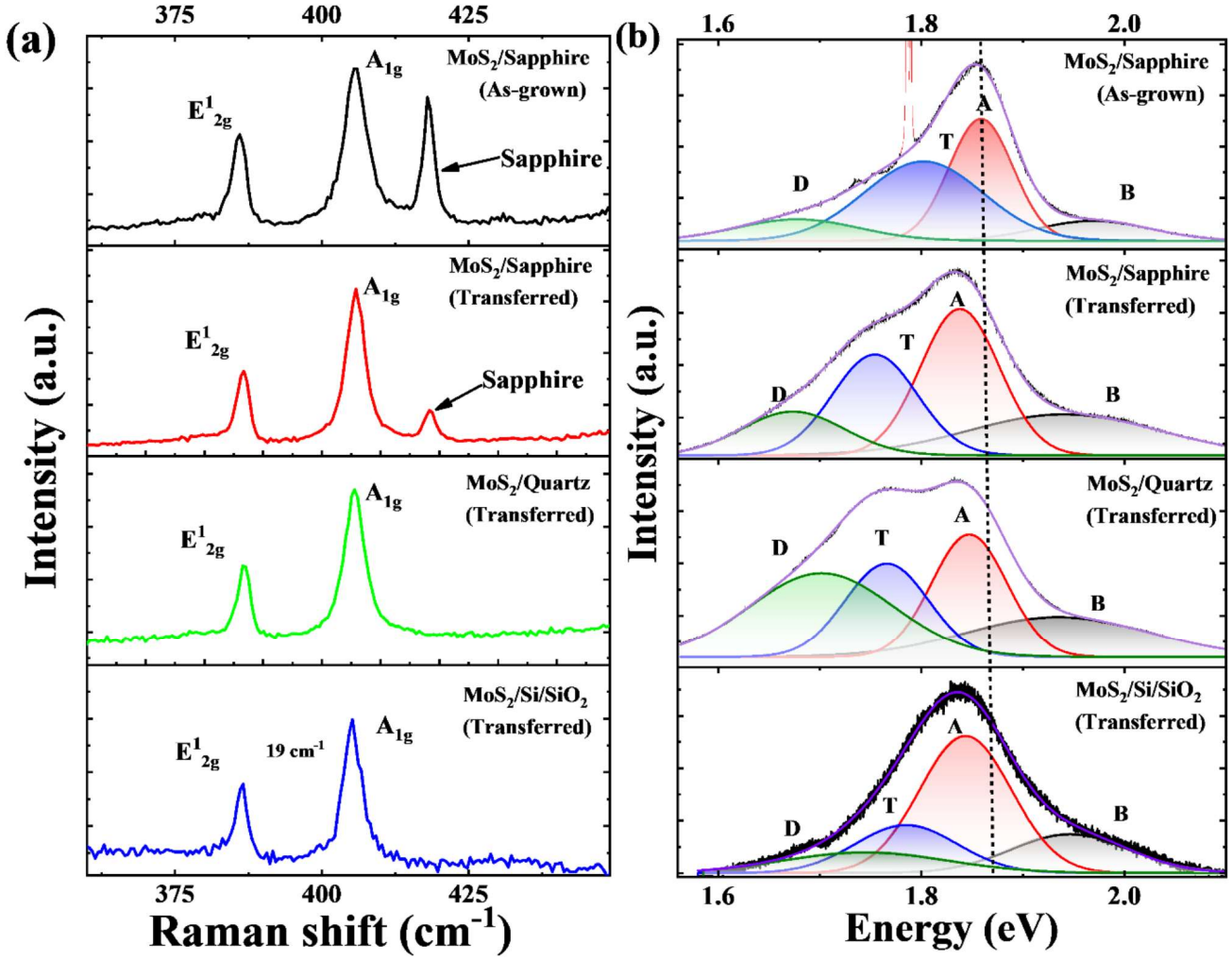

Fig. 2. (**a**) Raman spectra of ML MoS_2 on four different substrates. (**b**) Deconvolution of the PL spectra of as-grown and transferred ML MoS_2 into four curves (combination of Gaussian and Lorentzian). A, B, T, and D represent contributions of A-exciton, B-exciton, trion, and defect emission, respectively to the total PL.

X-ray photoelectron spectroscopy (XPS) study

The variation in the intensity of defect-related PL across different samples (Fig. 2b) suggests the presence of varying levels and types of defects in the ML MoS_2 samples. To quantitatively assess the presence of defects, we conducted X-ray photoelectron spectroscopy (XPS) measurements. High-resolution XPS spectra of Mo 3d for all samples are shown in Fig. 4a–d. The Mo 3d spectrum exhibits two prominent emission peaks at 232 eV (Mo $3d_{3/2}$) and 229.6 eV (Mo $3d_{5/2}$), corresponding to the Mo^{4+} state in MoS_2[66,67]. Moreover, a peak at 226.6 eV is attributed to the S 2s state, as reported previously[68,69]. Another small peak appears in all four samples around 236 eV with different intensities. This peak corresponds to the Mo^{6+} state, indicative of molybdenum oxides (MoO_3) formation[67]. The XPS spectra were fitted using a Voigt profile on a Shirley-type background to determine the contribution of each peak. The area under the oxide (Mo-O) peaks serves as a measure of oxidation-related defects in the samples. The percentage contributions (i.e., area integral percentages) of the Mo-O (Mo^{6+}) peaks, calculated from Fig. 4, are 13.9, 9.8, 10.2, and 20.2% for the as-grown and transferred MoS_2 on sapphire, quartz, and Si/SiO_2, respectively. These results indicate that the density of oxygen-related defects is comparatively lower in the transferred samples on sapphire and quartz compared to the as-grown and transferred samples on Si/SiO_2.

The as-grown MoS_2 samples on sapphire contain oxygen-related defects primarily due to the residual oxygen present during the CVD process or the deposition of unreacted MoO_3 on the sapphire surface[70,71]. However, during the transfer process, MoS_2 is moved from its original growth substrate to a new substrate (sapphire or quartz). The transfer process involves steps such as cleaning and annealing[72], which can reduce or eliminate these residuals and oxygen-related defects. As a result, the transferred MoS_2 samples on sapphire and quartz exhibit lower oxygen defect densities compared to the as-grown samples on sapphire.

Furthermore, we calculated the stoichiometric ratios of Mo to S from the XPS data (a detailed analysis is provided in the Supporting Information). We have found that the ratio of Mo: S is 1:1.9 in as-grown MoS_2 on sapphire, and 1:1.75, 1:1.7 and 1:1.88 in transferred MoS_2 on sapphire, quartz, and Si/SiO_2, respectively. Consequently, the estimated sulfur deficiency is 5%, 12.5%, 15%, and 6% for the as-grown MoS_2 on sapphire

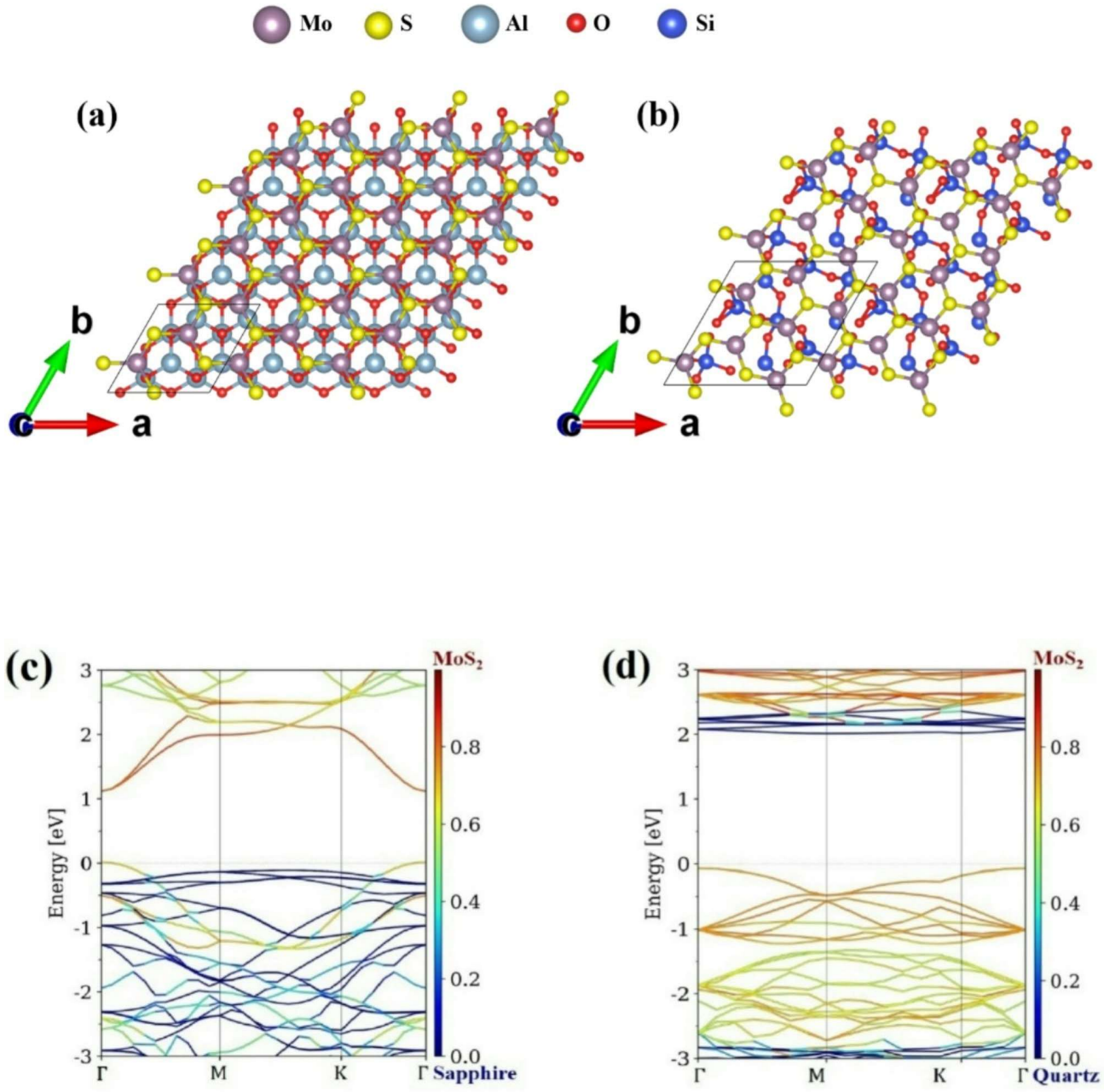

Fig. 3. The optimized structure of MoS_2 on top of (**a**) sapphire and (**b**) quartz. Band structure of (**c**) MoS_2/Sapphire and (**d**) MoS_2/Quartz calculated using DFT.

and for MoS_2 transferred onto sapphire, quartz, and Si/SiO_2, respectively. The XPS analysis indicates a notable increase in sulfur vacancies in the samples transferred onto sapphire and quartz. This observation correlates with the variation in defect-related PL intensity, where the defect-PL follows the trend: as-grown < Si/SiO_2 < sapphire < quartz. This trend is consistent with the increase in sulfur vacancies, suggesting that sulfur vacancies are the predominant defect type in transferred ML MoS_2 on sapphire and quartz.

Transient optical response

To investigate the influence of substrate material on exciton dynamics in ML MoS_2, we performed TA measurements on our samples. The TA spectra for as-grown ML MoS_2 on sapphire and transferred MoS_2 on various substrates, measured at both room temperature and at 77 K, are presented in Fig. 5a,b. The TA spectra exhibit two prominent features: ground state bleach (GSB) corresponding to A and B excitonic transitions and positive photoinduced absorption (PIA) observed on the low-energy side of the TA spectra (not present in MoS_2/Si/SiO_2). The appearance of GSB at exciton resonance is attributed to Pauli blocking[73,74]. Whereas, PIA is associated with phenomena such as carrier-induced broadening, biexciton formation, or free carrier absorption[75–77]. The

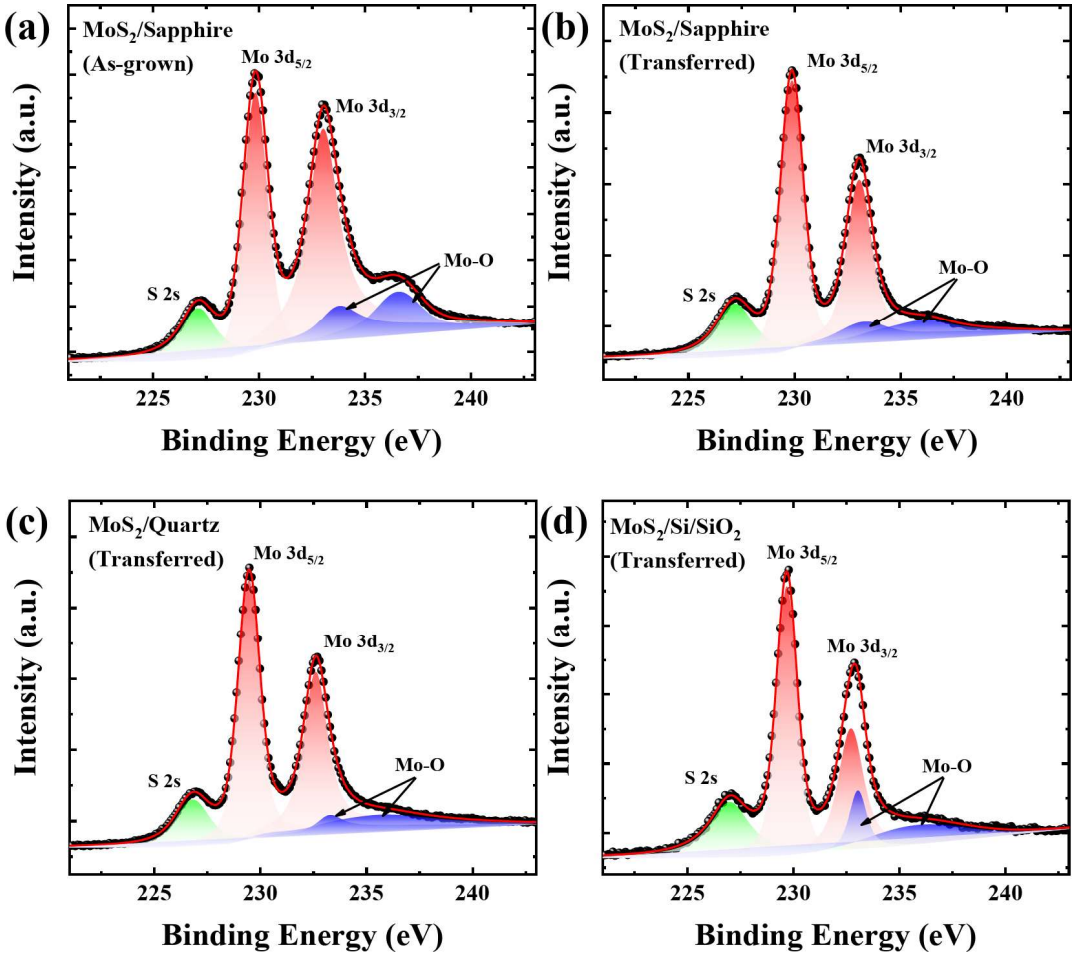

Fig. 4. XPS spectra of MoS_2 ML on (**a**) sapphire (as-grown), (**b**) sapphire (transferred), (**c**) quartz (transferred), (**d**) Si/SiO_2 (transferred) substrates with component peak-fitting. Red solid lines represent the overall fit to experimental data (black dots). The colour regions under the overall fitted curve show contributions of different states.

broadening of GSB bands in the TA spectra of transferred samples is notably more pronounced compared to that of the as-grown ML MoS_2 (Fig. 5a). This broadening can be attributed to an increased density of defect states in the transferred samples. We compared the decay kinetics of the A-exciton bleach across all samples (Fig. 5c) and observed that samples transferred onto sapphire and quartz display a positive ΔA signal following the initial negative bleach signal. Such a sign-changing behavior in the A-exciton bleach signal is commonly associated with mid-gap defect states in TMDs[78]. Therefore, the comparison of bleach kinetics suggests a higher density of mid-gap defect states in samples transferred onto sapphire and quartz compared to the other samples. These mid-gap defects are likely correlated with the higher density of sulfur vacancies, as indicated by the XPS analysis and supported by previous literature[79–81].

The bleach signals corresponding to the A and B excitonic transitions of as-grown MoS_2 exhibit a blue-shift at low temperature (Fig. 5b). This blue-shift is likely due to the suppression of electron-phonon interactions and lattice contraction, which results in an increased optical bandgap at lower temperatures[82–86]. Additionally, a shoulder feature around 1.86 eV appears in the A-exciton bleach of as-grown ML MoS_2 at low temperature (Fig. 5b). This shoulder could be attributed to charged excitons or defect-bound excitons[59,87]. However, trions (charged excitons) are typically formed after excitons, and thus, are unlikely to contribute to the bleach shoulder. Therefore, this shoulder peak is likely associated with excitons trapped by defect states within the ML MoS_2. In contrast, transferred samples on sapphire and quartz exhibit a splitting of the bleach band (Fig. 5b). The low-energy bleach component is attributed to excitons trapped in defect states, which have energy levels.

significantly below those of band-edge excitons. The observed splitting and appearance of separate bleach bands for trapped excitons at low temperature can be explained by the blue-shift of the A-exciton bleach due to the increase in bandgap and the reduced linewidth broadening of free and bound exciton transitions.

We compared the kinetics of the low-energy bleach band for all samples at low temperature (Fig. 5d). The negative ΔA followed by a high positive signal indicates a high density of defects in samples transferred onto sapphire and quartz. The TA kinetics at the split bands (1.83 and 1.89 eV) for MoS_2 on sapphire and quartz exhibit notable differences at 77 K (Figure S6). While ΔA remains negative for the high-energy bleach bands, it transitions to positive values for the low-energy bands. The prominent splitting of the A-exciton bleach band

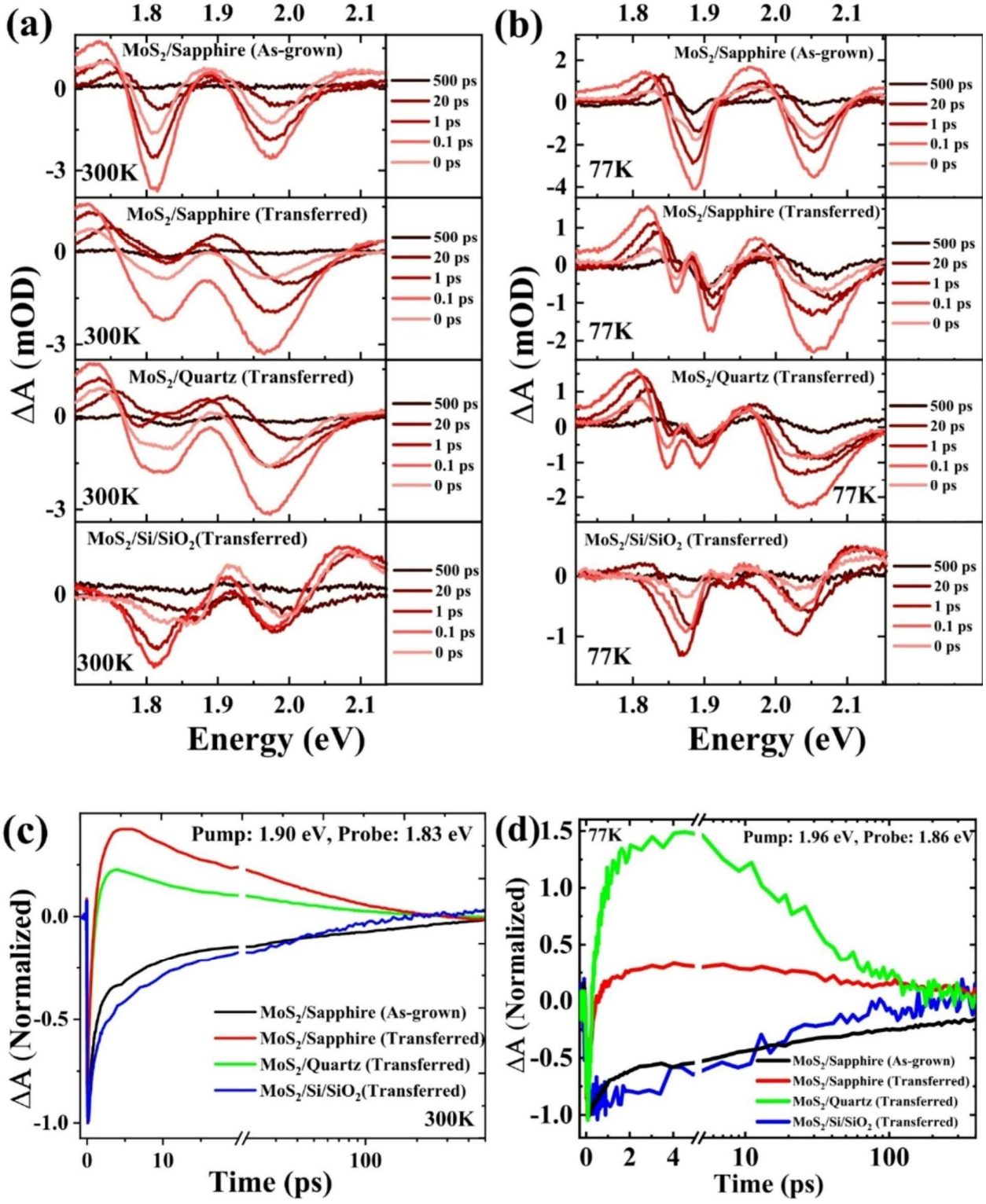

Fig. 5. TA spectra of as-grown and transferred ML MoS_2 (spot size of white light probe ~ $8.6 \times 10^{-4} cm^2$) at (**a**) room temperature (300 K) and (**b**) low temperature (77 K). The experiments were conducted at an excitation energy 2.33 eV and fluence $5.17 \times 10^{-13} \mathrm{cm}^{-2}$. (**c**) Comparison of the decay kinetics of A-exciton at 300 K and (**d**) comparison of the decay kinetics of low energy bleach bands at 77 K. The spectra of the probe beams (generated from TOPAS) used for kinetics measurements are shown in Figure S6 (e, f).

at low temperature and the sign-changing behavior of ΔA suggest that the transient optical response of MoS_2 transferred onto sapphire and quartz is predominantly influenced by mid-gap defects, likely originating from sulfur vacancies.

Exciton capturing in ML MoS_2

Both steady-state and TA studies indicate that transferring ML MoS_2 onto different substrates introduces additional defects and strain into the MoS_2 layer. To further investigate the dynamical behavior of excitons under varying levels of strain and defect density, we performed TA kinetics measurements at different spectral positions. Figure 6a presents the excitation fluence-dependent decay kinetics of the A-exciton in as-grown MoS_2, using pump and probe photon energies of 1.9 and 1.83 eV, respectively, which are resonant with the A-excitonic transition. The TA kinetics were analyzed by fitting the data to the following exponential decay function (with $n = 3$),

$$\Delta A = \sum_{i=1}^{n} A_i exp(-t/T_i) \quad (1)$$

where, ΔA represents the differential absorption, As are preexponential factors, t stands for the time and T is the decay time of a particular exponential component.

The fitted curves are shown in Fig. 6a, and fitting parameters are provided in Table S2. We observed three decay components: a fast component (~ 0.26–0.34 ps), an intermediate component (~ 7–14 ps), and a slow component (~ 110–140 ps). The fast decay component, occurring on the sub-picosecond timescale, could be attributed to processes such as hot carrier cooling, carrier-phonon scattering, or carrier trapping by defect states[74,88]. Since the excitation energy was only slightly above the band edge, the generation of hot carriers is negligible.

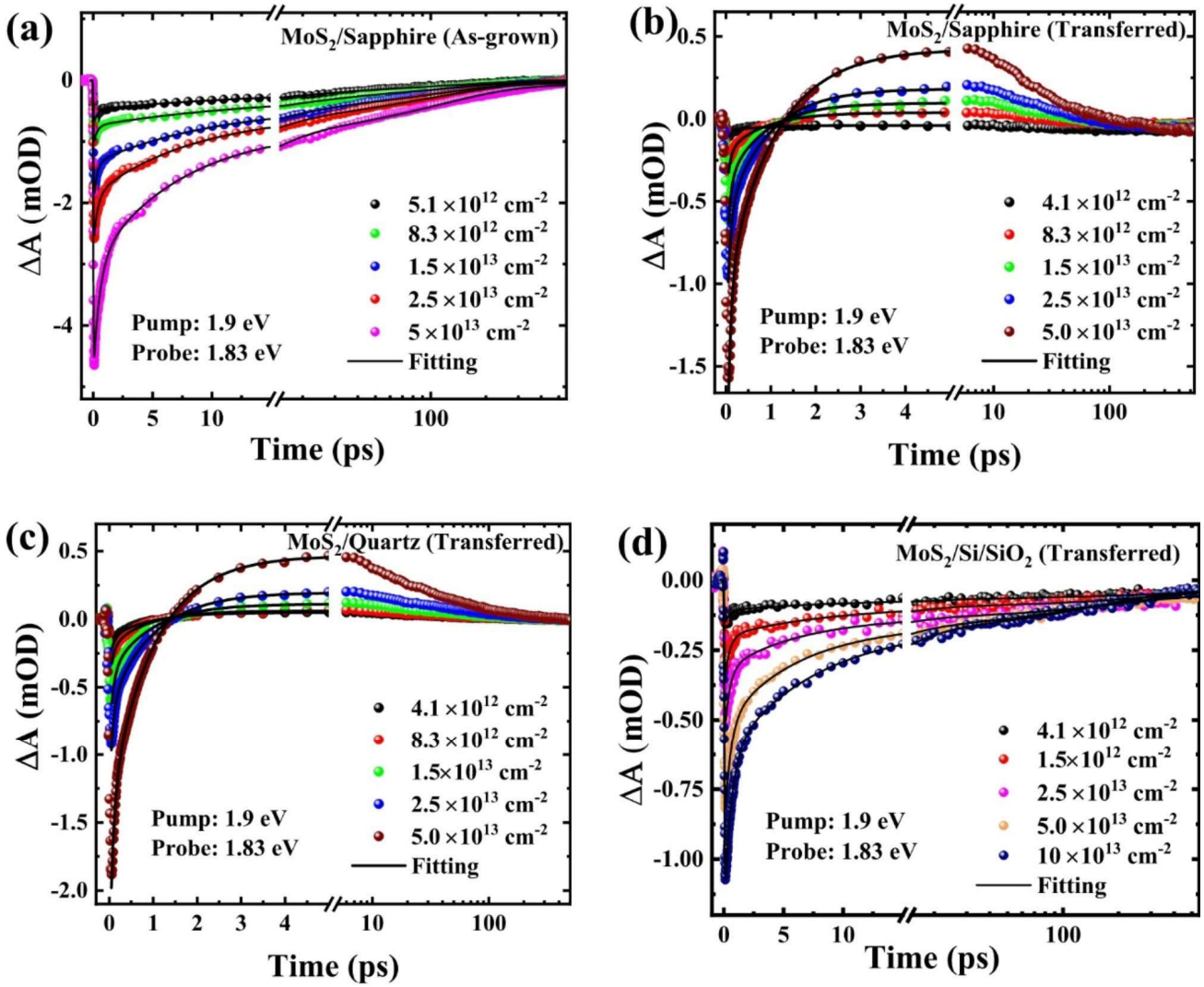

Fig. 6. Fluence-dependent TA kinetics measured at A-excitonic bleach of (**a**) as-grown and transferred ML MoS_2 on (**b**) sapphire, (**c**) quartz, and (**d**) Si/SiO_2 substrates at 300 K. The black lines are tri-exponential fits to experimental data.

Additionally, the time constant T_1 increases with excitation fluence and reaches a constant value, indicative of a defect-capturing process[89,90]. Therefore, T_1 is likely associated with the time required for excitons to be captured by defect states. The intermediate decay component (T_2) with a lifetime of ~ 7–13 ps, is characteristic of second-order relaxation processes such as Auger recombination, exciton-exciton annihilation (EEA)[89,91,92], and trion recombination[93]. The observed decrease in T_2 with increasing excitation fluence, accompanied by an increase in amplitude, suggests that this component is related to EEA. The slow component, with a time constant in the hundreds of picoseconds, is likely associated with radiative excitonic decay, as reported in the literature[44,92,94].

The decay kinetics of A-excitons in ML MoS_2 transferred onto sapphire and quartz exhibit distinct behaviors, as illustrated in Fig. 6b,c. In both cases, ΔA transitions from a negative to a positive value at high photon fluence. The initial part of the decay was fitted, revealing that a fast decay occurring on the sub-picosecond timescale (~ 0.07–0.1 ps) dominates the early decay (Table S3). According to previous studies, this behavior in TA kinetics could be attributed to PIA by trapped carriers in mid-gap defects, which can overshadow the bleach signal due to Pauli blocking[78,95]. Consequently, the positive shift in ΔA indicates a higher density of mid-gap defects in MoS_2 transferred onto sapphire and quartz compared to the as-grown sample. Conversely, the TA kinetics of MoS_2 transferred onto Si/SiO_2 (Fig. 6d) are similar to those of the as-grown MoS_2, showing no positive signal. This suggests that MoS_2 transferred onto Si/SiO_2, like the as-grown sample, has a lower density of sulfur defects. Recent studies suggest that the Si/SiO_2 substrate may passivate sulfur defects through adsorption O_2 at vacancy sites[79,96]. However, shallow traps due to oxygen vacancies still contribute to carrier decay in all samples. Therefore, the recombination dynamics of excitons and carriers in ML MoS_2 are influenced by both the substrate material and the preparation method (as-grown or transferred), due to the formation of varying concentrations of mid-gap and shallow defects. A schematic representation of the carrier dynamics, based on TA measurements, is illustrated in Fig. 7a alongside the band structure of ML MoS_2.

To quantify the capture time of carriers by defect states, we measured the kinetics of the PIA at 1.77 eV, which is attributed to absorption by trapped charges[89]. The fitting results for the growth kinetics at 1.77 eV are presented in Figure S7. The data indicate that the rise of the PIA signal at 1.77 eV is comparable to the initial sub-picosecond decay of the A-exciton bleach at the same fluence (Tables S2, S3, and S4). This observation further suggests that the PIA at 1.77 eV is associated with absorption by defect carriers. The rise time of the PIA signal reflects the carrier capture time by defect states. Comparison of the exciton capture times (Table 1) reveals that carrier capture is faster in MoS_2 transferred onto quartz and sapphire than in MoS_2 transferred onto Si/SiO_2 and as-grown samples. The higher density of mid-gap states in MoS_2 transferred onto quartz and sapphire likely accelerates the carrier capture rate in these samples.

Auger recombination of excitons

It is well known that in strongly confined systems such as quantum dots and 2D materials, strong optical excitation can result in the annihilation of excitons[97,98]. Due to enhanced Coulomb interactions, MoS_2 ML exhibits bound excitons, and strong exciton-exciton coupling results in EEA (at high excitation densities), which is a bimolecular process involving two or more excitons. Other second-order processes, such as biexciton formation, are negligible at the temperature investigated here (Fig. 6a,d)[99,100]. Additionally, the significant inhomogeneous broadening of the samples made it difficult to clearly differentiate between exciton and biexciton differential absorption. In the presence of EEA, the rate equation for a bimolecular recombination is described by[98,101]

$$\frac{dN(t)}{dt} = -\frac{1}{T}N(t) - \frac{1}{2}kN^2(t) \tag{2}$$

where N(t) denotes the exciton population at a time t, k represents the rate constant for EEA. The solution of this equation can, in principle, be utilized to analyze TA kinetics; however, for pedagogical clarity, we considered the two components separately. The first term of Eq. (2) represents first-order excitonic recombination, which dominates only at longer timescales. Conversely, EEA, being faster than monomolecular excitonic recombination, predominates at early times when the exciton density is high. Therefore, the annihilation rate can be determined by solving Eq. (2) considering only the second term. The solution to this rate equation is presented below.

$$N(t) = \frac{N_0}{1 + kN_0t}$$
$$\left(\frac{N_0}{N(t)} - 1\right) = (kN_0)\,t \tag{3}$$

where N_0 is the initial exciton density. We fitted the TA kinetics corresponding to A-excitons of ML MoS_2 grown on sapphire (Fig. 7b) and transferred on Si/SiO_2 (Fig. 7c) with Eq. (3). The values of EEA rates obtained from the fitting are presented in Table 2. A notable disparity in the EEA rates between the transferred ML MoS_2 and its as-grown counterpart was uncovered. Our findings suggest that the average EEA rate in transferred MoS_2 ($0.106 \pm 0.005\, cm^2/sec$) is lower than the as-grown ML ($0.204 \pm 0.002\, cm^2/sec$). This discrepancy further supports the notion that substrate-induced defects and strain significantly affect EEA. The introduction of defects during the transfer process serves as nonradiative recombination sites for excitons, competing with the annihilation process. Consequently, these defect states can alter the spatial distribution and mutual interaction of excitons, thereby influencing their probability of annihilation. The lower EEA rate in ML MoS_2 transferred on Si/SiO_2 could be a consequence of its higher density of oxygen defects (as evident from XPS measurements) compared to as-grown MoS_2. Moreover, induced strain during transfer process can modify the electronic band structure, affecting the exciton binding energy and subsequently influencing the formation, diffusion, and

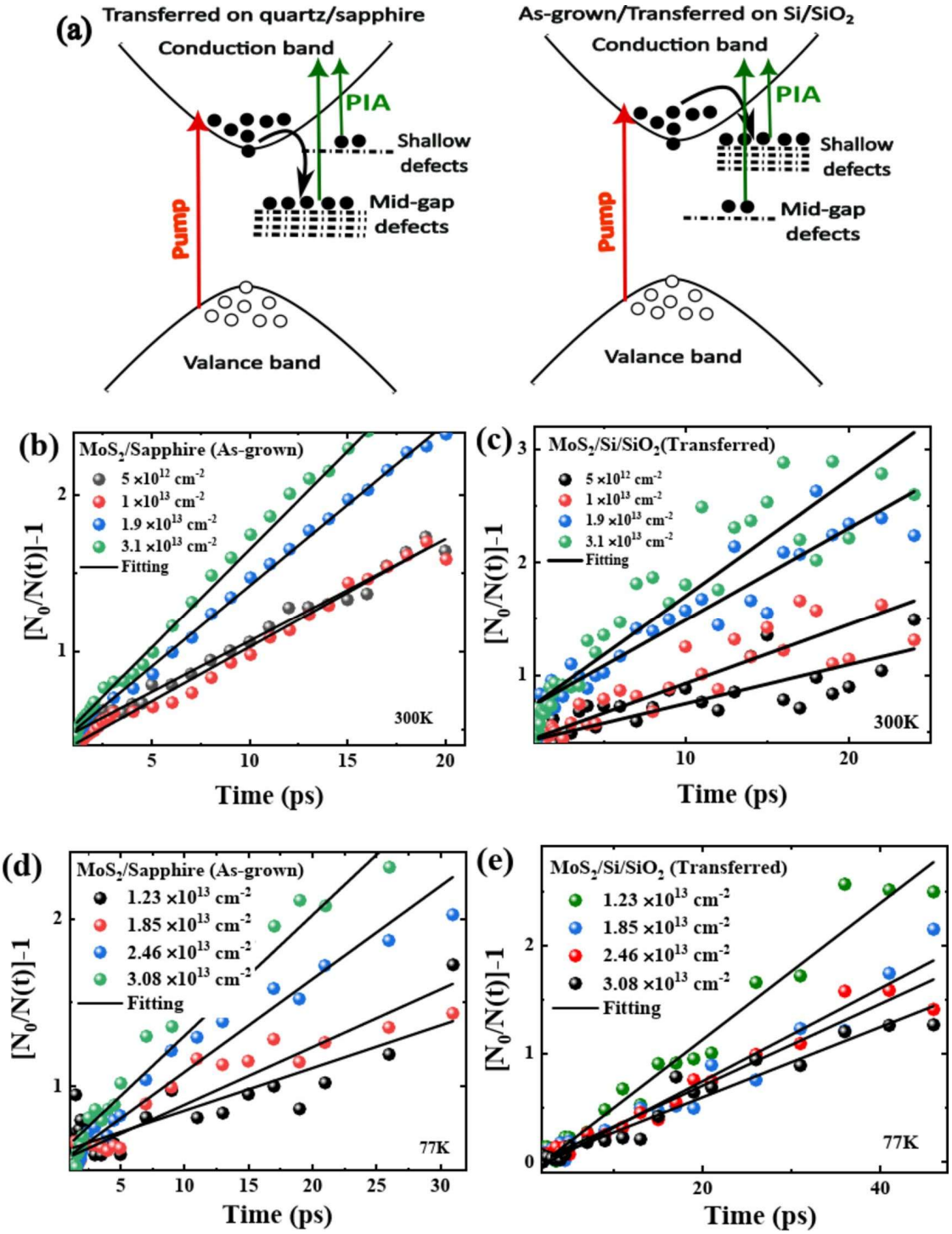

Fig. 7. (**a**) Schematic representation of the processes occurring in as-grown and transferred ML MoS_2 on Si/SiO_2 (right) and transferred on quartz and sapphire (left). Fitting of A-exciton kinetics of MoS_2 (**b**) as-grown on sapphire and (**c**) transferred on Si/SiO_2 substrates at room temperature with EEA model (Eq. 3). Fitting of A-exciton kinetics of MoS_2 (**d**) as-grown on sapphire and (**e**) transferred on Si/SiO_2 substrates at low temperature (77 K) with EEA model (Eq. 3).

Sample	MoS_2/Sapphire (As-grown)	MoS_2/Sapphire (Transferred)	MoS_2/Quartz (Transferred)	MoS_2/Si/SiO_2 (Transferred)
Defect-capturing time (ps)	0.32	0.07	0.08	0.41

Table 1. Defect-capturing time in ML MoS_2 on different substrates.

Fluence (cm^{-2})	EEA rate at 300 K (cm^2/sec)		Fluence (cm^{-2})	EEA rate at 77 K (cm^2/sec)	
	MoS_2/Sapphire (As-grown)	MoS_2/Si/SiO_2 (Transferred)		MoS_2/Sapphire (As-grown)	MoS_2/Si/SiO_2 (Transferred)
5.0×10^{12}	0.360 ± 0.002	0.145 ± 0.005	1.23×10^{13}	0.057 ± 0.003	0.024 ± 0.005
1.0×10^{13}	0.192 ± 0.002	0.118 ± 0.005	1.85×10^{13}	0.051 ± 0.003	0.029 ± 0.005
1.9×10^{13}	0.150 ± 0.002	0.092 ± 0.004	2.46×10^{13}	0.062 ± 0.003	0.019 ± 0.004
3.1×10^{13}	0.112 ± 0.002	0.067 ± 0.004	3.08×10^{13}	0.064 ± 0.003	0.013 ± 0.004
Average rate	0.204 ± 0.002	0.106 ± 0.005	Average rate	0.059 ± 0.003	0.021 ± 0.005

Table 2. EEA rates at different temperatures obtained by fitting GSB kinetics using EEA model (Eq. 3).

interaction of excitons. Thus, both strain and defects could play a pivotal role in determining the fluence range over which excitons do not undergo annihilation.

Furthermore, the A-exciton bleach kinetics of ML MoS_2 grown on sapphire (Fig. 7d) and transferred on Si/SiO_2 (Fig. 7e) measured at 77 K were fitted using Eq. (3). The average annihilation rates are found to be $0.059 \pm 0.003\, cm^2/sec$ for the MoS_2/Sapphire and $0.021 \pm 0.005\, cm^2/sec$ for the MoS_2/Si/SiO_2 (Table 2). Thus, the EEA rate is greatly reduced at low temperature. At low temperature, the thermal energy available to excitons decreases, leading to slower diffusion and a lower probability of exciton encounter, which in turn reduces the rate of annihilation. Additionally, the phonon population diminishes at low temperature, leading to a decrease in phonon-assisted exciton relaxation pathways. This reduction in phonon-mediated recombination processes could suppress EEA. It is noteworthy that the determination of the annihilation rate constant in the other two samples transferred on sapphire and quartz is not feasible because PIA signals due to trapped carriers supersede the bleach signal in the time window where EEA takes place (Fig. 6b,c).

It is evident from the above discussion that the interplay between defects and Auger-type recombination (EEA) plays a significant role in shaping the carrier dynamics in 2D materials like MoS_2. Recent studies have further highlighted the intricate relationships underlying these processes. For example, Wang et al.[102] highlighted the critical role of defect states in carrier trapping and their subsequent impact on recombination dynamics. Based on the dependence of the measured data on the pump fluence and temperature, they pointed out that other mechanisms of nonradiative recombination and carrier capture by defects are insignificant. Strong Coulomb interactions in 2D materials make Auger scattering more effective. Similarly, Shin et al.[103] provided in-depth analysis of how defect-induced trapping competes with Auger recombination, emphasizing the necessity of understanding these interactions for optimizing material performance.

Furthermore, the effects of strain on ultrafast exciton dynamics in 2D materials have garnered significant attention. Several recent studies[104–106] have shown that strain can dramatically influence exciton behavior, modifying lifetimes and recombination pathways. In this work, we observed that transfer-induced strain influences carrier dynamics in 2D MoS_2, contributing to the deeper understanding of strain engineering in 2D materials. Our findings demonstrate that transfer-induced strain can be a powerful tool to modulate exciton dynamics, with implications for the design of next-generation optoelectronic devices.

Our results highlight the critical role of sulfur vacancies in modulating the optical properties of MoS_2. The ability to control sulfur vacancies in MoS_2 by transferring it onto different substrates opens up promising avenues for future device applications[107]. These defects can enhance the electrical conductivity and carrier density of MoS_2, making it a promising material for use in electronic and optoelectronic devices[108]. For instance, sulfur vacancies have been shown to improve the performance of MoS_2-based transistors and sensors by increasing their sensitivity and response time[107,109]. Sulfur vacancies in MoS_2 introduce localized states within the bandgap, which can act as active sites for adsorption, enhancing the sensitivity and response time of sensors[110]. In the context of transistors, while defects are generally viewed as detrimental, controlled introduction of sulfur vacancies can lower the contact resistance and improve the charge carrier injection efficiency, this can lead to enhanced overall performance of the transistors[111]. Yin et al.[112] have shown that due to the strong trap effect, device based on TMDs can function as an infrared detector with high photoresponsivity and a high photo-switching ratio. It can also act as non-volatile optoelectronic memory with a high program/erase ratio and fast switching times. Additionally, the enhanced emission properties due to sulfur defects can be leveraged in developing more efficient LEDs and photodetectors[113]. Moreover, the ability to control sulfur vacancies offers pathways to tailor the electrical properties of MoS_2, making it an excellent candidate for next-generation transistors and flexible electronics[107,108]. The substrate-induced variations in sulfur vacancy densities can be strategically employed to design MoS_2-based devices with optimized performance and functionality[114,115]. The reduced EEA rate can improve the exciton lifetime, leading to higher device efficiency and stability[116,117]. By controlling the EEA rate through substrate choice and defect engineering, it is possible to tailor the optical and electronic properties of MoS_2, optimizing device performance for specific applications[118].

Conclusions

We have investigated the optical properties of ML MoS_2 grown on sapphire and transferred onto sapphire, quartz, and Si/SiO_2. Our comprehensive study, encompassing measurements of absorption, emission, and DFT calculations, reveals that substrate or air bubble-induced strains can modify the optical properties of MoS_2 by altering its band structure. XPS analysis unveils the presence of both sulfur and oxygen-induced defects in our samples, with defect PL increasing in MoS_2 transferred onto sapphire and quartz substrates due to an increased density of sulfur vacancies. Results from our femtosecond pump-probe spectroscopy measurements indicate

that both oxygen and sulfur vacancies govern the charge carrier dynamics. The carrier capture time depends on the substrate, primarily due to the variation in sulfur vacancies in as-grown and transferred MoS_2. Excitons decay via EEA at high excitation fluences, and at room temperature, the EEA rate of MoS_2 grown on sapphire (0.250 cm^2/sec) is much higher than that of MoS_2 transferred onto Si/SiO_2 (0.106 cm^2/sec). This change in the EEA rate could be attributed to substrate-induced defects (oxygen vacancies). Moreover, the EEA rate is greatly decreased at low temperature (77 K) due to a reduction in phonon-assisted exciton recombination. Leveraging the sensitivity of exciton dynamics in ML MoS_2 to the surrounding environment, particularly the substrate, offers promising avenues for further exploration and optimization of device design and performance.

Methodology

Sample preparation

ML MoS_2 films were grown on sapphire substrates by CVD in a horizontal 3-inch tube furnace. Molybdenum trioxide (MoO_3) and sulfur powders served as the growth reactants. The transition metal source and sapphire substrate were placed at the central high-temperature heating zone, while the sulfur powder was positioned upstream and heated with a heating belt. The ML MoS_2 was grown at 830 °C, with the sulfur temperature maintained at 132 °C. An argon (Ar) gas flow at 100 sccm was used as the carrier gas under a base pressure of 30 Torr during the growth process.

Transfer process

After CVD growth, the as-grown MoS_2 films were transferred from sapphire substrates to different target substrates (quartz, sapphire, and Si/SiO_2) using a wet transfer method with polymethyl methacrylate (PMMA) as a supporting layer. First, a layer of PMMA was spin-coated on the MoS_2 film grown on the sapphire substrate. The coated film was then soaked in a hot ammonia solution to detach the MoS_2 from the sapphire substrate. The detached MoS_2/PMMA was soaked in deionized water and subsequently picked up by the target substrate. After baking at 85 °C for 15 min, the sample was soaked in acetone and isopropyl alcohol to remove the PMMA layer.

Absorption, Raman and photoluminescence spectroscopy

The steady-state absorption spectrum was collected using a Shimadzu UV-2450 spectrometer (Agilent Technologies, USA). Photoluminescence (PL) and Raman measurements were performed at room temperature using Horiba Jobin-Yvon (Lab-RAM HR evolution) in the back-scattering configuration under an optical microscope. The samples were excited by a 532 nm laser through a 100X objective lens with a numerical aperture 0.9. The signals were analyzed by a monochromator and detected by an air-cooled CCD. The gratings with 300 and 1200 lines/mm were used for the PL and Raman measurements, respectively.

Femtosecond transient absorption (TA) spectroscopy

The TA spectroscopy system uses a femtosecond Ti: Sapphire amplifier (wavelength ~ 800 nm, repetition rate 1 kHz, and pulse width < 35 fs)[119]. The output from the amplifier (Spitfire Ace, Spectra physics) was divided into two components to generate pump and probe pulses. Pump pulses were obtained from the nonlinear optical parametric amplifier (TOPAS). The probe beam was a white light continuum (WLC) generated by focusing a small fraction of 800 nm light (from Spitfire Ace) on a CaF_2 crystal to obtain a stable and continuous white light probe. The probe beam was detected in both with and without pump conditions with the help of a mechanical chopper of frequency 500 Hz. A stepper motor was controlled the time delay between pump, and probe pulses with an optical delay line. TA spectra were recorded by dispersing the beam with a grating spectrograph (Acton Spectra Pro SP 2358) followed by a CCD array. Light pulses of particular wavelengths from another TOPAS were used as probes while measuring TA kinetics. Two photodiodes having variable gain were used to record TA kinetics. Low-temperature measurements were carried out using a temperature-controlled sample holder (Linkam Scientific Instruments, Model No. LTS420E-PB4) cooled with liquid nitrogen.

Data availability

The data that support the findings of this study are available from the corresponding author upon reasonable request.

Received: 22 October 2024; Accepted: 25 February 2025
Published online: 04 March 2025

References

1. Mak, K. F., Lee, C., Hone, J., Shan, J. & Heinz, T. F. Atomically thin MoS_2: A new direct-gap semiconductor. *Phys. Rev. Lett.* **105**, 136805 (2010).
2. Soni, A. & Pal, S. K. Valley degree of freedom in two-dimensional van der Waals materials. *J. Phys. D: Appl. Phys.* **55**, 303003 (2022).
3. Chernikov, A. et al. Exciton binding energy and nonhydrogenic rydberg series in monolayer WS_2. *Phys. Rev. Lett.* **113**, 076802 (2014).
4. Mayers, M. Z., Berkelbach, T. C., Hybertsen, M. S. & Reichman, D. R. Binding energies and spatial structures of small carrier complexes in monolayer transition-metal dichalcogenides via diffusion Monte Carlo. *Phys. Rev. B* **92**, 161404 (2015).
5. Lin, Y. et al. Dielectric screening of excitons and trions in single-layer MoS_2. *Nano Lett.* **14**, 5569–5576 (2014).
6. Vaquero, D. et al. Excitons, trions and Rydberg states in monolayer MoS_2 revealed by low-temperature photocurrent spectroscopy. *Commun. Phys.* **3**, 194 (2020).
7. Zhang, C., Wang, H., Chan, W., Manolatou, C. & Rana, F. Absorption of light by excitons and trions in monolayers of metal dichalcogenide MoS_2: Experiments and theory. *Phys. Rev. B* **89**, 205436 (2014).
8. Mak, K. F. et al. Tightly bound trions in monolayer MoS_2. *Nat. Mater.* **12**, 207–211 (2013).

9. You, Y. et al. Observation of biexcitons in monolayer WSe_2. *Nat. Phys.* **11**, 477–481 (2015).
10. Splendiani, A. et al. Emerging Photoluminescence in Monolayer MoS_2. *Nano Lett.* **10**, 1271–1275 (2010).
11. Mueller, T. & Malic, E. Exciton physics and device application of two-dimensional transition metal dichalcogenide semiconductors. *NPJ 2D Mater. Appl.* **2**, 29 (2018).
12. Zhao, H. et al. Strong optical response and light emission from a monolayer molecular crystal. *Nat. Commun.* **10**, 5589 (2019).
13. Baugher, B. W. H., Churchill, H. O. H., Yang, Y. & Jarillo-Herrero, P. Optoelectronic devices based on electrically tunable p–n diodes in a monolayer dichalcogenide. *Nat. Nanotechnol.* **9**, 262–267 (2014).
14. Amani, M. et al. Growth-substrate induced performance degradation in chemically synthesized monolayer MoS_2 field effect transistors. *Appl. Phys. Lett.* **104**, 203506 (2014).
15. Li, C. et al. Engineering graphene and TMDs based van der Waals heterostructures for photovoltaic and photoelectrochemical solar energy conversion. *Chem. Soc. Rev.* **47**, 4981–5037 (2018).
16. Yu, X. & Sivula, K. Toward large-area solar energy conversion with semiconducting 2D transition metal dichalcogenides. *ACS Energy Lett.* **1**, 315–322 (2016).
17. Wang, H., Feng, H. & Li, J. Graphene and graphene-like layered transition metal dichalcogenides in energy conversion and storage. *Small* **10**, 2165–2181 (2014).
18. Choi, W. et al. Recent development of two-dimensional transition metal dichalcogenides and their applications. *Mater. Today* **20**, 116–130 (2017).
19. Radisavljevic, B., Radenovic, A., Brivio, J., Giacometti, V. & Kis, A. Single-layer MoS_2 transistors. *Nat. Nanotechnol.* **6**, 147–150 (2011).
20. Luhar, B. et al. Charge transfer mediated photoluminescence engineering in WS_2 monolayers for optoelectronic application. *ACS Appl. Nano Mater.* **7**, 22350–22359 (2024).
21. Xie, Y. et al. Growth of monolayer WS_2 single crystals with atmospheric pressure CVD: Role of temperature. *MRS Adv.* **4**, 255–262 (2019).
22. Mandyam, S. V., Kim, H. M. & Drndić, M. Large area few-layer TMD film growths and their applications. *J. Phys.: Mater.* **3**, 024008 (2020).
23. Sharma, M., Singh, A., Aggarwal, P. & Singh, R. Large-area transfer of 2D TMDCs assisted by a water-soluble layer for potential device applications. *ACS Omega* **7**, 11731–11741 (2022).
24. Akinwande, D., Petrone, N. & Hone, J. Two-dimensional flexible nanoelectronics. *Nat. Commun.* **5**, 5678 (2014).
25. Cheng, J., Wang, C., Zou, X. & Liao, L. Recent advances in optoelectronic devices based on 2D materials and their heterostructures. *Adv. Opt. Mater.* **7**, 1800441 (2019).
26. Soni, A., Ghosal, S., Kundar, M., Pati, S. K. & Pal, S. K. Long-lived interlayer excitons in WS2/ruddlesden–popper perovskite van der waals heterostructures. *ACS Appl. Mater. Interfaces* **16**, 35841–35851 (2024).
27. Fuhrer, M. S. & Hone, J. Measurement of mobility in dual-gated MoS_2 transistors. *Nat. Nanotechnol.* **8**, 146–147 (2013).
28. Yu, Z. et al. Analyzing the carrier mobility in transition-metal dichalcogenide MoS_2 field-effect transistors. *Adv. Funct. Mater.* **27**, 1604093 (2017).
29. Buscema, M., Steele, G. A., van der Zant, H. S. J. & Castellanos-Gomez, A. The effect of the substrate on the Raman and photoluminescence emission of single-layer MoS_2. *Nano Res.* **7**, 561–571 (2014).
30. Ge, Y., Wan, W., Feng, W., Xiao, D. & Yao, Y. Effect of doping and strain modulations on electron transport in monolayer MoS_2. *Phys. Rev. B* **90**, 035414 (2014).
31. Feng, J., Qian, X., Huang, C.-W. & Li, J. Strain-engineered artificial atom as a broad-spectrum solar energy funnel. *Nat. Photon.* **6**, 866–872 (2012).
32. Lloyd, D. et al. Band gap engineering with ultralarge biaxial strains in suspended monolayer MoS_2. *Nano Lett.* **16**, 5836–5841 (2016).
33. Tyurnina, A. V. et al. Strained bubbles in van der Waals heterostructures as local emitters of photoluminescence with adjustable wavelength. *ACS Photon.* **6**, 516–524 (2019).
34. Wang, H., Zhang, C. & Rana, F. Surface recombination limited lifetimes of photoexcited carriers in few-layer transition metal dichalcogenide MoS_2. *Nano Lett.* **15**, 8204–8210 (2015).
35. Danovich, M., Zólyomi, V., Fal'ko, V. I. & Aleiner, I. L. Auger recombination of dark excitons in WS_2 and WSe_2 monolayers. *2d Mater.* **3**, 035011 (2016).
36. Verma, A., Soni, A., Sarkar, A. S. & Pal, S. K. Defect-mediated saturable absorption and carrier dynamics in tin (II) monosulfide quantum dots. *Opt. Lett.* **48**, 4641–4644 (2023).
37. Peimyoo, N. et al. Chemically driven tunable light emission of charged and neutral excitons in monolayer WS_2. *ACS Nano* **8**, 11320–11329 (2014).
38. Lien, D.-H. et al. Electrical suppression of all nonradiative recombination pathways in monolayer semiconductors. *Science* **364**, 468–471 (2019).
39. Bernardi, M., Ataca, C., Palummo, M. & Grossman, J. C. Optical and electronic properties of two-dimensional layered materials. *Nanophotonics* **6**, 479–493 (2017).
40. Dhakal, K. P. et al. Confocal absorption spectral imaging of MoS_2: Optical transitions depending on the atomic thickness of intrinsic and chemically doped MoS_2. *Nanoscale* **6**, 13028–13035 (2014).
41. Hill, H. M. et al. Observation of excitonic rydberg states in monolayer MoS_2 and WS_2 by photoluminescence excitation spectroscopy. *Nano Lett.* **15**, 2992–2997 (2015).
42. Li, H. et al. From bulk to Monolayer$_2$: Evolution of Raman scattering. *Adv. Funct. Mater.* **22**, 1385–1390 (2012).
43. Gnanasekar, P. et al. Promoter-free synthesis of monolayer MoS_2 by chemical vapour deposition. *CrystEngComm* **20**, 4249–4257 (2018).
44. Soni, A., Kushavah, D., Lu, L.-S., Chang, W.-H. & Pal, S. K. Efficient multiple exciton generation in monolayer MoS_2. *J. Phys. Chem. Lett.* **14**, 2965–2972 (2023).
45. Conley, H. J. et al. Bandgap engineering of strained monolayer and bilayer MoS_2. *Nano Lett.* **13**, 3626–3630 (2013).
46. Cun, H. et al. Wafer-scale MOCVD growth of monolayer MoS_2 on sapphire and SiO_2. *Nano Res.* **12**, 2646–2652 (2019).
47. Kang, L. et al. Epitaxial growth of highly-aligned MoS_2 on c-plane sapphire. *Surface Sci.* **720**, 122046 (2022).
48. Krustok, J. et al. Optical study of local strain related disordering in CVD-grown $MoSe_2$ monolayers. *Appl. Phys. Lett.* **109**, 253106 (2016).
49. Li, H. et al. Optoelectronic crystal of artificial atoms in strain-textured molybdenum disulphide. *Nat. Commun.* **6**, 7381 (2015).
50. Chae, W. H., Cain, J. D., Hanson, E. D., Murthy, A. A. & Dravid, V. P. Substrate-induced strain and charge doping in CVD-grown monolayer MoS_2. *Appl. Phys. Lett.* **111**, 143106 (2017).
51. Rice, C. et al. Raman-scattering measurements and first-principles calculations of strain-induced phonon shifts in monolayer MoS_2. *Phys. Rev. B* **87**, 081307 (2013).
52. Seravalli, L. et al. Built-in tensile strain dependence on the lateral size of monolayer MoS_2 synthesized by liquid precursor chemical vapor deposition. *Nanoscale* **15**, 14669–14678 (2023).
53. Liu, S. et al. Room-temperature valley polarization in atomically thin semiconductors via chalcogenide alloying. *ACS Nano* **14**, 9873–9883 (2020).
54. Zhumagulov, Y. V., Vagov, A., Gulevich, D. R., Faria Junior, P. E. & Perebeinos, V. Trion induced photoluminescence of a doped MoS_2 monolayer. *J. Chem. Phys.* **153**, 044132 (2020).

55. Basu, N. et al. Strain relaxation in monolayer MoS_2 over flexible substrate. *RSC Adv.* **13**, 16241–16247 (2023).
56. Harats, M. G., Kirchhof, J. N., Qiao, M., Greben, K. & Bolotin, K. I. Dynamics and efficient conversion of excitons to trions in non-uniformly strained monolayer WS_2. *Nat. Photon.* **14**, 324–329 (2020).
57. Castellanos-Gomez, A. et al. Local strain engineering in atomically thin MoS_2. *Nano Lett.* **13**, 5361–5366 (2013).
58. Niehues, I. et al. Strain control of exciton-phonon coupling in atomically thin semiconductors. *Nano Lett.* **18**, 1751–1757 (2018).
59. Tongay, S. et al. Defects activated photoluminescence in two-dimensional semiconductors: Interplay between bound, charged and free excitons. *Sci. Rep.* **3**, 2657 (2013).
60. Madapu, K. K., Bhuyan, C. A. & Dhara, S. Origin of bound exciton emission in CVD-grown monolayer MoS_2. *Phys. Rev. B* **108**, 085429 (2023).
61. Baniecki, J. D. et al. Strain dependent electronic structure and band offset tuning at heterointerfaces of AS_nO_3 (A=Ca, Sr, and Ba) and $SrTiO_3$. *Sci. Rep.* **7**, 41725 (2017).
62 Tian, F. et al. Strain-dependent band structures and electronic properties in Sb/Bi lateral heterostructures calculated by first principles. *Physica Status Solidi (RRL) – Rapid Res. Lett.* **15**, 2100148 (2021).
63. Dimple, Jena, N., Behere, S. D. & De Sarkar, A. The effects of different possible modes of uniaxial strain on the tunability of electronic and band structures in MoS_2 monolayer nanosheet via first-principles density functional theory. *Pramana* **89**, 2 (2017).
64. Sah, R. K., Tang, H., Shahi, C., Ruzsinszky, A. & Perdew, J. P. Effect of strain on the band gap of monolayer MoS_2. *Phys. Rev. B* **110**, 144109 (2024).
65. Wang, C., Li, S., Wang, S., Zhao, P. & Zhuo, R. First principles study of the effect of uniaxial strain on monolayer MoS_2. *Phys. E: Low-Dimens. Syst. Nanostructures* **144**, 115401 (2022).
66. Heo, S. N., Ishiguro, Y., Hayakawa, R., Chikyow, T. & Wakayama, Y. Perspective: Highly ordered MoS_2 thin films grown by multi-step chemical vapor deposition process. *APL Mater.* **4**, 030901 (2016).
67. Heo, S., Hayakawa, R. & Wakayama, Y. Carrier transport properties of MoS_2 field-effect transistors produced by multi-step chemical vapor deposition method. *J. Appl. Phys.* **121**, 024301 (2017).
68. Amin, R., Hossain, M. A. & Zakaria, Y. Interfacial kinetics and ionic diffusivity of the electrodeposited MoS_2 film. *ACS Appl. Mater. Interfaces* **10**, 13509–13518 (2018).
69. Gao, J. et al. Aging of transition metal dichalcogenide monolayers. *ACS Nano* **10**, 2628–2635 (2016).
70. Suenaga, K. et al. Surface-Mediated aligned growth of monolayer MoS_2 and in-plane heterostructures with graphene on sapphire. *ACS Nano* **12**, 10032–10044 (2018).
71. Lin, Z. et al. Controllable growth of large-size crystalline mos_2 and resist-free transfer assisted with a Cu thin film. *Sci. Rep.* **5**, 18596 (2015).
72. Yu, H. et al. Wafer-scale growth and transfer of highly-oriented monolayer MoS_2 continuous films. *ACS Nano* **11**, 12001–12007 (2017).
73. Wang, R. et al. Ultrafast and spatially resolved studies of charge carriers in atomically thin molybdenum disulfide. *Phys. Rev. B* **86**, 045406 (2012).
74. Nie, Z. et al. Ultrafast carrier thermalization and cooling dynamics in few-layer MoS_2. *ACS Nano* **8**, 10931–10940 (2014).
75. Sim, S. et al. Exciton dynamics in atomically thin MoS_2: Interexcitonic interaction and broadening kinetics. *Phys. Rev. B* **88**, 075434 (2013).
76. Shukla, A. et al. Effect of confinement on the exciton and biexciton dynamics in perovskite 2D-nanosheets and 3D-nanocrystals. *J. Phys. Chem. Lett.* **11**, 6344–6352 (2020).
77. Seo, S. B. et al. Ultrafast tunable broadband optical anisotropy in two-dimensional ReS_2. *Phys. Rev. Appl.* **18**, 014010 (2022).
78. Chen, K. et al. Experimental evidence of exciton capture by mid-gap defects in CVD grown monolayer $MoSe_2$. *NPJ 2D Mater. Appl.* **1**, 15 (2017).
79. Wu, A., Song, Q. & Liu, H. Oxygen atom adsorbed on the sulphur vacancy of monolayer MoS_2: A promising method for the passivation of the vacancy defect. *Comput. Theor. Chem.* **1187**, 112906 (2020).
80. Kc, S., Longo, R. C., Addou, R., Wallace, R. M. & Cho, K. Impact of intrinsic atomic defects on the electronic structure of MoS_2 monolayers. *Nanotechnology* **25**, 375703 (2014).
81. Lu, C.-P., Li, G., Mao, J., Wang, L.-M. & Andrei, E. Y. Bandgap, mid-gap states, and gating effects in MoS_2. *Nano Lett.* **14**, 4628–4633 (2014).
82. Liu, H.-L. et al. Temperature-dependent optical constants of monolayer MoS_2, $MoSe_2$ WS_2, and WSe_2: Spectroscopic ellipsometry and first-principles calculations. *Sci. Rep.* **10**, 15282 (2020).
83. Li, H. & Zhang, X. H. Temperature-dependent photoluminescence and time-resolved photoluminescence study of monolayer molybdenum disulfide. *Opt. Mater.* **107**, 110150 (2020).
84. Korn, T., Heydrich, S., Hirmer, M., Schmutzler, J. & Schüller, C. Low-temperature photocarrier dynamics in monolayer MoS_2. *Appl. Phys. Lett.* **99**, 102109 (2011).
85. Choi, B. K. et al. Temperature dependence of band gap in $MoSe_2$ grown by molecular beam epitaxy. *Nanoscale Res. Lett.* **12**, 492 (2017).
86. Li, H., Zhu, X., Tang, Z. K. & Zhang, X. H. Low-temperature photoluminescence emission of monolayer MoS_2 on diverse substrates grown by CVD. *J. Luminescence* **199**, 210–215 (2018).
87. Chow, P. K. et al. Defect-induced photoluminescence in monolayer semiconducting transition metal dichalcogenides. *ACS Nano* **9**, 1520–1527 (2015).
88. Wang, T. et al. Hot carrier cooling and trapping in atomically thin WS_2 probed by three-pulse femtosecond spectroscopy. *ACS Nano* **17**, 6330–6340 (2023).
89. Soni, A., Kushavah, D., Lu, L.-S., Chang, W.-H. & Pal, S. K. Ultrafast exciton trapping and exciton-exciton annihilation in large-area CVD-grown monolayer WS_2. *J. Phys. Chem. C* **125**, 23880–23888 (2021).
90. Xu, S., Yang, J., Jiang, H., Su, F. & Zeng, Z. Transient photoconductivity and free carrier dynamics in a monolayer WS_2 probed by time resolved Terahertz spectroscopy. *Nanotechnology* **30**, 265706 (2019).
91. Sun, D. et al. Observation of rapid exciton-exciton annihilation in monolayer molybdenum disulfide. *Nano Lett.* **14**, 5625–5629 (2014).
92. Cunningham, P. D., McCreary, K. M. & Jonker, B. T. Auger recombination in chemical vapor deposition-grown monolayer WS_2. *J. Phys. Chem. Lett.* **7**, 5242–5246 (2016).
93. Fan, P. et al. Trion-induced distinct transient behavior and stokes shift in WS_2 monolayers. *J. Phys. Chem. Lett.* **10**, 3763–3772 (2019).
94. Tsai, H.-S. et al. Ultrafast exciton dynamics in scalable monolayer MoS_2 synthesized by metal sulfurization. *ACS Omega* **5**, 10725–10730 (2020).
95. Chen, K. et al. Carrier trapping by oxygen impurities in molybdenum diselenide. *ACS Appl. Mater. Interfaces* **10**, 1125–1131 (2018).
96. Rao, R. et al. Dynamics of cleaning, passivating and doping monolayer MoS_2 by controlled laser irradiation. *2d Mater.* **6**, 045031 (2019).
97. Zhu, H., Yang, Y. & Lian, T. Multiexciton annihilation and dissociation in quantum confined semiconductor nanocrystals. *Acc. Chem. Res.* **46**, 1270–1279 (2013).
98. Yuan, L. & Huang, L. Exciton dynamics and annihilation in WS_2 2D semiconductors. *Nanoscale* **7**, 7402–7408 (2015).

99. Lee, H. S., Kim, M. S., Kim, H. & Lee, Y. H. Identifying multiexcitons in MoS_2 monolayers at room temperature. *Phys. Rev. B* **93**, 140409 (2016).
100. Wang, W. et al. Studying of the biexciton characteristics in monolayer MoS_2. *J. Phys. Chem. C* **124**, 1749–1754 (2020).
101. Sim, S. et al. Role of weak interlayer coupling in ultrafast exciton-exciton annihilation in two-dimensional rhenium dichalcogenides. *Phys. Rev. B* **101**, 174309 (2020).
102. Wang, H., Zhang, C. & Rana, F. Ultrafast dynamics of defect-assisted electron-hole recombination in monolayer MoS_2. *Nano Lett.* **15**, 339–345 (2015).
103. Shin, H. J., Bae, S. & Sim, S. Ultrafast auger process in few-layer $PtSe_2$. *Nanoscale* **12**, 22185–22191 (2020).
104. Hong, H. et al. Modulation of carrier lifetime in MoS_2 monolayer by uniaxial strain. *Chin. Phys. B* **29**, 077201 (2020).
105. Mondal, N., Azam, N., Gartstein, Y. N., Mahjouri-Samani, M. & Malko, A. V. Photoexcitation dynamics and long-lived excitons in strain-engineered transition metal dichalcogenides. *Adv. Mater.* **34**, 2110568 (2022).
106. Suk, S. H. et al. Sub-picosecond, strain-tunable, polarization-selective optical switching via anisotropic exciton dynamics in quasi-1D $ZrSe_3$. *Light Sci. Appl.* **13**, 240 (2024).
107. Zhang, X. et al. Unravelling the effect of sulfur vacancies on the electronic structure of the MoS_2 crystal. *Phys. Chem. Chem. Phys.* **22**, 21776–21783 (2020).
108. Wang, H., Xu, X. & Neville, A. Facile synthesis of vacancy-induced 2H-MoS_2 nanosheets and defect investigation for supercapacitor application. *RSC Adv.* **11**, 26273–26283 (2021).
109. Samy, O., Zeng, S., Birowosuto, M. D. & El Moutaouakil, A. A review on MoS_2 properties, synthesis, sensing applications and challenges. *Crystals* **11**, 355 (2021).
110. Miralrio, A., Rangel Cortes, E. & Castro, M. Electronic properties and enhanced reactivity of MoS_2 monolayers with substitutional gold atoms embedded into sulfur vacancies. *Appl. Surf. Sci.* **455**, 758–770 (2018).
111. Liu, D., Guo, Y., Fang, L. & Robertson, J. Sulfur vacancies in monolayer MoS_2 and its electrical contacts. *Appl. Phys. Lett.* **103**, 183113 (2013).
112. Yin, L. et al. Robust trap effect in transition metal dichalcogenides for advaanced multifunctional devices. *Nat. Commun.* **10**, 4133 (2019).
113. Lin, Y. et al. Enhanced emission from defect levels in multilayer MoS_2. *Adv. Opt. Mater.* **10**, 2201059 (2022).
114. Tan, A. M. Z., Freysoldt, C. & Hennig, R. G. Stability of charged sulfur vacancies in 2D and bulk MoS_2 from plane-wave density functional theory with electrostatic corrections. *Phys. Rev. Mater.* **4**, 064004 (2020).
115. Zhu, Y. et al. Room-temperature photoluminescence mediated by sulfur vacancies in 2D molybdenum disulfide. *ACS Nano* **17**, 13545–13553 (2023).
116. Ren, Z. et al. Efficient optical modulation of exciton state population in monolayer MoS_2 at room temperature. *Nanomaterials* **12**, 3133 (2022).
117. Lippert, S. et al. Influence of the substrate material on the optical properties of tungsten diselenide monolayers. *2d Mater.* **4**, 025045 (2017).
118. Korapati, P., Kumari, A. K., Kosuri, Y. R., Priya, B. K. & Dodda, V. R. K. R. The effect of substrate on enhancing the sensing properties of nitric oxide gas detection of MoS_2 thin film. *Emergent Mater.* **7**, 1779–1791 (2024).
119. Kushavah, D., Mushtaq, A. & Pal, S. K. Ultrafast and nonlinear optical properties of two-dimensional MO-doped dual phase inorganic lead halide perovskite. *J. Phys. Chem. C* **127**, 20014–20025 (2023).

Acknowledgements

AS and SKP gratefully acknowledge the financial support from the Scienceand Engineering Research Board (SERB), Government of India (Grant No.CRG/2018/003045). All authors thank the Advanced Materials ResearchCentre (AMRC) of IIT Mandi for providing experimental facilities. We alsoacknowledge the assistance of ChatGPT for editing English.

Author contributions

A.S. has done absorption, Raman, photoluminescence and XPS measurements. A.S. and N.K. did transient absorption measurements. A.S. analyzed the experimental data, prepared figures and draft the manuscript text. Y.Y.S. prepared samples under the supervision of W.H.C. H.S. and A.D.S. carried out ab initio calculations and wrote the theoretical part of the manuscript. S.K.P supervised experimental works and corrected the manuscript text. All authors reviewed the manuscript.

Declarations

Competing interests

The authors declare no competing interests.

Additional information

Supplementary Information The online version contains supplementary material available at https://doi.org/10.1038/s41598-025-92188-1.

Correspondence and requests for materials should be addressed to S.K.P.

Reprints and permissions information is available at www.nature.com/reprints.

Publisher's note Springer Nature remains neutral with regard to jurisdictional claims in published maps and institutional affiliations.

Open Access This article is licensed under a Creative Commons Attribution-NonCommercial-NoDerivatives 4.0 International License, which permits any non-commercial use, sharing, distribution and reproduction in any medium or format, as long as you give appropriate credit to the original author(s) and the source, provide a link to the Creative Commons licence, and indicate if you modified the licensed material. You do not have permission under this licence to share adapted material derived from this article or parts of it. The images or other third party material in this article are included in the article's Creative Commons licence, unless indicated otherwise in a credit line to the material. If material is not included in the article's Creative Commons licence and your intended use is not permitted by statutory regulation or exceeds the permitted use, you will need to obtain permission directly from the copyright holder. To view a copy of this licence, visit http://creativecommons.org/licenses/by-nc-nd/4.0/.

© The Author(s) 2025

THE JOURNAL OF PHYSICAL CHEMISTRY C
A JOURNAL OF THE AMERICAN CHEMICAL SOCIETY

pubs.acs.org/JPCC

Article

Ultrafast Exciton Trapping and Exciton−Exciton Annihilation in Large-Area CVD-Grown Monolayer WS_2

Ashish Soni, Dushyant Kushavah, Li-Syuan Lu, Wen-Hao Chang, and Suman Kalyan Pal*

Cite This: *J. Phys. Chem. C* 2021, 125, 23880−23888

Read Online

ACCESS | Metrics & More | Article Recommendations | Supporting Information

ABSTRACT: Two-dimensional (2D) transition-metal dichalcogenides (TMDCs) have shown promise for a variety of optoelectronic applications due to a wide range of optical, electrical, and mechanical properties. Large-area chemical vapor deposition (CVD)-grown TMDC flakes could be useful in such devices. However, the defects present in large-area TMDC flakes can significantly influence carrier dynamics and transport properties. Here, the ultrafast carrier dynamics of monolayer tungsten disulfide (WS_2) covering a large area of the substrate was explored using transient absorption spectroscopy. By monitoring the transient optical response, exciton trapping by oxygen-induced defects has been identified in monolayer WS_2. We observe excitation-density-dependent exciton decay dynamics for both band-edge and above band-edge excitations due to exciton−exciton annihilation. Our results demonstrate the impact of defect states on carrier recombination in CVD-grown TMDCs, which could pave the way for utilizing such materials in optoelectronic device applications.

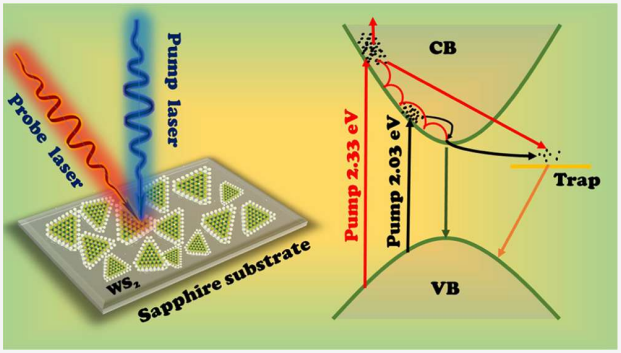

INTRODUCTION

Atomically thin transition-metal dichalcogenides (TMDCs) have set off a flood of research interest owing to their fascinating optical and electronic properties such as a direct band gap in a monolayer regime,[1] valley polarization,[2−4] and large excitonic binding energy.[5,6] The crystal of TMDCs is made of layers, which are coupled by van der Waals forces similar to graphene, and hence, their monolayers can easily be separated from each other. On the other hand, they exhibit a direct band gap in a single layer and strong photoluminescence, which differentiate them from graphene.[7−9] The valley degree of freedom (DOF) of 2D TMDCs has also opened up a new research area, valleytronics, where the DOF can be manipulated through an interplay between different valleys.[10] 2D TMDCs (MoS_2, WS_2, $MoSe_2$, WSe_2, etc.) have been reported to bring forth revolutionary progress toward the development of next-generation mechanically reconfigurable electronic devices.[11,12] Some of the recent demonstrations include LEDs,[13,14] lasers,[15] and photodetectors.[16,17] Although mechanically exfoliated 2D flakes are commonly used for device applications, the method has an inherent inability to be scaled up owing to its low yield and random nature. Chemical vapor deposition (CVD)-grown large-area 2D materials have the capability to deliver scalable production.[18] However, understanding the optoelectronic properties of large-area films is necessary to facilitate their device applications.

During the growth process of TMDCs by the CVD technique, some defects are always introduced due to reasons like thermal effect or concentration of precursors.[19,20] These defects can affect the charge transport, carrier dynamics, and crystal structure, which, in turn, affect the performance of TMDC devices.[21,22] There are several types of defects like chalcogen vacancy,[23] dislocations, nitrogen or oxygen impurity, etc.[24,25] that could be either beneficial or detrimental depending upon the application.[20,22,26] It is a fundamental necessity to understand the role of defect states on the exciton/carrier dynamics of TMDCs to get a better optical and electronic response from 2D optoelectronic devices. There are several theoretical[27,28] and experimental[29−31] reports investigating the role of defect states on the carrier dynamics of TMDCs. Xu et al.[29] employed the Drude−Smith model to monolayer WS_2 to explain that photoexcitation leads to free charge carriers, which undergo relaxation via Auger recombination and trapping. Gustafson and co-workers[32] demonstrated using time-resolved terahertz spectroscopy (TRTS) that the photoinduced increase in conductivity in monolayer WS_2 is due to defect-mediated positive trion formation. However, direct observation of defect trapping in large-area 2D TMDCs with the help of ultrafast optical spectroscopy is scarce.

Received: July 14, 2021
Revised: October 12, 2021
Published: October 26, 2021

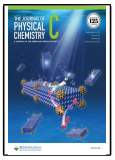

Downloaded via INDIAN INST OF TECH MANDI on December 7, 2021 at 15:09:47 (UTC).
See https://pubs.acs.org/sharingguidelines for options on how to legitimately share published articles.

ACS Publications

© 2021 American Chemical Society

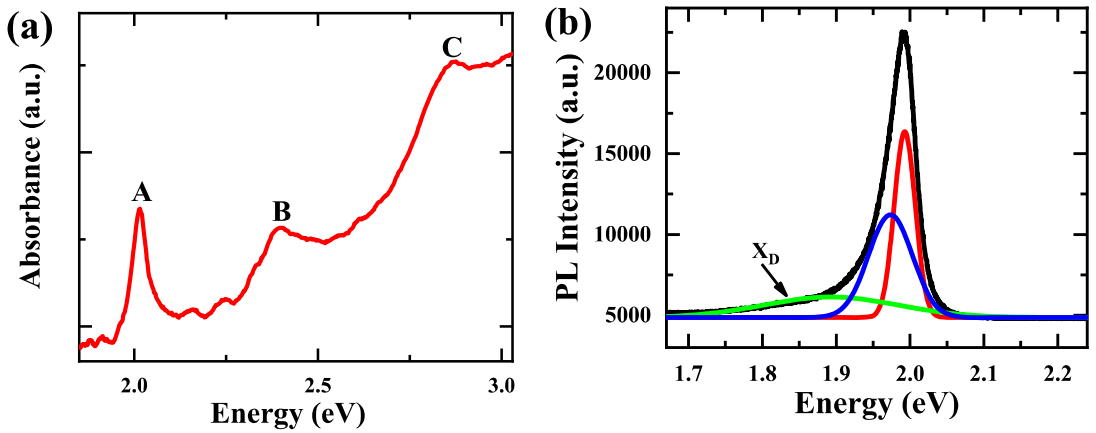

Figure 1. (a) Absorption spectrum of the CVD-grown WS_2 sample. (b) Photoluminescence spectrum of the WS_2 monolayer with excitation energy of 2.33 eV (532 nm). Spectral contributions of neutral (red), charged (blue), and defect (green) excitons obtained from the Lorentzian peak fitting.

In low dimensions, many-body processes like exciton−exciton interactions[33,34] including Auger recombination[35] start to occur at a high carrier density. Exciton−exciton annihilation (EEA) is an Auger recombination process where two or more excitons interact with each other, recombine, and transfer the energy to other exciton/charge carriers to form a high energy state, followed by rapid relaxation.[36] EEA has been explored in mechanically exfoliated WS_2 mono and bilayer samples using time-resolved photoluminescence (TRPL)[37] and transient absorption spectroscopy.[38]

In this work, we employed an ultrafast time-resolved spectroscopic technique to present an in-depth analysis of the evolution of exciton and trapped carriers following photoexcitation of single-layer WS_2. Specifically, we probe the excitonic band to observe the defect trapping of carriers. We observe a slow rise in the photoinduced absorption signal, which can be considered as an optical signature of ultrafast defect capturing and trapping of excitons. Our X-ray photoelectron spectroscopy (XPS) studies reveal that oxygen-related defect states trap excitons, which recombine radiatively to give rise to PL. Strong exciton−exciton annihilation is observed not only for the band edge but also for above band-edge excitations. Our results could be beneficial for developing various optoelectronic devices utilizing the CVD-grown TMDCs.

EXPERIMENTAL METHODS

Sample Preparation. High-quality monolayer WS_2 flakes were synthesized on a sapphire substrate by chemical vapor deposition in a one-inch horizontal hot wall furnace. Sulfur powder and a mixture of tungstic acid powder (H_2WO_4) with a 0.2 M KOH solution were used as growth reactants. The sapphire substrate and transition-metal source were placed at the central high-temperature heating zone, while the sulfur powder was placed upstream and heated using a heating belt. Monolayer WS_2 was grown at 850 °C at the center of the heating zone and the sulfur temperature was kept at 135 °C. During the growth process, a mixed gas of H_2/Ar with flow rates of 8/80 sccm was used as the carrier gas under a base pressure of 80 Torr.

Absorption Spectroscopy. The steady-state absorption spectrum was collected using a Shimadzu UV-2450 spectrometer (Agilent Technologies). All measurements were performed on the sapphire substrate at room temperature.

Raman and Photoluminescence Measurements. Photoluminescence (PL) and Raman spectra were performed at room temperature in the back-scattering configuration under an optical microscope. The sample was excited by a 532 nm laser through a 100× objective lens with a numerical aperture of N.A. = 0.9. The signals were analyzed by a monochromator using gratings with 300 line/mm and 1200 line/mm for the PL and Raman measurements, respectively. The signals were then detected by an air-cooled CCD.

Femtosecond Transient Absorption (TA) Spectroscopy. Femtosecond broadband TA measuring system is based on a femtosecond Ti: Sapphire amplifier (wavelength ∼ 800 nm and pulse width < 35 fs).[39,40] The output from the amplifier (Spitfire Ace, Spectra physics) was divided into two components to generate pump and probe pulses. Pump pulses (at 610 and 532 nm) were obtained from the nonlinear optical parametric amplifier (TOPAS). The probe beam was a white-light continuum (WLC), which was generated by focusing a small fraction of 800 nm light (from Spitefire Ace) on a sapphire crystal. To obtain a stable and continuous white-light probe, the 800 nm beam was adjusted using an iris and neutral density filter. The probe beam was split into two beams, named the reference and the sample beams. These two beams were detected separately so that the unsolicited noises can be eliminated. The detection of the probe beam was carried out in both conditions: with probe and without probe with the help of a mechanical chopper of frequency 500 Hz. The time delay between pump and probe pulses was controlled with an optical delay line driven by a stepper motor. TA spectra were recorded by dispersing the beam with a grating spectrograph (Acton Spectra Pro SP 2358) followed by a CCD array. The WLC probe confronted group velocity dispersion (GVD), which was compensated with the help of a chirp correction program (Pascher Instrument). Light pulses of a particular wavelength from another TOPAS were used as a probe during the measurement of TA kinetics. Two photodiodes having variable gain were used to record TA kinetics. TA decay traces were fitted with multiexponential functions by taking into account the instrument response function.

RESULTS AND DISCUSSION

Characterization of the Sample. Large-area WS_2 flakes were grown on sapphire substrate by CVD (see Supporting Information). The flakes are clearly visible from the optical

https://doi.org/10.1021/acs.jpcc.1c06267
J. Phys. Chem. C 2021, 125, 23880−23888

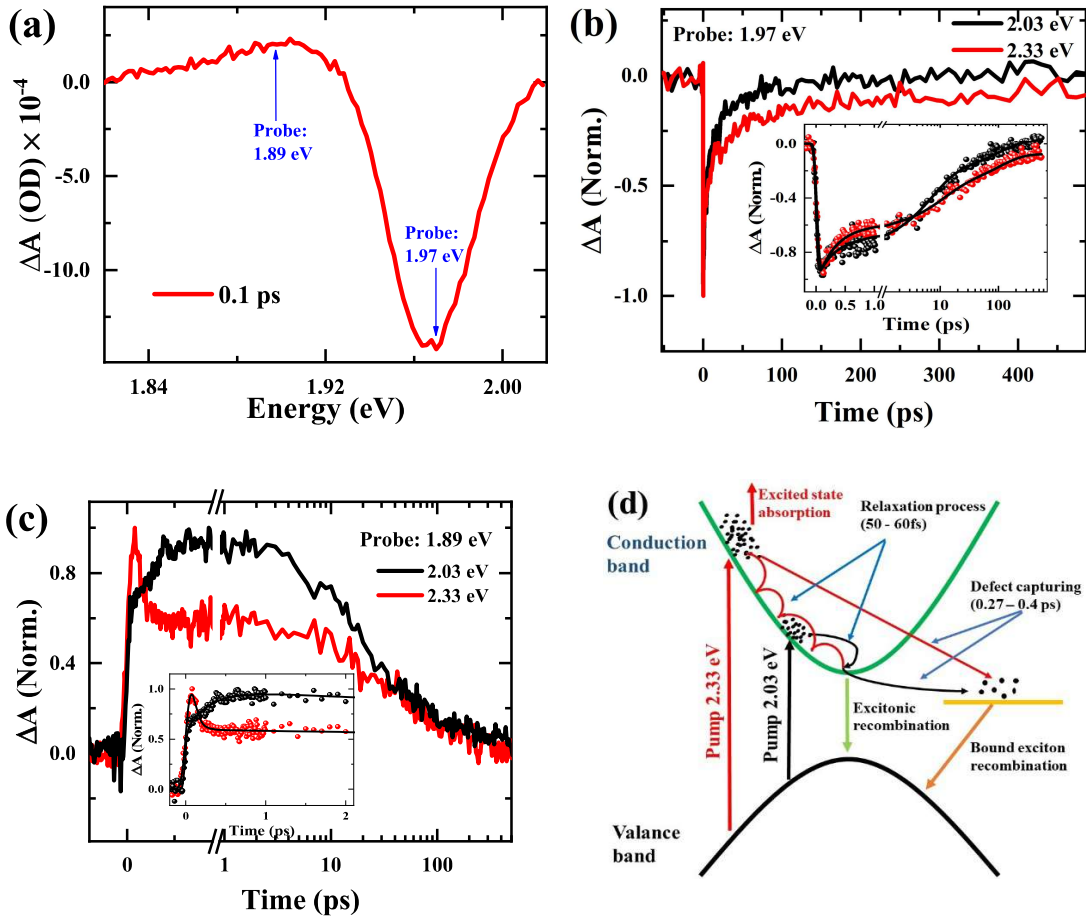

Figure 2. (a) Transient absorption (TA) spectrum of monolayer WS_2 at a pump-photon density 1.5×10^{14} cm^{-2}. The sample was excited with a femtosecond laser beam of photon energy 2.33 eV (wavelength 532 nm). Vertical arrows indicate probe energies at which TA kinetics were measured. (b) Normalized TA kinetics of the WS_2 monolayer probed at 1.97 eV (630 nm) for pump-photon energies of 2.03 eV (610 nm) (black) and 2.33 eV (532 nm) (red). The pump-photon density was 1.5×10^{14} cm^{-2}. Inset: normalized TA kinetics at 1.97 eV showing the difference at an early time due to different pump energies. Solid lines are fitting results using eq 1. (c) TA kinetics of monolayer WS_2 measured at 1.89 eV with excitation energies of 2.33 (red) and 2.03 eV (black). Inset: comparison of TA signals for both excitations at an early time. Solid lines represent multiexponential fitting to the experimental data. (d) Schematic representation of the dynamic processes occurring in monolayer WS_2 under light exposure.

image of the sample shown in Figure S1a. The steady-state absorption spectrum in Figure 1a shows three peaks at 2.02 eV (615 nm), 2.39 eV (518 nm), and 2.88 eV (430 nm). We labeled them A, B, and C peaks according to Wilson and Yoffe's nomenclature. The low-energy peaks A and B represent the excitonic feature corresponding to the vertical transition at K/K' points of the Brillouin zone and arise due to the splitting of mainly the valance band through spin−orbit coupling.[41,42] The strong absorption peak C at higher energy is associated with the band nesting effect in the $\Gamma-K$ point of the Brillouin zone.[43,44] The energetic position of the absorption peaks is in good agreement with that of monolayer WS_2.[41] We estimate the number of layers present in CVD-grown WS_2 flakes using Raman spectroscopy. Two characteristic Raman modes corresponding to E^1_{2g} (in-plane vibration) and A_{1g} (out-of-plane vibration) at 356 and 417 cm^{-1}, respectively, are present in the Raman spectrum of WS_2 (Figure S1b). The observed Raman features are consistent with previous reports on monolayer WS_2.[45,46] Figure 1b shows the PL spectrum of WS_2 dominated by emission from the free neutral A exciton and the charged exciton (trion) at ∼2.00 and ∼1.95 eV, respectively.[30,47] The spectral feature that appeared near 1.89 eV is ascribed to the defect-bound exciton.[30,48]

Photoinduced Bleaching and Absorption. The transient absorption (TA) spectrum of our CVD-grown monolayer WS_2 sample at a pump fluence of 1.5×10^{14} cm^{-2} is shown in Figure 2a. Here, we employed femtosecond pump-probe optical spectroscopy to scrutinize the spectral features arising due to ultrafast photoexcitation of monolayer WS_2. A clear bleach signal is observed around 1.97 eV (630 nm) where the A exciton band is present in the steady-state absorption spectrum (Figure 1a). Therefore, the origin of such a sharp negative peak could be phase-space filling at the A exciton state of WS_2. The phase-space filling effect in 2D materials is the consequence of the Pauli exclusion principle where a charge carrier of an existing exciton occupies the available phase space, suppressing the optical transition that forms the same exciton.[49] Another remarkable feature of the TA spectra is the appearance of a positive signal around 1.89 eV (655 nm). Such a photoinduced absorption band could arise due to the transitions of the carriers from an excited state[50] or from a trap state present below the conduction band[51] to another higher

https://doi.org/10.1021/acs.jpcc.1c06267
J. Phys. Chem. C 2021, 125, 23880−23888

excited state. The pump-generated charge carriers may immediately absorb the probe beam or after relaxing to the trap state, giving rise to the positive signal in TA spectra.[52]

Exciton Trapping. To gain an in-depth knowledge of the time evolution of excitons and charge carriers, we examine the excitation−photon energy dependence of the TA kinetics by fixing the probe energy (1.97 eV) near the A exciton. Figure 2b shows bleach kinetics at excitation−photon energies of 2.03 and 2.33 eV. There is a clear difference in the bleach recovery process (inset of Figure 2b).

To understand the processes involved in the recovery of bleach signal, we fitted TA kinetics by a triexponential function

$$\Delta A = A_1 \exp(-t/\tau_1) + A_2 \exp(-t/\tau_2) + A_3 \exp(-t/\tau_3) \quad (1)$$

where A_i and τ_i (i = 1−3) represent the amplitudes and decay times of the decay components, respectively. The fitting of experimental data with eq 1 (inset of Figure 2b) yields a fast, an intermediate, and a slow decay component with decay times of ∼0.3, 7−10, and ∼100 ps, respectively (Table 1). It should

Table 1. Parameter Values Obtained from the Fitting of TA Kinetics at 1.97 eV (Photobleaching) Corresponding to Excitation Energies of 2.33 and 2.03 eV

pump-photon energy (eV)	pump fluence (cm^{-2})	τ_1 (ps)	A_1 (%)	τ_2 (ps)	A_2 (%)	τ_3 (ps)	A_3 (%)
2.03	4.2×10^{13}	0.11	26	13.04	48	100	25
	6.4×10^{13}	0.14	33	8.58	49	100	18
	1.5×10^{14}	0.26	20	6.95	72	100	8
	2.0×10^{14}	0.31	39	5.11	57	100	4
	2.4×10^{14}	0.42	21	4.84	78	100	1
2.33	4.2×10^{13}	0.24	41	10.17	29	100	29
	6.4×10^{13}	0.26	43	11.79	33	100	25
	1.5×10^{14}	0.35	37	10.78	41	100	21
	2.0×10^{14}	0.28	34	8.84	46	100	20
	2.4×10^{14}	0.31	33	8.43	42	100	26

be noted that the fast decay time increases with the increasing pump fluence. According to previous studies, the bleach kinetics at an early time could be affected by several processes like carrier relaxation (cooling), trapping of charge carriers, exciton−exciton interaction, and other Auger processes (e.g., recombination of multiple carriers or excitons) simultaneously.[53−55]

One of the reasons for the observed fast decay component could be the cooling of hot carriers to the band edge.[35] In monolayer WS_2, the excess energy corresponding to the B exciton absorption is comparable with the ionization energy of A exciton.[56] Therefore, excitation with a photon of energy 2.33 eV can lead to the generation of hot carriers and the cooling of such carriers can be responsible for the short-lived decay component of the bleach signal. However, in the case of band-edge excitation (excitation energy ∼2.03 eV), the possibility of the generation of a hot carrier is very slim. Moreover, carrier cooling time should not be dependent on excitation fluence (Table 1). Hence, the sub-picosecond component in the bleach kinetics should not arise from carrier relaxation. Another possible mechanism that can induce fast decay component to TA kinetics is the trapping of charge carriers by the defect states that are present below the excitonic level in 2D TMDCs. With the increasing excitation fluence, the trap-induced charge carrier decay should become slower due to the filling effects of the available defect states.[29] As the decay time τ_1 follows a similar trend, it could be associated with the capture of the electron/hole of an exciton by the defect states. It is evident from the PL study (Figure 1b) that trions are formed in our sample due to photoexcitation. The recombination of trions leads to the depopulation of the conduction band and can affect the TA kinetics of the bleach band. Recently, Fan et al.[57] reported the recombination time of trion (11.2 ps) in monolayer WS_2 from TA spectral measurements. Therefore, the intermediate decay time (τ_2) could be associated with the recombination of trions. However, τ_2 decreases with the increasing pump fluence (Table 1). Its fluence dependence is in accordance with the behavior of an Auger process and hence could also be assigned to the process like exciton−exciton interaction.[31] The longer decay component (τ_3) is ascribed to the radiative excitonic recombination or carrier-phonon scattering, which is reported to occur in a few hundreds of picoseconds.[31,35,58]

To understand uniquely the dynamic process occurring in monolayer WS_2 under light illumination, we probed the sample at an energy below the band gap. Figure 2c shows the TA kinetics measured at 1.89 eV with excitation−photon energies of 2.33 and 2.03 eV. For both the excitations, we observe positive TA signals, which correspond to photoinduced absorption (PIA). Clearly, the dynamic behavior of TA kinetics at an early time is dependent on excitation energy. While the TA signal at pump energy of 2.33 eV exhibits a very fast (decay time ∼60 fs) decay, there is a slow rise (time ∼0.28 ps) in the kinetics at 2.03 eV excitation (inset of Figure 2c). In quantum-confined semiconductors, the optoelectronic properties are dominated by excitons formed via cooling of initially photoexcited nonequilibrium charge carriers.[59] The generation of charge carriers for 2.33 eV excitation gives rise to free carrier absorption (FCA) at 1.89 eV. Exciton formation that occurs via cooling of photogenerated hot carriers could therefore cause the observed ultrafast decay (60 fs).

In the case of band-edge excitation (2.03 eV), the rise time of the positive TA signal at 1.89 eV is the same as that of the fast recovery time of the bleach signal at 1.97 eV. Thus, the absorption increase at 1.89 eV at an early time could be associated with the absorption of the probe light by the defect-captured electrons/holes (Figure 2d). In the capture process, the electrons/holes generated by the pump laser can be trapped by some defects present in the material. After the defect states are occupied by carriers, a probe photon can excite electron/hole from defect states to some higher excited states by increasing the absorption of the probe. This mechanism is dominant in materials with a large number of defects. There are many types of defects like chalcogen atom vacancy,[23,60] metal atom vacancy,[61] and nitrogen/oxygen impurities[62] in CVD-grown monolayer TMDCs. The appearance of PL peak around 1.89 eV (Figure 1b) suggests the presence of mid-gap defects in our CVD-grown monolayer WS_2 sample. This further confirms that the defect states are not only able to capture the photoexcited excitons but also assist their radiative recombination. Thus, it is very reasonable to ascribe the slow rise (0.28 ps) of the PIA signal to exciton trapping by the defect states. In fact, the whole exciton is trapped and forms a defect-bound exciton when an electron or a hole is trapped.[62,63] The decay of the PIA signal (corresponding to excitation energy 2.03 eV) after the positive peak is attributed to the recombination of the trapped exciton (Figure 2d). Nevertheless, the PIA signals after ∼10 ps for

https://doi.org/10.1021/acs.jpcc.1c06267
J. Phys. Chem. C 2021, 125, 23880−23888

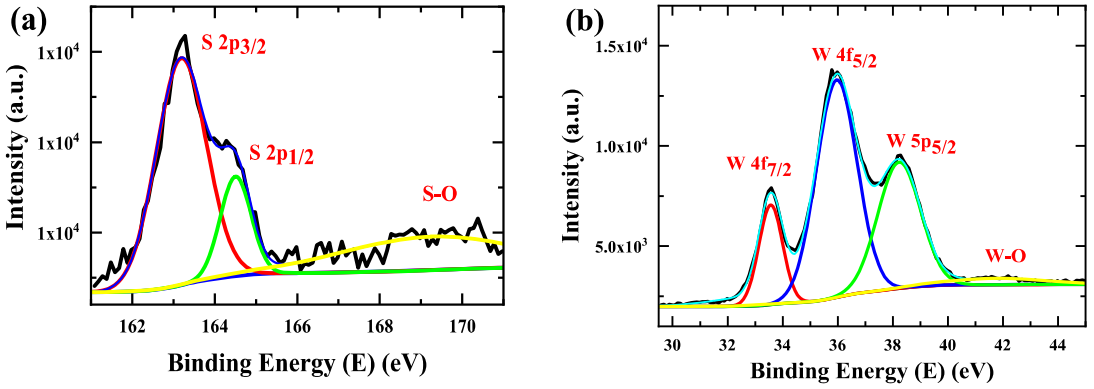

Figure 3. High-resolution X-ray photoelectron spectroscopy (XPS) results of the CVD-grown WS_2 monolayer sample: (a) S 2p peaks and (b) W 4f and 5p peaks.

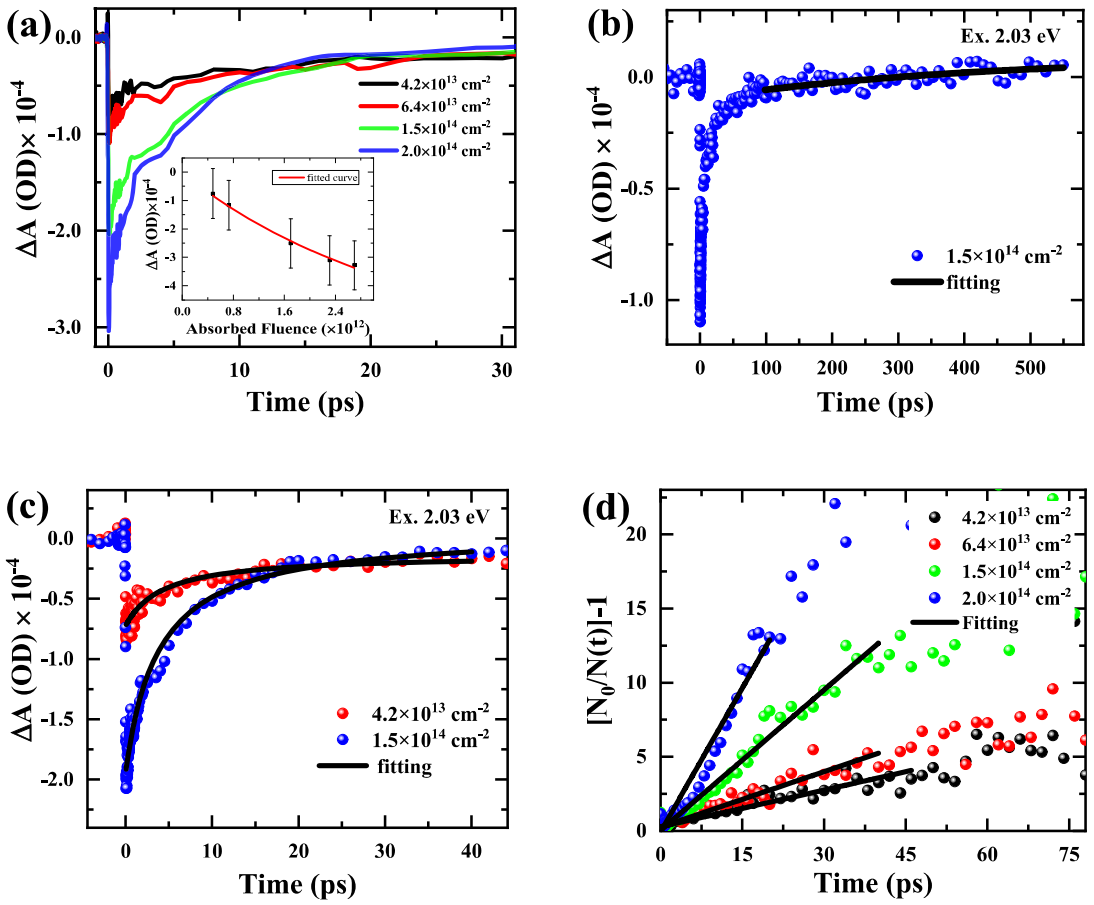

Figure 4. (a) Pump fluence dependent TA kinetics of the WS_2 sample measured at 1.97 eV with an excitation−photon energy of 2.03 eV. Inset: plot of absorption change as a function of absorbed photon density fitted with the saturable absorption model. (b) TA kinetics at 1.97 eV for a pump fluence of 1.5×10^{14} cm^{-2}. A black line shows the single exponential fitting of the decay curve after 100 ps. (c) TA decay dynamics at 1.97 eV corresponding to the excitation−photon energies of 2.03 eV fitted with the EEA model. (d) Quantity $[N_0/N(t)] - 1$ (calculated from the kinetics data) as a function of the pump-probe delay. The black lines are linear fits using eq 5.

both the excitation energies follow similar dynamics (Figure 2c) suggesting that the same process (recombination of trapped exciton) is responsible for the decay of TA signal at long times. The signature of exciton trapping is not visible in the PIA signal for 2.33 eV excitation (Figure 2c) because of the combined effect of charge carrier relaxation (causes signal decay) and trapping (causes signal rise) before 10 ps.

To know about the nature of the defect states, we performed X-ray photoelectron spectroscopy (XPS) measurements on our monolayer WS_2 sample (Figure 3). The characteristic XPS peaks of WS_2 appear at 33.5, 35.6, and 38.2 eV corresponding to W $4f_{7/2}$, W $4f_{5/2}$, and W $5p_{5/2}$, respectively. The observed peak positions are consistent with the previously reported values.[64−66] We estimated the composition ratio W:S from the Gaussian−Lorentzian fitting of XPS peaks and obtained a value

https://doi.org/10.1021/acs.jpcc.1c06267
J. Phys. Chem. C 2021, 125, 23880−23888

Table 2. Exciton−Exciton Annihilation Rates for Different Pump Fluences Obtained from Fitting

pump fluence (cm^{-2})	4.2×10^{13}	6.4×10^{13}	1.5×10^{14}	average
annihilation rate (ρ) (cm^2/s)	0.113 ∓ 0.001	0.113 ∓ 0.002	0.176 ∓ 0.003	0.134 ∓ 0.002

of 1:1.77. The deviation of the atomic ratio from the theoretical value (1:2) infers that there are many chalcogen vacancies in our sample. Interestingly, we also observe two more peaks around 170 and 42 eV related to oxides of sulfur and tungsten, respectively. Such oxide peaks are evidence of the presence of oxygen-related defects in the sample.[67,68] The oxygen-related defects are created in the CVD-grown sample because of the reaction of sulfur vacancies formed during the growth process and the oxygen atoms. We have observed that the intensity of the defect-related PL is increased in an aged sample containing more oxygen-related defects (Figure S2b). Therefore, mainly oxygen-related impurities could be responsible for exciton trapping in monolayer WS_2.

Exciton−Exciton Annihilation. In the previous section, we have mentioned that the decay time τ_2 (6−10 ps) originates from the Auger-like processes. To further study such processes, we compare A exciton bleach kinetics (till 30 ps) measured at different pump fluences. Figure 4a shows that the initial signal strength depends strongly on the incident photon density. Assuming one absorbed pump-photon generates one exciton, we calculate the density of the pump-generated excitons (N) from pump fluence and the absorbance of the sample at the pump energy. It is clear from the inset of Figure 4a that ΔA does not vary linearly with the absorbed photon density, rather absorption exhibits a saturation behavior. According to the saturation absorption model[34]

$$\Delta A = \frac{kN}{N + N_s} \tag{2}$$

where k is a constant, N and N_s are the exciton density and saturation exciton density, respectively. Fitting of the data with eq 2 yields a saturation absorption density of 5.2×10^{12} cm^{-2}. The absorption of the probe is governed by the saturable absorption model because of the phase-space filling effect. This observation further supports the fact that the bleach signal comes from the phase-space filling effect at the A exciton state.

The density-dependent decay in bleach kinetics (Figure 4a) is expected in a strongly interacting exciton system because of exciton−exciton annihilation (EEA). According to the previous reports, the rate of decay of the exciton density in the presence of EEA is given by eq 3[69]

$$\frac{dN(t)}{dt} = -\frac{1}{T}N(t) - \frac{1}{2}\rho N(t)^2 \tag{3}$$

where T is the excitonic lifetime and ρ is the EEA rate. The annihilation dominates at early times when the exciton density is high, but at long times, the dynamics is mainly due to the monomolecular excitonic decay. We indeed found that the decay after 100 ps can be fitted well with a single exponential function (Figure 4b). The solution for the second term (neglecting the first term) in eq 3 can be expressed as

$$N(t) = \frac{N_0}{1 + \rho N_0 t} \tag{4}$$

where N_0 is the initially generated exciton density. The EEA model (eq 4) provides a good fit to the experimental data, as shown in Figure 4c. Interestingly, the bleach kinetics corresponding to the excitation−photon energy of 2.33 eV follows the EEA model too (Figure S3). It should be noted that the EEA model does not fit well the kinetics below 1 ps because exciton trapping dominates at an early part of the decay kinetics. Equation 4 can also be written as

$$\frac{N_0}{N(t)} - 1 = \rho N_0 t \tag{5}$$

We fitted the data measured at an excitation energy of 2.03 eV for different fluences using eq 5 (Figure 4d). The fitting is not good at the pump fluence of 2.0×10^{14} cm^{-2} because ΔA at this fluence is not linear to the absorbed photon density (inset of Figure 4a) and hence the assumption that one photon creates one exciton does not hold. We estimate the annihilation rate from the slope of the straight lines shown in Figure 4d and find an average value of 0.134 ∓ 0.002 cm^2/s (Table 2). The previously reported EEA rate in CVD-grown monolayer WS_2 is 0.089 ∓ 0.001 cm^2/s.[35] This small discrepancy in the values of annihilation rate could be due to the substrate effect on the phonon and exciton dispersions as we used sapphire substrate instead of SiO_2/Si (used in ref 33). Steinhoff et al.[70] suggested that the dielectric medium of the substrate influences the excitons in 2D materials and hence the interaction between excitons. According to Yu et al.,[71] the EEA process in 2D TMDCs depends on the substrate. We must mention that the rate of bi-exciton formation has a quadratic dependence on the excitonic density.[72,73] However, the bi-exciton formation in TMDCs is insignificant at room temperature and favorable at cryogenic temperatures.[74] The presence of a strong EEA even above band-edge excitation infers that defect-mediated carrier and/or exciton recombination channels are not major decay routes in the CVD-grown monolayer WS_2.

CONCLUSIONS

In summary, the effect of atomic-scale point defects on the dynamics of photocarriers in a CVD-grown monolayer WS_2 has been investigated using ultrafast pump-probe spectroscopy. Our TA kinetic measurements reveal that charge carriers generated by incident photons undergo trapping in a sub-picosecond time scale followed by the formation of defect-bound excitons. Such bound excitons recombine radiatively to give rise to a defect-related peak in the PL spectrum. XPS studies infer that the oxygen-induced defects could be responsible for the trapping of excitons. The excitation-intensity-dependent exciton decay dynamics show pronounced exciton−exciton annihilation even above band-edge excitation. These results suggest that defect-mediated carrier recombination may not be the dominant loss channel in the CVD-grown WS_2, which is very important to the design of efficient optoelectronic devices based on the CVD-grown 2D TMDCs.

ASSOCIATED CONTENT

Supporting Information

The Supporting Information is available free of charge at https://pubs.acs.org/doi/10.1021/acs.jpcc.1c06267.

https://doi.org/10.1021/acs.jpcc.1c06267
J. Phys. Chem. C 2021, 125, 23880−23888

Experimental methods including sample preparation and additional experimental results (PDF)

AUTHOR INFORMATION

Corresponding Author

Suman Kalyan Pal − *School of Basic Sciences, Indian Institute of Technology Mandi, Kamand 175005 Himachal Pradesh, India; Advanced Materials Research Centre, Indian Institute of Technology Mandi, Kamand 175005 Himachal Pradesh, India;* orcid.org/0000-0003-2498-6217; Email: suman@iitmandi.ac.in

Authors

Ashish Soni − *School of Basic Sciences, Indian Institute of Technology Mandi, Kamand 175005 Himachal Pradesh, India; Advanced Materials Research Centre, Indian Institute of Technology Mandi, Kamand 175005 Himachal Pradesh, India;* orcid.org/0000-0001-7429-576X

Dushyant Kushavah − *School of Basic Sciences, Indian Institute of Technology Mandi, Kamand 175005 Himachal Pradesh, India; Advanced Materials Research Centre, Indian Institute of Technology Mandi, Kamand 175005 Himachal Pradesh, India;* orcid.org/0000-0001-5745-9435

Li-Syuan Lu − *Department of Electrophysics, National Yang Ming Chiao Tung University, Hsinchu 30010, Taiwan*

Wen-Hao Chang − *Department of Electrophysics, National Yang Ming Chiao Tung University, Hsinchu 30010, Taiwan; Research Center for Applied Sciences, Academia Sinica, Taipei 11529, Taiwan;* orcid.org/0000-0003-4880-6006

Complete contact information is available at: https://pubs.acs.org/10.1021/acs.jpcc.1c06267

Notes

The authors declare no competing financial interest.

ACKNOWLEDGMENTS

A.S., D.K., and S.K.P. are thankful to the Advanced Materials Research Centre of IIT Mandi for experimental facilities. S.K.P. acknowledges the financial support from Science and Engineering Research Board (SERB), Government of India (Grant No. CRG/2018/003045). D.K. is thankful to SERB for financial support (Project No: PDF/2018/003146).

REFERENCES

(1) Wei, K.; Liu, Y.; Yang, H.; Cheng, X.; Jiang, T. Large range modification of exciton species in monolayer WS_2. *Appl. Opt.* **2016**, *55*, 6251−6255.

(2) Paradisanos, I.; McCreary, K. M.; Adinehloo, D.; Mouchliadis, L.; Robinson, J. T.; Chuang, H.-J.; Hanbicki, A. T.; Perebeinos, V.; Jonker, B. T.; Stratakis, E.; et al. Prominent room temperature valley polarization in WS_2/graphene heterostructures grown by chemical vapor deposition. *Appl. Phys. Lett.* **2020**, *116*, No. 203102.

(3) Zeng, H.; Dai, J.; Yao, W.; Xiao, D.; Cui, X. Valley polarization in MoS_2 monolayers by optical pumping. *Nat. Nanotechnol.* **2012**, *7*, 490−493.

(4) Mak, K. F.; He, K.; Shan, J.; Heinz, T. F. Control of valley polarization in monolayer MoS_2 by optical helicity. *Nat. Nanotechnol.* **2012**, *7*, 494−498.

(5) Liu, H.-L.; Shen, C.-C.; Su, S.-H.; Hsu, C.-L.; Li, M.-Y.; Li, L.-J. Optical properties of monolayer transition metal dichalcogenides probed by spectroscopic ellipsometry. *Appl. Phys. Lett.* **2014**, *105*, No. 201905.

(6) Zhu, B.; Chen, X.; Cui, X. Exciton Binding Energy of Monolayer WS_2. *Sci. Rep.* **2015**, *5*, No. 9218.

(7) Choi, S. Y.; Yip, C. T.; Li, G.-C.; Lei, D. Y.; Fung, K. H.; Yu, S. F.; Hao, J. Photoluminescence enhancement in few-layer WS_2 films via Au nanoparticles. *AIP Adv.* **2015**, *5*, No. 067148.

(8) Splendiani, A.; Sun, L.; Zhang, Y.; Li, T.; Kim, J.; Chim, C.-Y.; Galli, G.; Wang, F. Emerging Photoluminescence in Monolayer MoS_2. *Nano Lett.* **2010**, *10*, 1271−1275.

(9) Li, W.-F.; Fang, C.; van Huis, M. A. Strong spin-orbit splitting and magnetism of point defect states in monolayer WS_2. *Phys. Rev. B* **2016**, *94*, No. 195425.

(10) Gong, Z.; Liu, G.-B.; Yu, H.; Xiao, D.; Cui, X.; Xu, X.; Yao, W. Magnetoelectric effects and valley-controlled spin quantum gates in transition metal dichalcogenide bilayers. *Nat. Commun.* **2013**, *4*, No. 2053.

(11) Mak, K. F.; Shan, J. Photonics and optoelectronics of 2D semiconductor transition metal dichalcogenides. *Nat. Photonics* **2016**, *10*, 216−226.

(12) Ray, R.; Sarkar, A. S.; Pal, S. K. Improving carrier transport in polymer films by incorporating MoS_2 nanosheets. *J. Phys. D: Appl. Phys.* **2020**, *53*, No. 275109.

(13) Wang, C.; Yang, F.; Gao, Y. The highly-efficient light-emitting diodes based on transition metal dichalcogenides: from architecture to performance. *Nanoscale Adv.* **2020**, *2*, 4323−4340.

(14) Andrzejewski, D.; Oliver, R.; Beckmann, Y.; Grundmann, A.; Heuken, M.; Kalisch, H.; Vescan, A.; Kümmell, T.; Bacher, G. Flexible Large-Area Light-Emitting Devices Based on WS_2 Monolayers. *Adv. Optical Mater.* **2020**, *8*, No. 2000694.

(15) Wu, S.; Buckley, S.; Schaibley, J. R.; Feng, L.; Yan, J.; Mandrus, D. G.; Hatami, F.; Yao, W.; Vučković, J.; Majumdar, A.; et al. Monolayer semiconductor nanocavity lasers with ultralow thresholds. *Nature* **2015**, *520*, 69−72.

(16) Patel, A. B.; Chauhan, P.; Machhi, H. K.; Narayan, S.; Sumesh, C. K.; Patel, K. D.; Soni, S. S.; Jha, P. K.; Solanki, G. K.; Pathak, V. M. Transferrable thin film of ultrasonically exfoliated $MoSe_2$ nanocrystals for efficient visible-light photodetector. *Physica E Low Dimens. Syst. Nanostruct.* **2020**, *119*, No. 114019.

(17) Wei, X.; Yan, F.-G.; Shen, C.; Lv, Q.-S.; Wang, K.-Y. Photodetectors based on junctions of two-dimensional transition metal dichalcogenides. *Chin. Phys. B* **2017**, *26*, No. 038504.

(18) Shi, Y.; Li, H.; Li, L.-J. Recent advances in controlled synthesis of two-dimensional transition metal dichalcogenides via vapour deposition techniques. *Chem. Soc. Rev.* **2015**, *44*, 2744−2756.

(19) Li, X.; Li, X.; Zang, X.; Zhu, M.; He, Y.; Wang, K.; Xie, D.; Zhu, H. Role of hydrogen in the chemical vapor deposition growth of MoS_2 atomic layers. *Nanoscale* **2015**, *7*, 8398−8404.

(20) Lin, Z.; Carvalho, B. R.; Kahn, E.; Lv, R.; Rao, R.; Terrones, H.; Pimenta, M. A.; Terrones, M. Defect engineering of two-dimensional transition metal dichalcogenides. *2D Mater.* **2016**, *3*, No. 022002.

(21) Jiang, J.; Xu, T.; Lu, J.; Sun, L.; Ni, Z. Defect Engineering in 2D Materials: Precise Manipulation and Improved Functionalities. *Research* **2019**, *2019*, 1−14.

(22) Hu, Z.; Wu, Z.; Han, C.; He, J.; Ni, Z.; Chen, W. Two-dimensional transition metal dichalcogenides: interface and defect engineering. *Chem. Soc. Rev.* **2018**, *47*, 3100−3128.

(23) Pandey, M.; Rasmussen, F. A.; Kuhar, K.; Olsen, T.; Jacobsen, K. W.; Thygesen, K. S. Defect-Tolerant Monolayer Transition Metal Dichalcogenides. *Nano Lett.* **2016**, *16*, 2234−2239.

(24) Barja, S.; Refaely-Abramson, S.; Schuler, B.; Qiu, D. Y.; Pulkin, A.; Wickenburg, S.; Ryu, H.; Ugeda, M. M.; Kastl, C.; Chen, C.; et al. Identifying substitutional oxygen as a prolific point defect in monolayer transition metal dichalcogenides. *Nat. Commun.* **2019**, *10*, No. 3382.

(25) Chee, S.-S.; Lee, W.-J.; Jo, Y.-R.; Cho, M. K.; Chun, D.; Baik, H.; Kim, B.-J.; Yoon, M.-H.; Lee, K.; Ham, M.-H. Atomic Vacancy Control and Elemental Substitution in a Monolayer Molybdenum Disulfide for High Performance Optoelectronic Device Arrays. *Adv. Funct. Mater.* **2020**, *30*, No. 1908147.

(26) Liu, J.; Lo, T. W.; Sun, J.; Yip, C. T.; Lam, C. H.; Lei, D. Y. A comprehensive comparison study on the vibrational and optical

properties of CVD-grown and mechanically exfoliated few-layered WS2. *J. Mater. Chem. C* **2017**, *5*, 11239−11245.
(27) Wang, H.; Strait, J. H.; Zhang, C.; Chan, W.; Manolatou, C.; Tiwari, S.; Rana, F. Fast exciton annihilation by capture of electrons or holes by defects via Auger scattering in monolayer metal dichalcogenides. *Phys. Rev. B* **2015**, *91*, No. 165411.
(28) Cappelluti, E.; Roldán, R.; Silva-Guillén, J. A.; Ordejón, P.; Guinea, F. Tight-binding model and direct-gap/indirect-gap transition in single-layer and multilayer MoS_2. *Phys. Rev. B* **2013**, *88*, No. 075409.
(29) Xu, S.; Yang, J.; Jiang, H.; Su, F.; Zeng, Z. Transient photoconductivity and free carrier dynamics in a monolayer WS_2 probed by time resolved Terahertz spectroscopy. *Nanotechnology* **2019**, *30*, No. 265706.
(30) Chow, P. K.; Jacobs-Gedrim, R. B.; Gao, J.; Lu, T.-M.; Yu, B.; Terrones, H.; Koratkar, N. Defect-Induced Photoluminescence in Monolayer Semiconducting Transition Metal Dichalcogenides. *ACS Nano* **2015**, *9*, 1520−1527.
(31) Liu, H.; Wang, C.; Zuo, Z.; Liu, D.; Luo, J. Direct Visualization of Exciton Transport in Defective Few-Layer WS_2 by Ultrafast Microscopy. *Adv. Mater.* **2020**, *32*, No. 1906540.
(32) Gustafson, J. K.; Cunningham, P. D.; McCreary, K. M.; Jonker, B. T.; Hayden, L. M. Ultrafast Carrier Dynamics of Monolayer WS_2 via Broad-Band Time-Resolved Terahertz Spectroscopy. *J. Phys. Chem. C* **2019**, *123*, 30676−30683.
(33) Lee, Y.; Ghimire, G.; Roy, S.; Kim, Y.; Seo, C.; Sood, A. K.; Jang, J. I.; Kim, J. Impeding Exciton−Exciton Annihilation in Monolayer WS_2 by Laser Irradiation. *ACS Photonics* **2018**, *5*, 2904−2911.
(34) Sarkar, A. S.; Mushtaq, A.; Kushavah, D.; Pal, S. K. Liquid exfoliation of electronic grade ultrathin tin(II) sulfide (SnS) with intriguing optical response. *npj 2D Mater. Appl.* **2020**, *4*, No. 1.
(35) Cunningham, P. D.; McCreary, K. M.; Jonker, B. T. Auger Recombination in Chemical Vapor Deposition-Grown Monolayer WS_2. *J. Phys. Chem. Lett.* **2016**, *7*, 5242−5246.
(36) Li, Y.; Shi, J.; Chen, H.; Wang, R.; Mi, Y.; Zhang, C.; Du, W.; Zhang, S.; Liu, Z.; Zhang, Q.; et al. The Auger process in multilayer WSe_2 crystals. *Nanoscale* **2018**, *10*, 17585−17592.
(37) Yuan, L.; Huang, L. Exciton dynamics and annihilation in WS_2 2D semiconductors. *Nanoscale* **2015**, *7*, 7402−7408.
(38) Fu, Y.; He, D.; He, J.; Bian, A.; Zhang, L.; Liu, S.; Wang, Y.; Zhao, H. Effect of Dielectric Environment on Excitonic Dynamics in Monolayer WS_2. *Adv. Mater. Interfaces* **2019**, *6*, No. 1901307.
(39) Kushavah, D.; Mushtaq, A.; Ghosh, S.; Pal, S. K. Ultrafast and nonlinear optical properties of two-dimensional CdSe nanostructures prepared using MoS_2 nanosheets as template. *Physica E Low Dimens. Syst. Nanostruct.* **2021**, *130*, No. 114682.
(40) Ghosh, S.; Ray, R.; Pal, S. K. Ultrafast Many-Particle Phenomena in Lead Bromide Hybrid Perovskite Nanocrystals Under Strong Optical Excitation. *J. Phys. Chem. C* **2021**, *125*, 3198−3205.
(41) Bernardi, M.; Ataca, C.; Palummo, M.; Grossman, J. C. Optical and Electronic Properties of Two-Dimensional Layered Materials. *Nanophotonics* **2017**, *6*, 479−493.
(42) Mak, K. F.; Lee, C.; Hone, J.; Shan, J.; Heinz, T. F. Atomically Thin MoS_2: A New Direct-Gap Semiconductor. *Phys. Rev. Lett.* **2010**, *105*, No. 136805.
(43) Hill, H. M.; Rigosi, A. F.; Roquelet, C.; Chernikov, A.; Berkelbach, T. C.; Reichman, D. R.; Hybertsen, M. S.; Brus, L. E.; Heinz, T. F. Observation of Excitonic Rydberg States in Monolayer MoS_2 and WS_2 by Photoluminescence Excitation Spectroscopy. *Nano Lett.* **2015**, *15*, 2992−2997.
(44) Zhao, W.; Ghorannevis, Z.; Chu, L.; Toh, M.; Kloc, C.; Tan, P.-H.; Eda, G. Evolution of Electronic Structure in Atomically Thin Sheets of WS_2 and WSe_2. *ACS Nano* **2013**, *7*, 791−797.
(45) Berkdemir, A.; Gutiérrez, H. R.; Botello-Méndez, A. R.; Perea-López, N.; Elías, A. L.; Chia, C.-I.; Wang, B.; Crespi, V. H.; López-Urías, F.; Charlier, J.-C.; et al. Identification of individual and few layers of WS_2 using Raman Spectroscopy. *Sci. Rep.* **2013**, *3*, No. 1755.
(46) del Corro, E.; Botello-Méndez, A.; Gillet, Y.; Elias, A. L.; Terrones, H.; Feng, S.; Fantini, C.; Rhodes, D.; Pradhan, N.; Balicas, L.; et al. Atypical Exciton−Phonon Interactions in WS_2 and WSe_2 Monolayers Revealed by Resonance Raman Spectroscopy. *Nano Lett.* **2016**, *16*, 2363−2368.
(47) Liu, H.; Wang, C.; Liu, D.; Luo, J. Neutral and defect-induced exciton annihilation in defective monolayer WS_2. *Nanoscale* **2019**, *11*, 7913−7920.
(48) Carozo, V.; Wang, Y.; Fujisawa, K.; Carvalho, B. R.; McCreary, A.; Feng, S.; Lin, Z.; Zhou, C.; Perea-López, N.; Elías, A. L.; et al. Optical identification of sulfur vacancies: Bound excitons at the edges of monolayer tungsten disulfide. *Sci. Adv.* **2017**, *3*, No. e1602813.
(49) Wang, K.; Wang, J.; Fan, J.; Lotya, M.; O'Neill, A.; Fox, D.; Feng, Y.; Zhang, X.; Jiang, B.; Zhao, Q.; et al. Ultrafast Saturable Absorption of Two-Dimensional MoS_2 Nanosheets. *ACS Nano* **2013**, *7*, 9260−9267.
(50) Aleithan, S. H.; Livshits, M. Y.; Khadka, S.; Rack, J. J.; Kordesch, M. E.; Stinaff, E. Broadband femtosecond transient absorption spectroscopy for a CVD MoS_2 monolayer. *Phys. Rev. B* **2016**, *94*, No. 035445.
(51) Vega-Mayoral, V.; Vella, D.; Borzda, T.; Prijatelj, M.; Tempra, I.; Pogna, E. A. A.; Dal Conte, S.; Topolovsek, P.; Vujicic, N.; Cerullo, G.; et al. Exciton and charge carrier dynamics in few-layer WS_2. *Nanoscale* **2016**, *8*, 5428−5434.
(52) Karmakar, R.; Adarsh, K. V. In *Unravelling the Role of Trap States on Carrier Dynamics of WS_2 Quantum Dots*, Conference on Lasers and Electro-Optics, Washington, DC, 2020/05/10. Optical Society of America: Washington, DC, 2020; p SW3G.6.
(53) Vega-Mayoral, V.; Borzda, T.; Vella, D.; Prijatelj, M.; Pogna, E. A. A.; Backes, C.; Coleman, J. N.; Cerullo, G.; Mihailovic, D.; Gadermaier, C. Charge trapping and coalescence dynamics in few layer MoS_2. *2D Mater.* **2017**, *5*, No. 015011.
(54) Ahmed, S.; Jiang, X.; Zhang, F.; Zhang, H. Pump−probe microspectroscopy and 2D materials. *J. Phys. D: Appl. Phys.* **2020**, *53*, No. 473001.
(55) Cunningham, P. D.; McCreary, K. M.; Hanbicki, A. T.; Currie, M.; Jonker, B. T.; Hayden, L. M. Charge Trapping and Exciton Dynamics in Large-Area CVD Grown MoS_2. *J. Phys. Chem. C* **2016**, *120*, 5819−5826.
(56) Chernikov, A.; Berkelbach, T. C.; Hill, H. M.; Rigosi, A.; Li, Y.; Aslan, O. B.; Reichman, D. R.; Hybertsen, M. S.; Heinz, T. F. Exciton Binding Energy and Nonhydrogenic Rydberg Series in Monolayer WS_2. *Phys. Rev. Lett.* **2014**, *113*, No. 076802.
(57) Fan, P.; Zheng, B.; Sun, X.; Zheng, W.; Xu, Z.; Ge, C.; Liu, Y.; Zhuang, X.; Li, D.; Wang, X.; et al. Trion-Induced Distinct Transient Behavior and Stokes Shift in WS_2 Monolayers. *J. Phys. Chem. Lett.* **2019**, *10*, 3763−3772.
(58) Tsai, H.-S.; Huang, Y.-H.; Tsai, P.-C.; Chen, Y.-J.; Ahn, H.; Lin, S.-Y.; Lu, Y.-J. Ultrafast Exciton Dynamics in Scalable Monolayer MoS_2 Synthesized by Metal Sulfurization. *ACS Omega* **2020**, *5*, 10725−10730.
(59) Bergren, M. R.; Palomaki, P. K. B.; Neale, N. R.; Furtak, T. E.; Beard, M. C. Size-Dependent Exciton Formation Dynamics in Colloidal Silicon Quantum Dots. *ACS Nano* **2016**, *10*, 2316−2323.
(60) Yuan, S.; Roldán, R.; Katsnelson, M. I.; Guinea, F. Effect of point defects on the optical and transport properties of MoS_2 and WS_2. *Phys. Rev. B* **2014**, *90*, No. 041402.
(61) Zhou, W.; Zou, X.; Najmaei, S.; Liu, Z.; Shi, Y.; Kong, J.; Lou, J.; Ajayan, P. M.; Yakobson, B. I.; Idrobo, J.-C. Intrinsic Structural Defects in Monolayer Molybdenum Disulfide. *Nano Lett.* **2013**, *13*, 2615−2622.
(62) Tongay, S.; Suh, J.; Ataca, C.; Fan, W.; Luce, A.; Kang, J. S.; Liu, J.; Ko, C.; Raghunathanan, R.; Zhou, J.; et al. Defects activated photoluminescence in two-dimensional semiconductors: interplay between bound, charged and free excitons. *Sci. Rep.* **2013**, *3*, No. 2657.
(63) Attaccalite, C.; Bockstedte, M.; Marini, A.; Rubio, A.; Wirtz, L. Coupling of excitons and defect states in boron-nitride nanostructures. *Phys. Rev. B* **2011**, *83*, No. 144115.

https://doi.org/10.1021/acs.jpcc.1c06267
J. Phys. Chem. C 2021, 125, 23880−23888

(64) Gao, J.; Li, B.; Tan, J.; Chow, P.; Lu, T.-M.; Koratkar, N. Aging of Transition Metal Dichalcogenide Monolayers. *ACS Nano* **2016**, *10*, 2628−2635.
(65) Reale, F.; Palczynski, P.; Amit, I.; Jones, G. F.; Mehew, J. D.; Bacon, A.; Ni, N.; Sherrell, P. C.; Agnoli, S.; Craciun, M. F.; et al. High-Mobility and High-Optical Quality Atomically Thin WS_2. *Sci. Rep.* **2017**, *7*, No. 14911.
(66) Mao, X.; Xu, Y.; Xue, Q.; Wang, W.; Gao, D. Ferromagnetism in exfoliated tungsten disulfide nanosheets. *Nanoscale Res. Lett.* **2013**, *8*, No. 430.
(67) Escalera-López, D.; Griffin, R.; Isaacs, M.; Wilson, K.; Palmer, R. E.; Rees, N. V. MoS_2 and WS_2 nanocone arrays: Impact of surface topography on the hydrogen evolution electrocatalytic activity and mass transport. *Appl. Mater. Today* **2018**, *11*, 70−81.
(68) Perrozzi, F.; Emamjomeh, S. M.; Paolucci, V.; Taglieri, G.; Ottaviano, L.; Cantalini, C. Thermal stability of WS_2 flakes and gas sensing properties of WS_2/WO_3 composite to H_2, NH_3 and NO_2. *Sens. Actuators, B* **2017**, *243*, 812−822.
(69) Kumar, N.; Cui, Q.; Ceballos, F.; He, D.; Wang, Y.; Zhao, H. Exciton-exciton annihilation in $MoSe_2$ monolayers. *Phys. Rev. B* **2014**, *89*, No. 125427.
(70) Steinhoff, A.; Florian, M.; Jahnke, F. Dynamical screening effects of substrate phonons on two-dimensional excitons. *Phys. Rev. B* **2020**, *101*, No. 045411.
(71) Yu, Y.; Yu, Y.; Xu, C.; Barrette, A.; Gundogdu, K.; Cao, L. Fundamental limits of exciton-exciton annihilation for light emission in transition metal dichalcogenide monolayers. *Phys. Rev. B* **2016**, *93*, No. 201111.
(72) Benjamin, E.; Yallapragada, V. J.; Amgar, D.; Yang, G.; Tenne, R.; Oron, D. Temperature Dependence of Excitonic and Biexcitonic Decay Rates in Colloidal Nanoplatelets by Time-Gated Photon Correlation. *J. Phys. Chem. Lett.* **2020**, *11*, 6513−6518.
(73) Chan, B.; Hirao, K. Rapid Prediction of Ultraviolet−Visible Spectra from Conventional (Non-Time-Dependent) Density Functional Theory Calculations. *J. Phys. Chem. Lett.* **2020**, *11*, 7882−7885.
(74) Sun, D.; Rao, Y.; Reider, G. A.; Chen, G.; You, Y.; Brézin, L.; Harutyunyan, A. R.; Heinz, T. F. Observation of Rapid Exciton−Exciton Annihilation in Monolayer Molybdenum Disulfide. *Nano Lett.* **2014**, *14*, 5625−5629.

https://doi.org/10.1021/acs.jpcc.1c06267
J. Phys. Chem. C 2021, 125, 23880−23888

Journal of Physics D: Applied Physics

TOPICAL REVIEW

Valley degree of freedom in two-dimensional van der Waals materials

To cite this article: Ashish Soni and Suman Kalyan Pal 2022 *J. Phys. D: Appl. Phys.* **55** 303003

View the article online for updates and enhancements.

You may also like

- Detection of both optical polarization and coherence transfers to excitonic valley states in CVD-grown monolayer MoS_2
Eito Asakura, Masaki Suzuki, Shutaro Karube et al.
- Valleytronics in two-dimensional materials with line defect
Hongyu Tian, Chongdan Ren and Sake Wang
- Valley manipulation in monolayer transition metal dichalcogenides and their hybrid systems: status and challenges
Siwen Zhao, Xiaoxi Li, Baojuan Dong et al.

The Electrochemical Society
Advancing solid state & electrochemical science & technology
242nd ECS Meeting
Oct 9 – 13, 2022 • Atlanta, GA, US
Submit your abstract
Extended abstract submission deadline: April 22, 2022
Connect. Engage. Champion. Empower. Accelerate.
MOVE SCIENCE FORWARD

This content was downloaded from IP address 14.139.34.9 on 12/04/2022 at 14:31

IOP Publishing Journal of Physics D: Applied Physics
J. Phys. D: Appl. Phys. **55** (2022) 303003 (24pp) https://doi.org/10.1088/1361-6463/ac5bc9

Topical Review

Valley degree of freedom in two-dimensional van der Waals materials

Ashish Soni[1,2] **and Suman Kalyan Pal**[1,2,*]

[1] School of Basic Sciences, Indian Institute of Technology Mandi, Kamand, Mandi 175005, Himachal Pradesh, India
[2] Advanced Materials Research Centre, Indian Institute of Technology Mandi, Kamand, Mandi 175005, Himachal Pradesh, India

E-mail: suman@iitmandi.ac.in

Received 2 October 2021, revised 30 January 2022
Accepted for publication 8 March 2022
Published 12 April 2022

Abstract

Layered materials can possess valleys that are indistinguishable from one another except for their momentum. These valleys are individually addressable in momentum space at the K and K′ points in the first Brillouin zone. Such valley addressability opens up the possibility of utilizing the momentum states of quasi-particles as a completely new paradigm in both quantum and classical information processing. This review focuses on the physics behind valley polarization and discusses carriers of valley degree of freedom (VDF) in layered materials. We then provide a detailed survey of simple spectroscopic techniques commonly utilized to identify and manipulate valley polarization in van der Waals layered materials. Finally, we conclude with recent developments in the manipulation of VDF for device applications and associated challenges.

Keywords: valley polarization, 2D materials, valley degree of freedom, exciton, valley lifetime

(Some figures may appear in colour only in the online journal)

1. Introduction

Two-dimensional materials are members of a family of layered crystal structures whose atoms are connected through strong intra-layer bonds but have weak interlayer van der Waals (vdW) coupling. Graphene, an atomically thin carbon layer, was the first well-known 2D material [1, 2]. It exhibits interesting 2D Dirac fermion-like features (e.g. integer and fractional quantum Hall effects) [3, 4] and ballistic conduction of charge carriers [1, 5]. Graphene is not ideal for electronic applications because of its zero-bandgap semi-metallic nature. However, the bandgap of graphene can be opened up by applying a magnetic field [6], creating a heterostructure [7–9], or preparing a bilayer [10]. Inspired by the fascinating properties and applications of graphene, researchers have developed a plethora of 2D materials. The 2D materials that emerged after the discovery of graphene include transition-metal dichalcogenides (TMDCs) [11], transition-metal monochalcogenides (TMMCs) [12], hexagonal boron nitride (h-BN) [13], black phosphorous (BP) [14], and graphitic carbon nitride [15]. The extraordinary electronic properties of these novel 2D materials make them interesting for applications in diverse technologies (e.g. sensors, LEDs, field effect transistors (FETs), catalysis, biomedicine, and environmental science) [16–21].

In a crystalline solid, a local energy minimum in the conduction band (CB) or a local energy maximum in the valence band (VB) in the momentum space is known as a valley.

* Author to whom any correspondence should be addressed.

 © 2022 IOP Publishing Ltd

In addition to charge and spin, a carrier is assigned a valley degree of freedom, indicating the valley that the carrier occupies. Electrons, holes, or excitons can populate the valleys to store and carry information and form the basis of the so-called valleytronics [22–24]. While electronics utilizes the charges of carriers and spintronics exploits carrier spin, in valleytronics, the valley pseudospin of a quasi-particle forms the basis of a possible new technology.

Few conventional semiconductors (e.g. silicon, aluminum arsenide, and bismuth) have multiple valleys in the CB (figure 1(a)) [25]. In silicon (Si), six equivalent valleys lie along the Δ-direction and near the zone boundary (X). Recently, efforts have been made to manipulate the VDF in traditional semiconductors [23]. Valley-polarized current has been generated and detected in bulk diamond [26]. The charge conductivity of bismuth can be controlled by manipulating the polarization of Dirac valleys using a magnetic field [27]. The valley degeneracy in Si-based systems is increased by introducing valley splitting, which can be tuned by controlling the applied electrostatic potential [28, 29]. Despite a few encouraging results, the difficulty with these materials is to maintain the VDF using simple external agents such as an electric field, a magnetic field, light, strain, etc.

Two-dimensional materials may intrinsically possess or be tailored to produce contrasting valley properties that can be exploited in valleytronics. In 2D-dimensional materials with hexagonal honeycomb structures (e.g. graphene and TMDCs), two valleys are present at the $+K$ and $-K$ points at the edges of the Brillouin zone (figure 1(b)) [30]. Among the 2D materials, valley-contrasting physics was first detected and manipulated in graphene [2, 31, 32]. Graphene exhibits contrasting circular dichroism in different k-space regions due to inversion symmetry breaking [33, 34]. Therefore, it obeys a valley-contrast optical selection rule, which can be exploited for optoelectronics applications in which light polarization information can be converted into electronic information [31, 35, 36]. In 2010, Mak *et al* proposed a new direct bandgap semiconductor, 2D MoS_2, that exhibits very high luminescence quantum efficiency compared to that of the bulk material [37, 38]. Polarization can be achieved and manipulated in monolayer MoS_2 through the optical pumping of circularly polarized light [39–41]. Valley-selective photoluminescence (PL) has been detected in many other TMDCs (e.g. $MoSe_2$, WS_2, and WSe_2) [42, 43]. Both graphene and 2D TMDCs have non-centrosymmetric hexagonal crystal structures, which cause inversion symmetry breaking and result in valley-contrast properties. Graphene does not naturally possess valley-selective circular dichroism, but it can exhibit valley polarization under the influence of an external magnetic or electric field. The valleys of these vdWs layered materials can be coupled with circularly polarized photons, leading to valley-selective circular dichroism [44, 45]. Although 2D TMMCs and BP exhibit VDF, the nature of the valleys in such materials is quite different from those of graphene and TMDCs, and valley polarization can be created in them using linear polarized light [46–48]. The main advantage of 2D materials over traditional semiconducting materials is that 2D materials host inequivalent valleys and valley polarization can easily be generated (e.g. by applying polarized light).

The practical realization of valleytronics devices is highly dependent on our understanding of VDF in 2D materials, including the manipulation of valley pseudospin. Graphene and TMDCs which have hexagonal crystal structures possess inequivalent valleys at the K and K' points. Moreover, both of them show valley-selective circular dichroism due to coupling with circularly polarized photons that follows similar optical selection rules. Here, we present the necessary valley physics to understand the origin of valley-contrast properties in such 2D vdW materials. The details of the carriers of valley pseudospin in layered materials will be discussed here. This review will attempt to summarize the techniques currently used to investigate the VDF in 2D vdW systems. Finally, we will explore the available ways of manipulating valley polarization and valley coherence in 2D hexagonal materials.

2. Valley physics

The valleys in crystalline solids can be equivalent or inequivalent, depending on the nature of the unit cell. When there is some asymmetry in the unit cell, valleys exhibit different characteristics. For example, in the hexagonal graphene lattice, which can be considered as a superposition of two identical sub-lattices offset by the carbon–carbon bond length (figure 1(c)), two inequivalent (since the two sublattices are distinct) but otherwise identical valleys are present at the K and K' points in the Brillouin zone. The K and K' points in graphene are related to inversion and time-reversal symmetry [51]. Due to the broken sublattice symmetry in 2D TMDCs, the valleys located at K and K' are degenerate but have opposite momentum [25]. To differentiate these valleys, a new index, known as valley pseudospin (τ_z), has been introduced [31]. It is called pseudospin because it carries information, i.e. up/-down or valley one or two, in the same way as spin. The values of τ_z for TMDCs are ± 1, which describe the position of a particle: in the K valley or the K' valley [31]. In 2D materials, there are two physical quantities—orbital angular momentum and Berry curvature, which are different in the K and K' valleys.

2.1. Orbital magnetic moment (m)

The orbital magnetic moment is one of the valley-contrast parameters in 2D materials [52, 53]. It can be regarded as the self-rotation of the electron wave packet clockwise in one valley (at K) and anticlockwise in the other valley (at K'), which gives rise to an opposite value of m (figure 1(d)). The spin magnetic moment is different for the spin-up and -down states; in the same way, the orbital angular moment discriminates between different valley states. The valley-contrast magnetic moment can be defined as [31]

$$\boldsymbol{m}(\boldsymbol{k}) = \boldsymbol{\tau}_Z \frac{3ea^2\boldsymbol{\Delta}t^2}{4h(\boldsymbol{\Delta}^2 + 3q^2a^2t^2)} \tag{1}$$

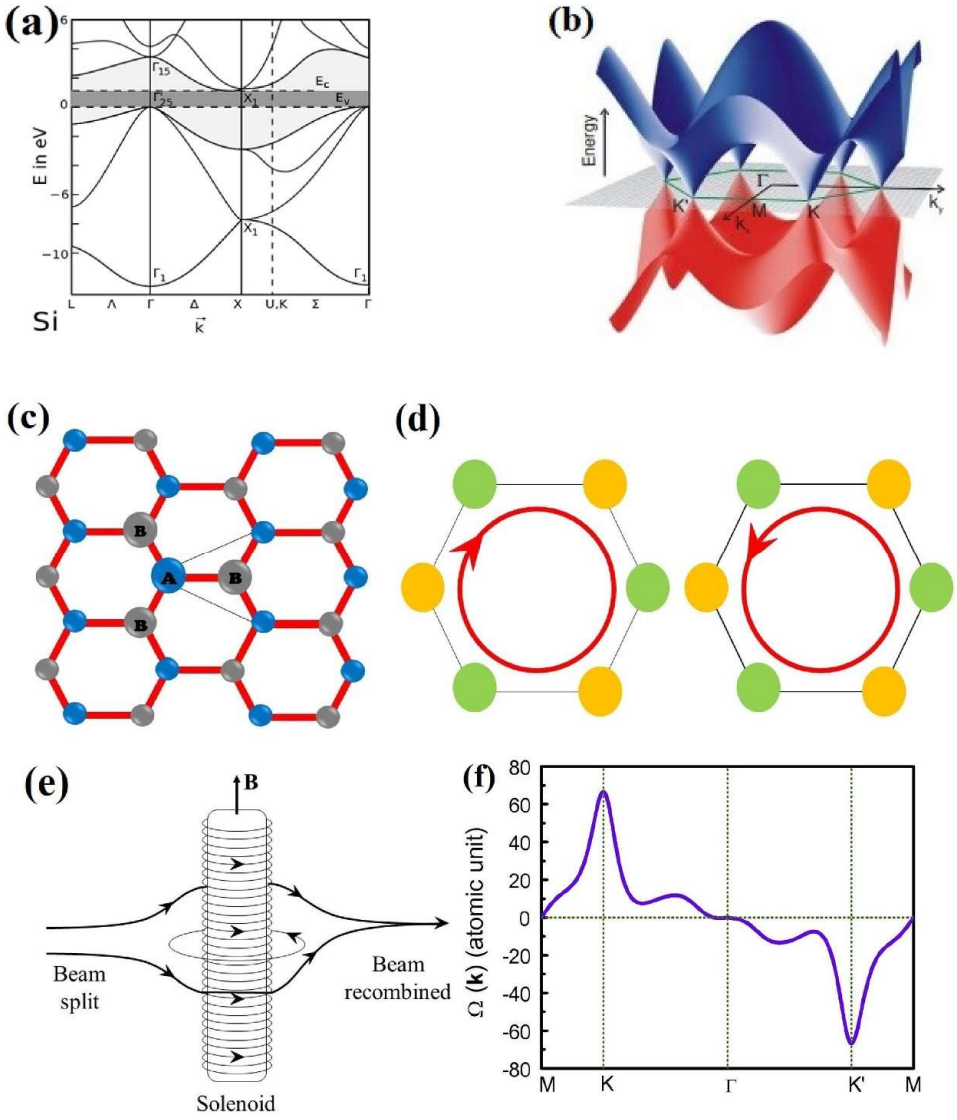

Figure 1. (a) Energy band structure of silicon showing multiple valleys [49]. Image has been obtained by the author(s) from the Wikimedia website where it was made available [by Cepheiden] under a CC BY-SA 2.5 licence. It is included within this article on that basis. It is attributed to [Cepheiden] (b) Schematic drawing of the characteristic Dirac cones of the graphene band structure. Reproduced from [30]. © IOP Publishing Ltd. All rights reserved. (c) Hexagonal graphene lattice consisting of two triangular sublattices (A and B). (d) Self-rotation of the electronic wave packet in the K and K′ valleys. (e) Pictorial view of the Aharonov–Bohm experiment. (f) Barry curvature of MoS_2 along with high symmetry lines. Figure reprinted with permission from [50], Copyright (2012) American Physical Society.

where $\tau_z = \pm 1$ labels the two valleys, $m(\boldsymbol{k})$ is the orbital magnetic momentum, q is the canonical momentum taken from the valley centre, a is the the lattice constant, t is the nearest-neighbour hopping energy, and Δ is the energy difference between sublattices. The orbital magnetic moment in a crystal is related to some fundamental symmetries (time-reversal symmetry and inversion symmetry). Time reversal is the name of a particular symmetry transformation that stands for an inversion of the direction of time [54], while spatial inversion symmetry refers to symmetry under a reversal of the directions of all the coordinate axes [55]. The signs of both m and τ_z are changed by a time-reversal symmetry operation. On the contrary, only τ_z (not m) changes sign under spatial inversion. This implies that m can only be zero when the system remains invariant under both time-reversal and inversion symmetries. The value of the orbital magnetic moment can be nonzero only in systems with broken inversion symmetry. Although the K and K' points are time-reversed images of one another, the orbital angular momenta are inequivalent at these points in hexagonal 2D materials due to the violation of spatial inversion symmetry.

2.2. Berry phase and curvature

The adiabatic theorem in quantum mechanics states that a system will remain in its time-dependent ground state if the Hamiltonian is changed slowly. In reality, when the Hamiltonian of a system travels around a closed loop in the parameter space, an irreducible phase known as the Berry phase can be developed [56]. The Berry phase is a geometrical phase acquired during the adiabatic evolution of a quantum state. The foremost features of the Berry phase are as follows: (a) it is geometric, (b) it is gauge invariant, and (c) it has close analogies to gauge field theories and differential geometry [57, 58]. The Berry phase effect is observed in crystalline solids with band structures [59]. Under the free electron approximation, the Hamiltonian for a single electron in a crystal lattice is expressed as

$$H = \frac{\widehat{\boldsymbol{p}}^2}{2m} + V(\boldsymbol{r}) \tag{2}$$

where $V(\boldsymbol{r})$ is the periodic potential. According to Bloch's theorem, the energy eigenstates of a periodic Hamiltonian can be written in the form [60]:

$$\psi_{nk}(r+a) = e^{ika}\psi_{nk}(r) \tag{3}$$

where a is the Bravais lattice vector, n is the band index, and $\hbar\boldsymbol{k}$ is the crystal momentum. Although the Hamiltonian of the system is k-independent, the boundary condition depends on $\boldsymbol{k}$. The Hamiltonian can be made k-dependent through a unitary transformation of the form

$$H(\boldsymbol{k}) = e^{-i\boldsymbol{k}.\boldsymbol{r}}He^{i\boldsymbol{k}.\boldsymbol{r}} = \frac{\left(\widehat{\boldsymbol{p}} + \hbar\boldsymbol{k}\right)^2}{2m} + V(\boldsymbol{r}). \tag{4}$$

The function $u_{n\boldsymbol{k}}(\boldsymbol{r}) = e^{-i\boldsymbol{k}.\boldsymbol{r}}\psi_{n\boldsymbol{k}}(\boldsymbol{r})$, satisfies the periodic boundary condition

$$u_{n\boldsymbol{k}}(\boldsymbol{r}+\boldsymbol{a}) = u_{n\boldsymbol{k}}(\boldsymbol{r}). \tag{5}$$

All such eigenfunctions belong to the same Hilbert space. Therefore, the Brillouin zone can be the parameter space of the transformed Hamiltonian $H(\boldsymbol{k})$ with $|u_n(\boldsymbol{k})\rangle$ as the basis function.

Since the $\boldsymbol{k}$ dependence of the basis function is inherent to the Bloch problem, various Berry phase effects can be expected in crystals. For example, in crystals, if $\boldsymbol{k}$ is considered to be in the momentum space, then a Berry phase will be associated with the Bloch state:

$$\Phi_{\mathrm{B}} = \oint C d\boldsymbol{k}.\langle u_n(\boldsymbol{k})|i\Delta_{\boldsymbol{k}}|u_n(\boldsymbol{k})\rangle = \oint C d\boldsymbol{k}.\boldsymbol{\Omega}_n(\boldsymbol{k}). \tag{6}$$

The Berry curvature of the energy bands of crystalline solids is defined as

$$\Omega_n(\boldsymbol{k}) = \Delta_{\boldsymbol{k}} \times \langle u_n(\boldsymbol{k})|i\Delta_{\boldsymbol{k}}|u_n(\boldsymbol{k})\rangle. \tag{7}$$

It depends on the wave function and is hence an intrinsic property of the crystal. It plays a vital role in the accurate description of the dynamics of Bloch electrons.

In the Aharonov–Bohm effect, which is a purely quantum mechanical phenomenon, an electromagnetic potential $(\varphi, \boldsymbol{A})$ affects an electrically charged particle, even if both the magnetic $(\boldsymbol{B})$ and electric (ε) fields are zero in that region [61]. A beam of electrons is split into two and sent past a solenoid on different sides of it (figure 1(e)). Suppose the solenoid contains a magnetic field (a non-zero vector potential outside the solenoid). In this case, the electronic state will acquire an additional phase (Φ), which is proportional to the magnetic flux (ϕ_{m}) inside the solenoid

$$\Phi = \frac{e}{\hbar}\oint A(\boldsymbol{r}) = \frac{e}{\hbar}\phi_{\mathrm{m}}. \tag{8}$$

$$\phi_{\mathrm{m}} = \int \mathrm{d}\boldsymbol{a}\cdot\boldsymbol{B} \tag{9}$$

where $\mathrm{d}\boldsymbol{a}$ and $\boldsymbol{B}$ are the cross-sectional areas of the solenoid and the magnetic field, respectively. This effect is known as the magnetic Aharonov–Bohm effect. Making an analogy between the Berry-phase effect and the magnetic Aharonov–Bohm effect, the Berry phase and Berry curvature can be considered as a magnetic flux and a magnetic field in the momentum space, respectively [62].

The value of the Berry curvature is nonzero for crystals with broken time-reversal or inversion symmetry. Two-dimensional TMDCs have non-zero Berry curvature due to the absence of an inversion center in the structure. In these materials, maximum Berry curvatures are observed at the K and K' points (figure 1(f)) [50]. The Berry curvature introduces energy splitting between exciton states with opposite angular momentums by modifying the effective Hamiltonian for excitons [63]. Another example of a system in which both symmetries are not simultaneously present is monolayer graphene with a staggered sublattice potential, in which inversion symmetry is broken [64]. The Berry curvature of this system possesses opposite signs at the valleys K and K' due to time-reversal symmetry [31, 65]. As the energy gap approaches zero, the Berry phase of an electron after completing one cycle around the valley becomes $\pm\pi$. The intrinsic graphene sheet exhibits a Berry phase of π [4, 34].

2.3. Valley-selection rule

When a Bloch electron travels adiabatically in a non-degenerate energy band, in general, the real-space dimension of the associated wave packet is much larger than the lattice constant, but much smaller than the length scale of the external perturbation [66, 67]. Therefore, the wave packet and the wave vector of the electron can be considered independently. In this case, we can describe the motion of electrons in the crystal lattice by the semi-classical equation in which the wave function is a Bloch function and the mean velocity is related to the electronic energy gradient of the band [68, 69]. When the periodicity, as well as the applied magnetic field, are taken into consideration, an anomalous velocity exists due to the Berry curvature of the electronic band. The Berry curvature of the Bloch states exists in the absence of external fields and

manifests itself in a quasi-particle velocity when the crystal momentum is changed by external forces [70, 71].

The semi-classical dynamics of a Bloch electron under applied electric and magnetic fields can be expressed as

$$\frac{\mathrm{d}\boldsymbol{r}}{\mathrm{d}t} = \frac{1}{\hbar}\frac{\partial E_n(\boldsymbol{k})}{\partial k} - \frac{\mathrm{d}\boldsymbol{k}}{\mathrm{d}t} \times \Omega_n(\boldsymbol{k}) \tag{10}$$

$$\hbar\frac{\mathrm{d}\boldsymbol{k}}{\mathrm{d}t} = -e\boldsymbol{\varepsilon} - e\frac{\mathrm{d}\boldsymbol{k}}{\mathrm{d}t} \times \vec{\boldsymbol{B}} \tag{11}$$

where $E_n(\boldsymbol{k})$ is the energy dispersion of the nth band, $\boldsymbol{r}$ is the crystal momentum and the position of the electron wave packet, and ε and $\vec{\boldsymbol{B}}$ represent the applied electric and magnetic fields, respectively. The Berry curvature can be defined in terms of the Berry phase relation

$$\boldsymbol{A}_n(\boldsymbol{k}) = \langle u_n(\boldsymbol{k}) | i\nabla_{\boldsymbol{k}} | u_n(\boldsymbol{k}) \rangle \tag{12}$$

as

$$\Omega_n(\boldsymbol{k}) = \nabla_k \times \boldsymbol{A}_n(\boldsymbol{k}). \tag{13}$$

According to the Kubo formula [68, 72, 73], the Berry curvature of the Bloch states can also be written as

$$\Omega_n(\boldsymbol{k}) = i\frac{\hbar^2}{m^2}\sum\nolimits_{n'\neq m} \frac{\langle u_n | v | u_{n'} \rangle \times \langle u_{n'} | v | u_n \rangle}{\left[E_n^0 - E_{n'}^0\right]^2} \tag{14}$$

where E_n^0 is the energy dispersion of the nth band, and $\boldsymbol{v}$ is the velocity operator. Since the equations of motion remain invariant under symmetry operations, $\Omega_n(\boldsymbol{k}) = -\Omega_n(-\boldsymbol{k})$ under time-reversal symmetry, and $\Omega_n(\boldsymbol{k}) = \Omega_n(-\boldsymbol{k})$ under inversion symmetry. Therefore, valley-contrast properties appear when one of the symmetries is broken.

Berry curvature gives rise to an anomalous transverse velocity (Hall velocity) in a 2D crystal in the presence of an electric field [59]:

$$\boldsymbol{v}_\perp = \frac{\mathrm{d}\boldsymbol{k}}{\mathrm{d}t} \times \Omega_n(\boldsymbol{k}). \tag{15}$$

As the directions of the electron velocity are opposite in opposite valleys, the electron motion in a particular valley can be selected by changing the direction of the applied electric field.

The electron energy dispersion can be written in terms of the orbital angular momentum as

$$E_n(\boldsymbol{k}) = E_n^0(\boldsymbol{k}) - \boldsymbol{m}_n(\boldsymbol{k}).\boldsymbol{B} \tag{16}$$

where

$$\boldsymbol{m}(\boldsymbol{k}) = i\frac{e\hbar}{m^2}\sum_{n'\neq n} \frac{\langle u_n | v | u_{n'} \rangle \times \langle u_{n'} | v | u_n \rangle}{\left[E_n^0 - E_{n'}^0\right]}. \tag{17}$$

The valley magnetic moment of a valley carrier interacts with an external magnetic field, giving rise to a valley Zeeman effect similar to the spin Zeeman effect. Therefore, an external magnetic field can be an additional way of controlling the VDF. Nonetheless, due to the finite orbital magnetic moment, the valley carriers interact differently with left and right circularly polarized light [40, 41, 74]. Such optical circular dichroism due to the orbital magnetic moment provides an optical selection rule for valley carriers [25].

In monolayer TMDCs, contrasting $\boldsymbol{\Omega}$ and $\boldsymbol{m}$ values in the $\pm K$ valley gives rise to valley selection rules. In the tight-binding approximation, the Hamiltonian of a single TMDC sheet depends on nearest-neighbour hopping energy (hopping integral) t and the energy difference between sublattices $\boldsymbol{\Delta}$. The low-energy description of the Hamiltonian near the Dirac points is given by [42, 75]

$$\widehat{\boldsymbol{H}} = \boldsymbol{a}t(\boldsymbol{\tau}_z\boldsymbol{k}_x\sigma_x + \boldsymbol{k}_\gamma\sigma_\gamma) + \frac{\boldsymbol{\Delta}}{2}\sigma_z \tag{18}$$

where σ is the Pauli matrix, accounting for the sublattice index and the lattice constant. According to this model, the valley-contrast Berry curvature takes the form

$$\boldsymbol{\Omega}_{\mathrm{c}}(\boldsymbol{k}) = -\hat{\boldsymbol{z}}\frac{2a^2t^2\boldsymbol{\Delta}}{\left(2a^2t^2k^2 + \boldsymbol{\Delta}^2\right)^{3/2}}\boldsymbol{\tau}_z. \tag{19}$$

As the values of $\boldsymbol{\tau}_z = \pm 1$, Ω_{c} assumes equal but opposite values in the K or K' valleys of monolayer TMDCs. The valley-contrast Ω_{c} gives rise to a current of the carriers, whose sign depends on the valley index (τ_z) when exposed to an in−plane electric field. The photoexcited electrons and holes move to the two opposite edges of the TMDC sheet, developing a transverse bias (figure 2(a)) [42, 76]. This phenomenon is known as the valley Hall effect.

According to the massive Dirac fermion model, the orbital angular momentum can be expressed as

$$\boldsymbol{m}(\boldsymbol{k}) = -\hat{\boldsymbol{z}}\frac{2a^2t^2\boldsymbol{\Delta}}{4a^2t^2\boldsymbol{k}^2 + \boldsymbol{\Delta}^2}\frac{e}{2\hbar}\boldsymbol{\tau}_z. \tag{20}$$

In the low-energy limit ($\boldsymbol{k}\rightarrow 0$), the orbital magnetic moment is [31]

$$m(m_{1,2}) = \boldsymbol{\tau}_z\mu_{\mathrm{B}}^* \text{ with } \mu_{\mathrm{B}}^* = \frac{e\hbar}{2m_{\mathrm{e}}^*} \tag{21}$$

where $m_{\mathrm{e}}^* = (2\Delta\hbar^2)/(3a^2t^2)$ is the effective mass of the electron at the bottom of the band. As a result, monolayer TMDCs exhibit valley-contrast magnetic moments, which can be detected through an applied magnetic field (figure 2(a)) [42].

The optical circular dichroism in 2D TMDCs is given by

$$\eta(\boldsymbol{k}) = -\frac{\boldsymbol{m}(\boldsymbol{k}).\hat{\boldsymbol{z}}}{\mu_{\mathrm{B}}^*(\boldsymbol{k})} = -\frac{\Omega(\boldsymbol{k}).\hat{\boldsymbol{z}}}{\mu_{\mathrm{B}}^*(\boldsymbol{k})}\frac{e}{2\hbar}\boldsymbol{\Delta}(\boldsymbol{k}). \tag{22}$$

In the Brillouin zone, at high symmetry points, the Bloch states are invariant under a q-fold discrete rotation about the direction of light propagation: $\Re\left(\frac{2\pi}{q},\hat{\boldsymbol{z}}\right)\left|\Psi_{c(\boldsymbol{k}),\boldsymbol{k}}\right\rangle = e^{-i\frac{2\pi}{q}l_{c(v)}}\left|\Psi_{c(v),\boldsymbol{k}}\right\rangle$. The azimuthal selection rule for interband transitions due to circularly polarized light is $l_v \pm 1 = l_c + qN$ [33], where l_v and l_c are azimuthal quantum numbers. In TMDCs, the right and left circularly polarized lights couple

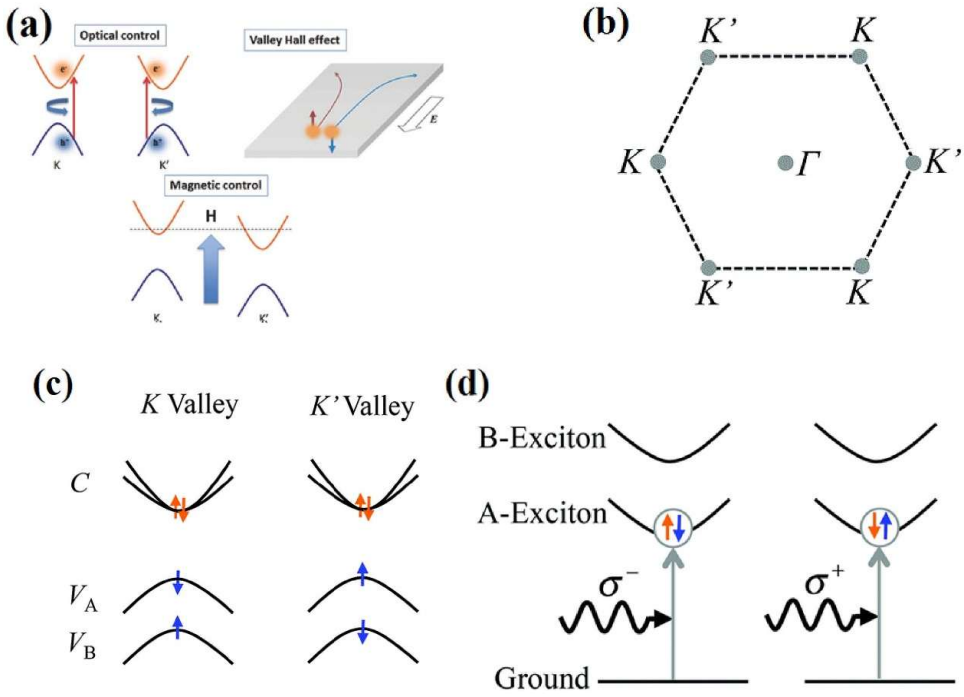

Figure 2. (a) Various methods (i.e. optical, magnetic, and electrostatic) of controlling the VDF. [42] John Wiley & Sons. [© 2018 WILEY-VCH Verlag GmbH & Co. KGaA, Weinheim]. (b) The K and K′ valleys in momentum space. (c) Electronic band structures at the K and K' valleys with their spin orientations (up and down arrows). (d) Spin orientations of the A excitons (at the K and K' valleys) and their coupling with circularly polarized light. (b)–(d) Reproduced from [77] with permission from the Royal Society of Chemistry.

to interband transitions in the K and K' valleys, respectively [66].

The lattice of 2D TMDC crystals has no inversion symmetry, and therefore its six energy valleys in momentum space constitute two inequivalent sets (K and K') (figure 2(b)). The strong spin-orbital coupling between the d orbitals of the chalcogenide atoms introduces large splits in the valence bands of such crystals [78, 79]. The spin splitting in different valleys is opposite, due to time-reversal symmetry and the lack of inversion symmetry in space. The spins of the holes in the V_A band are $-3/2$ and $+3/2$, respectively, while the spins in the V_B band assume the values $+1/2$ and $-1/2$ in the respective valleys (figure 2(c)) [77]. Because of this unique spin feature, the spin and valley degrees of freedom of holes are inherently coupled in the valence bands [25, 80]. However, the degeneracy of the CBs near the band minima in TMDCs (figure 2(c)) [77] provides interesting spin and valley structures, which gives rise to spin- and valley-selective optical coupling [81]. The holes in the V_A and V_B bands are combined with the electrons in the CB to form A and B excitons, respectively (figure 2(d)) [77]. In the K valley, a spin-down hole ($-3/2$) and either a spin-up ($+1/2$) or a spin-down ($-1/2$) electron constitute an A-exciton. The spin of the exciton in the first case is -1(down) and hence it couples to right circularly polarized photons (figure 2(d)). The second exciton is a dark exciton with a spin of -2, which does not couple to photons. Conversely, a bright A-exciton in the K' valley is formed from a spin-up hole ($+3/2$) and a spin-down electron ($-1/2$); this exciton has a spin of $+1$ (a spin-up exciton), and hence couples to left circularly polarized photons (figure 2(d)). Hence, both spin- and valley-polarized excitons can be created in 2D TMDC crystals using circularly polarized lights of different kinds [41, 81].

2.4. Valley coherence

Valley coherence is a coherent superposition of two valley states with a fixed phase relationship. The valley indexes of 2D vdW materials can constitute a quantum two-level system, and the excited carriers in the K and K' valleys form excitons with pseudospins of $+1$ and -1 (the corresponding states are $|+1\rangle$ and $|-1\rangle$). The valley pseudospin of excitons, electrons, or holes can be used to perform quantum gate operations. A quantum state does not have to be composed of just a single particle (e.g. an exciton) in the state $|+1\rangle$ or $|-1\rangle$, but can also be formed by a coherent superposition of two states of two particles as $|X\rangle = 1/\sqrt{2}(|+1\rangle + |-1\rangle)$ [82]. In TMDCs, quantum coherence can be realized in well-separated band extrema in momentum space. Valley coherence allows the manipulation of the VDF and can be generated by linearly polarized light [83, 84]. Basically, linearly polarized light is a superposition of right and left circularly polarized photons, which simultaneously excite both valleys. The degree of valley

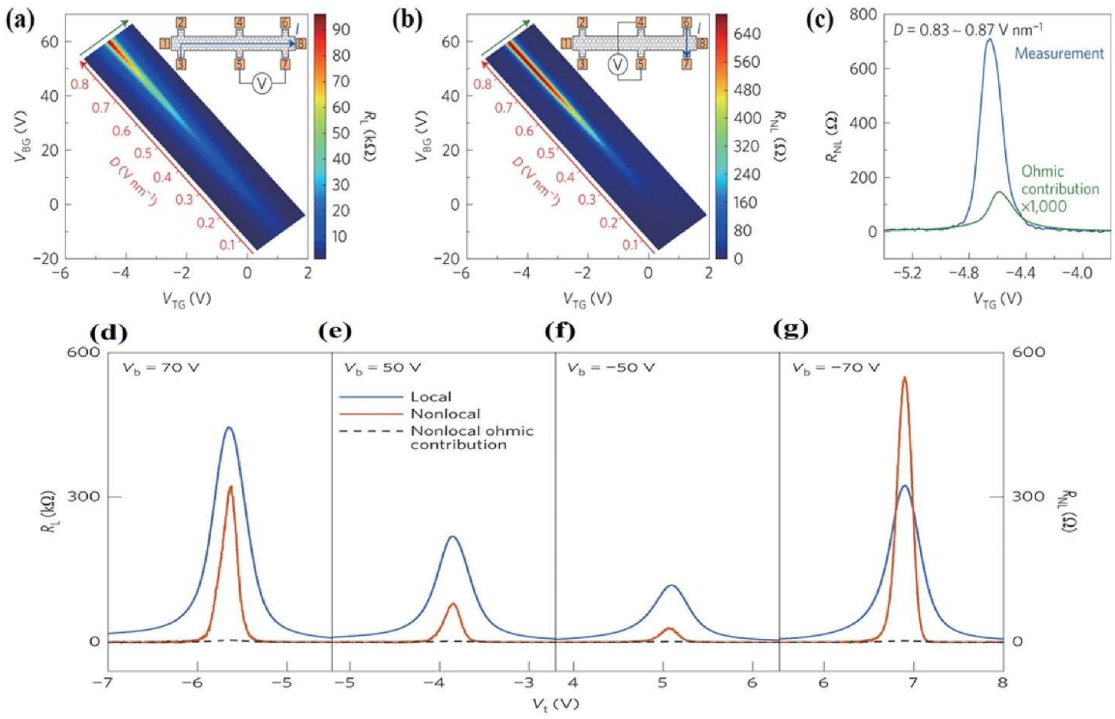

Figure 3. (a), (b) Measured local (R_L) and non-local (R_{NL}) resistances. Dependence of R_L and R_{NL} on the gate voltage, respectively. Back and top gate displacements are defined as $D_{BG} = \varepsilon_{BG}\left(V_{BG} - {V_{BG}}^0\right)/d_{BG}$ and $D_{TG} = -\varepsilon_{TG}\left(V_{TG} - {V_{TG}}^0\right)/d_{TG}$, respectively. (c) Comparison of the experimentally measured R_{NL} and a calculation of the ohmic contribution. (a)–(c) Reprinted by permission from Springer Nature Customer Service Centre GmbH: [Springer Nature] [Nature Physics] [93], copyright (2015). (d)–(g) Variation of R_L and R_{NL} with V_t (voltage applied to the top gates) at fixed V_b (voltage at bottom gates) at varying voltages. The sample dimensions were $5\mu m \times 1.5\mu m$. The dashed lines represent the expected ohmic non-local contributions. Reprinted by permission from Springer Nature Customer Service Centre GmbH: [Springer Nature] [Nature Physics] [36], copyright (2015).

coherence (DOVC) or linear polarization is expressed by the following relation

$$\theta = \frac{I(\|) - I(\perp)}{I(\|) + I(\perp)} \tag{23}$$

where $I(\|)$ and $I(\perp)$ are the parallelly and perpendicularly polarized emission intensities with respect to the polarization state of excitation, respectively. The coherence between the different valleys was first demonstrated in monolayer WSe_2 by monitoring the linearly polarized emission [85, 86]. The DOVC in a WSe_2 monolayer has been reported to be ∼40% at 30 K [85]. Zhu *et al* observed DOVCs of around 4% and 80% for monolayer and bilayer WS_2, respectively at 10 K [87]. Valley coherence has also been detected in CVD-grown monolayer MoS_2 at cryogenic temperatures (20 K) under nearly resonant excitation [82]. Giant exciton valley coherence (DOVC∼74%) has been reported in multilayer WS_2 large single crystals at room temperature [88]. In addition, perfect valley coherence (100% DOVC) has been achieved in monolayer MoS_2 sandwiched between two graphene layers [89].

3. Valley carriers

Like charge and spin, valley information can also be transported through materials. There are many carriers of valley pseudospin, such as free electrons and holes, doped electrons and holes, and quasi-particles such as neutral, charged, and bound excitons. Due to the availability of various valley information carriers, several different methods can be used to control the transport of valley polarization.

3.1. Electrons and holes

Hall currents flow transversely to the applied electric field in graphene placed on top of h-BN, even without a magnetic field [90]. Opposing Hall currents arise due to carriers located in opposite valleys [25, 31]. The inversion symmetry broken by the superlattice potential induced by the h-BN substrate gives rise to the Hall currents [91, 92]. Pure valley current flows through dual-gated bilayer graphene (BG) and produces a large non-local resistance that scales cubically with the local resistivity (figure 3) [93]. A pronounced non-local response in the resistance has also been observed as a result of the topological transport of valley pseudospin in BG

(figures 3(d)–(g)) [36]. In BG, carriers that are doped by applying an out−of−plane electric field carry the valley information [36, 93]. These carriers of valley pseudospin can easily be injected using an electric field and controlled by electric or magnetic fields. The lifetimes of these valley carriers are very long (∼ns) [94].

Optically injected electrons and holes exhibit valley polarization in TMDCs. In monolayer TMDCs, the electrons (injected through optical excitation following the valley optical selection rules) from different valleys are moved in opposite directions across the sample and produce valley current [76, 95]. Optically generated carriers are also responsible for valley polarisation in bilayer TMDCs [76, 96, 97]. The advantages of such carriers are that they can easily be created using light and have a long lifetime [98–100]. The valley current can be generated using an electric field [101] and controlled by electric and magnetic fields.

3.2. Intralayer excitons

In low-dimensional materials, quasi-states (excitons, trions, and biexcitons) are formed due to weak electrostatic screening and large Coulomb interactions [102–104]. An exciton is the combined state of an electron in the CB and a hole in the VB [105–108]. In a doped semiconductor, the neutral exciton can be combined with an extra electron or hole to form a charged exciton or trion [109, 110]. The enhanced Coulomb interaction in 2D materials (e.g. TMDCs) leads to the formation of biexcitons [111, 112].

Monolayer TMDCs have a direct bandgap and exhibit a great resonance in their optical responses, such as absorption and PL due to the formation of neutral (X^0) and charged ($X^{\pm}$) excitons (figure 4(a)). The typical absorption spectra of monolayer TMDCs consist of several characteristic peaks due to exciton resonance and interband transitions [113]. Theoretical studies of such systems have reported unusual features in the density of states, i.e. 'band nesting' (figure 4(b)) [114]. According to these studies, the location of the band nesting region is near the midway point between Γ and K', where the CB and the VB are parallel to each other. The conduction band minima and valence band maxima are both located at the K/K' point of the Brillouin zone. Hence, the optical response of monolayer TMDCs is dominated by valley excitons (bound electron–hole pairs in the valleys).

Figure 4(c) shows the PL and differential reflectance spectra of monolayer MoS_2, $MoSe_2$, WS_2, and WSe_2 on a quartz substrate [115]. The peaks A and B are associated with the excitons that reside at the K and K' points. A strong absorption peak (similar to the C peak in figure 4(c)) is observed when the conduction and VBs are nested. As a consequence of the strong quantum confinement, the exciton binding energy in TMDCs is exceptionally high, about 0.5 eV [113, 116]. These excitons are bright excitons in which electrons and holes remain in the same valley. Therefore, bright excitons have a binary valley pseudospin similar to those of free electrons and holes. For excitons, the Coulomb interactions between charges are of two types: direct and exchange. While the binding energy of excitons is predominantly due to the direct part, the exchange Coulomb interaction results in a diagonal energy shift and off-diagonal coupling in the valley configurations [117]. The electron–hole exchange interaction between the excitons in the two valleys is equivalent to an in-plane effective magnetic field at the valley pseudospin [66, 118]. This effective magnetic field gives rise to the valley–orbit coupling, and the bright exciton dispersion is split into two branches that have in-plane valley pseudospins (figure 4(d)) [117].

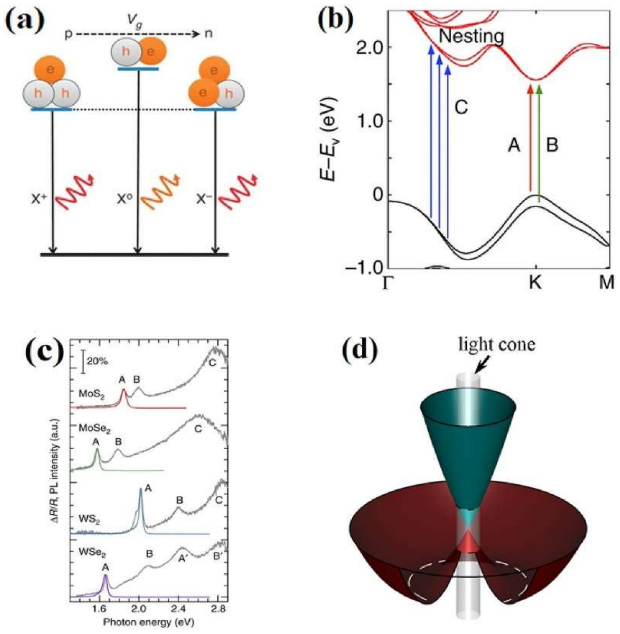

Figure 4. (a) Illustration of exciton and trion states in TMDCs and associated transitions. Reprinted by permission from Springer Nature Customer Service Centre GmbH: [Springer Nature] [Nature Communications] [119], copyright (2013). (b) The calculated energy band diagram of monolayer MoS_2. The transition in A, B and band nesting are represented by arrows. (c) PL spectra (red, green, blue, and purple curves) and differential reflectance spectra (grey curves) of MoS_2, $MoSe_2$, WS_2, and WSe_2. (b), (c) Reprinted by permission from Springer Nature Customer Service Centre GmbH: [Springer Nature] [Nature Communications] [115], copyright (2014). (d) Valley–orbit splitting of a bright exciton by the intervalley electron–hole exchange interaction. (b), (c) Reprinted by permission from Springer Nature Customer Service Centre GmbH: [Springer Nature] [Nature Communications] [118], copyright (2014).

Due to the substantial resonant excitonic absorption [37] of monolayer TMDCs, valley excitons can play an essential role in TMDC-based valleytronics devices [117]. These devices are expected to be easily initialized using light [39, 120], and readout can be performed using photon polarization [40, 120]. Valley excitons can be controlled by both magnetic [121–123] and optical fields [124, 125]. The major issue with this kind of valley carrier is the short (few nanoseconds) exciton lifetime [126, 127] and very short (few picoseconds) valley lifetimes [128, 129].

Nonetheless, recent theoretical and experimental reports suggest that dark excitons can play an important role in

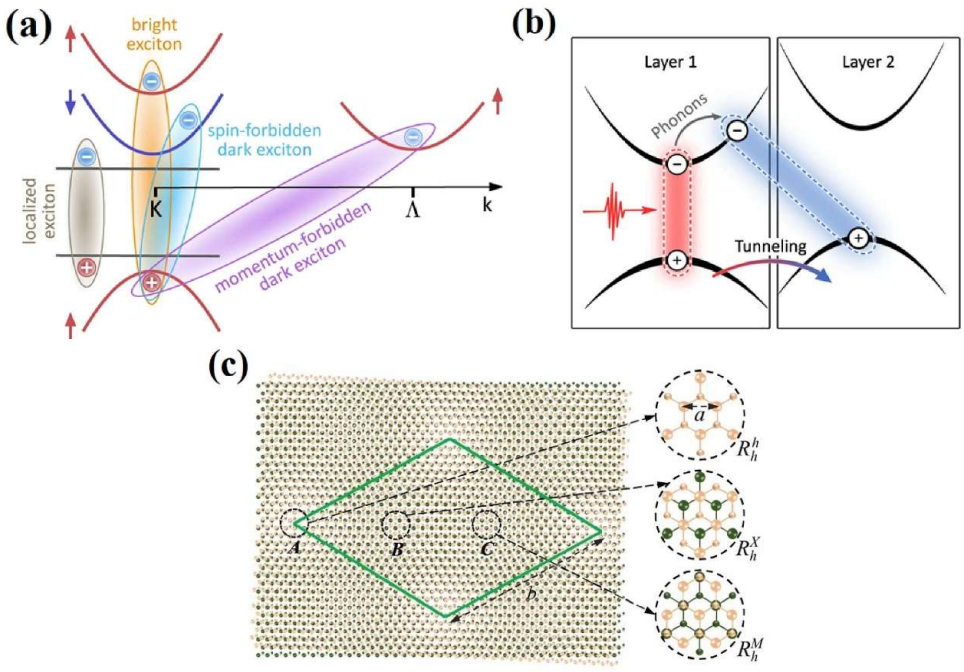

Figure 5. (a) Schematic representation of bright excitons, spin-forbidden dark excitons, and momentum-forbidden dark excitons in atomically thin nanomaterials. (b) Interlayer excitons are formed from the electrons and holes present in different layers. (a), (b) Reproduced from [116]. CC BY 4.0. (c) Moiré pattern in a heterostructure (MoX_2/WX_2). A supercell is indicated by the green quadrilateral. The insets are close-ups of three locales. Reproduced with permission from [159]. CC BY-NC 4.0.

determining the valley degree of polarization in 2D materials [116, 130, 131]. The dark exciton ground state is a huge reservoir for valley polarization. Intravalley bright and dark exciton scatterings help to maintain a Boltzmann distribution of the bright exciton states in the same valley [130]. In TMDCs, the degree of circular polarization is directly related to the alignment of bright and dark exciton states. The PL quantum yield of tungsten-based TMDCs was found to increase at higher temperatures. This observation can be explained by the presence of dark exciton states whose energy is lower than those of the bright state.

Dark excitons can be classified as spin-forbidden and momentum-forbidden dark excitons (figure 5(a)). The spin–orbit interaction removes the spin degeneracy of the CB of TMDCs, leading to different spins for CB electrons. The signs of spin for CB electrons are different for tungsten- and molybdenum-based TMDCs [132]. As a result, spin-forbidden dark excitons can be formed in such systems (figure 5(a)). The energy of the spin-forbidden dark exciton is less than that of the bright exciton in molybdenum-based TMDCs, whereas its energy is lower than that of the bright exciton in tungsten-based TMDCs. These dark states can be brightened by applying strong in-plane magnetic fields, which mix the spin-split bands through the Zeeman effect [133, 134]. The result is the relaxation of the spin-selection rule and the brightening of dark excitons. The PL of dark excitons has been demonstrated in low-temperature magneto-PL experiments. In the presence of a magnetic field, the PL spectra of WS_2 monolayers exhibit a doublet structure due to the splitting of the spin-forbidden states [133]. Moreover, spin-forbidden dark excitons in WSe_2 have been activated on silver surfaces through coupling to surface plasmon modes [135].

The excitons that are formed due to Coulomb interactions between electrons and holes located in different valleys are momentum-forbidden dark excitons. In tungsten-based TMDCs, dark excitons are formed from an electron in the Λ valley and a hole in the K (figure 5(a)) [136]. These excitons can emit PL through phonon-assisted radiative recombination [137]. Another way of achieving PL in these dark excitons could be exciton–molecule coupling [138]. In the presence of high-dipole molecules, the translational symmetry of the TMDCs becomes disturbed, which can enable the $K \rightarrow \Lambda$ transition by supplying the required momentum. Theoretical studies suggest that dark excitons can be created in the monolayer of TMDC ternary alloys ($Mo_{1-x}W_xX_2$) [131, 139].

3.3. Interlayer excitons

The long valley polarization lifetime that is required in valleytronic devices can be achieved by creating interlayer excitons. In vertically stacked 2D heterostructures, even when the electrons and holes are located in different TMDC layers, interlayer excitons are formed due to the strong Coulomb interaction (figure 5(b)) [140–146]. A type-II band alignment can be seen in a certain combination of TMDCs when they are vertically stacked [146–150]. In such vertical heterostructures, interlayer charge transfer occurs because of the staggered band alignment and large band offsets [140, 141, 151]. As a result of

the absence of a depletion region in such p-n junctions, electrons and holes are primarily localized in different layers [152–154]. These excitons are stable at room temperature and do not dissociate, even in the presence of external fields, due to the high binding energies (∼100 meV) [146, 155, 156]. Interlayer excitons have been identified in several TMDC heterostructures through their PL signatures [141–143, 157, 158]. The mechanical stacking of one 2D layer on top of another causes a mismatch in the lattice constants, and a twist between the two layers of a heterostructure leads to a Moiré pattern in real space (figure 5(c)) [159, 160]. The pattern depends on the twist angle between the two layers; therefore, the optical response of the heterostructures can be controlled by tuning the relative orientation of the layers [161–163].

The CBs and VBs of the two layers of a heterostructure are different, which makes interlayer excitons momentum-space indirect. These excitons are also spatially indirect, since their constituent electrons and holes reside in different 2D layers. The result is a much longer interlayer exciton lifetime than those of the intralayer excitons in monolayers [141, 142]. The interlayer exciton lifetime in WSe_2-$MoSe_2$ heterostructures is an order of magnitude longer than that of intralayer excitons [141, 142]. A valley lifetime of 40 nanoseconds has been achieved by creating interlayer exciton spin-valley polarization using circularly polarized light in WSe_2-$MoSe_2$ heterostructures [164]. The lifetime of interlayer excitons can be increased further by making a strongly confining trap array using a WSe_2/WS_2 heterostructure on a patterned substrate [165]. Interlayer excitons can be generated and controlled by applying an electric field. One of the most prominent examples of this is the optical and electrical generation of long-lived neutral and charged interlayer excitons in h-BN–encapsulated vdW heterostructures of $MoSe_2$ and WSe_2 [157, 166].

Two kinds of interlayer exciton (direct and indirect) have been observed in vdW heterostructures [158]. These excitons exhibit PL lifetimes of several tens of nanoseconds. In heterostructures of monolayers of $MoSe_2$ and WSe_2, the low-energy interlayer exciton is indirect both in real and reciprocal space. In contrast, the high-energy interlayer exciton is only indirect in real space [158]. The interlayer dark excitons in 2D heterostructures can survive for a very long time (∼microsecond) [167]. Such long-lived excitons are produced by magnetic-field-suppressed valley mixing and hence can be controlled by the magnetic field.

3.4. Bound excitons

Bound excitons are formed in 2D TMDCs when electrons and holes are trapped in defects that are formed due to impurities and/or strain in samples. Such defects can affect the momentum-space valley properties by localizing excitons in real space, and hence valley polarization can be controlled by manipulating defects in 2D vdW materials. PL produced by bound excitons is observed at low temperatures [168]. These emission lines are spectrally narrow and are observed below the broad PL peak corresponding to the bright excitons [169–171]. In fact, the strong single-photon emission from TMDC monolayers appears due to the existence of bound excitons [172, 173]. The narrow emission lines emitted from both CVD-grown and exfoliated samples exhibit a fine-structure doublet [169, 170, 173]. In the absence of a magnetic field, the doublet is cross-linearly polarized [170].

A large Zeeman split (much more extensive than that of intrinsic excitons) is observed in WSe_2 in the presence of a transverse magnetic field (applied in the Faraday geometry) [170]. The increase of the spectral splitting of the doublet with the strength of the applied magnetic field suggests a shift of the selection rule from linearly polarized to circularly polarized [169, 173, 174]. Under a high magnetic field (>5 T), the selection rule becomes similar to that for the recombination of excitons in a regular WSe_2 lattice. In the absence of a magnetic field, the mixing of circularly polarized transitions occurs at the two valleys (K and K'), which results in two linearly polarized transitions with an energy split. The linearly polarized doublet basically originates as a result of the asymmetry of the confining potential [170]. Due to the dominance of Zeeman splitting over the exchange energy, circularly polarized selection rules become relevant for strong magnetic fields. This means that bound exciton states are probably superpositions of intrinsic valley exciton states, and hence single localized valley excitons can be exploited as a basis for valleytronics. Although bound excitons exhibit a long lifetime (∼ns) [170, 172, 173] and can be controlled by magnetic [170, 173] and optical [170, 175] fields, it may be a real challenge to manipulate valley properties by tuning defects.

3.5. Trions

Charged excitons (trions), which are three-body bound states of electrons and holes, could potentially function as carriers in valleytronics [176–178] due to their much longer valley lifetime than that of excitons [176, 178], robust valley polarization, and coupling to the additional charge [179]. There are two types of trion: bright and dark [180]. Bright trions can have an intravalley singlet state in which carriers are located within one valley, and an intervalley triplet state with an exciton is located in one valley, and a charge carrier (electron/hole) is located in another valley. The fine structure of trions appears due to the exchange interaction, which splits the energy levels of singlet and triplet trions [181]. The energy of the singlet trion state is lower than that of the triplet state [119, 182–184]. In doped semiconductors, after the recombination of the electrons and holes of negatively charged trions, the background electron gas becomes spin-polarized [185–187]. In TMDCs, the residual charge can exhibit a definitive valley index and spin orientation, and, therefore, trions can be exploited to manipulate the VDF [188, 189]. The spin and valley lifetimes of trions are generally long because the intervalley scattering of the extra charge present in trions requires the simultaneous transfer of large momentum and a spin flip. Trions in 2D TMDCs exhibit a relaxation time of tens of picoseconds, which is much longer than the ultrafast exciton relaxation time [128, 190, 191]. The chemical doping of monolayer MoS_2 leads to a large increase of the trion nonradiative lifetime [192]. A recent study demonstrated that chemical doping causes the conversion of excitons into trions in WS_2 monolayers, where the emission becomes

dominated by trions with a strong valley polarization [193]. As a result of chemical doping, exciton emission is strongly quenched but highly valley polarized.

The excitation caused by a linearly polarized light creates a coherent superposition state of two trion valley configurations [194]. In the first trion configuration a σ^+ photon and a spin-down electron are present, whereas the second configuration consists of a σ^- photon and a spin-up electron. The superposition of these trion states leads to a spin-photon entangled state, $|\sigma^+ \mid \downarrow\rangle + |\sigma^- \mid \uparrow\rangle$. Trion valley polarization cannot be detected through linearly polarized emission due to the orthogonal spin states. Trion valley coherence has been resonantly generated and detected in monolayer $MoSe_2$ using 2D coherent spectroscopy (three-pulse four-wave mixing technique) [194, 195]. When an in-plane electric field is applied, an anomalous transverse motion is induced, which gives rise to the trion Hall effect [117, 196]. The intense polarization of the trion complexes in a WS_2 monolayer encapsulated in hBN under an applied magnetic field suggests that magnetic fields could be used to control trion valley polarization [197]. Valley polarization in 2D TMDCs can be manipulated by modulating the electron–hole exchange interaction experienced by the exciton and trion by applying an electric field [198].

4. Some ways to detect the valley polarisation

4.1. Polarization-resolved PL

The valley properties of 2D materials can be investigated by monitoring the contrast between valley pseudospins in the K and K' valleys. Because the two valleys absorb left and right circularly polarized light differently, the basic mechanism generally used in this context is circularly polarized optical excitation [31, 33]. The valley polarization of materials that exhibit PL can be measured via the circular dichroism of their PL [199]. When this approach is used, polarization-sensitive PL measurements are carried out following the selective excitation of electrons in one of the valleys by circularly polarized light. The main aim here is to assess the k-resolved degree of optical polarization or the degree of circular polarization, which can be defined as

$$\rho = \frac{I(\sigma^+) - I(\sigma^-)}{I(\sigma^+) + I(\sigma^-)} \tag{24}$$

where $I(\sigma^+)$ and $I(\sigma^-)$ are the PL intensities of the right- and left-handed circular components, respectively. The intensities of the PL for the σ^+ (left-handed) and σ^- (right-handed) polarizations of monolayer MoS_2 at a low temperature (83 K) are very different (figure 6(a)). Upon excitation by a σ^+ light at 1.96 eV, monolayer MoS_2 exhibits a circular polarization of ∼50% [41]. However, the reported experimental values of polarization are inconsistent [39–41, 200]. The value of ρ varies from 100% to 32% [39, 40, 200]. The helicity parameter (ρ) is intimately linked to the A-exciton PL energy. It is found to be 100% for PL energies in the range 1.90–1.95 eV and decreases to 5% for PL energies below 1.8 eV (figure 6(b)) [40]. Nonetheless, the degree of circular polarization of MoS_2 decreases as a function of the photo-excitation energy and possesses a very high value for resonant excitation near the bandgap. In fact, it decreases following a power law as the excitation energy increases (figure 6(c)) [201]. Kioseoglou *et al* [201] proposed a phonon-assisted intervalley scattering-based model to explain the variation in the reported values of the degree of circular polarization for MoS_2.

The valley polarization of monolayer WS_2 has been explored through polarization-dependent PL [87, 97]. Under near-resonance conditions, the monolayer exhibits a degree of circular polarization of 40% at 10 K (figure 6(d)) [87]. The degree of circular polarization is insensitive to PL energy, but decays with increasing temperature and drops to 10% at room temperature. However, it decreases as the excitation energy changes from near-resonance to off-resonance. Interestingly, robust PL circular dichroism was observed for bilayer WS_2 under both resonance and off-resonance excitations [87]. The degree of circular polarization of bilayer WS_2 under near-resonant excitation is 95% at 10 K and decreases to 60% at room temperature. The robustness of the valley polarization in bilayer WS_2 is the result of the coupling of spin, layer, and valley degrees of freedom. According to Nayak *et al* [97], the effects of shorter exciton lifetime, smaller exciton-binding energy, extra spin-conserving channels, local spin polarization, and selective valley excitation can also contribute to the robustness of circular polarization in bilayers. Moreover, high valley polarization in other monolayer TMDCs has been detected through PL measurements [85, 202].

4.2. Valley Hall effect

As discussed in the previous sections, there could be a valley-dependent Berry phase effect that leads to a valley contrasting Hall transport. The charge carriers in the K and K' valleys turn in opposite directions perpendicular to an in-plane electric field, giving rise to the valley Hall Effect. This effect can be used to identify the valley polarization in 2D materials [36]. In the case of net valley polarization, a transverse Hall current can be generated upon the application of an in-plane electric field in a valley filter device [22]. This Hall current causes a measurable transverse voltage, which can give a local mapping of the valley polarization of the sample (figure 7(a)) [31]. The valley Hall effect (VHE) can create an electrical response in remote regions, which can be exploited to experimentally identify the presence of Hall currents [90].

Graphene has Berry curvature due to the presence of a nonzero Berry phase [203]. When the crystallographic axes of graphene and hBN are aligned, the inversion symmetry is broken, and a finite Berry curvature is developed [92, 204]. The Hall current in such a system has been detected through non-local measurements (figure 7(b)). The origin of the non-local signal in a graphene/hBN device can be considered to be a combination of the VHE and a reverse VHE. A current applied (J) between any two contacts (figure 7(b)) induces a valley current J_v in the direction perpendicular to J. The valley current creates an imbalance in valley populations, $\delta_\mu = \mu_K - \mu_{K'}$ between two distant contacts ($\mu_{K,K'}$ are the chemical potentials in the valleys K and K'). As a result, a voltage

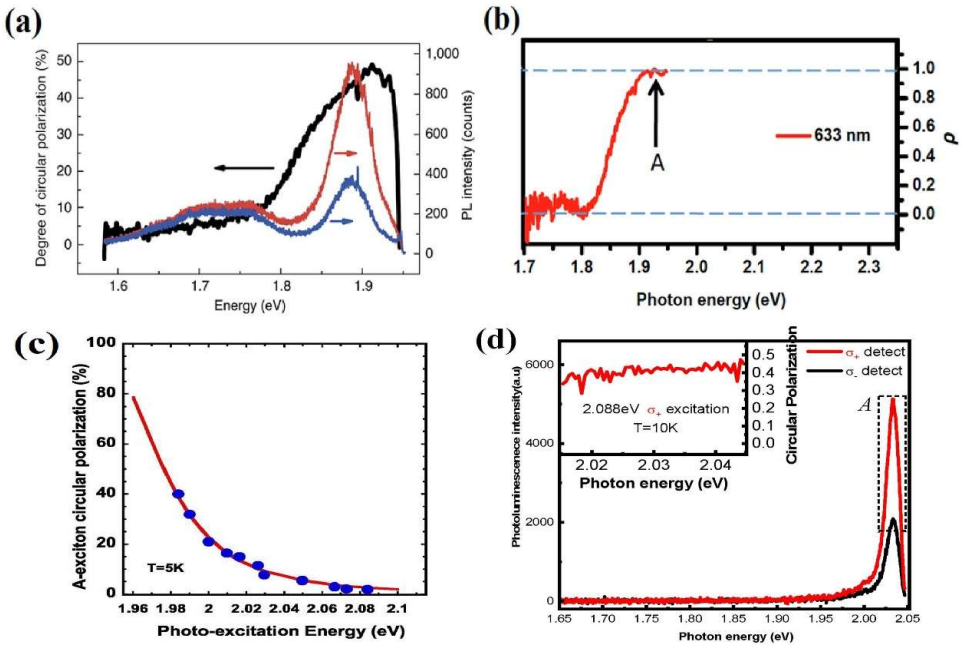

Figure 6. (a) Circularly polarized PL spectra with $\sigma+$ (left-handed) (red) and $\sigma-$ (right-handed) (blue) polarizations of monolayer MoS_2 at 83 K along with the degree of circular polarisation (black). Reprinted by permission from Springer Nature Customer Service Centre GmbH: [Springer Nature] [Nature Communications] [41], copyright (2012). (b) The helicity parameter (ρ) corresponding to the A-excitons of monolayer MoS_2 at an excitation photon energy of 1.96 eV. Reprinted by permission from Springer Nature Customer Service Centre GmbH: [Springer Nature] [Nature Nanotechnology] [40], copyright (2012). (c) Degree of circular polarization of A-excitons of a single layer of MoS_2 as a function of the photo-excitation energy. The solid line is the fit with a power law. Reprinted from [201], with the permission of AIP Publishing. (d) Polarization resolved PL spectra with σ^+ (red) and σ^- (black) detection under near-resonant σ^+ excitation (2.088 eV). The degree of circular polarization at the PL peak is presented in the inset. Reproduced with permission from [87].

(E) response is generated due to the reverse VHE. In this scenario,

$$J_v = \sigma^v_{xy} E,\ E = \frac{\sigma^v_{xy}\rho_{xx}}{2e}\nabla\delta\mu, \tag{25}$$

where σ^v_{xy} is the valley Hall conductivity and ρ_{xy} is the longitudinal resistivity. The charge-neutral valley current can persist over extended distances in the absence of intervalley scattering and generate non-local electrical signals [205–208]. The VHE-induced non-local resistance (R_{NL}) can be expressed in terms of the relation [90],

$$R_{NL} = (\omega/2\xi)(\sigma^v_{xy})^2\rho^3_{xx}\exp(-L/\xi), \tag{26}$$

where L is the distance between the current path and the voltage probes, ω is the device width, and ξ is a constant. Sui *et al* described a method for artifact-free measurement of R_{NL} [36].

A non-zero value of R_{NL} is observed if there is valley polarization. Graphene/hBN aligned devices exhibit prominent sharp peaks of R_{NL} at the main and hole-side nonlocal points. However, no non-local signal has been detected in (graphene/hBN) nonaligned devices from which valley polarization is absent (figure 7(c)) or in gapless bilayer graphene (BLG) in which inversion symmetry is present (figure 7(d)). Under a transverse electric field, BLG exhibits a giant nonlocal response due to the topological transport of valley pseudospin (figures 3(d)–(g)) [36]. In BLG, the intrinsic inversion symmetry is broken by the perpendicular electric field, which results in valley polarization [76, 96, 101].

The valley polarization in TMDCs can be monitored by measuring the photoinduced anomalous Hall effect (AHE) [76]. A Hall bar device of TMDC with a long Hall probe and a short conduction channel (figure 8(a)) is used to measure the Hall effect. The reasons for this device structure are (i) to produce a photocurrent near the centre of the device, so that the Hall probe can efficiently pick up any Hall voltage and (ii) to reduce the background photovoltage generated at the metal–semiconductor contacts of the Hall probe. Circularly polarized light is shone on the Hall bar device to produce valley polarization in TMDCs through the breaking of time-reversal symmetry (figure 8(a)). The Hall voltage is measured between the A and B contacts of the Hall probe (figure 8(a)) by applying a source–drain voltage (V_x) across the short channel. A positive Hall voltage is observed for a monolayer MoS_2 device for a positive bias when the polarization of the incident light is modulated from right- to left (R-L)-handed (figure 8(b)) [76]. The sign of the Hall voltage is reversed in the case of left- to right (L-R)-handed modulation of the polarization of the incident light. However, no Hall voltage is developed for linear (s-p) polarization. The photoinduced AHE in monolayer MoS_2 bears the signature of net valley

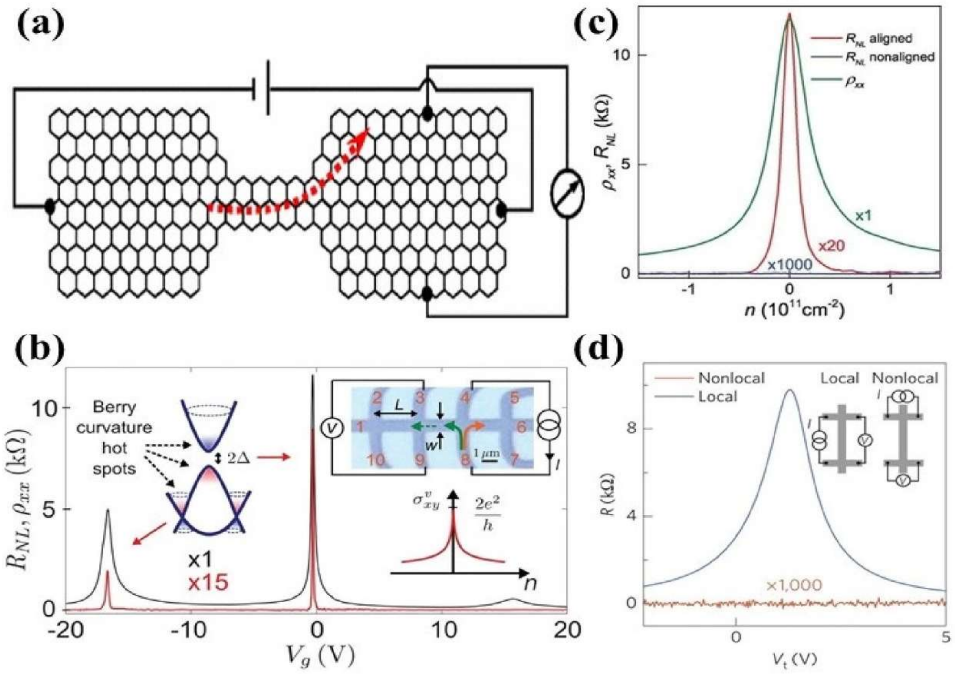

Figure 7. (a) A transverse voltage across a sample due to valley polarization created by the valley filter. Reprinted (figure) with permission from [31], copyright (2007) by the American Physical Society. (b) Non-local resistance in graphene superlattices (red curve) and longitudinal resistance (black curve) measured in graphene/hBN superlattices. Top right inset: Optical micrograph of the graphene/hBN device used for the non-local measurement. Left inset: illustration of the band structure of graphene superlattices, showing Berry curvature hot spots. Bottom right inset: modelled valley Hall conductivity for gapped Dirac fermions as a function of carrier density. (c) Longitudinal resistivity (ρ_{xx}) and R_{NL} near the main non-local point in superlattice devices (green and red). R_{NL} is zero for nonaligned devices (blue). (b), (c) From [90]. Reprinted with permission from American Association for the Advancement of Science (AAAS). (d) Variation of local (blue) and non-local (red) resistance with gate voltage in a bilayer graphene (BLG) sample. Inset: Schematic representation of local and non-local measurement setup. Reprinted by permission from Springer Nature Customer Service Centre GmbH: [Springer Nature] [Nature Physics] [36], copyright (2015).

polarization under polarized light. On the contrary, the AHE is completely absent from bilayer MoS_2 (figure 8(b)) suggesting an absence of valley polarization in bilayers due to the unbroken inversion symmetry [76]. Wavelength-dependent mapping of the VHE in a transistor (made out of TMDCs) suggests that the VHE in TMDCs arises upon illumination by light that has an energy equal to the energy of excitons or trions (figure 8(c)) [209]. The VHE in TMDCs is directly generated by trions. However, excitons break down at the interface between a metal and a semiconductor, generating free electrons and holes that result in a VHE. An intrinsic VHE has been observed without any extrinsic symmetry breaking in both monolayer and trilayer MoS_2, even at room temperature [210]. A very similar non-local signal due to VHE suggests that the valence band carriers mainly contribute to the VHE in monolayer and trilayer MoS_2. The VDF has even been identified in multilayer WSe_2 by probing the valley Hall effect [211]. A current is generated in the presence of a drain–source voltage as a consequence of photoinduced VHE (figure 8(d)). Valley polarization in multilayer WSe_2 is induced by breaking the spatial-inversion symmetry, which is achieved by applying a transverse electric field through an ionic liquid gate.

4.3. Valley Zeeman effect

Investigation of the resonance of excitons and other pseudostates in the presence of an external magnetic field is an excellent way to study the immeasurable properties of semiconductor materials. In recent years, several experiments have been developed using TMDCs in the magneto-optical domain [121, 122, 155, 212, 213]. One such experiment investigated the valley Zeeman effect, which is used to identify valley polarization in TMDCs. In the conventional Zeeman effect, a spin-dependent energy shift of the electronic energy levels takes place in the presence of an external magnetic field, thereby increasing the degeneracy. Similarly, the valley pseudospin of electrons in TMDCs can interact with an external magnetic field, producing the valley Zeeman effect. Valley Zeeman splitting and magnetic tuning of polarization have been observed using polarization-resolved magneto reflectance and magneto-PL measurements [213, 214].

Helicity-resolved PL in an external magnetic field has been observed in the perpendicular plane of a mechanically exfoliated TMDC layer [213]. To resolve the splitting between two valley excitons, the sample was both excited and detected with the same polarized light. The splitting can be determined by

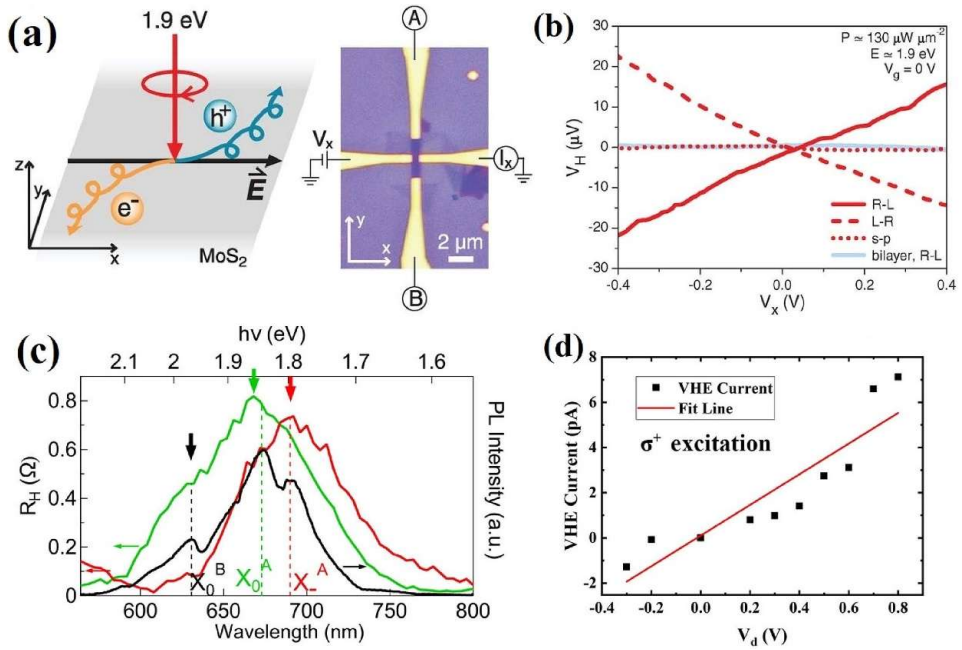

Figure 8. (a) Schematics of a Hall bar device (right) and a representation of the anomalous Hall effect induced by valley polarisation (left). (b) Dependence of the Hall voltage on the source–drain bias (V_x) of a monolayer device under R-L (red solid line), L-R (red dashed line), and *s-p* (red dot line) modulation, and a bilayer device under R-L modulation (blue solid line). (a), (b) From [76]. Reprinted with permission from the AAAS. (c) Spectral dependence of the Hall resistance in a bilayer 3R-MoS_2 device. Reprinted with permission from [209]. Copyright (2017) American Chemical Society. (d) Valley Hall current varies linearly with drain voltage V_d in multilayer WSe_2. Reprinted with permission from [211]. Copyright (2019) American Chemical Society.

addressing one valley at a time and comparing the peak positions of the PL for different polarizations. Representative PL spectra corresponding to different values of the magnetic field, B, are shown in figure 9(a). In the case of a zero magnetic field, the PL peaks associated with both valleys, i.e. K^+ (blue, σ^+) and K^- (red, σ^-) are identical (middle). On the other hand, under a high magnetic field (+7 T, top), both components' spectra are split, and σ^+ has a slightly lower energy than σ^-. In contrast, under a low magnetic field (−7 T, bottom), the σ^+ spectral component is shifted to a higher energy than that of the σ^- component (figure 9(c)). The observed splitting is a consequence of the *d*-orbital magnetic moment of tungsten and the valley magnetic moment, which is the lattice contribution to the Berry curvature [25]. Figure 9(b) shows the Zeeman splitting of the bands due to each of these two contributions. The conduction and valence bands under a zero (positive) magnetic field are denoted by dashed (solid) lines. Due to the spin splitting of ∼0.4 eV in the valence band, the K^+ (K^-) valley has only the spin-up (down) state. For the CB, the splitting is small, with opposite signs in the two valleys [215, 216]. The total Zeeman splitting of each band is determined by the sum of these three magnetic moment contributions. The Zeeman shift arising due to the spin magnetic moment in the CB is $\Delta_s = 2s_z\mu_B B$ where μ_B is the Bohr magneton (black arrow), whereas the atomic contribution in the valence band is $\Delta_\alpha = 2\tau_z\mu_B B$ (purple arrow), which contributes no shift in CB. The Zeeman shift that arises due to the valley magnetic moment is given by $\Delta_v = 2\alpha_i\tau_z\mu_B B$ (green arrow), where α_i is the valley g-factor.

Polarization-resolved magneto-PL and magneto-reflectance contrast measurements for the MLs of semiconducting $MoTe_2$ in magnetic fields of up to 29 T were carried out by Arora *et al* [214]. The σ^+ (orange) and σ^-(blue) components of the micro-reflectance contrast (μRC) spectra were measured for monolayer $MoTe_2$ exfoliated on Si/SiO_2 (figure 10(a)) and sapphire substrates (figure 10(b)) under different applied magnetic fields. The μRC spectrum can be obtained from the relation [214]

$$C(\lambda) = [R(\lambda) - R_0(\lambda)]/[R(\lambda) + R_0(\lambda)], \qquad (27)$$

where $R(\lambda)$ and $R_0(\lambda)$ are the wavelength-dependent reflectance spectra of the TMDC layer and the bare substrate, respectively. Zeeman splitting is clearly visible in the $X^0{}_A$ resonance, but the line shape of the resonance remains unchanged with the variation of the magnetic field. The value of Zeeman splitting for the *A* and *B* excitons can be used to find the g-factors. For ML $MoTe_2$ on a sapphire substrate, the value of g is -4.7 ± 0.4 and -3.8 ± 0.6 for the *A* and *B* excitons, respectively. Polarization-resolved micro-PL spectra for monolayer $MoTe_2$ at various applied magnetic fields can be seen in figure 10(c). Zeeman splitting is clearly visible in the $X^{\pm}$ and X_A^0 transitions. The transition energies for both

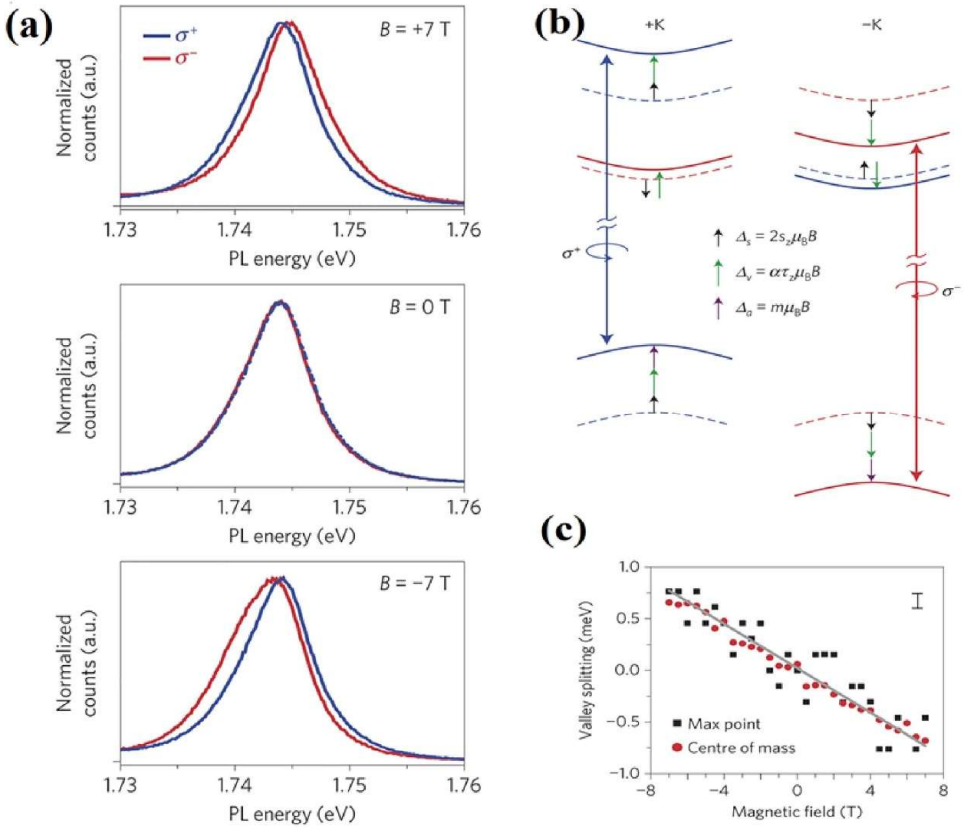

Figure 9. (a) Helicity-resolved photoluminescent spectra of WSe_2 under different magnetic fields. (b) Energy level diagram for the three contributions to valley Zeeman splitting, i.e. magnetic (black), atomic (purple), and valley (green) magnetic contributions. (c) Valley Zeeman splitting as a function of the magnetic field. (a)–(c) Reprinted by permission from Springer Nature Customer Service Centre GmbH: [Springer Nature] [Nature Physics] [213], copyright (2015).

the σ^+ and σ^-polarizations vary as a function of the magnetic field (figure 10(c)). Zeeman splitting decreases with an increase in the magnetic field (figure 10(e)). The average value of the g-factor estimated from PL measurements for neutral excitons (A and B) are $g_{X_A^0} = -4.7 \pm 0.4$ and $g_{X_B^0} = -3.8 \pm 0.6$ for ML on sapphire substrate [214]. Valley polarization is induced in TMDCs under an external magnetic field. Although the degree of circular polarization is zero in the absence of a magnetic field, it increases to 78% and 36% for neutral and charged excitons, respectively, under a magnetic field of 29 T (figure 10(f)). Many groups have demonstrated valley polarization in TMDCs through the valley Zeeman effect [214, 217–219].

5. Achieving and controlling the valley degree of freedom in optoelectronic devices

The main challenge in developing valleytronic devices is to achieve the ability to generate and manipulate permanent valley polarization. In TMDCs, optical excitonic transitions are dependent not only on the spin DOF, but they are also associated with the valley DOF [67]. Therefore, it is possible to interconvert valley polarization with the optical polarization of emitted and absorbed photons in 2D TMDCs. This means that valley polarization can be carried from one system to another by photons. Such valleytronics devices can be realized by developing a valley-polarized optoelectronic emitter and absorber (a valley optical interconnect).

In a recent report, Zhang *et al* demonstrated electrically switchable multilayer and monolayer WSe_2 p-n junctions, which emitted circularly polarized electroluminescence (EL) based on the VDF of the material [220]. They formed the junction using electrical double-layer (EDL) gating with multilayer WSe_2. EDL gating provides a very large gate field due to accumulation of carriers inside the 2D channel. There are two major difficulties with multilayer TMDCs: first, they have an indirect bandgap, which is undesirable for optoelectronic device applications, and second, restored inversion symmetry decreases the circular polarization. EDL gating overcomes these difficulties, as the large gate field produces higher carrier densities in the direct gap K and K' valleys and breaks

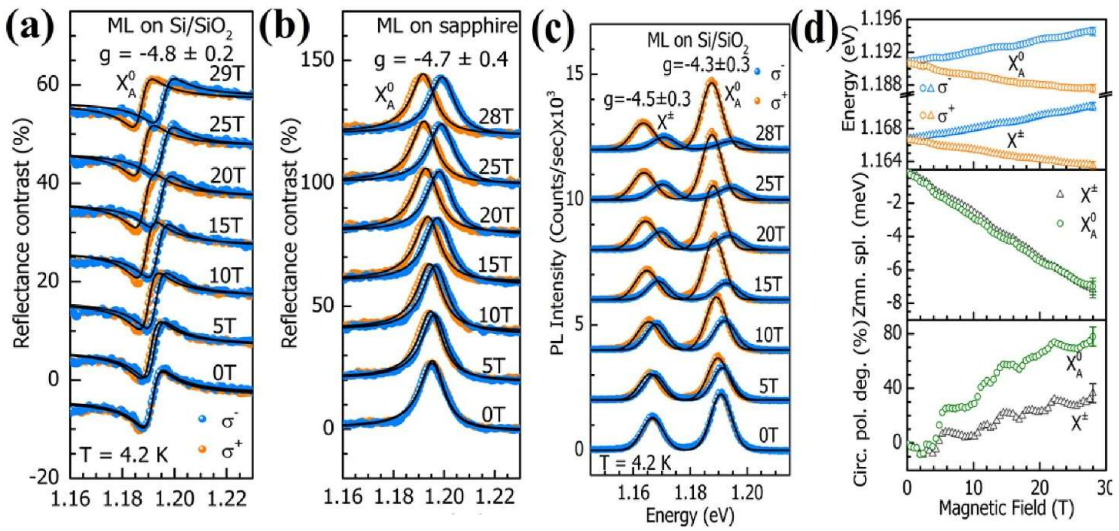

Figure 10. (a) Polarization-resolved micro-reflectance contrast spectra of mechanically exfoliated monolayer $MoTe_2$ on Si/SiO_2 and (b) sapphire substrates. (c) Helicity-resolved micro-PL spectra of neutral and charged excitons in monolayer $MoTe_2$ on Si/SiO_2 as a function of the magnetic field (solid black lines are the fitted curves). (d) Zeeman split transition energies, valley Zeeman splitting, and degree of circular polarization as a function of the magnetic field. (a)–(c) Reprinted with permission from [214]. Copyright (2016) American Chemical Society.

inversion symmetry. Hence, the multilayer EDL transistor operates in a similar way to the monolayer TMDC transistor [221]. The EL spectra of the EDL transistor are circularly polarized and the EL intensity increases with increasing gate voltage (figure 11(a)). The degree of polarization of the EL is comparable with that of the PL in monolayer TMDCs [39, 85]. The EL polarization is affected by changes in the bias of the source and drain, i.e. when the device is operated in p–n mode (current flows from right to left), the left circularly polarized emission dominates. In contrast, it decreases in n–p mode (figure 11(a)). This behaviour can be understood in the light of the variation of the electron–hole overlap distribution in the K and K' valleys as the bias is reversed (figure 11(b)).

Jae Dong Lee's research team discovered the formation of the valley magnetic domain (VMD) in TMDCs (MoS_2) [222]. As a result of the VMD, TMDCs can be used as semiconducting devices that differ from existing devices that only allow current to flow in one direction under the influence of an external voltage. Control of the electric current can be achieved through VMD manipulation. Reversal of the electric field direction leads to VMD switching, which can be exploited in monolayer TMDCs to realize transverse diodes. Single-bit dynamic random-access memory (DRAM) has been demonstrated using two transverse diodes (two strained MoS_2 ribbons) (figure 11(c)) [222]. In the write process, a far-infrared wave (FIR) falls on the 'WRITE' channel (the MoS_2 ribbon on the left), producing a transverse current that charges the capacitor, recording a 'one' bit (figure 11(c) left). FIR light is applied to the 'READ' channel (the MoS_2 ribbon on the right), producing a transverse current flow out of the capacitor to discharge the capacitor during the read process (figure 11(c), right). In this type of memory device, read and write processes can be performed with THz speed.

Chiral valley Hall states have been generated in between layers of oppositely gated 2D graphene [224, 225]. Such states are called kink states, and enable several *in situ* transmission control mechanisms. The kink states of BG can be exploited for applications in waveguides, valves, and electron beam splitters.

Optical manipulation of valley behaviours has been successfully achieved at cryogenic temperatures. Phonon-assisted intervalley scattering increases at high temperatures, resulting in volatile valley states, which reduce the handedness of PL at room temperature. Valley-optical cavity hybrid systems can be used to maintain the handedness of PL at room temperature [226]. However, control of valley properties at room temperature is still limited due to imperfect spatial and spectral overlap between excitons and optical cavities. Recently, near-unity spin polarization has been realized in 2D vdW heterostructures by reducing their carrier lifetimes [227]. Li *et al* demonstrated room-temperature valleytronic building blocks that play a role similar to that of transistors in electronics [228]. They generated long-lived valley-polarized carriers in MoS_2 under linearly polarized infrared excitation using chiral nanocrescent plasmonic antennae. The field enhancement and near-field coupling properties of surface plasmon resonance have been widely exploited to modulate the valley polarization of TMDCs. A recent review discussed the mechanisms of plasmonic modulation of valleytronic emission in TMDCs using surface plasmon polaritons and localized surface plasmons (LSPs) [229]. Wu *et al* reported a delicate way to manipulate quantum-information carriers—i.e. pairs of positive and negative charges confined to momentum valleys at room temperature in a monolayer WSe_2 [223]. The new manipulation strategy is based on the strong light–matter interactions between the valley excitons and a plasmonic chiral

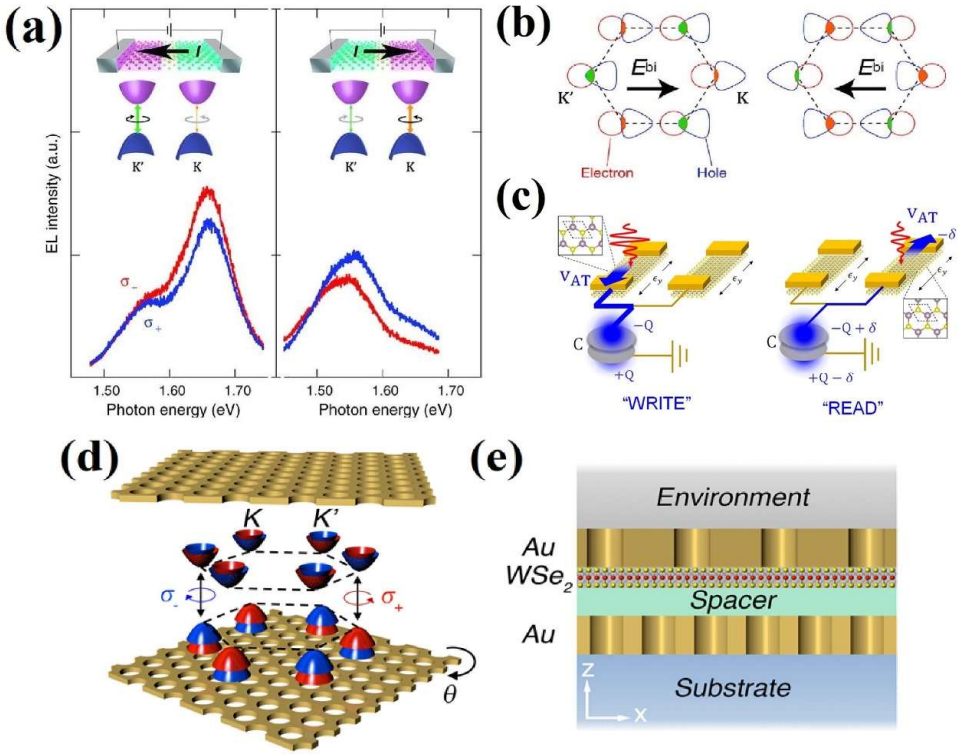

Figure 11. (a) Top: schematic illustration of circularly polarized EL for two opposite current directions. Bottom: contributions made to the EL by the K and K' valleys. (b) Schematic representation of electron–hole distribution and overlap (orange and green denote the K and K' valleys, respectively). (a), (b) From [220]. Reprinted with permission from the AAAS. (c) Schematics of READ and WRITE operations in a single-bit dynamic random-access memory (DRAM). Reprinted with permission from [222]. Copyright (2019) American Chemical Society. (d) Schematic of the WSe_2-MCM hybrid system. The monolayer WSe_2 is represented in reciprocal space, illustrating the band structure and the optical selection rule. (e) Cross-sectional schematic showing the design of the WSe_2-MCM hybrid system. (d), (e) [223] John Wiley & Sons. [Copyright © 2019 WILEY-VCH Verlag GmbH & Co. KGaA, Weinheim].

metamaterial consisting of two layers of periodic Au nanohole arrays with a controllable interlayer in-plane rotation angle (θ) (figures 11(d) and (e)). Photoinduced nonreciprocity in monolayer WS_2 has been achieved by circularly polarized light, which exploited the valley-selective response of TMDCs [230]. This approach can be used to develop all-optical isolators and circulators integrated into photonic systems. Substitutional doping has also proved to be a useful approach to manipulating and improving valley polarization in 2D materials [231, 232]. The valley polarization of a MoS_2 monolayer has been improved by Re substitution, even at room temperature [231].

6. Manipulation of valley coherence

Like valley polarization, valley coherence is critically important for useful information processing applications. Manipulation of valley coherence forms the basis for controlling a single qubit in valley-based quantum information technology. Manipulation of valley coherence in 2D materials has been demonstrated in a number of previous reports [83, 84, 233, 234]. Using linearly polarized light, a coherent superposition of two states, $1/\sqrt{2}\left(|K\rangle + e^{-i\omega t}|K'\rangle\right)$ can be created at the equator of a Bloch sphere, in which ω is proportional to the energy difference between the K and K' valleys. Valley coherence in the Bloch sphere can be tracked by measuring the linear polarization of the PL as it is parallel to the excitation polarization. If the valley pseudospin is rotated by an angle of θ then the polarization of PL rotates by an angle $\theta/2$. The application of an electric or magnetic field can break the degeneracy between the K and K' states (figures 12(a) and (b)). The induced change in the transition energy of the two valleys due to external fields gives rise to a dynamic phase difference, which can cause rotation of the valley pseudospin in the equatorial plane of the Bloch sphere. Demonstrating the rotation of valley pseudospin and developing techniques to control arbitrary valley states are crucial steps towards the development of valleytronic devices. Wang *et al* reported that the direction of the linear polarization of PL can be rotated by applying an external magnetic field [83]. They reported a change of $27° \pm 4°$ in the phase angle under a magnetic field of 9 T. A very strong magnetic field is required to obtain stable rotation. Nonetheless, valley coherence in 2D materials can be improved by combining the effect of suppression in the exchange interaction due to enhanced dielectric screening and a reduction in the exciton lifetime due to fast interlayer transfer [89].

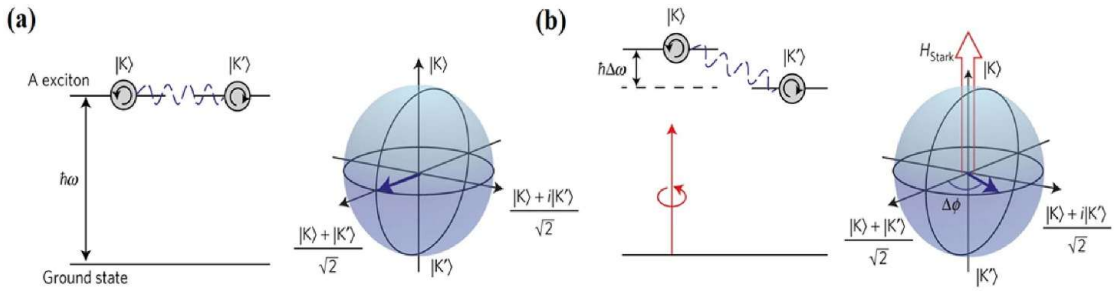

Figure 12. (a) Bloch sphere illustrations of coherent superposition of the K and K' states. (b) Breaking of degeneracy between K and K' by the application of an external control pulse. (a), (b) Reprinted by permission from Springer Nature Customer Service Centre GmbH: [Springer Nature] [Nature Physics] [84], copyright (2017).

7. Summary and future scope

In this review, we have presented a detailed account of the origin of VDF in 2D materials with hexagonal lattices. A significant amount of experimental work has investigated valley polarization by creating charge carriers, excitons, and other quasi-particles in graphene and TMDCs. Unfortunately, these carriers of valley pseudospin are short-lived and rapidly jump between the valleys, which hinders the storage of information for a longer time. Although interlayer and defect-bound excitons have shown promise in realizing long-lived valley-selective excitons, a concerted effort will be required to identify valley carriers with long lifetimes.

Dark excitons and trions could be excellent valley carriers, as they possess long lifetimes and better valley stability than the bright excitons and trions. A dark exciton or trion can decay into a phonon–photon pair with a particular handedness, depending on the direction of the decay process. The handedness of the emitted photon can be used to read the valley indices of the dark states, but research in this direction is still in its early stages.

Despite the rapid progress in the field of generation and modulation of valley polarization and coherence, there remain significant challenges to the practical development of valleytronic devices. One critical challenge is that almost all of the valley-dependent properties discovered to date have been observed at cryogenic temperatures. Further effort will be required to generate stable valley signatures at room temperatures and to develop methods for reading the valley indices for eventual applications of valleytronic technology.

Data availability statement

No new data were created or analysed in this study.

Acknowledgments

A S and S K P acknowledge the financial support of the Science and Engineering Research Board (SERB), Government of India (Grant No. CRG/2018/003045).

Certain images in this publication have been obtained by the author(s) from the Wikipedia/Wikimedia website, where they were made available under a Creative Commons licence or stated to be in the public domain. Please see individual figure captions in this publication for details. To the extent that the law allows, IOP Publishing disclaim any liability that any person may suffer as a result of accessing, using or forwarding the image(s). Any reuse rights should be checked and permission should be sought if necessary from Wikipedia/Wikimedia and/or the copyright owner (as appropriate) before using or forwarding the image(s).

Conflict of interest

The authors declare no conflict of interest.

ORCID iDs

Ashish Soni https://orcid.org/0000-0001-7429-576X
Suman Kalyan Pal https://orcid.org/0000-0003-2498-6217

References

[1] Novoselov K S, Geim A K, Morozov S V, Jiang D, Zhang Y, Dubonos S V, Grigorieva I V and Firsov A A 2004 Electric field effect in atomically thin carbon films *Science* **306** 666
[2] Lee C, Wei X, Kysar J W and Hone J 2008 Measurement of the elastic properties and intrinsic strength of monolayer graphene *Science* **321** 385
[3] Du X, Skachko I, Duerr F, Luican A and Andrei E Y 2009 Fractional quantum Hall effect and insulating phase of Dirac electrons in graphene *Nature* **462** 192–5
[4] Novoselov K S, Geim A K, Morozov S V, Jiang D, Katsnelson M I, Grigorieva I V, Dubonos S V and Firsov A A 2005 Two-dimensional gas of massless Dirac fermions in graphene *Nature* **438** 197–200
[5] Pal S K 2015 Versatile photoluminescence from graphene and its derivatives *Carbon* **88** 86–112
[6] Lu J-D and Chen X-S 2021 Strain-controlled valley polarization in a graphene under the modulation of a realistic magnetic field *J. Supercond. Nov. Magn.* **34** 2545–50

[7] Avetisyan A A, Partoens B and Peeters F M 2010 Stacking order dependent electric field tuning of the band gap in graphene multilayers *Phys. Rev.* B **81** 115432

[8] Kumar P, Herath T M and Apalkov V 2021 Ultrafast valley polarization in bilayer graphene *J. Appl. Phys.* **130** 164301

[9] Paradisanos I *et al* 2020 Prominent room temperature valley polarization in WS_2/graphene heterostructures grown by chemical vapor deposition *Appl. Phys. Lett.* **116** 203102

[10] Friedlan A and Dignam M M 2021 Valley polarization in biased bilayer graphene using circularly polarized light *Phys. Rev.* B **103** 075414

[11] Manzeli S, Ovchinnikov D, Pasquier D, Yazyev O V and Kis A 2017 2D transition metal dichalcogenides *Nat. Rev. Mater.* **2** 17033

[12] Wang H and Qian X 2017 Two-dimensional multiferroics in monolayer group IV monochalcogenides *2D Mater.* **4** 015042

[13] Liu L, Park J, Siegel D A, McCarty K F, Clark K W, Deng W, Basile L, Idrobo J C, Li A-P and Gu G 2014 Heteroepitaxial growth of two-dimensional hexagonal boron nitride templated by graphene edges *Science* **343** 163

[14] Asahina H and Morita A 1984 Band structure and optical properties of black phosphorus *J. Phys. C: Solid State Phys.* **17** 1839–52

[15] Wei K, Liu Y, Yang H, Cheng X and Jiang T 2016 Large range modification of exciton species in monolayer WS_2 *Appl. Opt.* **55** 6251–5

[16] Khan K, Tareen A K, Aslam M, Zhang Y, Wang R, Ouyang Z, Gou Z and Zhang H 2019 Recent advances in two-dimensional materials and their nanocomposites in sustainable energy conversion applications *Nanoscale* **11** 21622–78

[17] Wang Q, Rogers E T F, Gholipour B, Wang C-M, Yuan G, Teng J and Zheludev N I 2016 Optically reconfigurable metasurfaces and photonic devices based on phase change materials *Nat. Photon.* **10** 60–65

[18] Wu Q and Song Y J 2018 The environmental stability of large-size and single-crystalline antimony flakes grown by chemical vapor deposition on SiO_2 substrates *Chem. Commun.* **54** 9671–4

[19] Nourbakhsh A, Yu L, Lin Y, Hempel M, Shiue R-J, Englund D and Palacios T 2019 *Beyond-CMOS Technologies for Next Generation Computer Design* ed R O Topaloglu and H S P Wong (Cham: Springer International Publishing) pp 43–84

[20] Cao W, Kang J, Sarkar D, Liu W and Banerjee K 2015 2D semiconductor FETs—projections and design for Sub-10 nm VLSI *IEEE Trans. Electron Devices* **62** 3459–69

[21] Sarkar D, Xie X, Liu W, Cao W, Kang J, Gong Y, Kraemer S, Ajayan P M and Banerjee K 2015 A subthermionic tunnel field-effect transistor with an atomically thin channel *Nature* **526** 91–95

[22] Rycerz A, Tworzydło J and Beenakker C W J 2007 Valley filter and valley valve in graphene *Nat. Phys.* **3** 172–5

[23] Shkolnikov Y P, De Poortere E P, Tutuc E and Shayegan M 2002 Valley splitting of AlAs two-dimensional electrons in a perpendicular magnetic field *Phys. Rev. Lett.* **89** 226805

[24] Gunawan O, Shkolnikov Y P, Vakili K, Gokmen T, De Poortere E P and Shayegan M 2006 Valley susceptibility of an interacting two-dimensional electron system *Phys. Rev. Lett.* **97** 186404

[25] Xiao D, Liu G-B, Feng W, Xu X and Yao W 2012 Coupled spin and valley physics in monolayers of MoS_2 and other group-VI dichalcogenides *Phys. Rev. Lett.* **108** 196802

[26] Isberg J, Gabrysch M, Hammersberg J, Majdi S, Kovi K K and Twitchen D J 2013 Generation, transport and detection of valley-polarized electrons in diamond *Nat. Mater.* **12** 760–4

[27] Zhu Z, Collaudin A, Fauqué B, Kang W and Behnia K 2012 Field-induced polarization of Dirac valleys in bismuth *Nat. Phys.* **8** 89–94

[28] Hao X, Ruskov R, Xiao M, Tahan C and Jiang H 2014 Electron spin resonance and spin–valley physics in a silicon double quantum dot *Nat. Commun.* **5** 3860

[29] Salfi J, Mol J A, Rahman R, Klimeck G, Simmons M Y, Hollenberg L C L and Rogge S 2014 Spatially resolving valley quantum interference of a donor in silicon *Nat. Mater.* **13** 605–10

[30] Orlita M and Potemski M 2010 Dirac electronic states in graphene systems: optical spectroscopy studies *Semicond. Sci. Technol.* **25** 063001

[31] Xiao D, Yao W and Niu Q 2007 Valley-contrasting physics in graphene: magnetic moment and topological transport *Phys. Rev. Lett.* **99** 236809

[32] Gorbachev R V, Tikhonenko F V, Mayorov A S, Horsell D W and Savchenko A K 2007 Weak localization in bilayer graphene *Phys. Rev. Lett.* **98** 176805

[33] Yao W, Xiao D and Niu Q 2008 Valley-dependent optoelectronics from inversion symmetry breaking *Phys. Rev.* B **77** 235406

[34] Zhang Y, Tan Y-W, Stormer H L and Kim P 2005 Experimental observation of the quantum Hall effect and Berry's phase in graphene *Nature* **438** 201–4

[35] Grote H, Danzmann K, Dooley K L, Schnabel R, Slutsky J and Vahlbruch H 2013 First long-term application of squeezed states of light in a gravitational-wave observatory *Phys. Rev. Lett.* **110** 181101

[36] Sui M *et al* 2015 Gate-tunable topological valley transport in bilayer graphene *Nat. Phys.* **11** 1027–31

[37] Mak K F, Lee C, Hone J, Shan J and Heinz T F 2010 Atomically thin MoS_2: a new direct-gap semiconductor *Phys. Rev. Lett.* **105** 136805

[38] Xu K, Wang Z, Du X, Safdar M, Jiang C and He J 2013 Atomic-layer triangular WSe_2 sheets: synthesis and layer-dependent photoluminescence property *Nanotechnology* **24** 465705

[39] Zeng H, Dai J, Yao W, Xiao D and Cui X 2012 Valley polarization in MoS_2 monolayers by optical pumping *Nat. Nanotechnol.* **7** 490–3

[40] Mak K F, He K, Shan J and Heinz T F 2012 Control of valley polarization in monolayer MoS_2 by optical helicity *Nat. Nanotechnol.* **7** 494–8

[41] Cao T *et al* 2012 Valley-selective circular dichroism of monolayer molybdenum disulphide *Nat. Commun.* **3** 887

[42] Vitale S A, Nezich D, Varghese J O, Kim P, Gedik N, Jarillo-Herrero P, Xiao D and Rothschild M 2018 Valleytronics: opportunities, challenges, and paths forward *Small* **14** 1801483

[43] Feng S *et al* 2019 Engineering valley polarization of monolayer WS_2: a physical doping approach *Small* **15** 1805503

[44] Wu Y-C, Taniguchi T, Watanabe K and Yan J 2021 Enhancement of exciton valley polarization in monolayer MoS_2 induced by scattering *Phys. Rev.* B **104** L121408

[45] Zhao X W, Li Y, Liang R D, Hu G C, Yuan X B and Ren J F 2020 Enhanced valley polarization at valence/conduction band in transition-metal-doped WTe_2 under strain force *Appl. Surf. Sci.* **504** 144367

[46] Bao C and Zhou S 2020 Black phosphorous for pseudospintronics *Nat. Mater.* **19** 263–4

[47] Oliva R, Woźniak T, Dybala F, Tołłoczko A, Kopaczek J, Scharoch P and Kudrawiec R 2020 Valley polarization investigation of GeS under high pressure *Phys. Rev.* B **101** 235205

[48] Gomes L C and Carvalho A 2020 Electronic and optical properties of low-dimensional group-IV monochalcogenides *J. Appl. Phys.* **128** 121101

[49] Contributors W C 2020 "File: Band structure Si schematic.svg" Wikimedia Commons, the free media repository (available at: https://commons.wikimedia.org/w/index.php?title=File:Band_structure_Si_schematic.svg%26oldid=468018240Online) (Accessed 29 January 2022)

[50] Feng W, Yao Y, Zhu W, Zhou J, Yao W and Xiao D 2012 Intrinsic spin Hall effect in monolayers of group-VI dichalcogenides: a first-principles study *Phys. Rev.* B **86** 165108

[51] Fuchs J-N 2013 Dirac fermions in graphene and analogues: magnetic field and topological properties (arXiv: 1306.0380)

[52] Li W-F, Fang C and van Huis M A 2016 Strong spin-orbit splitting and magnetism of point defect states in monolayer WS_2 *Phys. Rev.* B **94** 195425

[53] Plechinger G *et al* 2016 Excitonic valley effects in monolayer WS_2 under high magnetic fields *Nano Lett.* **16** 7899–904

[54] Cong C, Shang J, Wang Y and Yu T 2018 Optical properties of 2D semiconductor WS_2 *Adv. Opt. Mater.* **6** 1700767

[55] Chen S-Y, Zheng C, Fuhrer M S and Yan J 2015 Helicity-resolved Raman scattering of MoS_2, $MoSe_2$, WS_2, and WSe_2 atomic layers *Nano Lett.* **15** 2526–32

[56] Berry M V 1984 Quantal phase factors accompanying adiabatic changes *Proc. R. Soc.* A **392** 45–57

[57] Simon B 1983 Holonomy, the quantum adiabatic theorem, and Berry's phase *Phys. Rev. Lett.* **51** 2167–70

[58] Son D T and Yamamoto N 2012 Berry curvature, triangle anomalies, and the chiral magnetic effect in fermi liquids *Phys. Rev. Lett.* **109** 181602

[59] Xiao D, Chang M-C and Niu Q 2010 Berry phase effects on electronic properties *Rev. Mod. Phys.* **82** 1959–2007

[60] Arnol'd V I 2013 *Mathematical Methods of Classical Mechanics* vol **60** (Berlin: Springer)

[61] Aharonov Y and Bohm D 1959 Significance of electromagnetic potentials in the quantum theory *Phys. Rev.* **115** 485–91

[62] Wang S and Wang J 2015 Spin and valley half-metal state in MoS_2 monolayer *Physica* B **458** 22–26

[63] Zhou J, Shan W-Y, Yao W and Xiao D 2015 Berry phase modification to the energy spectrum of excitons *Phys. Rev. Lett.* **115** 166803

[64] Zhou X, Su Z, Anishkin A, Haynes W J, Friske E M, Loukin S H, Kung C and Saimi Y 2007 Yeast screens show aromatic residues at the end of the sixth helix anchor transient receptor potential channel gate *Proc. Natl Acad. Sci. USA* **104** 15555

[65] Xiao D, Yao Y, Fang Z and Niu Q 2006 Berry-phase effect in anomalous thermoelectric transport *Phys. Rev. Lett.* **97** 026603

[66] Schaibley J R, Yu H, Clark G, Rivera P, Ross J S, Seyler K L, Yao W and Xu X 2016 Valleytronics in 2D materials *Nat. Rev. Mater.* **1** 16055

[67] Xu X, Yao W, Xiao D and Heinz T F 2014 Spin and pseudospins in layered transition metal dichalcogenides *Nat. Phys.* **10** 343–50

[68] Feng W, Liu C-C, Liu G-B, Zhou J-J and Yao Y 2016 First-principles investigations on the Berry phase effect in spin–orbit coupling materials *Comput. Mater. Sci.* **112** 428–47

[69] Tahir M and Schwingenschlögl U 2014 Tunable thermoelectricity in monolayers of MoS_2 and other group-VI dichalcogenides *New J. Phys.* **16** 115003

[70] Chang M-C and Niu Q 1996 Berry phase, hyperorbits, and the Hofstadter spectrum: semiclassical dynamics in magnetic Bloch bands *Phys. Rev.* B **53** 7010–23

[71] Sundaram G and Niu Q 1999 Wave-packet dynamics in slowly perturbed crystals: gradient corrections and Berry-phase effects *Phys. Rev.* B **59** 14915–25

[72] Thouless D J, Kohmoto M, Nightingale M P and den Nijs M 1982 Quantized Hall conductance in a two-dimensional periodic potential *Phys. Rev. Lett.* **49** 405–8

[73] Yao Y, Kleinman L, MacDonald A H, Sinova J, Jungwirth T, Wang D-S, Wang E and Niu Q 2004 First principles calculation of anomalous Hall conductivity in ferromagnetic bcc Fe *Phys. Rev. Lett.* **92** 037204

[74] Cha J J and Cui Y 2012 The surface surfaces *Nat. Nanotechnol.* **7** 85–86

[75] Semenoff G W 1984 Condensed-matter simulation of a three-dimensional anomaly *Phys. Rev. Lett.* **53** 2449–52

[76] Mak K F, McGill K L, Park J and McEuen P L 2014 The valley Hall effect in MoS_2 transistors *Science* **344** 1489–92

[77] Kumar N, He J, He D, Wang Y and Zhao H 2014 Valley and spin dynamics in $MoSe_2$ two-dimensional crystals *Nanoscale* **6** 12690–5

[78] Zhu Z Y, Cheng Y C and Schwingenschlögl U 2011 Giant spin-orbit-induced spin splitting in two-dimensional transition-metal dichalcogenide semiconductors *Phys. Rev.* B **84** 153402

[79] Molina-Sánchez A, Sangalli D, Hummer K, Marini A and Wirtz L 2013 Effect of spin-orbit interaction on the optical spectra of single-layer, double-layer, and bulk MoS_2 *Phys. Rev.* B **88** 045412

[80] Cheiwchanchamnangij T and Lambrecht W R L 2012 Quasiparticle band structure calculation of monolayer, bilayer, and bulk MoS_2 *Phys. Rev.* B **85** 205302

[81] Gong Z, Liu G-B, Yu H, Xiao D, Cui X, Xu X and Yao W 2013 Magnetoelectric effects and valley-controlled spin quantum gates in transition metal dichalcogenide bilayers *Nat. Commun.* **4** 2053

[82] Asakura E, Suzuki M, Karube S, Nitta J, Nagashio K and Kohda M 2019 Detection of both optical polarization and coherence transfers to excitonic valley states in CVD-grown monolayer MoS_2 *Appl. Phys. Express* **12** 063005

[83] Wang G, Marie X, Liu B L, Amand T, Robert C, Cadiz F, Renucci P and Urbaszek B 2016 Control of exciton valley coherence in transition metal dichalcogenide monolayers *Phys. Rev. Lett.* **117** 187401

[84] Ye Z, Sun D and Heinz T F 2017 Optical manipulation of valley pseudospin *Nat. Phys.* **13** 26–29

[85] Jones A M *et al* 2013 Optical generation of excitonic valley coherence in monolayer WSe_2 *Nat. Nanotechnol.* **8** 634–8

[86] Wang G, Glazov M M, Robert C, Amand T, Marie X and Urbaszek B 2015 Double resonant Raman scattering and valley coherence generation in monolayer WSe_2 *Phys. Rev. Lett.* **115** 117401

[87] Zhu B, Zeng H, Dai J, Gong Z and Cui X 2014 Anomalously robust valley polarization and valley coherence in bilayer WS_2 *Proc. Natl Acad. Sci. USA* **111** 11606–11

[88] Du L *et al* 2019 Giant valley coherence at room temperature in 3R WS_2 with broken inversion symmetry *Research* **2019** 6494565

[89] Gupta G, Watanabe K, Taniguchi T and Majumdar K 2021 Observation of perfect valley coherence in monolayer MoS_2 through giant enhancement of exciton coherence time (arXiv:2106.03359)

[90] Gorbachev R V *et al* 2014 Detecting topological currents in graphene superlattices *Science* **346** 448–51

[91] Yankowitz M, Xue J, Cormode D, Sanchez-Yamagishi J D, Watanabe K, Taniguchi T, Jarillo-Herrero P, Jacquod P and LeRoy B J 2012 Emergence of superlattice Dirac points in graphene on hexagonal boron nitride *Nat. Phys.* **8** 382–6

[92] Hunt B *et al* 2013 Massive Dirac fermions and hofstadter butterfly in a van der Waals heterostructure *Science* **340** 1427–30

[93] Shimazaki Y, Yamamoto M, Borzenets I V, Watanabe K, Taniguchi T and Tarucha S 2015 Generation and detection of pure valley current by electrically induced Berry curvature in bilayer graphene *Nat. Phys.* **11** 1032–6

[94] Leutenantsmeyer J C, Ingla-Aynés J, Fabian J and van Wees B J 2018 Observation of spin-valley-coupling-induced large spin-lifetime anisotropy in bilayer graphene *Phys. Rev. Lett.* **121** 127702

[95] Barman P K, Sarma P V, Shaijumon M M and Kini R N 2019 High degree of circular polarization in WS_2 spiral nanostructures induced by broken symmetry *Sci. Rep.* **9** 2784

[96] Lee J, Mak K F and Shan J 2016 Electrical control of the valley Hall effect in bilayer MoS_2 transistors *Nat. Nanotechnol.* **11** 421–5

[97] Nayak P K, Lin F-C, Yeh C-H, Huang J-S and Chiu P-W 2016 Robust room temperature valley polarization in monolayer and bilayer WS_2 *Nanoscale* **8** 6035–42

[98] Hsu W-T, Chen Y-L, Chen C-H, Liu P-S, Hou T-H, Li L-J and Chang W-H 2015 Optically initialized robust valley-polarized holes in monolayer WSe_2 *Nat. Commun.* **6** 8963

[99] Ersfeld M *et al* 2020 Unveiling valley lifetimes of free charge carriers in monolayer WSe_2 *Nano Lett.* **20** 3147–54

[100] McCormick E J, Newburger M J, Luo Y K, McCreary K M, Singh S, Martin I B, Cichewicz E J, Jonker B T and Kawakami R K 2017 Imaging spin dynamics in monolayer WS_2 by time-resolved Kerr rotation microscopy *2D Mater.* **5** 011010

[101] Wu S *et al* 2013 Electrical tuning of valley magnetic moment through symmetry control in bilayer MoS_2 *Nat. Phys.* **9** 149–53

[102] Raja A *et al* 2019 Dielectric disorder in two-dimensional materials *Nat. Nanotechnol.* **14** 832–7

[103] Qiu D Y, da Jornada F H and Louie S G 2013 Optical spectrum of MoS_2: many-body effects and diversity of exciton states *Phys. Rev. Lett.* **111** 216805

[104] Wu F, Qu F and MacDonald A H 2015 Exciton band structure of monolayer MoS_2 *Phys. Rev.* B **91** 075310

[105] Mahan G D 1967 Excitons in degenerate semiconductors *Phys. Rev.* **153** 882–9

[106] Hill H M, Rigosi A F, Roquelet C, Chernikov A, Berkelbach T C, Reichman D R, Hybertsen M S, Brus L E and Heinz T F 2015 Observation of excitonic rydberg states in monolayer MoS_2 and WS_2 by photoluminescence excitation spectroscopy *Nano Lett.* **15** 2992–7

[107] Shi H, Yan R, Bertolazzi S, Brivio J, Gao B, Kis A, Jena D, Xing H G and Huang L 2013 Exciton dynamics in suspended monolayer and few-layer MoS_2 2D crystals *ACS Nano* **7** 1072–80

[108] Zhang J Z and Ma J Z 2019 Two-dimensional excitons in monolayer transition metal dichalcogenides from radial equation and variational calculations *J. Phys.: Condens. Matter* **31** 105702

[109] Pei J *et al* 2015 Exciton and trion dynamics in bilayer MoS_2 *Small* **11** 6384–90

[110] Patton B, Langbein W and Woggon U 2003 Trion, biexciton, and exciton dynamics in single self-assembled CdSe quantum dots *Phys. Rev.* B **68** 125316

[111] Kezerashvili R Y and Tsiklauri S M 2016 Trion and biexciton in monolayer transition metal dichalcogenides *Few-Body Syst.* **58** 18

[112] Li Z *et al* 2018 Revealing the biexciton and trion-exciton complexes in BN encapsulated WSe_2 *Nat. Commun.* **9** 3719

[113] Kaviraj B and Sahoo D 2019 Physics of excitons and their transport in two dimensional transition metal dichalcogenide semiconductors *RSC Adv.* **9** 25439–61

[114] Carvalho A, Ribeiro R M and Castro Neto A H 2013 Band nesting and the optical response of two-dimensional semiconducting transition metal dichalcogenides *Phys. Rev.* B **88** 115205

[115] Kozawa D *et al* 2014 Photocarrier relaxation pathway in two-dimensional semiconducting transition metal dichalcogenides *Nat. Commun.* **5** 4543

[116] Mueller T and Malic E 2018 Exciton physics and device application of two-dimensional transition metal dichalcogenide semiconductors *npj 2D Mater. Appl.* **2** 29

[117] Yu H, Cui X, Xu X and Yao W 2015 Valley excitons in two-dimensional semiconductors *Natl Sci. Rev.* **2** 57–70

[118] Yu H, Liu G-B, Gong P, Xu X and Yao W 2014 Dirac cones and Dirac saddle points of bright excitons in monolayer transition metal dichalcogenides *Nat. Commun.* **5** 3876

[119] Ross J S *et al* 2013 Electrical control of neutral and charged excitons in a monolayer semiconductor *Nat. Commun.* **4** 1474

[120] de Vivo L, Landi S, Panniello M, Baroncelli L, Chierzi S, Mariotti L, Spolidoro M, Pizzorusso T, Maffei L and Ratto G M 2013 Extracellular matrix inhibits structural and functional plasticity of dendritic spines in the adult visual cortex *Nat. Commun.* **4** 1484

[121] Srivastava A, Sidler M, Allain A V, Lembke D S, Kis A and Imamoğlu A 2015 Valley Zeeman effect in elementary optical excitations of monolayer WSe_2 *Nat. Phys.* **11** 141–7

[122] Wang G, Bouet L, Glazov M M, Amand T, Ivchenko E L, Palleau E, Marie X and Urbaszek B 2015 Magneto-optics in transition metal diselenide monolayers *2D Mater.* **2** 034002

[123] Stier A V, McCreary K M, Jonker B T, Kono J and Crooker S A 2016 Exciton diamagnetic shifts and valley Zeeman effects in monolayer WS_2 and MoS_2 to 65 Tesla *Nat. Commun.* **7** 10643

[124] Sie E J, McIver J W, Lee Y-H, Fu L, Kong J and Gedik N 2015 Valley-selective optical Stark effect in monolayer WS_2 *Nat. Mater.* **14** 290–4

[125] Kim J, Hong X, Jin C, Shi S-F, Chang C-Y S, Chiu M-H, Li L-J and Wang F 2014 Ultrafast generation of pseudo-magnetic field for valley excitons in WSe_2 monolayers *Science* **346** 1205–8

[126] Palummo M, Bernardi M and Grossman J C 2015 Exciton radiative lifetimes in two-dimensional transition metal dichalcogenides *Nano Lett.* **15** 2794–800

[127] Mohamed N B, Lim H E, Wang F, Koirala S, Mouri S, Shinokita K, Miyauchi Y and Matsuda K 2017 Long radiative lifetimes of excitons in monolayer transition-metal dichalcogenidesMX_2(M= Mo, W;X= S, Se) *Appl. Phys. Express* **11** 015201

[128] Mai C, Barrette A, Yu Y, Semenov Y G, Kim K W, Cao L and Gundogdu K 2014 Many-body effects in valleytronics: direct measurement of valley lifetimes in single-layer MoS_2 *Nano Lett.* **14** 202–6

[129] Dal Conte S *et al* 2015 Ultrafast valley relaxation dynamics in monolayer MoS_2 probed by nonequilibrium optical techniques *Phys. Rev.* B **92** 235425

[130] Baranowski M, Surrente A, Maude D K, Ballottin M, Mitioglu A A, Christianen P C M, Kung Y C, Dumcenco D, Kis A and Plochocka P 2017 Dark excitons and the elusive valley polarization in transition metal dichalcogenides *2D Mater.* **4** 025016

[131] Bragança H, Riche F, Qu F, Lopez-Richard V and Marques G E 2019 Dark-exciton valley dynamics in transition metal dichalcogenide alloy monolayers *Sci. Rep.* **9** 4575

[132] Kormányos A, Burkard G, Gmitra M, Fabian J, Zólyomi V, Drummond N D and Fal'ko V 2015 k · p theory for two-dimensional transition metal dichalcogenide semiconductors *2D Mater.* **2** 022001

[133] Molas M R, Faugeras C, Slobodeniuk A O, Nogajewski K, Bartos M, Basko D M and Potemski M 2017 Brightening of dark excitons in monolayers of semiconducting transition metal dichalcogenides *2D Mater.* **4** 021003

[134] Zhang X-X *et al* 2017 Magnetic brightening and control of dark excitons in monolayer WSe_2 *Nat. Nanotechnol.* **12** 883–8

[135] Zhou Y *et al* 2017 Probing dark excitons in atomically thin semiconductors via near-field coupling to surface plasmon polaritons *Nat. Nanotechnol.* **12** 856–60

[136] Zhang C, Chen Y, Johnson A, Li M-Y, Li L-J, Mende P C, Feenstra R M and Shih C-K 2015 Probing critical point energies of transition metal dichalcogenides: surprising indirect gap of single layer WSe_2 *Nano Lett.* **15** 6494–500

[137] Lindlau J, Robert C, Funk V, Förste J, Förg M, Colombier L, Neumann A, Courtade E, Shree S and Taniguchi T 2017 Identifying optical signatures of momentum-dark excitons in transition metal dichalcogenide monolayers (arXiv:1710.00988) (https://doi.org/10.1038/nnano.2016.282)

[138] Feierabend M, Berghäuser G, Knorr A and Malic E 2017 Proposal for dark exciton based chemical sensors *Nat. Commun.* **8** 14776

[139] Wang G *et al* 2015 Spin-orbit engineering in transition metal dichalcogenide alloy monolayers *Nat. Commun.* **6** 10110

[140] Fang H *et al* 2014 Strong interlayer coupling in van der Waals heterostructures built from single-layer chalcogenides *Proc. Natl Acad. Sci. USA* **111** 6198–202

[141] Rivera P *et al* 2015 Observation of long-lived interlayer excitons in monolayer $MoSe_2$–WSe_2 heterostructures *Nat. Commun.* **6** 6242

[142] Nagler P *et al* 2017 Interlayer exciton dynamics in a dichalcogenide monolayer heterostructure *2D Mater.* **4** 025112

[143] Fogler M M, Butov L V and Novoselov K S 2014 High-temperature superfluidity with indirect excitons in van der Waals heterostructures *Nat. Commun.* **5** 4555

[144] Gao S, Yang L and Spataru C D 2017 Interlayer coupling and gate-tunable excitons in transition metal dichalcogenide heterostructures *Nano Lett.* **17** 7809–13

[145] Hanbicki A T, Chuang H-J, Rosenberger M R, Hellberg C S, Sivaram S V, McCreary K M, Mazin I I and Jonker B T 2018 Double indirect interlayer exciton in a $MoSe_2$/WSe_2 van der Waals heterostructure *ACS Nano* **12** 4719–26

[146] Kamban H C and Pedersen T G 2020 Interlayer excitons in van der Waals heterostructures: binding energy, Stark shift, and field-induced dissociation *Sci. Rep.* **10** 5537

[147] Zheng S, Sun L, Yin T, Dubrovkin A M, Liu F, Liu Z, Shen Z X and Fan H J 2015 Monolayers of $W_xMo_{1-x}S_2$ alloy heterostructure with in-plane composition variations *Appl. Phys. Lett.* **106** 063113

[148] Kośmider K and Fernández-Rossier J 2013 Electronic properties of the MoS_2-WS_2 heterojunction *Phys. Rev.* B **87** 075451

[149] Chiu M-H, Zhang C, Shiu H-W, Chuu C-P, Chen C-H, Chang C-Y S, Chen C-H, Chou M-Y, Shih C-K and Li L-J 2015 Determination of band alignment in the single-layer MoS_2/WSe_2 heterojunction *Nat. Commun.* **6** 7666

[150] Ovesen S, Brem S, Linderälv C, Kuisma M, Korn T, Erhart P, Selig M and Malic E 2019 Interlayer exciton dynamics in van der Waals heterostructures *Commun. Phys.* **2** 23

[151] Hong X, Kim J, Shi S-F, Zhang Y, Jin C, Sun Y, Tongay S, Wu J, Zhang Y and Wang F 2014 Ultrafast charge transfer in atomically thin MoS_2/WS_2 heterostructures *Nat. Nanotechnol.* **9** 682–6

[152] Ceballos F, Bellus M Z, Chiu H-Y and Zhao H 2014 Ultrafast charge separation and indirect exciton formation in a MoS_2–$MoSe_2$ van der Waals heterostructure *ACS Nano* **8** 12717–24

[153] Gong Y *et al* 2014 Vertical and in-plane heterostructures from WS_2/MoS_2 monolayers *Nat. Mater.* **13** 1135–42

[154] Heo H *et al* 2015 Interlayer orientation-dependent light absorption and emission in monolayer semiconductor stacks *Nat. Commun.* **6** 7372

[155] Li Y *et al* 2014 Valley splitting and polarization by the Zeeman effect in monolayer $MoSe_2$ *Phys. Rev. Lett.* **113** 266804

[156] Van der Donck M and Peeters F M 2018 Interlayer excitons in transition metal dichalcogenide heterostructures *Phys. Rev.* B **98** 115104

[157] Jauregui L A *et al* 2019 Electrical control of interlayer exciton dynamics in atomically thin heterostructures *Science* **366** 870–5

[158] Miller B, Steinhoff A, Pano B, Klein J, Jahnke F, Holleitner A and Wurstbauer U J N L 2017 Long-lived direct and indirect interlayer excitons in van der Waals heterostructures *Nano Lett.* **17** 5229–37

[159] Yu H, Liu G-B, Tang J, Xu X and Yao W 2017 Moiré excitons: from programmable quantum emitter arrays to spin-orbit–coupled artificial lattices *Sci. Adv.* **3** e1701696

[160] Brem S, Linderälv C, Erhart P and Malic E 2020 Tunable phases of moiré excitons in van der Waals heterostructures *Nano Lett.* **20** 8534–40

[161] Patel H, Huang L, Kim C-J, Park J and Graham M W 2019 Stacking angle-tunable photoluminescence from interlayer exciton states in twisted bilayer graphene *Nat. Commun.* **10** 1445

[162] Wu F, Lovorn T and MacDonald A H 2018 Theory of optical absorption by interlayer excitons in transition metal dichalcogenide heterobilayers *Phys. Rev.* B **97** 035306

[163] Zuo L *et al* 2017 Polymer-modified halide perovskite films for efficient and stable planar heterojunction solar cells *Sci. Adv.* **3** e1700106

[164] Rivera P, Seyler K L, Yu H, Schaibley J R, Yan J, Mandrus D G, Yao W and Xu X 2016 Valley-polarized exciton dynamics in a 2D semiconductor heterostructure *Science* **351** 688–91

[165] Montblanch A R-P, Kara D M, Paradisanos I, Purser C M, Feuer M S, Alexeev E M, Stefan L, Qin Y, Blei M and Wang G 2020 Confinement of long-lived interlayer excitons in WS_2/WSe_2 heterostructures *Commun. Phys.* **4** 1–8

[166] Unuchek D, Ciarrocchi A, Avsar A, Watanabe K, Taniguchi T and Kis A 2018 Room-temperature electrical control of exciton flux in a van der Waals heterostructure *Nature* **560** 340–4

[167] Jiang C, Xu W, Rasmita A, Huang Z, Li K, Xiong Q and Gao W-B 2018 Microsecond dark-exciton valley polarization memory in two-dimensional heterostructures *Nat. Commun.* **9** 753

[168] Cadiz F *et al* 2017 Excitonic linewidth approaching the homogeneous limit in MoS_2-based van der Waals heterostructures *Phys. Rev.* X **7** 021026

[169] Srivastava A, Sidler M, Allain A V, Lembke D S, Kis A and Imamoğlu A 2015 Optically active quantum dots in monolayer WSe_2 *Nat. Nanotechnol.* **10** 491–6

[170] He Y-M *et al* 2015 Single quantum emitters in monolayer semiconductors *Nat. Nanotechnol.* **10** 497–502

[171] Chow P K, Jacobs-Gedrim R B, Gao J, Lu T-M, Yu B, Terrones H and Koratkar N 2015 Defect-induced

photoluminescence in monolayer semiconducting transition metal dichalcogenides *ACS Nano* **9** 1520–7
[172] Tonndorf P, Schmidt R, Schneider R, Kern J, Buscema M, Steele G A, Castellanos-Gomez A, van der Zant H S J, Michaelis de Vasconcellos S and Bratschitsch R 2015 Single-photon emission from localized excitons in an atomically thin semiconductor *Optica* **2** 347–52
[173] Chakraborty C, Kinnischtzke L, Goodfellow K M, Beams R and Vamivakas A N 2015 Voltage-controlled quantum light from an atomically thin semiconductor *Nat. Nanotechnol.* **10** 507–11
[174] Koperski M, Nogajewski K, Arora A, Cherkez V, Mallet P, Veuillen J Y, Marcus J, Kossacki P and Potemski M 2015 Single photon emitters in exfoliated WSe_2 structures *Nat. Nanotechnol.* **10** 503–6
[175] Kumar S, Kaczmarczyk A and Gerardot B D 2015 Strain-induced spatial and spectral isolation of quantum emitters in mono- and bilayer WSe_2 *Nano Lett.* **15** 7567–73
[176] Singh A *et al* 2016 Long-lived valley polarization of intravalley trions in monolayer WSe_2 *Phys. Rev. Lett.* **117** 257402
[177] Hoshi Y, Kuroda T, Okada M, Moriya R, Masubuchi S, Watanabe K, Taniguchi T, Kitaura R and Machida T 2017 Suppression of exciton-exciton annihilation in tungsten disulfide monolayers encapsulated by hexagonal boron nitrides *Phys. Rev.* B **95** 241403
[178] Zhang X *et al* 2019 Defect-controlled nucleation and orientation of WSe_2 on hBN: a route to single-crystal epitaxial monolayers *ACS Nano* **13** 3341–52
[179] Wang G, Bouet L, Lagarde D, Vidal M, Balocchi A, Amand T, Marie X and Urbaszek B 2014 Valley dynamics probed through charged and neutral exciton emission in monolayer WSe_2 *Phys. Rev.* B **90** 075413
[180] Fu J, Cruz J M R and Qu F 2019 Valley dynamics of different trion species in monolayer WSe_2 *Appl. Phys. Lett.* **115** 082101
[181] Plechinger G, Nagler P, Arora A, Schmidt R, Chernikov A, Del Águila A G, Christianen P C M, Bratschitsch R, Schüller C and Korn T 2016 Trion fine structure and coupled spin–valley dynamics in monolayer tungsten disulfide *Nat. Commun.* **7** 12715
[182] Mak K F, He K, Lee C, Lee G H, Hone J, Heinz T F and Shan J 2013 Tightly bound trions in monolayer MoS_2 *Nat. Mater.* **12** 207–11
[183] Lui C H, Frenzel A J, Pilon D V, Lee Y H, Ling X, Akselrod G M, Kong J and Gedik N 2014 Trion-induced negative photoconductivity in monolayer MoS_2 *Phys. Rev. Lett.* **113** 166801
[184] Singh A *et al* 2016 Trion formation dynamics in monolayer transition metal dichalcogenides *Phys. Rev.* B **93** 041401
[185] Dutt M V G *et al* 2005 Stimulated and spontaneous optical generation of electron spin coherence in charged GaAs quantum dots *Phys. Rev. Lett.* **94** 227403
[186] Anghel S, Singh A, Passmann F, Iwata H, Moore J N, Yusa G, Li X and Betz M 2016 Enhanced spin-polarization lifetimes in a two-dimensional electron gas in a gate-controlled GaAs quantum well *Phys. Rev.* B **94** 035303
[187] Vanelle E, Paillard M, Marie X, Amand T, Gilliot P, Brinkmann D, Lévy R, Cibert J and Tatarenko S 2000 Spin coherence and formation dynamics of charged excitons in $CdTe/Cd_{1-x-y}Mg_xZn_yTe$ quantum wells *Phys. Rev.* B **62** 2696–705
[188] Yang L, Sinitsyn N A, Chen W, Yuan J, Zhang J, Lou J and Crooker Scott A 2015 Long-lived nanosecond spin relaxation and spin coherence of electrons in monolayer MoS_2 and WS_2 *Nat. Phys.* **11** 830–4
[189] Song X, Xie S, Kang K, Park J and Sih V 2016 Long-lived hole spin/valley polarization probed by kerr rotation in monolayer WSe_2 *Nano Lett.* **16** 5010–4
[190] Poellmann C, Steinleitner P, Leierseder U, Nagler P, Plechinger G, Porer M, Bratschitsch R, Schüller C, Korn T and Huber R 2015 Resonant internal quantum transitions and femtosecond radiative decay of excitons in monolayer WSe_2 *Nat. Mater.* **14** 889–93
[191] Zhu C R, Zhang K, Glazov M, Urbaszek B, Amand T, Ji Z W, Liu B L and Marie X 2014 Exciton valley dynamics probed by Kerr rotation in WSe_2 monolayers *Phys. Rev.* B **90** 161302
[192] Zhang W, Tanaka K, Hasegawa Y, Shinokita K, Matsuda K and Miyauchi Y 2020 Bright and highly valley polarized trions in chemically doped monolayer MoS_2 *Appl. Phys. Express* **13** 035002
[193] Carmiggelt J J, Borst M and van der Sar T 2020 Exciton-to-trion conversion as a control mechanism for valley polarization in room-temperature monolayer WS_2 *Sci. Rep.* **10** 17389
[194] Hao K *et al* 2017 Trion valley coherence in monolayer semiconductors *2D Mater.* **4** 025105
[195] Cundiff S T, Bristow A D, Siemens M, Li H, Moody G, Karaiskaj D, Dai X and Zhang T 2012 Optical 2D fourier transform spectroscopy of excitons in semiconductor nanostructures *IEEE J. Sel. Top. Quantum Electron.* **18** 318–28
[196] Hichri A and Jaziri S 2020 Trion fine structure and anomalous Hall effect in monolayer transition metal dichalcogenides *Phys. Rev.* B **102** 085407
[197] Kapuściński P *et al* 2020 Valley polarization of singlet and triplet trions in a WS_2 monolayer in magnetic fields *Phys. Chem. Chem. Phys.* **22** 19155–61
[198] Chakraborty C, Mukherjee A, Qiu L and Vamivakas A N 2019 Electrically tunable valley polarization and valley coherence in monolayer WSe_2 embedded in a van der Waals heterostructure *Opt. Mater. Express* **9** 1479–87
[199] Liu S *et al* 2020 Room-temperature valley polarization in atomically thin semiconductors via chalcogenide alloying *ACS Nano* **14** 9873–83
[200] Sallen G *et al* 2012 Robust optical emission polarization in MoS_2 monolayers through selective valley excitation *Phys. Rev.* B **86** 081301
[201] Kioseoglou G, Hanbicki A T, Currie M, Friedman A L, Gunlycke D and Jonker B T 2012 Valley polarization and intervalley scattering in monolayer MoS_2 *Appl. Phys. Lett.* **101** 221907
[202] Tornatzky H, Kaulitz A-M and Maultzsch J 2018 Resonance profiles of valley polarization in single-layer MoS_2 and $MoSe_2$ *Phys. Rev. Lett.* **121** 167401
[203] Ando T, Nakanishi T and Saito R 1998 Berry's phase and absence of back scattering in carbon nanotubes *J. Phys. Soc. Japan* **67** 2857–62
[204] Woods C R *et al* 2014 Commensurate–incommensurate transition in graphene on hexagonal boron nitride *Nat. Phys.* **10** 451–6
[205] Abanin D A *et al* 2011 Giant nonlocality near the Dirac point in graphene *Science* **332** 328–30
[206] Renard J, Studer M and Folk J A 2014 Origins of nonlocality near the neutrality point in graphene *Phys. Rev. Lett.* **112** 116601
[207] Titov M *et al* 2013 Giant magnetodrag in graphene at charge neutrality *Phys. Rev. Lett.* **111** 166601
[208] Abanin D A, Shytov A V, Levitov L S and Halperin B I 2009 Nonlocal charge transport mediated by spin diffusion in the spin Hall effect regime *Phys. Rev.* B **79** 035304
[209] Ubrig N, Jo S, Philippi M, Costanzo D, Berger H, Kuzmenko A B and Morpurgo A F 2017 Microscopic

origin of the valley Hall effect in transition metal dichalcogenides revealed by wavelength-dependent mapping *Nano Lett.* **17** 5719–25
[210] Wu Z *et al* 2019 Intrinsic valley Hall transport in atomically thin MoS_2 *Nat. Commun.* **10** 611
[211] Guan H, Tang N, Huang H, Zhang X, Su M, Liu X, Liao L, Ge W and Shen B 2019 Inversion symmetry breaking induced valley Hall effect in multilayer WSe_2 *ACS Nano* **13** 9325–31
[212] Zou C *et al* 2018 Probing magnetic-proximity-effect enlarged valley splitting in monolayer WSe_2 by photoluminescence *Nano Res.* **11** 6252–9
[213] Aivazian G, Gong Z, Jones A M, Chu R-L, Yan J, Mandrus D G, Zhang C, Cobden D, Yao W and Xu X 2015 Magnetic control of valley pseudospin in monolayer WSe_2 *Nat. Phys.* **11** 148–52
[214] Arora A, Schmidt R, Schneider R, Molas M R, Breslavetz I, Potemski M and Bratschitsch R 2016 Valley Zeeman splitting and valley polarization of neutral and charged excitons in monolayer $MoTe_2$ at high magnetic fields *Nano Lett.* **16** 3624–9
[215] Kormányos A, Zólyomi V, Drummond N D, Rakyta P, Burkard G and Fal'ko V I 2013 Monolayer MoS_2: trigonal warping, the Γ valley, and spin-orbit coupling effects *Phys. Rev.* B **88** 045416
[216] Liu G-B, Shan W-Y, Yao Y, Yao W and Xiao D 2013 Three-band tight-binding model for monolayers of group-VIB transition metal dichalcogenides *Phys. Rev.* B **88** 085433
[217] Klein J *et al* 2021 Controlling exciton many-body states by the electric-field effect in monolayer MoS_2 *Phys. Rev. Res.* **3** L022009
[218] Wang T *et al* 2020 Giant valley-Zeeman splitting from spin-singlet and spin-triplet interlayer excitons in $WSe_2/MoSe_2$ heterostructure *Nano Lett.* **20** 694–700
[219] Zihlmann S, Cummings A W, Garcia J H, Kedves M, Watanabe K, Taniguchi T, Schönenberger C and Makk P 2018 Large spin relaxation anisotropy and valley-Zeeman spin-orbit coupling in WSe_2/graphene/h-BN heterostructures *Phys. Rev.* B **97** 075434
[220] Zhang Y J, Oka T, Suzuki R, Ye J T and Iwasa Y 2014 Electrically switchable chiral light-emitting transistor *Science* **344** 725–8
[221] Yuan H *et al* 2013 Zeeman-type spin splitting controlled by an electric field *Nat. Phys.* **9** 563–9
[222] Kim Y and Lee J D 2019 Anomalous electron dynamics induced through the valley magnetic domain: a pathway to valleytronic current processing *Nano Lett.* **19** 4166–73
[223] Wu Z, Li J, Zhang X, Redwing J M and Zheng Y 2019 Room-temperature active modulation of valley dynamics in a monolayer semiconductor through chiral Purcell effects *Adv. Mater.* **31** 1904132
[224] Li J, Zhang R-X, Yin Z, Zhang J, Watanabe K, Taniguchi T, Liu C and Zhu J 2018 A valley valve and electron beam splitter *Science* **362** 1149–52
[225] Jung J, Zhang F, Qiao Z and Macdonald A H 2011 Valley-Hall kink and edge states in multilayer graphene *Phys. Rev.* B **84** 075418
[226] Lundt N *et al* 2019 Optical valley Hall effect for highly valley-coherent exciton-polaritons in an atomically thin semiconductor *Nat. Nanotechnol.* **14** 770–5
[227] Zhang D *et al* 2020 Room temperature near unity spin polarization in 2D Van der Waals heterostructures *Nat. Commun.* **11** 4442
[228] Fang Y, Verre R, Shao L, Nordlander P and Käll M 2016 Hot electron generation and cathodoluminescence nanoscopy of chiral split ring resonators *Nano Lett.* **16** 5183–90
[229] Deng M, Wang X, Chen J, Li Z, Xue M, Zhou Z, Lin F, Zhu X and Fang Z 2021 Plasmonic modulation of valleytronic emission in two-dimensional transition metal dichalcogenides *Adv. Funct. Mater.* **31** 2010234
[230] Guddala S, Kawaguchi Y, Komissarenko F, Kiriushechkina S, Vakulenko A, Chen K, Alù A, Menon V M and Khanikaev A B 2021 All-optical nonreciprocity due to valley polarization pumping in transition metal dichalcogenides *Nat. Commun.* **12** 3746
[231] Zhu X *et al* 2021 Revealing the many-body interactions and valley-polarization behavior in Re-doped MoS_2 monolayers *Appl. Phys. Lett.* **118** 113101
[232] Wei X, Zhang J, Zhao B and Yang Z 2020 Coexistence of valley polarization and Chern insulating states in MoS_2 monolayers with n-p codoping *Sci. Rep.* **10** 9851
[233] Molas M R *et al* 2019 Probing and manipulating valley coherence of dark excitons in monolayer WSe_2 *Phys. Rev. Lett.* **123** 096803
[234] Rupprecht C *et al* 2020 Manipulation of room-temperature valley-coherent exciton-polaritons in atomically thin crystals by real and artificial magnetic fields *2D Mater.* **7** 035025